AD-A249 628

Form Approved
OMB No. 0704-0188

1a. REPORT SECURITY CLASSIFICATION	1b. RESTRICTIVE MARKINGS
Unclassified	

2a. SECURITY CLASSIFICATION AUTHORITY	3. DISTRIBUTION/AVAILABILITY OF REPORT
2b. DECLASSIFICATION/DOWNGRADING SCHEDULE	Approved for public release, distribution unlimited

DTIC
ELECTE
MAY 0 4 1992
S D
D

4. PERFORMING ORGANIZATION REPORT NUMBER(S)	5. MONITORING ORGANIZATION REPORT NUMBER(S)
VPI-AOE-188	

6a. NAME OF PERFORMING ORGANIZATION	6b. OFFICE SYMBOL (If applicable)	7a. NAME OF MONITORING ORGANIZATION
AOE Department		Office of Naval Research, Fluid Dynamics Program

6c. ADDRESS (City, State, and ZIP Code)	7b. ADDRESS (City, State, and ZIP Code)
Virginia Polytechnic Institute and State Univ. Blacksburg, VA 24061	800 N. Quincy St. Arlington, VA 22217

8a. NAME OF FUNDING/SPONSORING ORGANIZATION	8b. OFFICE SYMBOL (If applicable)	9. PROCUREMENT INSTRUMENT IDENTIFICATION NUMBER
Defense Advanced Research Projects Agency		N00014-90-J-1909

8c. ADDRESS (City, State, and ZIP Code)	10. SOURCE OF FUNDING NUMBERS			
Submarine Technology Program 1400 Wilson Blvd. Arlington, VA 22209	PROGRAM ELEMENT NO.	PROJECT NO.	TASK NO	WORK UNIT ACCESSION N

11. TITLE (Include Security Classification)

An Experimental Study of the Relationship Between Velocity and Pressure Fluctuations in a Wing-Body Junction

12. PERSONAL AUTHOR(S)
M. C. Rife, W. J. Devenport, and R. L. Simpson

13a. TYPE OF REPORT	13b. TIME COVERED	14. DATE OF REPORT (Year, Month, Day)	15. PAGE COUNT
Technical	FROM 12/1/90 TO 1/24/92	1992 January 25	233

16. SUPPLEMENTARY NOTATION

17. COSATI CODES			18. SUBJECT TERMS (Continue on reverse if necessary and identify by block number)
FIELD	GROUP	SUB-GROUP	Boundary Layer Three-Dimensional Separation Turbulence
13	10	01	
14	02		

19. ABSTRACT (Continue on reverse if necessary and identify by block number)

Velocity and pressure fluctuations were measured in a wind tunnel in the plane of symmetry in front of a wing-body junction at an approach free-stream velocity U_{ref} = 28.3 m/s and momentum thickness Reynolds number Re_θ = 6900. The cylindrical wing shape was a 3.2 elliptic nose attached to a NACA 0020 tail at maximum thickness. A two component laser Doppler anemometer was used to make the velocity measurements. Pressure measurements were made at two locations upstream of the wing by a pair of Sennheiser microphones. A relationship between the velocity and pressure was determined to reveal the bimodal structure of the flow field.

Histograms and power spectra of both quantities are presented along with cross-spectra and cross-correlations. The velocity power spectra revealed spectral slopes of -1 through out the entire flow field. Velocity and pressure autospectra show the bimodal

(over)

20. DISTRIBUTION/AVAILABILITY OF ABSTRACT	21. ABSTRACT SECURITY CLASSIFICATION
☒ UNCLASSIFIED/UNLIMITED ☐ SAME AS RPT ☐ DTIC USERS	None
22a. NAME OF RESPONSIBLE INDIVIDUAL	22b. TELEPHONE (Include Area Code) 22c. OFFICE SYMBOL

DD Form 1473, JUN 86   Previous editions are obsolete.   SECURITY CLASSIFICATION OF THIS PAGE

Unclassified

92   4 30   027

Table of Contents

92-11892

List of Figures

List of Tables

List of Symbols

C . . . . chord length of appendage

$C_{p'}$ . . . . coefficient of the root mean square pressure

f . . . . frequency

G_{xy} . . . . one-sided cross-spectral density function, equation (3)

G_{xx}, G_{yy} . . . . one-sided auto-spectral density functions, equation (2)

P . . . . mean pressure

p . . . . instaneous pressure fluctuation

$\overline{p^2}$ . . . . mean square of the pressure

r . . . . time lag in seconds

R_{xy} . . . . cross-correlation function

R_{xx}, R_{yy} . . . . auto-correlation functions

Re_{θ} . . . . Reynolds number based on momentum thickness

t . . . . thickness of appendage

T . . . . time in seconds

U,V,W	....	time-mean velocity components in X,Y,Z directions
U_c	....	velocity of a coherent structure
U_e	....	boundary layer edge velocity
U_{ref}	....	reference velocity
u,v,w	....	instantaneous X,Y,Z velocity fluctuations
$-\bar{u}\bar{v},-\bar{u}\bar{w},-\bar{v}\bar{w}$	.....	time-mean Reynolds stresses
u^2, v^2	....	turbulence normal stresses
$\overline{u^2},\overline{v^2}$	....	mean square of the velocity component
X	....	streamwise direction
Y	....	direction normal to X and Z
Z	....	transverse direction

Greek Symbols

$\delta_{99.5}, \delta$	....	boundary layer thicknesses, where $U/U_{ref} = .995$ and U/U_{ref}
θ	....	boundary layer momentum thickness
γ^2_{xy}	....	ordinary coherence function, equation (4)
γ_b	....	proportion of time backflow exists
Φ	....	phase angle between two signals, equation (5)
ρ_{xy}	....	cross-correlation coefficient function, equation (6)
τ_w	....	wall shear stress

1.0 Introduction

Turbulent wing-body junction flows are complex and highly three-dimensional. This type of flow is created when a turbulent boundary layer encounters an obstruction projecting from a surface. Typically, this obstruction has an airfoil cross-section, figure 1. The oncoming turbulent boundary layer has a spanwise distribution of vorticity. As the boundary layer meets the obstruction, the large streamwise adverse pressure gradient it experiences causes it to separate from the wall. The initially spanwise vorticity present in the boundary layer wraps around the appendage and forms a horseshoe vortex. This vortex has counter-rotating legs which contribute streamwise vorticity to the flow downstream. Between the leading edge and maximum thickness of the wing the flow is accelerated, downstream of the maximum thickness an adverse pressure gradient is encountered. At the trailing edge of the airfoil, this may cause a small region of separation may occur.

These flows are of considerable interest to engineers. Bridge supports, aircraft wings, ship hull appendage junctions, and turbo-machines are just a few of

the areas in which this flow occurs. The junction vortex can cause erosion around bridge supports, excessive noise and vibration in aircraft wings and ship hulls due to increased turbulence, and high rates of heat transfer in turbo-machines. Greater knowledge of these flows through research will allow their adverse effects to be controlled.

Considerable research has been done on the flow past a wing-body junction. However, the majority of it has been in reference to the mean velocity and the average turbulence field. Dickinson (1986) studied a NACA 0020 airfoil and an airfoil with a 3:2 elliptical nose section and a NACA 0020 tail. Using oil flows and oil dots along the test wall, he found the expected three-dimensional separation line located upstream of the nose. A line of apparently low shear between the separation location and the wing nose was also found. Cross hot-film probes were also used to take mean and fluctuating three-dimensional velocity measurements downstream of the nose. Dickinson found that the blunter the nose the stronger the cross-flow velocities associated with the junction vortex. He speculated that inside the three-dimensional separation the secondary flow consists of a primary vortex and a small counter-rotating vortex in the corner of the wing-body junction.

Kubendran, McMahon, and Hubbartt (1985) and Mehta (1984) used hot wires to study the flow field in the nose region of wing-body junctions. Their measurements showed the size and strength of the junction vortex to be dependent on nose bluntness. The mean and turbulent flow quantities in the juncture are in turn dependant on the junction vortex. Abid and Schmitt (1986) studied the flow

field in the nose region of a streamlined circular cylinder with a three color laser doppler velocimeter. Their velocity measurements confirm the presence of the three-dimensional separation found by flow visualization techniques. They believe that their mean velocity measurements confirm the presence of two vortical structures inside the separated region. These two vortices are thought to be the two large vortices in the four vortex model of Norman (1972) shown in figure 2. The two smaller vortices were not seen because of their small spatial extent.

Hasan, Casarella, and Rood (1985) studied the flow past a wing-body junction with hot wires and microphones. Significant increases in turbulence levels were found in the boundary layer and secondary flow. These have been attributed to the low frequency organized motion associated with the mean junction vortex. Wall pressure fluctuation measurements made near the nose show an increase in root mean square pressure compared to those in the onset boundary layer. An increase in low frequency content of the pressure is evident as the wing is approached.

Agarwal (1989) studied the pressure fluctuations under the flow-field produced by a 3:2 elliptic nosed, NACA 0020 tailed, cylindrical airfoil. Histograms and spectra of his pressure measurements were produced. From these he found an increase in the root mean square of the pressure at the nose of a wing body junction. These pressure increases are under the flow region associated with the junction vortex.

Although most research in wing-body junctions has concentrated on the mean velocity and turbulence, several researchers have produced work attempting to define

the instantaneous flow structure. Rood (1984) used hot films to study the flow around bodies with elliptic noses, parallel sides, and circular arc tails. Of his several conclusions, three have particular interest for this study. First the mean flow was found to be characterized by a root vortex originating with the separation from the wall immediately upstream from the wing leading edge. Secondly, a characteristic or resonant frequency for the horseshoe vortex apex (defined as the origin of the wall separation upstream from the wing leading edge) was not found. Finally, three frequency bands were defined which were presumed to be associated with different flow disturbance structures. Structures in bandwidth I are characterized by $f^*\delta/U = .003$ to $f^*\delta/U = .0975$. The frequencies f have been non-dimensionalized on the boundary layer thickness δ and the free stream velocity U. These are present only in the onset boundary layer. The range $f^*\delta/U = .0375$ to $f^*\delta/U = .12$ is found in the region of boundary layer interaction around and downstream from the wing and away from the wall and is called bandwidth II. Bandwidth III, $f^*\delta/U = .00075$ to $f^*\delta/U = .015$, was found to be clearly the result of the wing's presence as this bandwidth appears in the wing-body junction wake flow.

Another experiment to define the instantaneous flow structure in the nose region of a wing-body junction was conducted by Devenport and Simpson (1990b). Three component laser Doppler velocimeter measurements were made along the plane of symmetry upstream of a model with a 3:2 elliptic nose mated to a NACA 0020 tail at the maximum thickness. An oil flow taken by Devenport and Simpson (1990b) is shown in figure 3. This figure shows the three-dimensional separation line

located at approximately $x/t = -.47$ and the presumed line of low shear much nearer the wing. The region between the separation line and the wing contains the junction vortex. Figure 4 is the mean velocity vectors in the plane of symmetry produced from Devenport and Simpson (1990b). The mean junction vortex is evident in the region of $x/t = -.1$ to $x/t = -.3$, with x being the streamwise coordinate and t being the body thickness. In the vicinity of the junction vortex, maximum values for turbulent stresses were found to be much greater than in normal turbulent boundary layers. The peak values of $\overline{v^2}$ and $-\overline{uv}$ were observed in an area of high mean velocity gradient near the mean vortex center. However, maximum $\overline{u^2}$ was found close to the wall in a region of intense back flow. A plot of contours of turbulence kinetic energy production is shown in figure 5. The regions of maximum turbulence energy production are in the vicinity of the locations of the maximum turbulent normal stresses. Associated with these stresses are bimodal (double peaked) probability density functions of velocity. Figure 6 shows some representative probability density functions of U component velocity fluctuations from Devenport and Simpson (1990b). These types of probability densities occur in both the u and v velocity components in a region centered around the mean junction vortex. For the u component functions one of the peaks is always centered around zero velocity while the other peak is at some negative velocity. These facts lead to the names of zero flow and backflow for the two modes encountered. By decomposing the bimodal probability density functions into their component distributions in an approximate way Devenport and Simpson (1990b) drew velocity vector plots showing possible flow

structure associated with each mode, figure 7. Devenport and Simpson (1990b) also estimated the proportion of time the backflow mode existed at streamwise locations in the bimodal zone. Contours of this parameter, called γ_b, are shown in figure 8.

Kim (1991) studied the flow around a 3:2 elliptical nosed NACA 0020 tailed cylindrical airfoil in a water tunnel at two Reynolds numbers, $Re_\theta = 330$ and $Re_\theta = 1100$. At the higher Reynolds number only laser velocimeter measurements were made in the plane of symmetry at the nose. Laser velocimeter measurements and hydrogen bubble wire flow visualizations were made at the lower Reynolds number. The laser velocimeter measurements revealed much of the same flow features as Devenport and Simpson (1990b) documented. The bimodal histograms seen by Devenport and Simpson (1990b) were found as well as the large backflow near the wall. The helium bubble wire visualizations showed what appear to be multiple vortices interacting near the juncture. Kim (1991) proposed a series of leap frogging vortices to explain these visualizations. A primary vortex near the wing is leap frogged by a series of secondary vortices which bring high momentum fluid into the primary vortex. According to Kim (1991) the vortex stretches at a faster rate as it gains strength. He proposed that after the stretching of the vortex, the backflow reaches far upstream and forms a large but weak junction vortex structure.

The works of Rood (1984), Devenport and Simpson (1990b), and Agarwal (1989) provide the justification for the present research. The goal of this work is to provide a better understanding of the instantaneous flow structure at the nose of a wing-body junction. This was accomplished by studying the relationship between the

velocity field and the wall pressure fluctuations at the nose of a wing-body junction. To study this relationship, simultaneous velocity and pressure fluctuation measurements were made in the plane of symmetry upstream of a wing body junction. The same wind tunnel, wing model, and flow conditions used by Devenport and Simpson (1990b) and Agarwal (1989) were employed allowing direct comparison with previous results.

2.0 Experimental Apparatus and Techniques

2.1 Facilities and Equipment

2.1.1 Wind Tunnel

All measurements were made in the low speed boundary layer tunnel at Virginia Tech which is a blow down open circuit wind tunnel. Air is supplied by a centrifugal blower to a fixed-setting flow damper and into the plenum. In the plenum, there is a section of honeycomb to remove the mean swirl and seven screens to reduce the mean turbulence level. After the plenum, a two-dimensional four to one contraction ratio nozzle further reduces the turbulence levels and accelerates the flow to test speed. This tunnel has been used extensively by other researchers at Virginia Tech (Ahn (1986), Devenport and Simpson (1990b), and Agarwal (1989)).

The test section of the wind tunnel, shown in figure 9, is 6 m long and .91 m wide with a rectangular cross-section. The upper wall, made from plexiglas reinforced with aluminum channel, is curved to provide a further 1.5 to 1 contraction

at the test section entrance. The throat of this contraction is 25.4 cm high and is reached after 1.63 m. This part of the upper wall of the contraction is supported by adjustable brackets to allow a change in contraction if necessary. Further downstream the upper wall is almost parallel to the lower wall. It diverges only slightly with downstream distance to provide a zero pressure gradient flow in this region of the test section. The side walls are made of float plate glass to allow the use of laser anemometry. Plexiglas wall liners are used to support the upper wall beginning 1.09 m downstream of the throat of the contraction. In the vicinity of the model, there are removable liner sections. With no model present these are left in place to provide a zero pressure gradient flow. The lower test wall is made of 19 mm thick fin-form plywood. At the nose of the model, the lower test wall is made of plexiglas to allow velocity measurements by a laser through the lower wall. To seed the flow for laser measurements a slot is located just upstream of the test section entrance.

The boundary layer along the lower wall is tripped at the test section entrance by a .63 cm high rearward facing step. Ahn 1986 studied the boundary layer properties of this tunnel with no model present. The statistical and spectral properties were found to be like those of an equilibrium boundary layer. Measurements made in the boundary layer closely satisfy the two dimensional momentum integral equation. No preferred frequencies were found in the velocity and pressure spectra.

The turbulence intensity of the tunnel main stream at 27 m/s is .2% (Devenport and Simpson 1990b). On the test wall, the root mean square pressure coefficient due to acoustic noise, C_p', is .0042126.

2.1.1 Model

The wing is cylindrical with a chord c of 30.5 cm, a height of 22.9 cm and maximum thickness t of 7.17 cm. Its cross-section consists of a 3:2 elliptical nose, with its major axis aligned with the chord, mated to a NACA 0020 tail at maximum thickness, figure 10. The wing is mounted at zero angle of attack and zero sweep with its leading edge 2.92 m downstream of the test section entrance. The boundary layer on the wing is tripped by .635 cm wide 120 grit sand paper strips mounted 2.29 cm upstream of the wing maximum thickness.

As recommended by Dechow (1977), a 37 mm gap was left between the wing and the upper test section wall to prevent a second junction vortex from forming and interfering with downstream measurements. To minimize the blockage effects of the wing, the removable sections of the wall liners were removed during measurements. Steps left by the liners were covered with tape to provide a smooth transition.

2.2 Instrumentation

2.2.1 Microphones

Sennheiser MKH-110 microphones were used to make pressure fluctuation measurements. The unmodified microphones have a frequency range of 1 to 20000

Hz and a sensitivity of 20 mV/Pa. The power for the microphones was supplied by a highly stable Hewlett Packard 6213a 0-12 V variable power supply.

Two microphones were mounted in separate, identical plexiglas housings. Two microphone, housing combinations were mounted on the same base as shown in figure 11. When mounted in the housing, the 13.5 mm diameter diaphragm of the microphone was 1 mm away from the upper housing surface. Four of the five 0.63 mm openings in each housing were covered by cellophane tape during data acquisition. To achieve the smallest possible spacing, the two holes closest to each other were left open for pressure measurements. Simpson, Ghodbane, and McGrath (1987) calibrated these microphone and housing combinations with a Genrad Modal 1956 sound-level calibrator between 125 Hz and 4 Khz and 74 Db to 114 Db sound pressure levels. A calibrator consisting of a sealed volume with an oscillating piston was used for calibration at low frequencies. The sensitivity at low frequencies was found to be 20 Mv/Pa. The frequency response (in Mv/Pa) of these microphones in their housings is given by

$$20/(1-0.43787 \times f^2 - 0.0800 \times f^4 + 0.0493292 \times f^6)^{\frac{1}{2}} \quad (1)$$

where the frequency, f, is in Khz. This equation indicates that the microphone sensitivity is reduced above 1.5 Khz because of the housing.

The microphones were positioned in a slot in front of the wing (see figure 10) with their holes aligned with the plane of symmetry and their tops flush with the test

floor. To reduce interference caused by tunnel vibration, the microphones were supported directly from the laboratory floor. The gaps between microphone housings and the lower tunnel test wall were sealed with cellophane tape which prevented any tunnel vibration from being transmitted to the microphones.

However, the pressure fluctuation measurements were still contaminated by acoustic noise. In the past, techniques have been used to cancel the acoustic contribution to the microphone signal. In a nominally two-dimensional flow Simpson, Ghodbane, and McGrath (1987) used two microphones at the same streamwise location but separated by a large spanwise distance to cancel the contribution from acoustic noise to the microphone signal. By calculating the mean square value of the difference between the two signals, the actual turbulent pressure spectrum was found. To cancel the vibrational and acoustic noise content Agarwal (1989) used two microphones on a common mount. Subtraction of the two signals then canceled the acoustic and vibrational noise and also some of the turbulence produced signal below 2 Khz. However, neither of these techniques were suitable for use in the present experiment. The subtraction technique of Agarwal 1989 would cancel the low frequency contributions of the turbulent flow. The technique of Simpson et al (1987) would not be satisfactory due to the spanwise differences in the pressure field at the nose of the wing. For this reason no effort was made to eliminate contamination by acoustic noise. The magnitude of this contamination and its effects on the results will be discussed later.

The outputs of the two microphones were connected to a Data 6000 model 611 Data Precision Waveform Analyzer. The Data 6000 was operated remotely by an IBM PC/AT through an IEEE 488 interface, as shown in figure 12. All data were continuously recorded on a hard disk for later processing. The Data 6000 has a 14 bit analog to digital converter. With a ±5.0 V input, a resolution of 0.6 mv is achieved. To remove their bias voltage, the microphones outputs were AC coupled to the Data 6000.

Due to an oversight, the Sennheiser microphones were used with an operating voltage of 5 V instead of the recommended 8 V. After completion of the measurements, the Genrad Model 1956 sound-level calibrator (used by Simpson et al (1987)) was used to investigate the effects of this oversight. Figure 13 shows the output voltage ratios in Db versus frequency for five sound pressure levels. The mean db value for all the data points is 2.078 db corresponding to $V_5/V_8 \approx 0.8$ where V_5 is the voltage output at 5 volts operating voltage and V_8 is the voltage output at 8 volts operating voltage. All data points except the lowest frequency points at 74 db are easily within ±1 db of the mean. This point is thought to be in error because of difficulty in reading the microphone output at this low sound pressure level.

2.2.2 Laser Doppler Anemometer

Velocity measurements were made with a two component laser Doppler velocimeter (LDV). The velocimeter uses a Coherent Innova 90 argon-ion laser. This laser operates at a wavelength of 514.5 nm and at a power level of just over 1 W. The laser beam is passed through a two axis Bragg cell which has 21.5 Mhz and

15 Mhz transducers to diffract the light in the horizontal and vertical planes respectively. The transducers are powered by two interaction model ME transmitters. The optical system was designed by Simpson and Chew (1979) and produces convergent beams that enter the tunnel through one of its grass side walls.

When the unshifted beam and the 21.5 Mhz beam are crossed, they produce a moving fringe pattern in the measurement volume sensitive to the streamwise component of the velocity, see figure 10. These two beams enter the tunnel at a slight angle (approximately 1°) to the lower test wall to prevent the lower test wall from interfering with the beam paths when near wall measurements are made. The unshifted beam and -15 Mhz shifted beam lie in the same vertical plane. When crossed they produce a moving fringe pattern sensitive to the vertical velocity component.

Seeding material, dioctal phthalate smoke, is introduced into the boundary layer at the leading edge of the test section floor, see figure 9. The smoke is produced by an aerosol generator described by Simpson and Chew (1979), and originally designed by Echols and Young (1963).

Light scattered from the measurement volume was collected through the opposite test section side wall by a large lens and a Thorn EMI photo-multiplier tube. The PM tube was placed approximately 15° off the laser beam axis in the downstream direction to reduce the effects of glare. This collection of forward scattered light provides an increase in the intensity of the light collected when compared to back scatter collection. This increases the data rate of the LDV system.

The output of the PM tube was connected to the input of a TSI model 1990C frequency counter. The input signal was conditioned with a high pass filter, lower limit set at 10 Mhz, and a low pass filter, upper limit set at 50 Mhz. To ensure that the measurement volume was focused on the PM tube pinhole, the filtered signal was run through a swept spectrum analyzer and displayed on an oscilloscope. This allowed a subjective judgement to be made on the quality of the input signal. A second oscilloscope was used to display the counter output and asses its quality. The counter output was connected to the Data 6000 which is described in the microphone instrumentation section, see figure 11. Data rates of 20,000 bursts per second were easily obtainable at measurement locations far from the lower test wall. Velocity measurements could be made as close as .005 inches above the lower test wall. However close to the wall data rates were lower, 10,000 to 15,000 bursts per second, due to glare caused by the laser beams striking the lower test wall.

2.3 Experimental Methods

2.3.1 Data Acquisition

The coordinate system used for this experiment is a right handed system with its origin at the junction of the wing leading edge and the lower test wall, see figure 10. X and U are defined positive in the downstream direction with Y and V positive vertically upwards.

Measurement locations are shown in figure 14. Eight streamwise locations were chosen for velocity measurements upstream of the wing leading edge. At each streamwise location, thirteen vertical locations, spaced logarithmically, were used to make a velocity profile. This measurement grid encompasses the bimodal region found by Devenport and Simpson (1990b), see figure 4. Both U and V component velocity measurements were made at these locations, but at different times. The microphone pinholes were positioned at $x/t=-.20$ and $x/t=0.0$. The position $x/t=-.20$ was chosen because it lies below the approximate center of the mean junction vortex and the bimodal region. The location $x/t=0.0$ was chosen since it was thought that pressure fluctuations here might also be representative of the large scale instantaneous flow structure.

Data was recorded simultaneously from the two microphones and the LDV frequency counter by the Data 6000 on separate channels. Each signal was sampled at 10 Khz. Data was recorded in loads, each load containing 10,242 points for each channel, just over 1 second of continuous data 30 such loads were taken for each position of the LDV.

2.3.2 Data Reduction

A 512 bin histogram of each velocity signal was made. These histograms were used to calculate the mean and other statistical properties of velocity.

Fast Fourier transforms were performed on the velocity and pressure signals in blocks of 512 or 2048 points. In the later case, blocks were constructed from every

fourth point of the data record, i.e. an effective sampling frequency of 2500 Hz. This allowed both high and low frequency range spectra to be calculated.

The frequency domain data obtained was used to estimate the one-sided autospectral density function by

$$G_{xx}(f) = \frac{2\Delta t}{N}\overline{|X(f)|^2} \qquad (2)$$

where $X(f)$ is the raw FFT, Δt the sampling period, and N the block length. Ninety blocks were used to calculate the average autospectral density functions. No filtering or windowing was used during the calculation of the auto spectral density function.

Functions of the relationship between two signals were calculated between the velocity and each of the pressure signals and between the two pressure signals from the Fourier transforms mentioned above. First, a one sided cross-spectral density estimate was computed using the equation

$$G_{xy}(f) = \frac{2\Delta t}{N}\overline{[X^*(f)Y(f)]} \qquad (3)$$

where $X(f)$ and $Y(f)$ are the fourier transforms of the two signals and a * denotes the complex conjugate. Again the average was taken over ninety blocks.

The ordinary coherence function, γ_{xy}^2, was then calculated from the cross-spectral density function, G_{xy}, and the autospectral density functions, G_{xx} and G_{yy}, of the two signals of interest.

$$\gamma^2_{xy}(f) = \frac{|G_{xy}(f)|^2}{G_{xx}(f)G_{yy}(f)} \qquad (4)$$

The phase spectrum was calculated as

$$\phi(f) = \tan^{-1}[\frac{Q_{xy}(f)}{C_{xy}(f)}] \qquad (5)$$

where C_{xy} and Q_{xy} are the real and imaginary parts of G_{xy} respectively.

Another relationship between pressure and velocity which was calculated was the cross-correlation coefficient function. This involved the calculation of the cross-correlation function and the two auto-correlation functions by applying an inverse FFT to the averaged cross and autospectra.

The cross-correlation coefficient function is given by

$$\rho_{xy}(r\Delta t) = \frac{R_{xy}(r\Delta t)}{\sqrt{R_{xx}(0)R_{yy}(0)}} \qquad r = 0,1,2,...m \qquad (6)$$

where R_{xy}, R_{xx}, and R_{yy} are the cross and autocorrelation functions, $r\Delta t$ is the time lag which is an integer (r) multiple of the original sampling period (Δt). The symbols $\rho_{up}(\tau)$ and $\rho_{vp}(\tau)$ are used to refer to the cross-correlation between the u component velocity or v component velocity and the indicated pressure.

Since the acoustic noise contaminating the microphone signals would have been uncorrelated with the velocity field, it should have had no effect on the functions of the relationship between velocity and pressure fluctuations. Mathematically this can be shown by assuming the total pressure signal is given by

$$p = p_{acoustic} + p_{turbulent} \qquad (7)$$

and the velocity signal is

$$v = v_{turbulent} \qquad (8)$$

The average of the product of the total pressure signal and velocity signal is given by

$$\overline{pv} = \overline{p_{turbulent}v_{turbulent}} + \overline{p_{acoustic}v_{turbulent}} \qquad (9)$$

The acoustic pressure and turbulent velocity field are uncorrelated; therefore, the second term on the right hand side is zero. Thus $\gamma^2_{xy}(f)$, $\Phi(f)$, and $\rho_{xy}(r\Delta t)$ are unaffected by the acoustic pressure. The only reduced data the acoustic data would have affected are the pressure autospectral density functions and results derived from them.

Further data reduction in the form of conditional averaging was also performed. This technique will be discussed when the results are presented to allow a clearer understanding of the technique.

2.4 Uncertainties

Uncertainties in mean velocity components U, V and mean square $\overline{u^2}$, $\overline{v^2}$ measured with the LDV, normalized on U_{ref}, are presented in table 1. These were calculated using the method of Kline and McClintock (1953) for 95% confidence limits.

Uncertainties in the position of the LDV are very important since the region of measurement was small (29×9 mm) and has high streamwise and normal to the wall velocity gradients. Any error in placement could create a velocity profile different than expected. The measurement volume was positioned in the streamwise direction by examining its image on a plexiglas plate scored with lines at the desired streamwise measurement locations. The initial intention was to measure vertical profiles at the same streamwise locations studied by Devenport and Simpson (1990b). Adjustments to the streamwise locations to correct for systematic errors in the above technique caused the final X locations to be different. The uncertainty in X from this technique is estimated to be ±.13 mm or $1.8×10^{-3}$ t. The vertical location of the measurement volume was fixed by comparison with the near-wall mean velocity profiles of Devenport and Simpson (1990b). Y locations could not be measured

directly with sufficient accuracy because of the microphones mounted in the lower test wall. The uncertainty in Y is estimated to be ±.14 mm or 2.0×10^{-3} t.

Uncertainties were computed for the auto-spectral density functions and joint record functions using formulae of Bendat and Piersol (1986). The normalized random error for auto-spectral density functions is given by,

$$\epsilon_r[G_{xx}(f)] = \frac{1}{\sqrt{n_d}} \qquad (10)$$

where $\epsilon_r[G_{xx}(f)]$ is the random error in the auto-spectral density function and n_d is the number of distinct records. In the present experiment $n_d = 90$; therefore, $\epsilon_r[G_{xx}(f)] = .105$, i.e. 10.5%.

To calculate the normalized random error in the ordinary coherence function, γ_{xy}^2 the formula

$$\epsilon[\gamma_{xy}^2] = \frac{\sqrt{2}(1-\gamma_{xy}^2)}{|\gamma_{xy}|\sqrt{n_d}} \qquad (11)$$

was used. Table 2 shows the error in various values of the coherence function. The 100% error for $\gamma_{xy}^2 = .235$ indicates that values of coherence below this have no statistical significance.

For the phase angle, Bendat and Piersol (1986) recommend using the standard deviation instead of the normalized random error since Φ_{xy} may be zero. The standard deviation of Φ_{xy} in radians is given by

$$\Phi'_{xy} = \frac{(1-\gamma^2_{xy})^{\frac{1}{2}}}{|\gamma_{xy}|\sqrt{2n_d}} \qquad (12)$$

95% confidence limits may be obtained by multiplying by two. These results are also tabulated in table 2.

Tables 3 and 4 are the random errors in the cross- correlation coefficient function between the u component velocity and pressure fluctuations and the v component velocity and pressure fluctuations respectively. The error in the cross-correlation coefficient function, ρ_{xy}, is computed from

$$e[\rho_{xy}(\tau)] = \sqrt{[\frac{\delta\rho_{xy}}{\delta R_{xy}}e[R_{xy}(\tau)]]^2 + [\frac{\delta\rho_{xy}}{\delta R_{xx}}e[R_{xx}(0)]]^2 + [\frac{\delta\rho_{xy}}{\delta R_{yy}}e[R_{yy}(0)]]^2} \qquad (13)$$

where the error in the cross-correlation function R_{xy} is given by

$$e[R_{xy}(\tau)] = \frac{1}{\sqrt{2BT}}[1+\rho^{-2}_{xy}(\tau)]^{\frac{1}{2}} \qquad (14)$$

in which τ is the time lag, B is the frequency range of interest, and T is the record length. The error in the auto-correlation functions, R_{xx} and R_{yy}, is given by

$$e[R_{xx}(0)] = \frac{1}{\sqrt{BT}} \qquad (15)$$

Note that the errors in tables 3 and 4 do not account for the finite record lengths used in calculating R_{xy}. True uncertainties are therefore likely to be larger than these estimates.

3.0 Results and Discussion

3.1 Introduction

The experiment was conducted with a free stream velocity, U_{ref}, of 28.3 m/s $\pm 1\%$ as recorded by the pitot static probe located at the throat of the test section, see figure 9. This corresponds to a Reynolds number, Re_θ, based on the momentum thickness of the approach boundary layer, measured 2.15 t upstream of the wing of 6900.

Figures 15 and 16, taken from Devenport (1991), show mean velocity and turbulence intensity profiles measured in the onset boundary layer at $x/t = -2.15$, $z/t = 0.0$, under almost identical conditions. The boundary layer thickness here is 0.5 t. Other boundary layer properties are listed in table 5.

Experimental results will be presented and discussed below in three separate sections containing respectively; velocity measurements, pressure measurements, and measurements illustrating the relationship between velocity and pressure fields.

3.2 Velocity Measurements

3.2.1 Comparisons With Previous Work

Measurements of time mean U and V components of velocity were used to draw mean velocity vectors in the plane of symmetry upstream of the wing. These are compared to similar measurements made by Devenport and Simpson (1990b) (here after referred to as DS (1990b)) in figure 17.

This figure shows that, on average, fluid away from the wall and near the wing is turned toward the wall. The presence of the wall forces this fluid upstream away from the wing. This backflow is slowed as it meets the oncoming boundary layer and moves away from the wall creating a large area of recirculation known as the mean junction vortex. The region where the backflow pulls away from the lower wall (between $x/t = -.25$ and $x/t = -.30$) is the approximate location at which the line of low shear observed in oil flow visualizations by DS (1990b), crosses the plane of symmetry, $x/t = -.27$, (figure 3). Also shown in figure 3 (but not by the vectors) is the primary separation at $x/t = -.47$. Considering the differences in measurement locations, agreement between the two mean vector fields is satisfactory.

Profiles of mean axial velocity, U/U_{ref}, measured with the LDV are compared with similar measurements made by DS (1990b) in figure 18. Each streamwise mean velocity profile from the present experiment is plotted with the two nearest profiles of DS (1990b).

These profiles show the increase in the U component backflow velocity as the wing is approached. A maximum backflow velocity of $U/U_{ref} = -.5$ is reached at $x/t = -.193$ and $y/t = .00477$. Moving further downstream, a slight decrease in backflow is observed due to the increase in the vertical velocity contribution to the total velocity vector.

Bearing in mind the differences in streamwise location the agreement between the present measurements and those of DS (1990b) is, at most points, within the stated uncertainties. Some of the largest differences occur near $x/t = -.237$ where differences between the present measurement locations and those of DS (1990b) are greatest.

Figures 19 and 20 compare contours of turbulence normal stresses $\overline{u^2}/U_{ref}^2$ and $\overline{v^2}/U_{ref}^2$. In the present data set the u component of turbulence normal stress reaches a maximum $\overline{u^2}/U_{ref}^2 = .08$ at $x/t = -.237$ and $y/t = -.007$, figure 19b. The maximum u turbulence normal stress from the data of DS (1990b) reaches a higher value, $\overline{u^2}/U_{ref}^2 = .09$ at $x/t = -.21$ and $y/t = .005$, figure 19a. Both of these maxima occur in an area of intense backflow. The maximum of v component turbulence normal stress, $\overline{v^2}/U_{ref}^2$, in the present data set is 0.05 and occurs at $x/t = -.237$ and $y/t = .05$, (figure 20). Again the maxima of DS (1990b), figure 20a, is higher, $\overline{v^2}/U_{ref}^2 = .07$, and occurs further downstream, $x/t = -.20$, $y/t = .04$. Both of these maxima occur close to the center of the mean junction vortex.

Differences between data sets in the locations of the maxima are at least partly due to differences in measurement location. In both data sets, the true

maxima may have been missed since they probably occur at a location at which no measurements where taken. The contours of values below the maxima, for example $\overline{u^2}/U_{ref}^2$ < .04, cover approximately the same regions in both data sets. Note that the appearance of these contours is fairly dependent on the interpolation scheme used to contour the data. Bearing this in mind the two sets of contours compare reasonably well.

Associated with the turbulence normal stress maxima are bimodal histograms of velocity fluctuations. Histograms of u component velocity fluctuations at $x/t = -.237$, shown in figure 21, are strongly bimodal in the near wall region, $y/t < .01894$ where they clearly have two peaks. The two peaks are the result of two different flow modes. One peak is centered around the tick on the abscissa which represents zero velocity and is known as the zero flow mode. The second peak is at a negative velocity; therefore, it is known as the backflow mode. In the region of $y/t = .02319$ to $y/t = .04551$, a single peak begins to dominate with a much less pronounced secondary peak. Above $y/t = .04551$, no bimodal behavior is exhibited by the u component at this streamwise location. As can be seen by comparison with figure 6, these histograms are very similar to those measured by DS (1990b). The v component histograms at $x/t = -.237$, shown in figure 22, are also bimodal but much further from the wall, $y/t = .01540$ to $y/t = .0572$. In both U and V components, the most bimodal histograms appear at the same locations as their respective turbulence normal stress maxima since an increase in the variance of a histogram is an increase in turbulence normal stress.

In figures 17, 19, and 20 a region enclosed by a dashed line has been shown. This area is called the bimodal zone. The dashed line marks the outer limits at which u or v histograms show bimodal behavior. As can be seen in figure 17, the bimodal zone encompasses the majority of the mean junction vortex. The bimodal zone in the present study has approximately the same extent as the zone found by DS (1990).

Outside of the bimodal region, the velocity histograms take on a more Gaussian-like form. Figures 23 and 24 are u component histograms measured at $x/t = -.0421$ and $x/t = -.391$ respectively, provided for comparison with the bimodal histograms. The u component histograms at $x/t = -.0421$, figure 23, show the intense backflow near the lower test wall associated with this region of the flow field, but do not show a zero flow mode associated with the bimodal region. At $x/t = -.391$, the u component histograms, figure 24, show mostly positive velocities at all vertical locations as would be expected in the onset boundary layer. The v component histograms at $x/t = -.0421$, figure 25, have a large negative component. The v histograms at $x/t = -.391$, figure 26, all have almost zero mean. This is expected since this streamwise location is in the approach boundary layer and the mean velocity here is dominated by the U component.

3.2.2 Power Spectra

Figures 27 through 42 present non-dimensional spectra of the velocity components. Frequency has been normalized on t/U_{ref}, corresponding to the time it takes the free stream flow to travel one wing thickness. The spectra have been

non-dimensionalized on $1/U_{ref}/t$. This normalizing scheme allows direct comparisons between spectral levels at different measurement locations.

The low-frequency range spectra were calculated from 2048 point records (at every velocity measurement location) and showed considerable aliasing at non-dimensional frequencies above about $ft/U_{ref}=1$ due to the low effective sampling frequency (2500 Hz) and high frequency content of the signals. High-frequency range spectra were also calculated and those parts of the low-frequency spectra influenced by aliasing have been identified and removed. A few of the high-frequency range spectra, created from 512 point records (calculated at selected locations), show slight aliasing above $ft/U_{ref}=8$. The fact that this aliasing is more pronounced in the near wall region is a result of the lower data rate of the LDV here and therefore, a reduction in the effective sampling frequency.

Most of the u component spectra have a region of almost constant spectral level at frequencies below $ft/U_{ref}=0.1$. Above this frequency, the power density rolls off with a slope of -1 in most cases with a few instances of a -5/3 roll off. The v component spectra show similar trends except that the region of constant spectral level extends to higher frequencies $ft/U_{ref}=0.6$. Generally v component spectral levels are approximately an order of magnitude smaller than those of the u component. Overall, spectra measured in the onset boundary layer are similar to those of a two dimensional equilibrium boundary layer. In the bimodal zone, there is a dramatic increase in power density at low frequencies. Near the wing, spectral levels at high frequencies are greater than in other regions of the flow field.

Figures 27 and 35 show u and v power spectra measured in the onset boundary layer at $x/t = -.391$ between the wall and $y/t = .118$ ($y/\delta = .236$). These spectra display a roll off with a slope of -1 in power spectral density with frequency. They also show an increase in spectral level at low frequencies with y. Similar trends are seen in two-dimensional flat plate boundary layer and in two-dimensional adverse pressure gradient flows. Ahn (1986) studied a zero pressure gradient two dimensional turbulent boundary layer of Reynolds number $Re_\theta \approx 6400$. Some of his velocity spectra are plotted in figure 43 in terms of $k_1\delta$ versus $\Phi_{uu}(k_1\delta)/U_\tau^2$ where $k_1 = 2\pi f/U$, f is the frequency, U is the local velocity, δ is the boundary layer thickness, Φ_{uu} is the power spectral density function and U_τ is the friction velocity. These spectra show an increase in power density at low frequencies with increasing distance from the wall. Power densities near the wall $y/\delta \leq .297$ fall off with a -1 slope while those above this location follow a -5/3 slope. Simpson, Agarwal, Nagabushana and Olcmen (1989) studied adverse pressure gradient separating turbulent boundary layer flows and found the power spectral densities to follow a -1 slope upstream of separation at $y/\delta < .173$. However, they found that once separation occurred a -5/3 slope in the roll off dominated.

Figures 29 through 31 and 37 through 39 show the u and v power spectra in the bimodal zone, $x/t = -.294$, $x/t = -.237$, and $x/t = -.193$. Spectral densities at low frequencies are much greater here than elsewhere in the flow field. Figure 44 compares a u and v spectra taken in the onset boundary layer, $x/t = -.391$ and $y/t = .00677$, and one taken in the bimodal zone, $x/t = -.237$ and $y/t = .00477$. In both

the u and v component, figure 44 shows higher spectral densities at low frequencies in the bimodal zone than in the onset boundary layer.

Maximum power density in the bimodal zone is synonymous with the maximum turbulence normal stresses which are contoured in figures 19 and 20. The increase in turbulence normal stress appears to be caused entirely by the increase in spectral levels at low frequencies in this region since the high frequency spectral levels are approximately the same as that in the onset boundary layer. Thus, the bimodal zone appears to be a region where low frequency and presumably large scale turbulence is created. This is consistent with the findings of DS (1990) and Hassan et. al. (1985) who found the bimodal region to be dominated by large scale, low frequency coherent motions.

Figures 32 through 34 and 40 through 42 show the u and v component velocity spectra near the wing, $x/t=-.139$, $x/t=-.0856$, and $x/t=-.0421$. Approaching the wing, the velocity spectra change character again. The high spectral levels at low frequencies in the bimodal region disappear and fall below onset boundary layer levels for the u component. However, at high frequencies there is a slight increase in spectral level, particularly in the u component when compared to the onset boundary layer. These increases are greatest for the u component at frequencies of about $ft/U_{ref}=0.4$. However, for the v component near the wall, $y/t<0.01$, the spectral level is approximately the same at all frequencies as in the onset boundary layer. These observations are shown in figure 45 which compares a u and v spectra

taken in the onset boundary layer, $x/t = -.391$ and $y/t = .00677$, and one taken near the wing, $x/t = -.0421$ and $y/t = .00077$. This figure illustrates the trends discussed above.

The increase in spectral levels at high frequencies in the near wing locations is likely due to indirect effects of the large-scale structures in the bimodal zone. As the vortex becomes wrapped around the wing and stretched, it no longer moves downstream. This would prevent any large scale structures from the bimodal zone from reaching the juncture while it would allow for smaller scale structures from the outer measurement region to come down the wing into the juncture.

Another interesting feature of these u spectra measured above $y/t = .04$ at these streamwise locations, $x/t = -.0856$ and $x/t = -.0421$, are two plateaus of almost constant spectral density with frequency, figures 33 and 34. These spectra have an approximately constant spectral density at frequencies below $ft/U_{ref} = 0.07$ which is followed by a roll off, as do all other spectra. However, this roll off is short and followed by another constant spectral density region between $ft/U_{ref} = 0.2$ and $ft/U_{ref} = 0.9$ and a second roll off. This second plateau begins to fade away with increasing distance from the wall. These power spectra show a deficit of low frequency, $ft/U_{ref} < 1$, spectral density when compared to spectra in the onset boundary layer. Figure 46 is a comparison of the spectra taken in the onset boundary layer, $x/t = -.391$ and $y/t = .04751$, the bimodal zone, $x/t = -.237$ and $y/t = .04551$, and near the wing, $x/t = -.0421$ and $y/t = .04151$. There is a lack of low frequency and middle frequency power in the spectra taken near the wing. The second roll off contains approximately the same spectral levels at high frequencies

as seen in the outer measurement region at other streamwise locations. However, when these spectra are compared to those closer to the wall, a deficit in spectral densities at frequencies between $ft/U_{ref}=0.2$ and $ft/U_{ref}=0.9$ is apparent while the low frequency content is approximately the same.

The most universal feature of the velocity spectra is the slope of the roll off. At almost every location this follows a -1 slope. A few near wing spectra and some v spectra follow a -5/3 slope. According to Klebanoff (1975), the -5/3 slope exists in a region of homogeneous isotropic turbulence where equilibrium exists between the transfer and dissipation of energy. With a high Reynolds number, inertial forces will dominate the lower wave numbers in the equilibrium range and an equilibrium region of energy transfer from large to small eddies will exist. Klebanoff states that Tehen (1953) studied the effects of a mean velocity gradient on homogeneous isotropic turbulence and found that a region of -1 slope exists where the -5/3 slope would exist without the velocity gradient. Although the -1 slope is found throughout the present flow field, it is difficult to believe that this is due to an equilibrium region of energy transfer existing in the wing body junction bearing in mind the inherent three-dimensionality and non-equilibrium nature of the flow field. However, there appears to be no plausible alternative explanations for the existence of the -1 slope. It is interesting to note that the bandwidth were the -1 slope exists is the bandwidth containing the highest energy producing frequencies.

3.3 Pressure Fluctuation Measurements

3.3.1 Comparison With Previous Work

Figure 47 shows the comparisons of the ratio of $p_{rms}/(p_{rms})_{bl}$, where p_{rms} is the root mean square of the pressure fluctuation and $(p_{rms})_{bl}$ is the root mean square of the pressure under the onset boundary layer, versus x/t measured in the present experiment and in the experiments of Agarwal (1989) and Hasan *et al* (1985). For the present measurements $(p_{rms})_{bl}$ was found using the approach boundary layer skin friction data of Ahn (1986), which at $Re_\theta = 6400$ showed $C_f = .0038$, and the results of McGrath and Simpson (1987) at $Re_\theta = 6000$ which show that under a zero pressure gradient turbulent boundary layer $p_{rms}/\tau_w = 3.8$. To account for the lower than recommended operating voltage, the p_{rms} of the present experiment was divided by .8. For the data of Agarwal (1989), who studied the same flow investigated here, $(p_{rms})_{bl}$ was taken as his p_{rms} at $x/t = -1.11$. For the data of Hasan *et al* (1985) which was obtained in the flow past a wing body junction of the same wing shape but slightly higher free stream velocity, $(p_{rms})_{bl}$ was the root mean square of the wall pressure fluctuations under an equilibrium boundary layer.

Together these data show a slight increase in $p_{rms}/(p_{rms})_{bl}$ as the wing is approached and its adverse pressure gradient is encountered. Inside the bimodal zone, there is a dramatic increase in p_{rms} until a maximum is reached at approximately $x/t = -.23$ after which it falls. This large gradient of p_{rms} occurs in the vicinity of the mean junction vortex. The maximum p_{rms} occurs at the same approximate streamwise location as the maxima in u and v turbulence normal stresses.

The acoustic noise generated by the wind tunnel accounts for 28% of the mean square pressure fluctuation under the onset boundary layer (Devenport (1991)). Due to the large increase in p_{rms} inside the separation zone, the mean square of the acoustic noise accounts for only 0.5% of the total mean square pressure signal at $x/t = -.20$. therefore, no broad band acoustic noise is likely to be discernable in the pressure measurements taken at this location. However, the mean square of the acoustic noise accounts for 36% of the total mean square pressure at $x/t = 0.0$. Therefore, pressure signals measured at this location may contain significant broadband acoustic noise. As shown earlier, acoustic noise does not affect the relationships between the pressure and velocity signals because the noise and velocity field are uncorrelated. Only auto spectral density functions will be affected.

3.3.2 Histograms

Figure 48 shows the pressure fluctuation histograms of Agarwal (1989). No pressure fluctuation histograms of the present experiment are presented because the present microphones were not capable of mean pressure measurements.

Note the broadening of the peak in figure 48 at $x/t = -.234$ indicative of the bimodal unsteadiness. This bimodal pressure histogram occurs at the same streamwise location as the bimodal velocity histograms and is thus, presumably the result of the same phenomena.

3.3.3 Power Spectra

Figure 49 shows the normalized auto spectral density functions of the two pressure signals. These were computed from ninety 2048 point FFTs and ensemble averaged as discussed in the experimental methods section.

The frequency f has been normalized by the wing maximum thickness t and reference velocity U_{ref}. The auto spectral density G_{pp} has been non-dimensionalized by U_{ref}/q^2t where q^2 is the free stream dynamic pressure. These axes allow direct comparisons to be made between the two pressure fluctuation power densities to be made. Although acoustic noise was expected to account for 36% of the mean square pressure at $x/t=0.0$, it is not clearly visible in this power spectrum. There are no obvious spikes of noise in either spectrum.

The power spectral densities at both measurement locations show distinct characteristics. Under the junction at $x/t=0.0$, there is a region of constant spectral level, $G_{pp}U_{ref}/q^2t \approx 1.5 \times 10^{-5}$, between $ft/U_{ref}=.01$ and $ft/U_{ref}=.2$. Above $ft/U_{ref}=.2$, the spectral levels roll off with a slope of -2. However, under the bimodal zone, $x/t=-.20$, the power density has an entirely different shape. There is a peak spectral level at $ft/U_{ref}=.02$ of $G_{pp}U_{ref}/q^2t=3 \times 10^{-3}$. At frequencies above this, the spectral level rolls off with a slope of -1.

There are substantially higher pressure fluctuations spectral densities under the bimodal zone than under the junction at all frequencies. This is consistent with the trends seen in the velocity spectra. However, such a large difference in spectral densities, approximately two orders of magnitude, is a slight surprise. Possibly the

microphone located in the juncture is shielded by viscous forces and the wing and wall from a portion of the pressure fluctuations

Figure 50 shows the first moment of the pressure spectral densities.

$$\frac{G_{pp}}{p^2} \times f \qquad (16)$$

This type of plot shows the frequency ranges with the greatest contribution to the total pressure fluctuations.

The first moment of the spectrum taken at $x/t = 0.0$, figure 50, shows a distinct peak of $G_{pp}f/q^2 = 4 \times 10^{-6}$ at $ft/U_{ref} = 4 \times 10^{-1}$. The first moment of the spectra of the pressure taken at $x/t = -.20$ shows a frequency range, $ft/U_{ref} = 7 \times 10^{-2}$ to $ft/U_{ref} = 7 \times 10^{-1}$, of almost constant spectral density $G_{pp}f/q^2 = 2 \times 10^{-4}$. This constant level shows that a broad range of frequencies has a large contribution to the total pressure fluctuations; thus, there is no single characteristic frequency seen for the pressure fluctuations in the bimodal zone. The peak in the first moment of the spectra taken at $x/t = 0.0$ show pressure fluctuations in this region to be dominated by frequencies higher than found in the bimodal zone, which is consistent with the findings of the velocity spectra.

3.3.4 Relationship Between the Two Pressure Signals

Figure 51 shows the results illustrating the relationship between the two pressure signals. These were calculated using the methods discussed previously in the data reduction section. The frequencies are again non-dimensionalized on t/U_{ref},

the wing thickness and the reference velocity. The delay time, T, in seconds is normalized by U_{ref}/t.

Figure 51a shows the coherence between the two pressure signals. There appear to be two bands of coherence, one at a low frequency $ft/U_{ref} = 1 \times 10^{-2}$ to $ft/U_{ref} = 5 \times 10^{-2}$ and another of higher frequency, $ft/U_{ref} = 3 \times 10^{-1}$ to $ft/U_{ref} = 8 \times 10^{-1}$. However, since this coherence has almost 100% uncertainty as shown in table 2, it has little statistical significance. The phase between the two pressure signals, figure 51b, bears out this observation since it shows very little consistent variation.

Figure 51c shows the cross correlation coefficient function between the two pressure signals. The correlation is mostly negative showing that pressure changes at the microphone locations are opposite in sign. A negative correlation is seen at both negative and positive time lags suggesting disturbances that move upstream and downstream.

3.4 Measurements Illustrating the Relationship Between Velocity and Pressure

3.4.1 Time Series

Figures 52 through 54 and figures 55 through 57 show simultaneous time series records of u and v component fluctuations respectively and the two microphone pressure fluctuations at $x/t = -.20$ and $x/t = 0.0$ for three different U component velocity measurement locations. Pressure fluctuations have been normalized on the dynamic pressure, $q = \frac{1}{2}\rho U_{ref}^2$, and velocities on U_{ref}.

In the onset boundary layer represented by the velocity measurements at $x/t=-.391$ and $y/t=.01740$, shown in figures 52 and 55, the U component velocities show fluctuations around a positive mean while the v component velocities are centered around zero with smaller fluctuations. The u velocity at $x/t=-.237$ and $y/t=.01044$ shown in figure 53 are typical of those taken in the bimodal zone. Velocities in this region alternate between a negative value and a value near zero. This type of velocity signal is also seen for the v component as shown in figure 56. These two preferred velocities correspond to the backflow and zero flow modes seen in the bimodal histograms. Switches between the two modes appear to be random in occurrence and are of a much larger amplitude than any other velocity fluctuations seen elsewhere in the flow field. This large fluctuation may account for the increase in spectral level at low frequencies seen in the velocity power spectral densities in the bimodal zone. Figures 54 and 57 show velocity measurements made close to the corner of the wing body junction, $x/t=-.0421$ and $y/t=.00254$. The U component velocities at this location show slightly smaller fluctuations than in the onset boundary layer centered around a negative mean while the v component shows again small fluctuations around a slightly positive velocity.

The signal of the pressure taken at $x/t=0.0$ shows very small fluctuations in each of the three figures, very similar to the velocity at $x/t=-.0421$ and $y/t=.0254$, figure 52 while the pressure signal taken at $x/t=-.20$ shows much larger fluctuations. This signal shows some similarity to the u and v velocity signals in the bimodal zone shown in figures 53 and 56. There appear to be sudden falls and rises in the

pressure signal at x/t=-.20 that are similar to the bimodal switches seen in the velocity signals; large magnitude, random, and very sudden. Figure 56 highlights several bimodal switches (from low velocity to high velocity and back) in the v component velocity signal (events A, B, and C) and what appears to be a corresponding change in the pressure (events AA, BB, and CC). These events appear to have a positive correlation with almost no time lag between the occurrence of the two events. This is just a small sample of the switches seen in a single record (3414 data points). There are many more in this record alone and several hundred per data file.

The time series of the pressure signals in figure 55 have been highlighted to show the relationship between the two. Events A and B in the pressure at x/t=-.20 are sudden rises in pressure while events AA and BB are falls in pressure at x/t=0.0. The events in the pressure signal at x/t=0.0 lead the pressure rise at x/t=-.20 by approximately .1 seconds. Consistent with the relationship shown figure 51c these signals are changing in an opposite manner.

3.4.2 Cross-correlation Coefficient Functions

Figures 58 through 65 are the cross-correlation coefficient functions of the velocity and the pressure fluctuations at x/t=-.20. These figures contain information on the timing of events in the flow as well as information on the relationship between velocity and pressure fluctuations. In these figures a positive non-dimensional time lag is indicative of a disturbance appearing first at the velocity measurement location and then at the pressure measurement location.

At the three most upstream measurement locations, $x/t = -.391$, $x/t = -.342$, and $x/t = -.294$ figures 58 through 60, the cross correlation coefficient functions $\rho_{up}(\tau)$ follow the same pattern. Near the wall, $y/t < .05$, $\rho_{up}(\tau)$ is negative at most time lags and has a negative peak at zero or slightly positive time lag, and at large time lags, $TU_{ref}/t > 4$, becomes slightly positive. Further from the wall $\rho_{up}(\tau)$ has a positive peak at a time lag TU_{ref}/t of about 0.5. This increases in magnitude with distance downstream. For $TU_{ref}/t > 2$, this function is slightly negative and at all negative time lags it is essentially zero. Near the wall, $y/t < .05$, $\rho_{vp}(\tau)$ has a positive peak at approximately zero time lag with the exception of $x/t = -.294$ and $y/t = .00577$, figure 60, where $\rho_{vp}(\tau)$ is negative at zero time lag. Also in the near wall region $\rho_{vp}(\tau)$ becomes slightly negative at non-dimensional time lags greater than one, $TU_{ref/t} > 1$. Far from the wall $\rho_{vp}(\tau)$ completely reverses, forming a negative peak at zero time lag and a slightly positive value at positive non-dimensional time lags above 1.

Figure 66 shows a possible interpretation of these correlations, making the assumption that they are associated with the sudden pressure drop seen in the microphone signal at $x/t = -.20$ presumed to be associated with the bimodal switching. Figure 66 shows a single eddy rolling up and increasing in strength while its center moves downstream. As the eddy moves downstream over the microphone at $x/t = -.20$, a sudden drop in the pressure at the wall would occur because of the increase in near wall backflow velocities. Simultaneously locations upstream (i.e. $x/t = -.391$, $x/t = -.342$, and $x/t = -.294$) would experience an increase in u and a decrease in v

close to the wall and a decrease in u and an increase in v away from the wall, consistent with the observed correlations at zero time delay.

Moving downstream to $x/t = -.237$, figure 61, $\rho_{up}(\tau)$ follows approximately the same pattern as upstream with a negative correlation at non-dimensional lags TU_{ref}/t below 2 and a large negative peak at approximately zero lag at near wall locations, $y/t < .05$. Above $y/t = .05$, $\rho_{up}(\tau)$ develops a positive peak at zero time lag. This is accompanied by almost zero correlation for $TU_{ref}/t < -3$ and negative correlation above $TU_{ref}/t > 1$. $\rho_{vp}(\tau)$ however is much different. Across the entire profile the correlation has a large negative peak at zero time lag and a slight positive hump for $TU_{ref}/t > 2$. These observations are consistent with the upstream edge of the model eddy moving through $x/t = -.237$ at the same time as the sudden pressure drop at $x/t = -.20$, figure 66. The movement of the upstream edge of the eddy would cause the point where fluid lifts away from the wall to move downstream. This would cause the u component of velocity near the wall to increase from a negative value to near zero causing a negative correlation. At the same time, the fluid pulling away from the wall would be associated with an increase in the v velocity, again creating a negative correlation. The switch in sign of $\rho_{up}(\tau)$, seen in figure 61 at approximately $y/t = .05$ could be interpreted as the vertical location of the center of the model eddy, figure 66. Above this location the u velocity would decrease from a positive value towards zero while the v velocity would be increasing, thus causing positive $\rho_{up}(\tau)$ and negative $\rho_{vp}(\tau)$.

Figures 62 and 63 show the cross-correlation coefficient functions for $x/t = -.193$ and $x/t = -.139$ respectively. For $y/t < .05$ the u correlations have a large positive peak at zero time lag and a slight negative correlation for time lags above $TU_{ref}/t > 0$. Above $y/t = .05$, $\rho_{up}(\tau)$ develops a negative peak at zero time lag and a positive going peak at $TU_{ref}/t = .5$ followed by another smaller negative peak at approximately $TU_{ref}/t = 2$. The v component correlations again have a large positive peak at zero time lag and essentially zero correlation at most other times. Exceptions here are the two outer most measurement points, $y/t = .09121$ and $y/t = -.11601$ at $x/t = -.193$ (figure 62), where $\rho_{up}(\tau)$ becomes slightly negative at negative time lags and slightly positive at positive time lags. Again viewing figure 66, these results could be interpreted as the eddy moving over the microphone and simultaneously stretching around the wing and increasing in strength, thus decreasing in size. The increase in vorticity would cause the v component to increase negatively across both locations with the exception of the two outermost measurements points at $x/t = -.193$. Near the wall, the u component would simultaneously increase in negative magnitude while above the vortex center u would increase in positive magnitude thus accounting for the change in sign of $\rho_{up}(\tau)$ which occurs at $y/t = .05$, the proposed mid-height of the model eddy.

At the two locations closest to the wing $x/t = -.0856$ and $x/t = -.0421$, the cross-correlation functions, figures 64 and 65, show many of the same characteristics. Below the vortex center, $\rho_{up}(\tau)$ has a positive peak at approximately zero time lag with two slightly negative peaks, one to just either side of zero time lag.

Approaching $y/t=.05$, the negative peak at a negative time lag begins to disappear. Above $y/t=.05$, $\rho_{up}(\tau)$ has a dominant negative peak at zero time lag and the positive going peak seen in the two previous figures becomes just slightly positive at $TU_{ref}/t=.5$. $\rho_{vp}(\tau)$ on the other hand is essentially zero near the wall, $y/t<.02$. At $x/t=-.0856$, $\rho_{vp}(\tau)$ has a negative peak at a slightly positive time lag between $.05>y/t>.02$ while at $x/t=-.0421$ $\rho_{vp}(\tau)$ has a positive peak at zero time lag. Above $y/t=.05$ $\rho_{vp}(\tau)$ has a large positive peak at approximately zero time lag with essentially zero correlation at all other times. These results could be interpreted as fluid near the wall being pulled into the model vortex. The v component results are consistent with high momentum fluid from the outer measurement region coming into the region between the wing and model vortex. Since these correlations occur at a slight positive time lag, the velocity leads the pressure indicating that fluid intake down the leading edge of the wing occurs before the vortex rolls up. It appears that this intake of fluid may be the driving force behind the bimodal unsteadiness.

Figures 67 and 68 are contours of the cross-correlation coefficient function between velocity and pressure at $x/t=-.20$ at three different time lags for the u and v components respectively. Figure 67 shows the u component contours at a) $TU_{ref}/t=-.94$, b)$TU_{ref}/t=0$, and c) $TU_{ref}/t=.94$. If viewed as if the pressure at $x/t=-.20$ were dropping then the large regions of correlation occur where the model eddy would cause the greatest change in the u velocity. The areas of largest correlation are seen inside the bimodal region where it has been established that the velocity and pressure switch between two stable modes. As time increases, the correlations

become greatest at $TU_{ref}/t=0$ where the eddy is changing most rapidly. After the drop in pressure the eddy dissipates and the regions of correlation begin shrinking.

Figure 68 shows the component correlation contours at a) $TU_{ref}/t=-.94$, b) $TU_{ref}/t=0$, and c) $TU_{ref}/t=.94$. The areas in which the model predicts the greatest change in v velocity show up here as regions of high correlation. Upstream of $x/t=-.20$, the v component would be accelerated upward when the pressure at $x/t=-.20$ falls resulting in a negative correlation. Downstream of $x/t=-.20$, the fluid would be forced to the wall, thus giving a positive correlation as seen in figure 68.

Figures 69 through 76 are the cross-correlation coefficient functions between the two velocity components and the pressure fluctuations at $x/t=0.0$.

Figures 69 through 72, the four most upstream locations, $x/t=-.391$, $x/t=-.342$, $x/t=-.294$, and $x/t=-.237$ show similar trends in the shape of the cross-correlation functions. Below $y/t=.05$, $\rho_{up}(\tau)$ has a negative maximum at a negative time lag, $TU_{ref}/t=-3$, and a positive maximum at zero or slightly positive time lag. For $y/t>.05$, the outer measurement region, the positive peak of $\rho_{up}(\tau)$ diminishes while the negative peak becomes increasingly more negative and moves to approximately zero time lag. The magnitude of $\rho_{vp}(\tau)$ is essentially zero except in the outer measurement region where a small negative peak develops at zero or slightly negative time lag. The negative peaks in $\rho_{up}(\tau)$ in the outer region are indicative of the fluid in this region being accelerated when the pressure in the juncture decreases.

Moving downstream, the next two locations $x/t=-.193$ and $x/t=-.139$ (figures 73 and 74) have similar cross-correlation functions. Below $y_i t=.03$, $\rho_{up}(\tau)$ is dominated by a large positive peak at a slightly negative or zero time lag. There is also a smaller peak of negative correlation at approximately $TU_{ref}/t=-2$. In the same region, $\rho_{vp}(\tau)$ shows a positive peak at a slightly negative time lag which increases in magnitude with distance from the wall. Going further from the wall, the positive peak in $\rho_{up}(\tau)$ continues to decrease while a negative peak at approximately zero time lag grows. Simultaneously the positive peak in $\rho_{vp}(\tau)$ continues to grow and reaches a maximum at the outermost measurement point. These are accompanied by negative bumps of correlation at $TU_{ref}/t=-3.5$. The negative $\rho_{up}(\tau)$ in the outer region suggests an acceleration of fluid toward the wing as the pressure at $x/t=0.0$ is dropping. The large positive peak in $\rho_{vp}(\tau)$ here could be interpreted as fluid being pulled down toward the junction when the pressure in the junction is falling. Along the lower wall, the positive $\rho_{up}(\tau)$ may be interpreted as fluid being expelled along the wall from the junction and being pulled into the model eddy when the junction pressure drops. Figure 77 is a sketch illustrating the situation believed to be occurring. These events are entirely consistent with the previous model. However, in between $y/t=.045$ and $y/t=.075$, $\rho_{up}(\tau)$ behaves in a way inconsistent with the model. Complete consistency with the model would call for a location where $\rho_{up}(\tau)$ switches sign completely and suddenly as seen in the correlation with the pressure at $x/t=-.20$.

The two measurement locations near the wing $x/t = -.0856$ and $x/t = -.0421$ figures 75 and 76 share similar cross-correlation features. Below $y/t = .05$, $\rho_{up}(\tau)$ has two peaks of approximately the same magnitude: one negative at a slightly negative time lag; the other positive at approximately zero time lag. Above these locations, the large negative peak seen at all streamwise locations returns to $\rho_{up}(\tau)$. Across both measurement locations $\rho_{vp}(\tau)$ has an ever increasing positive peak at approximately zero time lag. These large positive peaks in $\rho_{vp}(\tau)$ are accompanied at $x/t = -.0421$ by smaller peaks of negative correlation at $TU_{ref}/t \approx -1.5$. The shape of $\rho_{up}(\tau)$ in the outer region and the shape of $\rho_{vp}(\tau)$ across both locations could be explained as has been done previously. However, the shape of $\rho_{up}(\tau)$ near the wall is difficult to explain within the confines of the proposed model.

Figures 78 and 79 are the contours of the cross-correlation coefficient function between velocity and pressure at $x/t = 0.0$ at three different time lags for the u and v component respectively. Figure 78 shows the u component correlation contours for a) $TU_{ref}/t = -.94$, b) $TU_{ref}/t = 0$, and c) $TU_{ref}/t = .94$. These contours show the large area in the outer measurement region over which the velocity and pressure are correlated. Along the lower test wall another area of correlation can be seen where fluid is ejected from the junction toward the model eddy. Figure 79 shows the v component correlation contours at a) $TU_{ref}/t = -.94$, b) $TU_{ref}/t = 0$, and c) $TU_{ref}/t = .94$. This shows the region near the wing where large correlations are present. The two areas of correlation in the outer measurement region seen in the u and v component suggest fluid from the outer region moves into the junction.

It is believed that for the most part, these correlations are unrelated to the upstream model eddy due to the suddenness of the spin up and pressure drop. However, the one exception is high momentum fluid brought down the face of the wing before the vortex rolls up. It is believed that this fluid energizes the vortex and causes the roll up.

This model vortex is consistent with the visualizations of Kim (1991). The primary vortex described by Kim (1991) would be seen as the proposed model eddy. The fluid seen coming down the wing to energize the vortex in the present study relates well to the leap frogging vortices which strengthen his primary vortex. In both models, this incoming fluid increases the strength of each vortex and increases the stretching rate.

3.4.3 Velocity Vectors Conditionally Averaged on a Pressure Change

To provide a better understanding of the flow structure U and V velocity signals measured at each point were conditionally averaged on the pressure signal at $x/t = -.20$. Figure 53 is a time series taken in the bimodal region which has markings on it to help understand the phase averaging process. The condition upon which averaging was based was a bimodal switch in pressure as discussed in section 3.4.1. To be considered a bimodal switch, the prospective point had to pass two criteria as defined by Olcmen, Simpson, Kim, and Ha (1991). First the signal had to cross a voltage threshold level, shown as a dashed horizontal line at $p'/q = .04$ in figure 53. A switching time criteria also had to be met. This consisted of a preset time for which the pressure signal had to remain above or below the threshold level

depending upon the direction of the switch. Points defined as bimodal switches were then classified as a rising pressure switch or a falling pressure switch and were identified by their time of occurrence from the beginning of the record.

As shown by the solid vertical line in figure 49, the time of the pressure switch was accessed in the velocity record. One hundred twenty eight points in the velocity signal on either side of the pressure switch point were added to individual elements of an array. The elements were then averaged over the total number of pressure switches found.

Figure 80 shows the vectors of velocity conditionally averaged on the pressure fall at $x/t = -.20$. This is a series of figures 5/10000 of a second apart. The actual crossing of the voltage threshold occurs at time 0.

This figure reveals a flow structure consistent with the model proposed in the previous section. Before the pressure fall (negative non-dimensional lags) a large elliptical vortex is seen with its center at approximately $x/t = -.265$ and $y/t = .04$. As the pressure at $x/t = -.20$ falls, the center of the vortex moves downstream to approximately $x/t = -.23$ and $y/t = .05$. While the vortex center moves downstream, the vortex simultaneously decreases in size and thus increases in strength. This decrease in size is most probably due to the vortex wrapping around the wing and becoming stretched.

Figure 81 shows the vectors of velocity conditionally averaged on a pressure increase at $x/t = -.20$. Before the pressure rise at $x/t = -.20$ occurs, the vortex is seen

to disappear. Which allows the backflow mode to reappear and cause the formation of the large elliptical vortex.

No other mode averaged analysis (cross-spectra or cross-correlation) was attempted because this would involve working with the turbulent signal and not the large scale features. It is believed that the turbulence in one mode or the other is carried by the fluid but is not a major contributor to the bimodal unsteadiness.

3.4.3 Coherence and Phase

The coherence and phase between velocity and pressure fluctuations show three separate regions; juncture, bimodal, and outer measurement, distinguished by coherence frequency content. In the juncture high frequency coherence is dominant. The bimodal region has a low frequency range of coherence while the outer measurement region contains frequencies in between the other two ranges, middle frequencies. These middle frequencies occur near the wall at some near wing streamwise measurement locations.

Figures 82 to 93 show the ordinary coherence functions and phase between the u component velocity and the pressure fluctuations at $x/t = -.20$. These follow many of the same trends in frequency content as do the velocity power spectra.

Figures 82 and 83 are the coherence and phase respectively at $x/t = -.294$. These are the most upstream locations showing significant coherence. The only significant coherence occurs at $y/t = .01640$ in the band $ft/U_{ref} = 6 \times 10^{-3}$ to $ft/U_{ref} = 0.5$ (which is considered the low frequency band) and has a maximum at $ft/U_{ref} = 8 \times 10^{-3}$. The phase at this location increases across the frequency band from $50°$ to $250°$.

Figure 84 shows the coherence at $x/t = -.237$ which is in the bimodal zone. In the near wall region $y/t < .04551$ the coherency occurs in a low frequency range of $ft/U_{ref} = 6 \times 10^{-3}$ to $ft/U_{ref} = 0.5$. The maximum coherence occurs at approximately $ft/U_{ref} = 5 \times 10^{-2}$. The phase of these locations, figure 85, increases across the bandwidth, starting at approximately 60° and ending at 210°. Above $y/t = .04551$, any significant coherence is in a higher frequency band of $ft/U_{ref} = 7 \times 10^{-2}$ to $ft/U_{ref} = 0.3$ (which is considered to be in the middle frequency range), centered at $ft/U_{ref} = 1.5 \times 10^{-1}$. The phase here is increasing across the band, from -50° to 50°. This is typical of the middle frequency range found in the outer measurement region.

Figure 86 shows the u coherence at $x/t = -.193$ which has two distinct characteristics. In the near wall region, $y/t = .01044$ and below, the coherence is purely in the high frequency range of $ft/U_{ref} = 0.2$ to $ft/U_{ref} 1.5$. Above this location the coherence begins to transition to lower frequencies. Between $y/t = .01540$ and $y/t = .02886$ the majority of the coherence occurs between $ft/U_{ref} = 1 \times 10^{-2}$ to $ft/U_{ref} = 0.3$. Above $y/t = .057$, any significant coherence occurs below $ft/U_{ref} = 0.1$. The phase, figure 87, of the high frequency coherence is at a negative angle and slightly decreasing across the band from -40° to -70°. In the region of low frequency coherence, the phase takes on a humped appearance. It increases at low frequencies, reaches a peak at $ft/U_{ref} = 1 \times 10^{-1}$, and then decreases across the higher frequencies. The phase at locations above $x/t = .04551$ increases beyond 180° and then falls back below 180°.

Figure 88 shows the coherence at $x/t = -.139$ which remains in the high frequency band seen in the near wall in figure 86 across the entire profile. However, in the outer measurement volume $y/t = .07$, it appears that a slight amount of middle frequency coherence remains. The phase at this location, figure 89, is different from the upstream locations just mentioned. The phase is constant at $0°$ across the entire bandwidth $ft/U_{ref} = 0.2$ to $ft/U_{ref} = 1.5$ below $y/t = .04651$. At this location and above it the phase increases across the bandwidth of coherence.

Figures 90 and 92 shows the coherence in the region near the wing and wall $x/t = -.0421$ and $x/t = -.0856$ (the juncture region) where coherence exists only at high non-dimensional frequencies between $ft/U_{ref} = 0.4$ and $ft/U_{ref} = 0.9$. The frequency of peak coherence is approximately $ft/U_{ref} = 7 \times 10^{-1}$ in this area. Figure 91 shows the phase at this location increasing across the frequency band from $-100°$ to $100°$. At $x/t = -.0421$, figure 90, there is no statistically significant coherence above $y/t = .04151$. At $x/t = -.0856$, figure 92, the coherence remains in the high frequency area. The phase, figure 93, here increases across the frequency band from $-100°$ to $100°$.

Figures 94 through 101 are the v component coherence and phase with the pressure at $x/t = -.20$. Figures 94, 96, and 98 show the v coherence at $x/t = -.193$, $x/t = -.237$, and $x/t = -.294$. The coherence here is all low frequency. Figures 95, 97, and 99 show the hump phase pattern seen in the U component low frequency phase. However at these locations there is very little near wall coherence. Locations upstream of $x/t = -.294$ do not show any significant coherence.

Figure 100 shows the coherence at $x/t=-.139$ which is low frequency across the entire profile. There is more coherence near wall here than at other locations. The phase here, figure 101, is the hump pattern found in the u component phase of low frequency coherence. This low frequency coherence is indicative of the bimodal zone. There is no significant coherence downstream of $x/t=-.139$.

Figures 102 and 103 are contours of the maximum u and v coherence with the pressure at $x/t=-.20$ in a given frequency range. Figure 102a shows the maximum u component coherence in the low frequency range of $ft/U_{ref}=6\times10^{-3}$ to $ft/U_{ref}=0.5$. The highest levels of coherence seen in this frequency range are in the bimodal zone. The area covered by the maximum coherence of the middle frequencies, $ft/U_{ref}=7\times10^{-2}$ to $ft/U_{ref}=0.3$, figure 102b is much larger than that covered by the low frequencies. The high frequency, $ft/U_{ref}=0.4$ to $ft/U_{ref}=0.9$, coherence, figure 102c, is seen mainly near the wing and wall. Figure 103a is the v component low frequency, $ft/U_{ref}=6\times10^{-3}$ to $ft/U_{ref}=0.5$, coherence. This figure is dominated by two large vertical regions of high coherence at $x/t=-.235$ and $x/t=-.14$. The middle frequency, $ft/U_{ref}=7\times10^{-2}$ to $ft/U_{ref}=0.3$, coherence, figure 103b, shows patterns similar to that seen in the low frequency coherence. Figure 103c shows the high frequency, $ft/U_{ref}=0.4$ to $ft/U_{ref}=0.9$, coherence. The areas of highest coherence are not found near the wing as expected but are away from the wall and upstream of the wing.

The u component contours are consistent with the proposed model. The majority of the low frequency u coherence is contained in the bimodal zone (figure

102a) where an increase in low frequency power spectral density is seen. For both velocity components, the increase in low frequency coherence is associated with the maxima in turbulence normal stress. Again the dominance of low frequency, large scale structures are seen in the bimodal zone. Thus the existence of a single large eddy in this area is further supported. As proposed in the model, the high frequency u coherence would occur near the juncture of the wing and body as seen in figure 102c. Coherence in the middle frequencies occurs over the majority of the measurement region. The high level of middle frequency coherence seen in the bimodal zone is believed to be due to overlapping of the low and middle frequency ranges.

The low and middle frequency v coherence is entirely consistent with the proposed model. The large vertical regions of high coherence occur were the v component would experience the greatest changes when the model eddy rolls up and travels downstream. The high frequency contour is different than would be expected with the proposed model. The highest coherence is seen away from the wing and away from the wall. It is possible that this is due to the damping effects of the wall.

Figures 104 through 127 are the coherence and phase plots for the two velocity components and the pressure at the juncture $x/t = 0.0$. Figures 104; 106; 108; and 110, show the u coherence at $x/t = -.391$, $x/t = -.342$, -.294 and $x/t = -.237$. There are significant levels of u coherence in the outer locations of the measurement region in the middle frequency band, $ft/U_{ref} = 4 \times 10^{-2}$ to $ft/U_{ref} = 0.5$, with a maximum at $ft/U_{ref} = 1.5 \times 10^{-1}$. The near wall points show very slight coherence in the same

frequency band. The phase at these locations, figures 105; 107; 109; and 111, is approximately constant across the frequency band in which significant coherence occurs.

The coherence at $x/t = -.193$, figure 112, shows no high frequency band at any vertical locations. Below $y/t = .01540$, the only significant coherence is in the frequency band of $ft/U_{ref} = 3 \times 10^{-2}$ to $ft/U_{ref} = 5 \times 10^{-1}$, the middle frequencies. At $y/t = .07243$, this band of coherence shows up again. The phase, figure 113, near the wall is slightly humped with a maximum at $ft/U_{ref} = 7 \times 10^{-2}$ while in the outer region the phase is constant at approximately 130° across the bandwidth.

At $x/t = -.139$, figure 114, the near wall points, $y/t < .02906$, show the middle frequency coherence moving slightly up in frequency to $ft/U_{ref} = 6 \times 10^{-2}$ to $ft/U_{ref} = 0.9$ from that found in upstream locations. Locations away from the wall, $y/t > .04651$, show what appear to be two coherency bands superimposed. There appears to be a peak at $ft/U_{ref} = 0.1$ and another at $ft/U_{ref} = 0.8$. The phase at this location, figure 115, decreases with frequency near the wall and increases with frequency away from the wall.

Figures 116 and 118 show the coherence of the u component at $x/t = -.0856$ and $x/t = -.0421$. The coherence plots show a main peak centered at $ft/U_{ref} = 8 \times 10^{-1}$ and what appears to be a secondary peak at $ft/U_{ref} = 1 \times 10^{-1}$. Near the wall the high frequency peak is dominant but at the outer edge of the measurement region the peaks have approximately the same coherence. The phase for these two locations figures 117 and 119 decreases across the band of coherence at near wall locations.

As distance away from the wall increases the phase becomes constant at approximately 130°.

Figures 120, 122, and 124, show the v coherence at $x/t = -.193$, $x/t = -.139$, and $x/t = -.0856$. All coherence is in the band $ft/U_{ref} = 3 \times 10^{-2}$ to $ft/U_{ref} = 5 \times 10^{-1}$ and occurs away from the wall, $y/t > 0.2$. The phase, figures 121, 123, and 125, at these locations decreases across the frequency band for all vertical locations at which a significant coherence exists.

Figure 126 is the v coherence at $x/t = -.0421$. Near the wall there is little coherence. Between $y/t = .00361$ and $y/t = .04151$, the coherence exists in the band $ft/U_{ref} = 4 \times 10^{-2}$ to $ft/U_{ref} = 0.9$. Above $y/t = .05310$, the coherence becomes weaker. The phase, figure 127, near the wall decreases across the frequency band. Away from the wall the phase increases slightly across the frequency band.

Figures 128 and 129 are the u and v contours of maximum coherence with the pressure at $x/t = 0.0$. Figure 128a shows the maximum u coherence in the low frequency range of $ft/U_{ref} 6 \times 10^{-3}$ to $ft/U_{ref} = 0.5$. There is no significant coherence present in the vicinity of the model eddy. The only coherence present is in an area associated with the middle frequencies. The maximum middle frequency u coherence is shown in figure 128b. Significant levels of coherence are seen in the outer measurement region away from the wall as well as close to the wing. Maximum high frequency u coherence is seen mainly near the juncture of the wing and body, figure 128c. Figure 129a is the low frequency v coherence with the pressure at $x/t = 0.0$. Again there is no significant coherence seen in the bimodal zone. Figure 129b shows

the middle frequency v coherence limited mainly to an area close to the wing. The coherence in this frequency range covers a larger area than the low frequency coherence. The high frequency v coherence in figure 129c occurs near the juncture as expected.

These contours are also consistent with the model presented. The extent to which the contours extend upstream away from the wall provide evidence for the theory of fluid from the outer measurement region being conducted to the juncture. The large region over which the middle frequency coherence exists suggests that this frequency range is not associated with the model eddy. The regions of low frequency coherence seen are believed to be due to the overlapping of the low and middle frequency ranges. The magnitude of high frequency coherence seen in the juncture is consistent with the increase in high frequency power spectral density seen in both velocity components. Thus it appears that structures which exist in the juncture are of higher frequency and smaller scale than the model eddy.

The phase angle between the pressure and velocity can be used to determine the time lag between the two phenomena. Using the formula

$$\Delta t = \frac{\phi}{2\pi f} \quad (17)$$

where ϕ is the phase angle at the same frequency, f, at which the coherency contours in figures 102, 103, 128, and 129 were calculated. In each of the three frequency

bands, a time delay, Δt, was calculated for all locations which show significant coherence.

For the low frequency range, the time delay between the u component and the pressure at $x/t = -.20$ shows no clear pattern. For the v component, the time delay at $x/t = -.139$ and $x/t = -.193$ again shows no pattern. Upstream of the pressure measurement location and far from the wall, the low frequency time delay becomes approximately seven seconds.

The middle frequency time delays between the two velocity components and the pressure at $x/t = -.20$ show very short delays $\Delta t < .5$ seconds just downstream of the pressure measurement, $x/t = -.193$ and $x/t = -.139$. Upstream of the pressure measurement location the delay increases. For both components the delay becomes approximately four seconds.

In the high frequency range, time delays appear only at locations downstream of the pressure measurement location $x/t \leq -.193$. For the u component near the pressure measurement location, $x/t = -.193$ and $x/t = -.139$, the time delays are negative and very small, on the order of .1 second. As the wing is approached the delays become positive and larger, approximately two second. The increase in time is expected due to the increasing distance from the pressure measurement location. The v component has time delays only at $x/t = -.139$. These are all approximately -.2 seconds.

The high frequency time delays are consistent with the delays seen in the cross-correlation coefficient functions seen in figures 58 through 65. The slight

negative time delay is seen in figures 62 and 63 where the maximum correlation for both velocity components occur. The increase in positive time delay as the wing is approached is seen in figures 64 and 65. This positive time lag means the velocity leads the pressure and that fluid comes down the face of the wing before the model eddy rolls up.

The middle frequency time delays are also consistent with the cross-correlation coefficient functions. They show a positive lag upstream of the pressure measurement location as do the cross-correlations. Since the low frequency time delays showed no coherent pattern they can not be compared to the cross-correlation coefficient functions.

The low frequency time delays for the phase between the u velocity and the pressure at $x/t = 0.0$ show a distinct pattern. Near the wing and wall $x/t = -.0421$ and $x/t = -.0856$ and $y/t < .01$, the u component time delay is approximately four seconds. In the outer measurement region, $y/t > .07$, at all streamwise locations the u component time delay becomes approximately five seconds. The low frequency v component time delay again shows no pattern.

The middle frequency u component time delay with the pressure at $x/t = 0.0$ shows the same pattern as the low frequency u time delay. Near the wing and wall $x/t = -.0421$ and $x/t = -.0856$ and $y/t < .015$, the time delay is about 1.75 seconds. At all streamwise locations in the outer measurement region, the time delay increases to approximately three seconds. The v component shows middle frequency time

delays at x/t = -.0421 and x/t = -.0856. At x/t = -.0856 and y/t > .05 the delay is three seconds. at x/t = -.0421 and y/t > .019 the time delay is .6 seconds.

For the high frequency u component, there is a time delay of .2 seconds at locations of x/t > -.139 and y/t < .02. Above y/t = .02 and st the same streamwise locations the time delay increases to .6 seconds. The v component high frequency time delay shows no coherent pattern.

The calculated time delays between the two velocity components and the pressure at x/t = 0.0 does not agree entirely with the cross-correlation coefficient functions given in figures 69 through 76. Upstream of x/t = -.193 figures 69 through 73, the outer measurement region time delays agree, both being positive. Thus showing the velocity leading the pressure. However, at x/t = -.139 and further downstream, the outer region time delays are opposite. The cross-correlation coefficients show a slightly negative time delay, figures 74 to 76, while a positive time delay was calculated. In the near wall region, the time delays again are consistent with one another.

4.0 Conclusions

Velocity and pressure fluctuations were measured in the plane of symmetry of a wing-body junction. A two component laser doppler anemometer was used to make the velocity measurements. Pressure measurements were made at two locations upstream of the wing by a pair of Sennheiser microphones. A relationship between these two signals was sought to determine the turbulent structure of the flow field.

The main conclusions to be drawn from this study are:

1.) The laser doppler velocimeter measurements show the same flow structure observed by Devenport and Simpson (1990b); mean junction vortex, bimodal velocity histograms, and large increases in turbulence normal stresses in the bimodal region.

2.) The wall pressure measurements show the same features observed by Agarwal (1989) and Hasan *et al* (1985) namely a dramatic increase in p_{rms} inside the bimodal zone over onset boundary layer levels.

3.) Velocity and pressure autospectra show the bimodal zone to be a region dominated by low frequency turbulent fluctuations centered at $ft/U_{ref} = 5 \times 10^{-2}$.

4.) In the bimodal zone, the velocity spectra show a region of -1 slope.

5.) Two point velocity/pressure correlations and cross-spectra suggest that the bimodal zone is dominated by low frequency ($ft/U_{ref}=6\times10^{-3}$ to $ft/U_{ref}=0.5$) turbulent structures that produce the characteristic bimodal unsteadiness.

6.) A model consistent with the observations of (5) has been proposed. The model involves a single vortex rolling up and traveling downstream. While the vortex is moving downstream, it stretches around the wing and eventually dissipates. An intake of fluid down the face of the wing occurs before the vortex roll up and may be the cause of the bimodal unsteadiness.

7.) Vectors of velocity averaged with a change in pressure tend to support a situation similar to the model proposed.

8.) This model is also consistent with the flow visualizations of Kim (1991).

9.) There are three bands of coherency seen in the wing body junction. The low frequency band $f^*t/U_{ref}=2\times10^{-3}$ to $f^*t/U_{ref}=5\times10^{-1}$ is seen primarily in the bimodal zone. The high frequency band $f^*t/U_{ref}=4\times10^{-2}$ to $f^*t/U_{ref}=3$ is seen primarily in the juncture. The middle frequency band $f^*t/U_{ref}=2\times10^{-2}$ to $f^*t/U_{ref}=6\times10^{-1}$ is seen in locations not containing one of the other two bands.

Although the model presented is consistent with the data obtained, further study may shed more light on the flow field. To gain a better understanding of the flow field a larger velocity measurement region than used in this experiment may prove helpful. An increase in the number of pressure measurement locations would also be a logical step.

References

Abid R. and Schmitt R., "Experimental Study of a Turbulent Horseshoe Vortex Using a Three-Component Laser Velocimeter", AIAA-86-1069. *AIAA/ASME 4th Fluid Mechanics, Plasma Dynamics and Lasers Conference*, Georgia, 1986.

Agarwal, N., private communication, 1989.

Ahn, S., "Some Unsteady Features of Turbulent Boundary Layers", Master's Thesis, Virginia Polytechnic Institute and State University, Blacksburg, VA, 1986.

Bendat, J. S., and Piersol, A. G., <u>Random Data Analysis and Measurement Procedures</u>, pp 361-424, John Wiley & Sons, New York, 1986.

Dechow, R. and Felsch, K. O., "Measurements of the Mean Velocity and of the Reynolds Stress Tensor in a Three-Dimensional Turbulent Boundary Layer Induced by a Cylinder Standing on a Flat Wall", *Turbulent Shear Flows Symposium, Pennsylvania State University*, pp. 9.11-9.20, 1977.

Devenport, W. J., private communication, 1991.

Devenport, W. J. and Simpson, R. L., "An Experimental Investigation of the Flow Past an Idealized Wing-Body Junction: Preliminary Data Report v. 5", AOE Dept., VPI&SU, 1990a.

Devenport, W. J. and Simpson, R. L., "Time-Dependent and Time-Averaged Turbulence Structure near the Nose of a Wing-Body Junction". *Journal of Fluid Mechanics*, Vol. 210, pp. 23-55, 1990b.

Devenport, W. J. and Simpson, R. L., "Time-Dependent Structure in Wing-Body Junction Flow" *Turbulent Shear Flows 6*, 1989.

Dickinson, S. C., "An Experimental Investigation of Appendage-Flat Plate Junction Flow Volume 1: Description", DTNSRDC-86/051, December 1986a.

Echols, W. H. and Young, J. A., "Studies of Portable Air-Operated Aerosol Generators", NRL Report 5929, 1963.

Eckerle, W. A., and Langston, L. S., "Horseshoe Vortex Formation Around a Cylinder", *Journal of Turbomachinery*, Vol. 109, pp. 278-285, April 1987.

Hasan, M. A. Z., Casarella, M. J., and Rood, E. P., "An Experimental Study of the Flow and Wall-Pressure Field Around a Wing-Body Junction", *Shear Flow-Structure Interaction Phenomena* (ed. A. Akay & M. Reischman), ASME NCA-1, pp. 89-95, 1985.

Hinze, J. O., Turbulence, McGraw-Hill Publishing Company, New York, 1987.

Klebanoff, F. S., "Characteristics of Turbulence in a Boundary Layer with Zero Pressure Gradient", NACA Technical Report 1247, 1975.

Kline, S. J. and McClintock, F. A., "Describing Uncertainty in Single-Sample Experiments", Mechanical Engineering, January, pp. 3-8, 1953.

Kirn, S., "Observation and Measurements of Flow Structures in the Stagnation Region of a Wing-Body Junction", PhD Dissertation, Virginia Polytechnic Institute and State University, Blacksburg, Va., 1991.

Kubendran, L. R, McMahon, J., and Hubbartt, J.E. AIAA-85-0040 "Turbulent Flow Around a Wing-Fuselage Type Juncture", *AIAA 23rd Aerospace Sciences Meeting*, 1985.

McGrath B. E., and Simpson R. L., "Some Features of Surface Pressure Fluctuations in Turbulent Boundary Layers with Zero and Favorable Pressure Gradients", NASA Contractor Report 4051, 1987.

Mehta, R. D., "Effect of Wing Nose Shape on the Flow in a Wing/Body Junction", *The Aero. J. of the Royal Aero. Soc.*, pp. 456-460, December 1984.

Norman, R. S., "On Obstacle Generated Secondary Flows in Laminar Boundary Layers and Transition to Turbulence", Ph.D. dissertation, Illinois Institute of Technology, 1972.

Olcmen, S., Simpson, R. L., Kim, S., and Ha, S. M., "Some Effects of Appendage Shape and a Fence Control Device on Appendage/Hull Junction Flows: Final Report", Report VPI-AOE-183, Dec., 1991.

Rood, E. P., "Experimental Investigation of the Turbulent Large Scale Temporal Flow in the Wing_Body Junction", Ph.D. dissertation, The Catholic University of America, 1984.

Simpson, R. L., Agarwal, N. K., Nagabushana, K. A., and Olcmen, S., "Spectral Measurements and Other Features of Separating Turbulent Flows", *AIAA-88-0616, AIAA 26th Aerospace Sciences Meeting*, Reno, NV, 1988.

Simpson, R. L. and Chew, Y. T., "Measurements in Steady and Unsteady Separated Turbulent Boundary Layers", Laser Velocimetry and Particle Sizing, Thompson, H. D. and Stevenson, W. H., Editors, NY: Hemisphere, pp 179-196, 1979.

Simpson, R. L., Ghodbane, M., and McGrath, B. E., "Surface Pressure Fluctuations in a Separating Turbulent Boundary Layer", *Journal of Fluid Mechanics*, vol. 177, pp. 167-186, 1987.

Tchen, C. M., "On the Spectrum of Energy in Turbulent Shear Flow", Res. Paper RP2388, Journal of Res., National Bureau of Standards, vol. 50, no. 1, Jan, 1953, pp. 51-62.

Thomas, A. S. W., and Bull, M. K., "On the Role of Wall-Pressure Fluctuations in Deterministic Motions in the Turbulent Boundary Layer", *Journal of Fluid Mechanics*, vol. 128, pp. 283-322, 1983.

Townsend, A. A., The Structure of Turbulent Shear Flow, Cambridge University Press, New York, 1976.

Figures
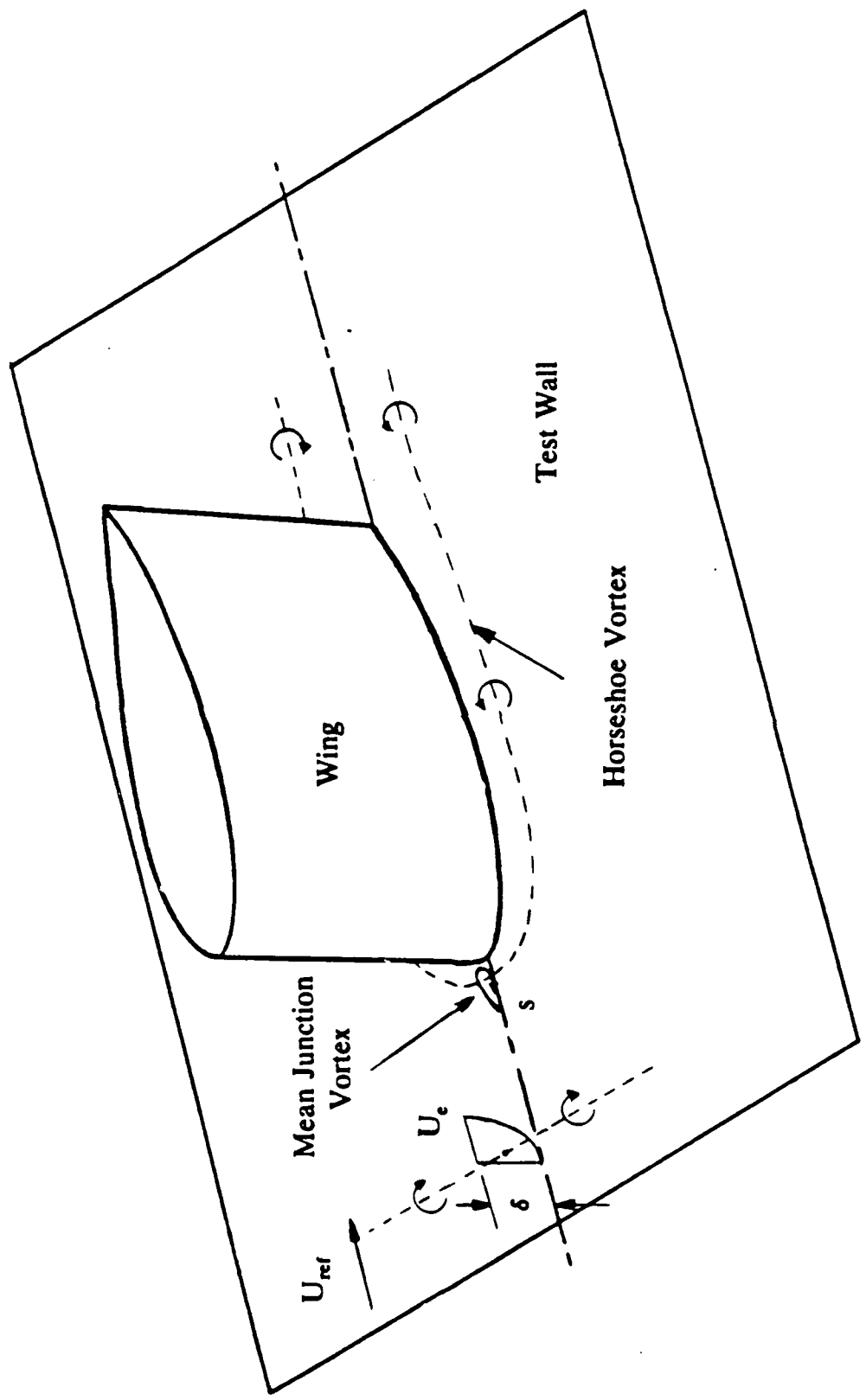
Figure 1: Schematic of a wing body junction flow
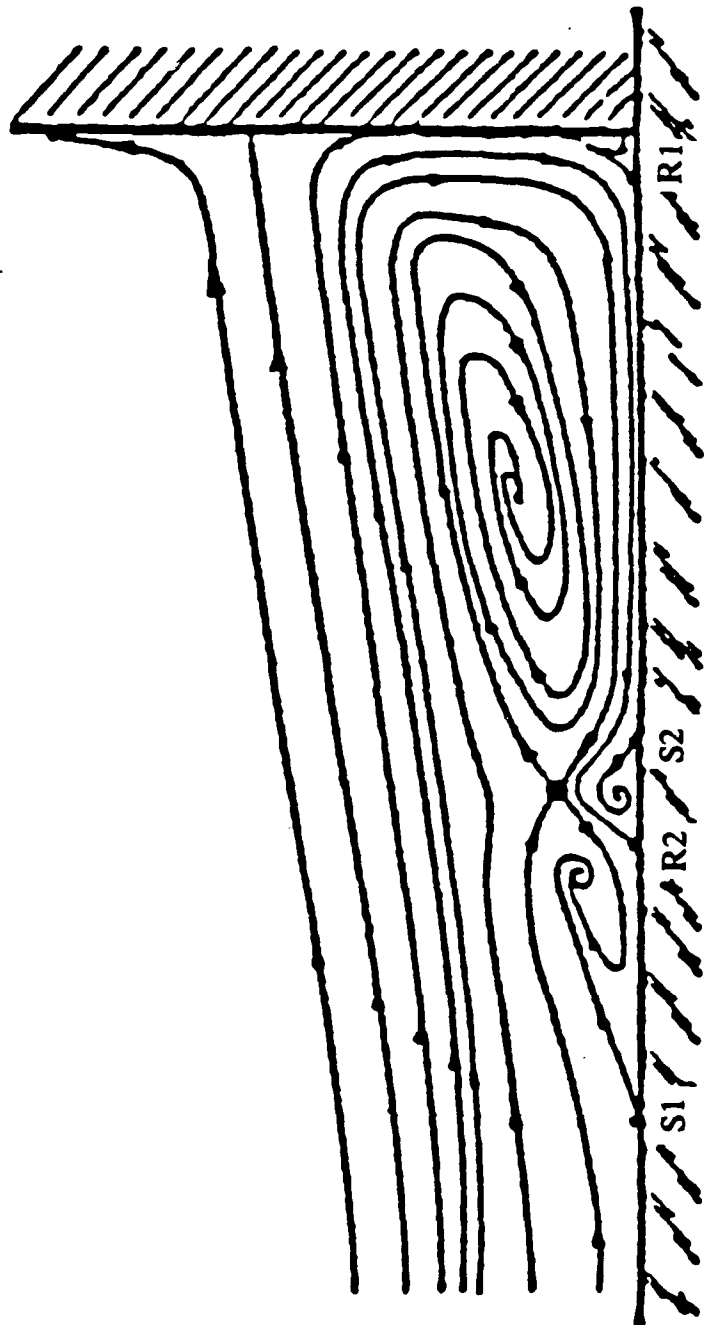
Figure 2: Four vortex model proposed by Norman (1972) from Abid and Schmitt (1986). S indicates a separation point and R is a reattachment point.

Line of Low Shear
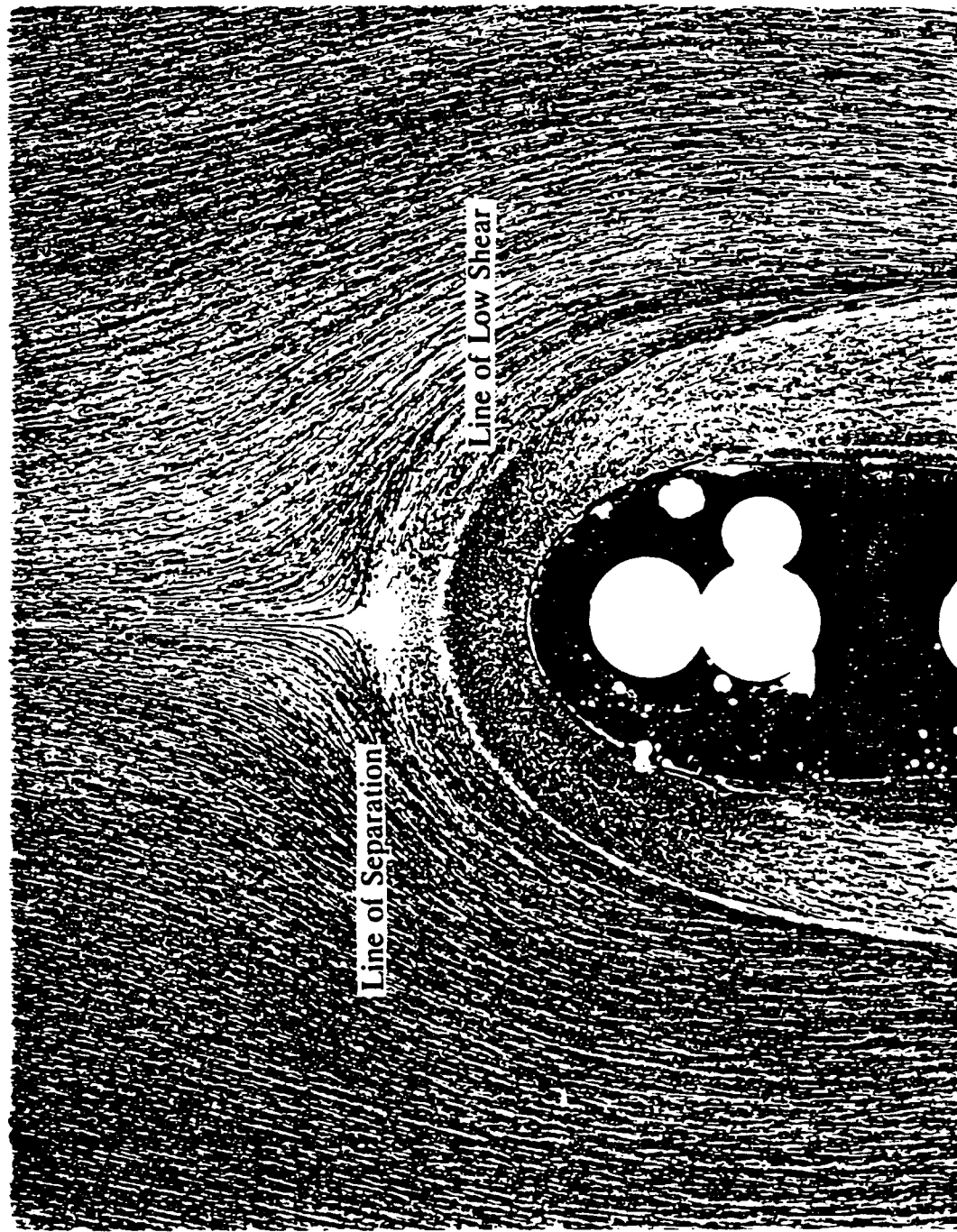
Line of Separation

Figure 3:   Oil flow in the nose region of the wing-body junction from Devenport and Simpson (1990b). Note line farthest away from nose is line of separation while line nearest nose is line of low shear.
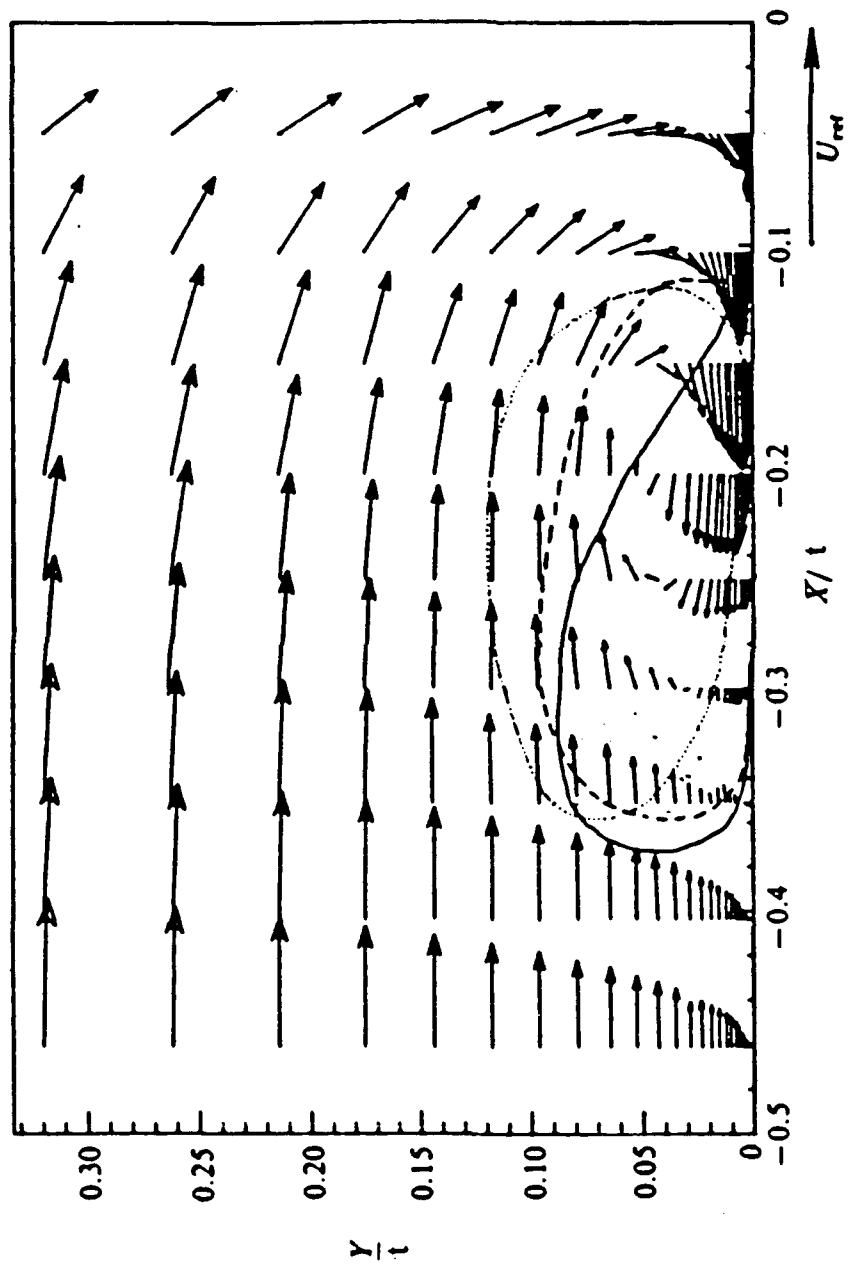
Figure 4:   Mean velocity vectors showing the mean junction vortex Devenport and
              Simpson (1990b). Solid line shows extent of U bimodal flow, dashed
              line shows extent of V bimodal, and dotted line shows extent of U-V
              bimodal flow.
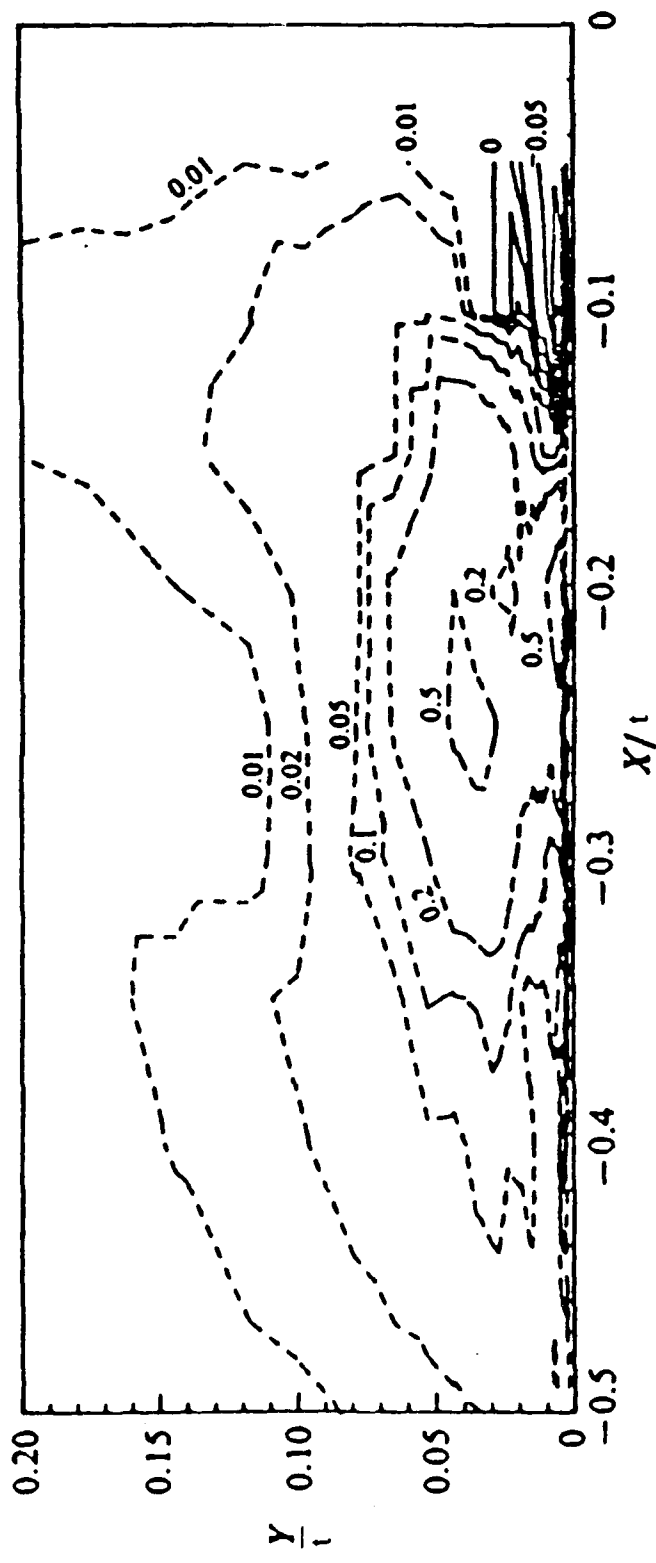
Figure 5: Contours of turbulence kinetic energy production from Devenport and Simpson (1990b).
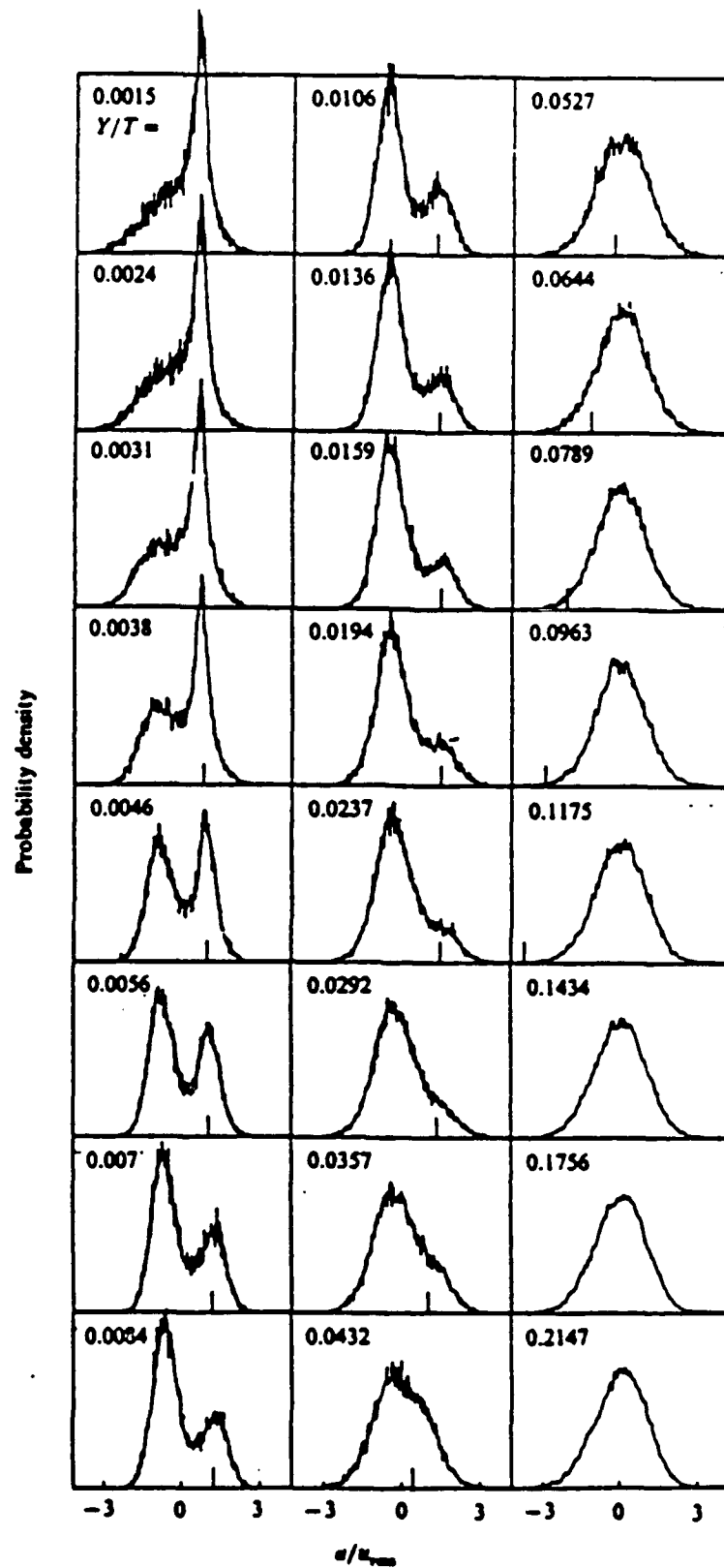
Figure 6:   Probability density functions at the streamwise position of x/t = -.20 from Devenport and Simpson.
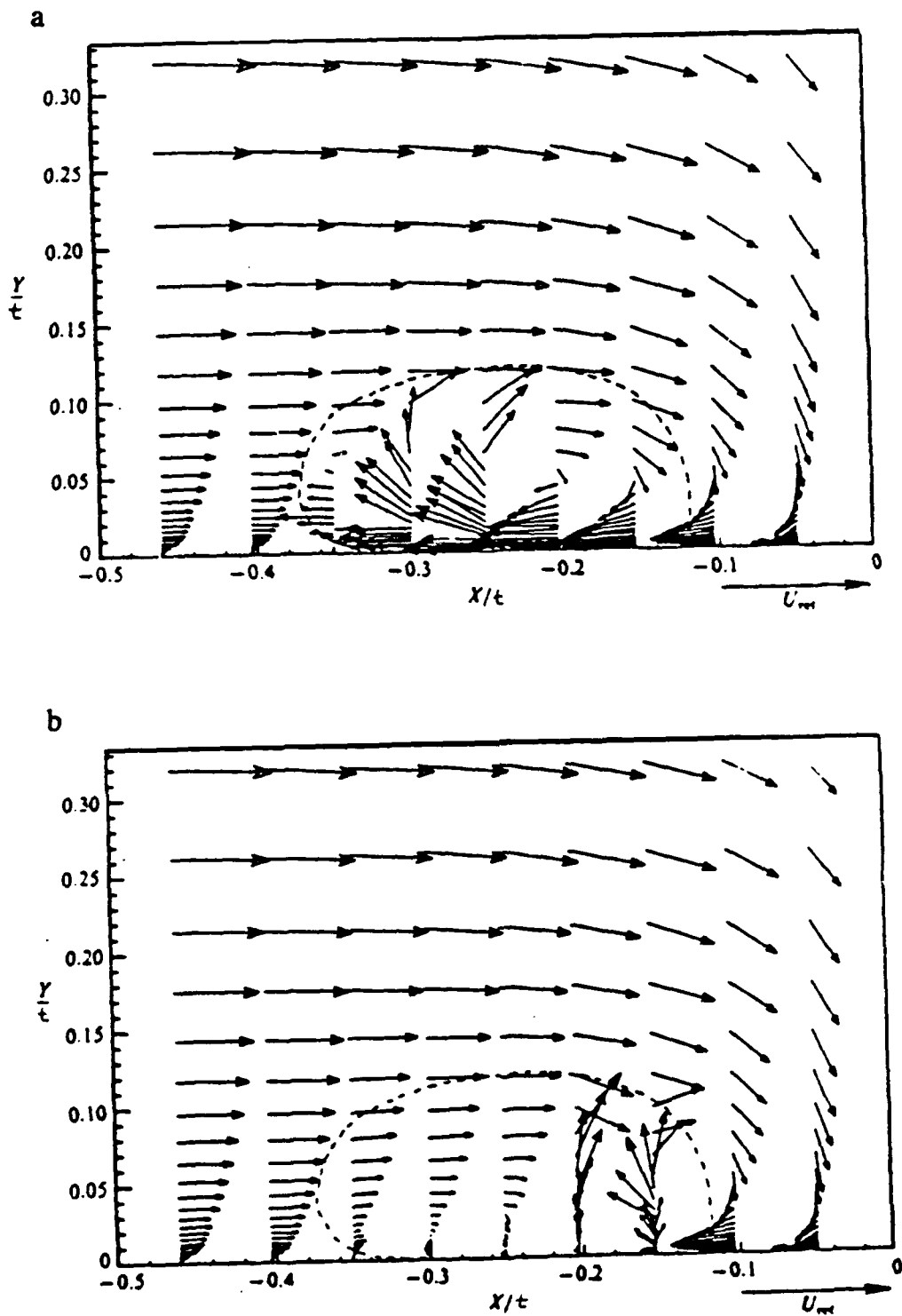
Figure 7:   Velocity vectors showing a. backflow mode and b. zero flow mode
from Devenport and Simpson. Dashed line indicates the extent of
the U and V bimodal flow zones.
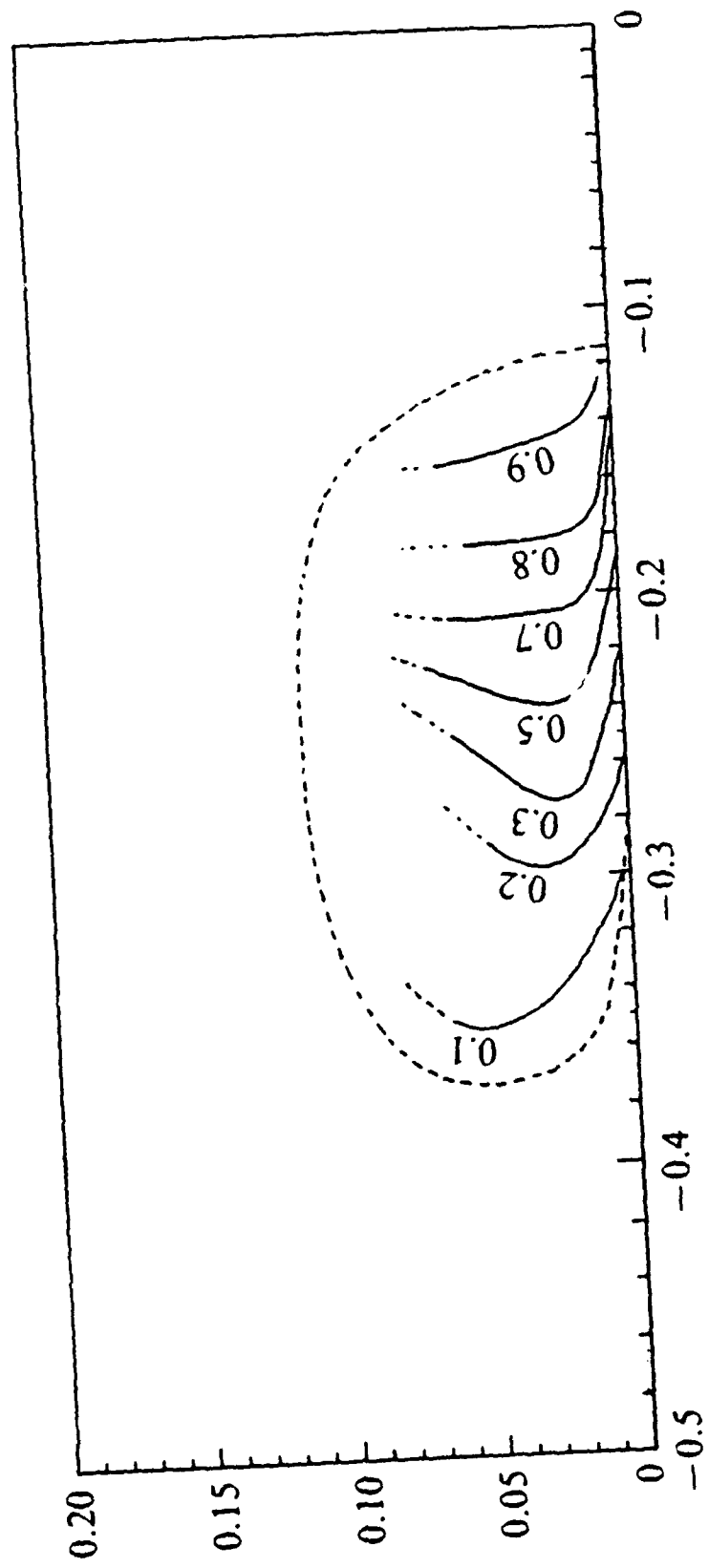
Figures

Figure 8:   Contours of γ_b (the period of time for which backflow exists).
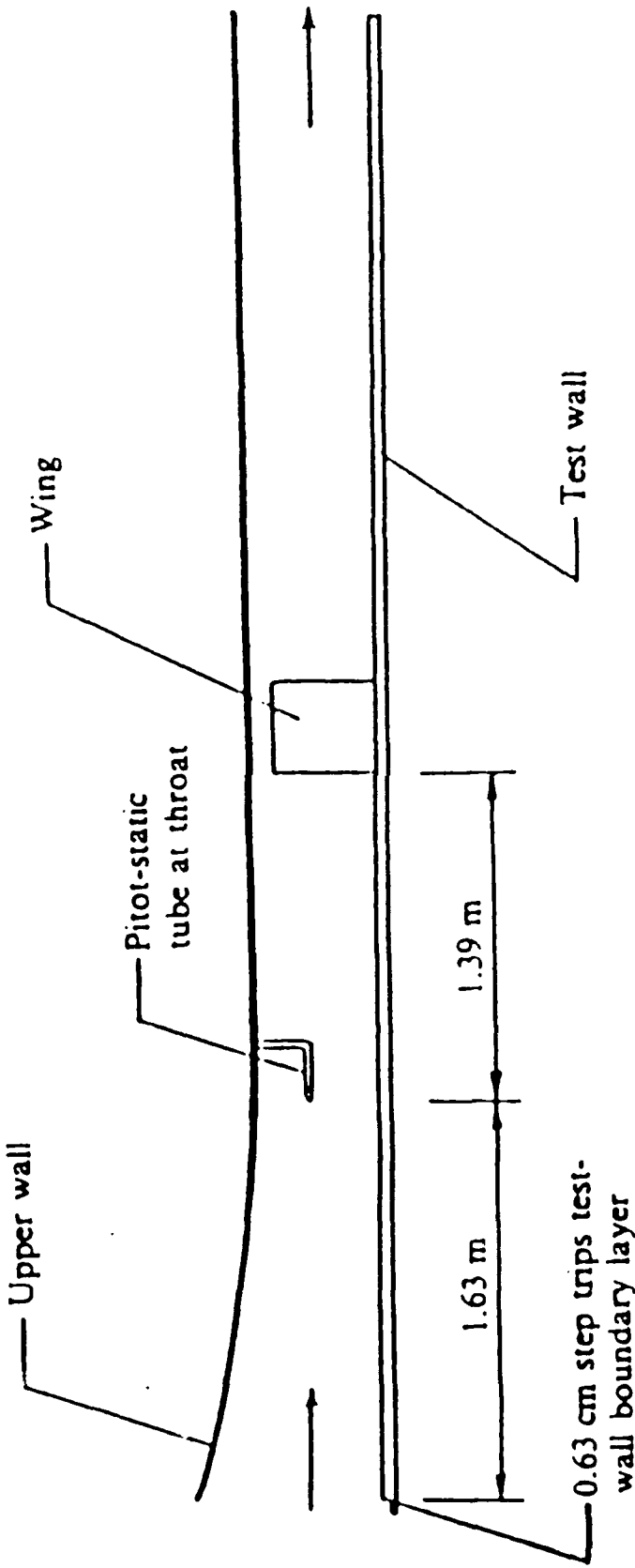
Figure 9: Side view schematic of boundary layer wind tunnel used for wing-body experiments.

Upper wall

Wing

Pitot-static tube at throat

Test wall

1.39 m

1.63 m

0.63 cm step trips test-wall boundary layer
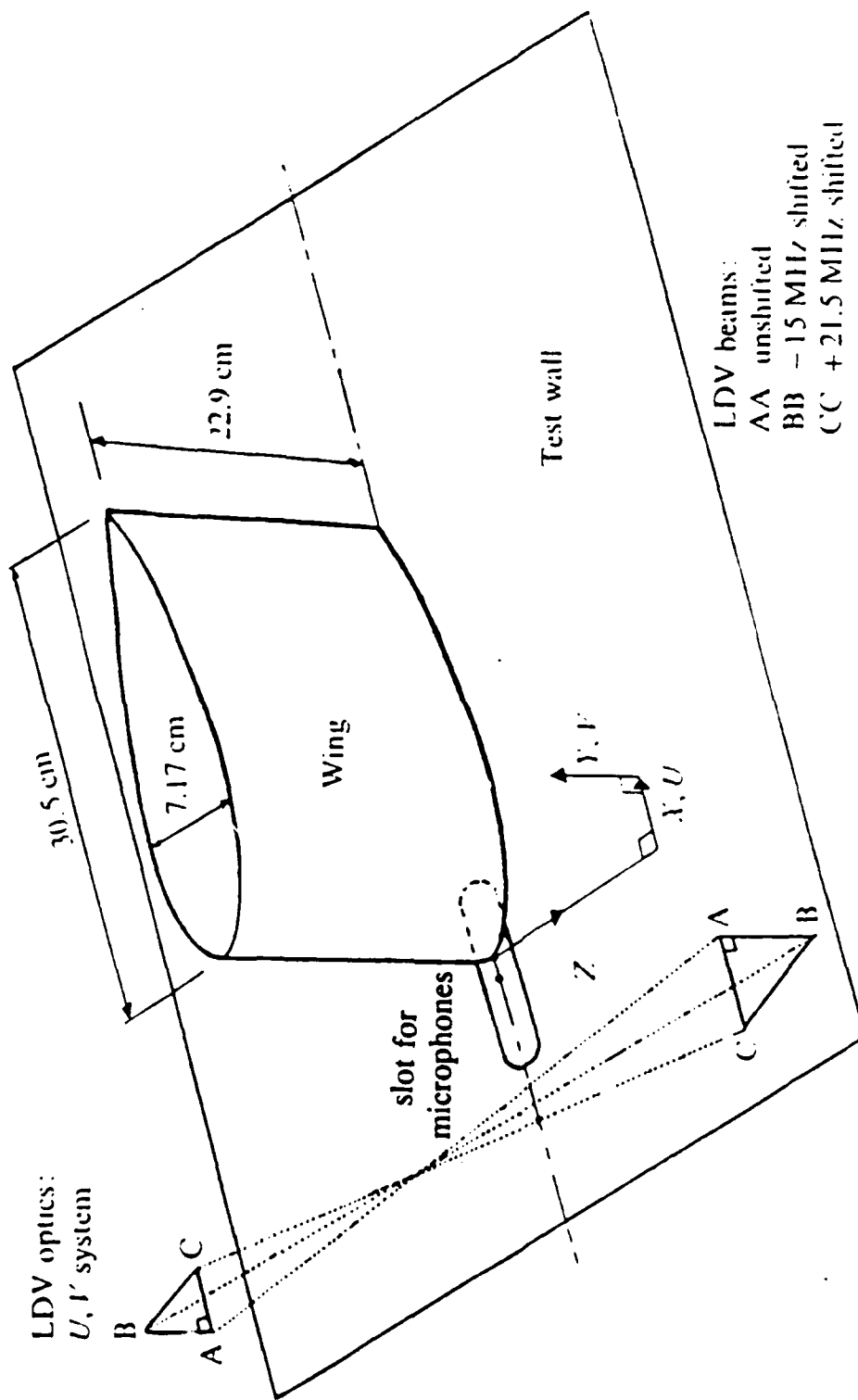
Figure 10: Perspective view of the wing-body junction. Note the two component LDV system and the slot for microphone placement.

.20 x/t

.635 mm Dia
openings
5 per housing

Microphone
Housings

Bracket

Support Rod
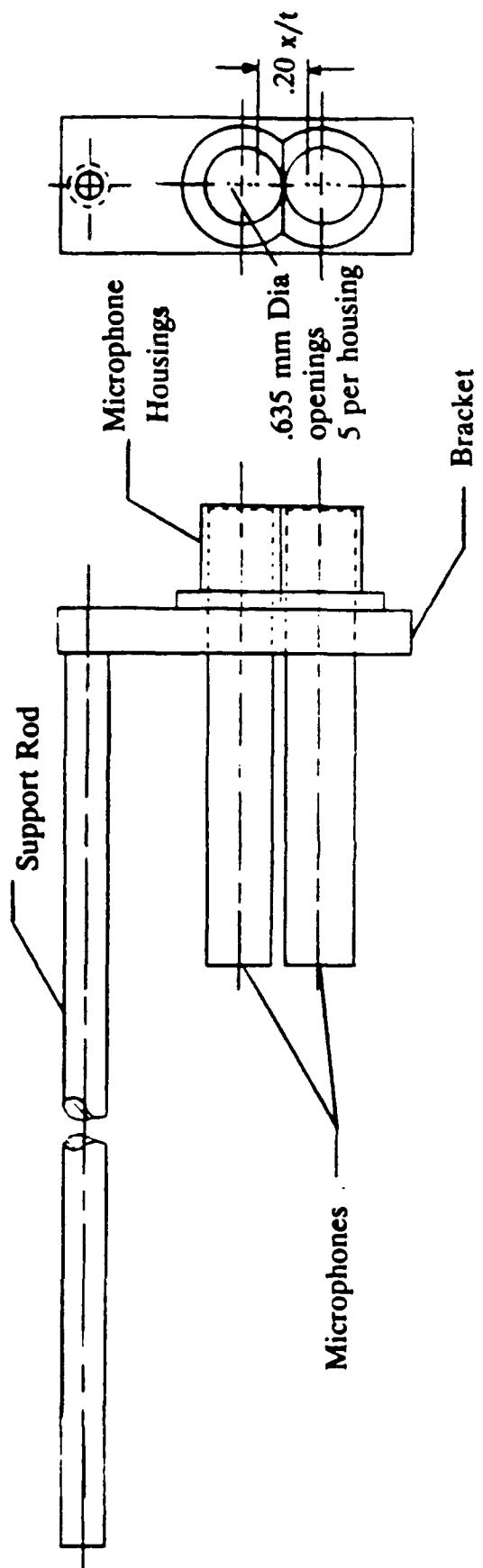
Microphones

Figure 11: Microphone housings and mounting bracket
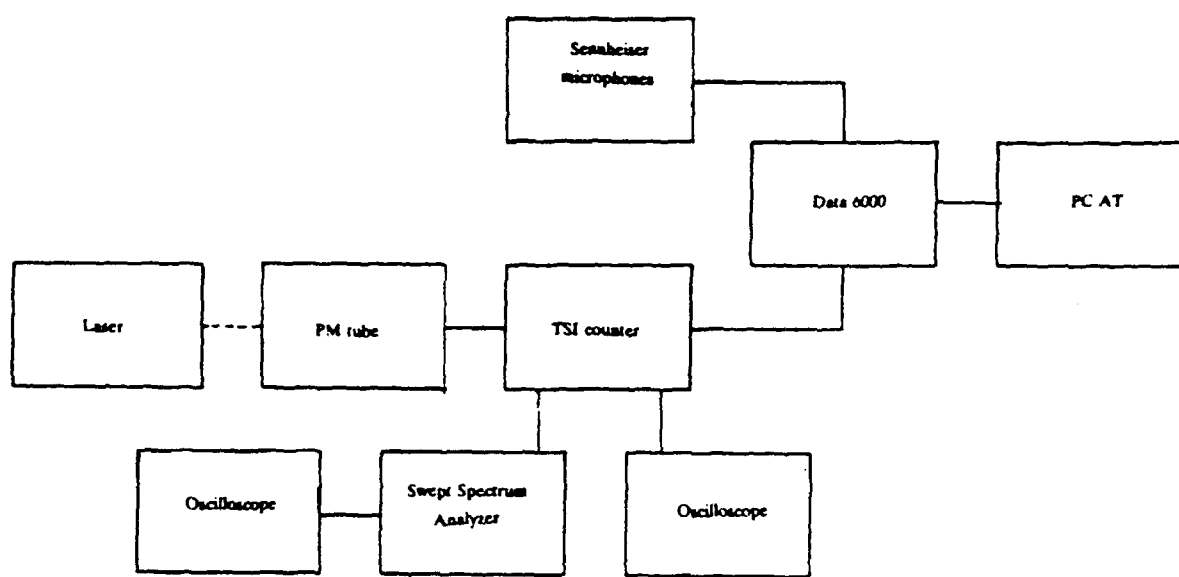
Figure 12:   Schematic of the data acquisition system used during the present
             experimental study
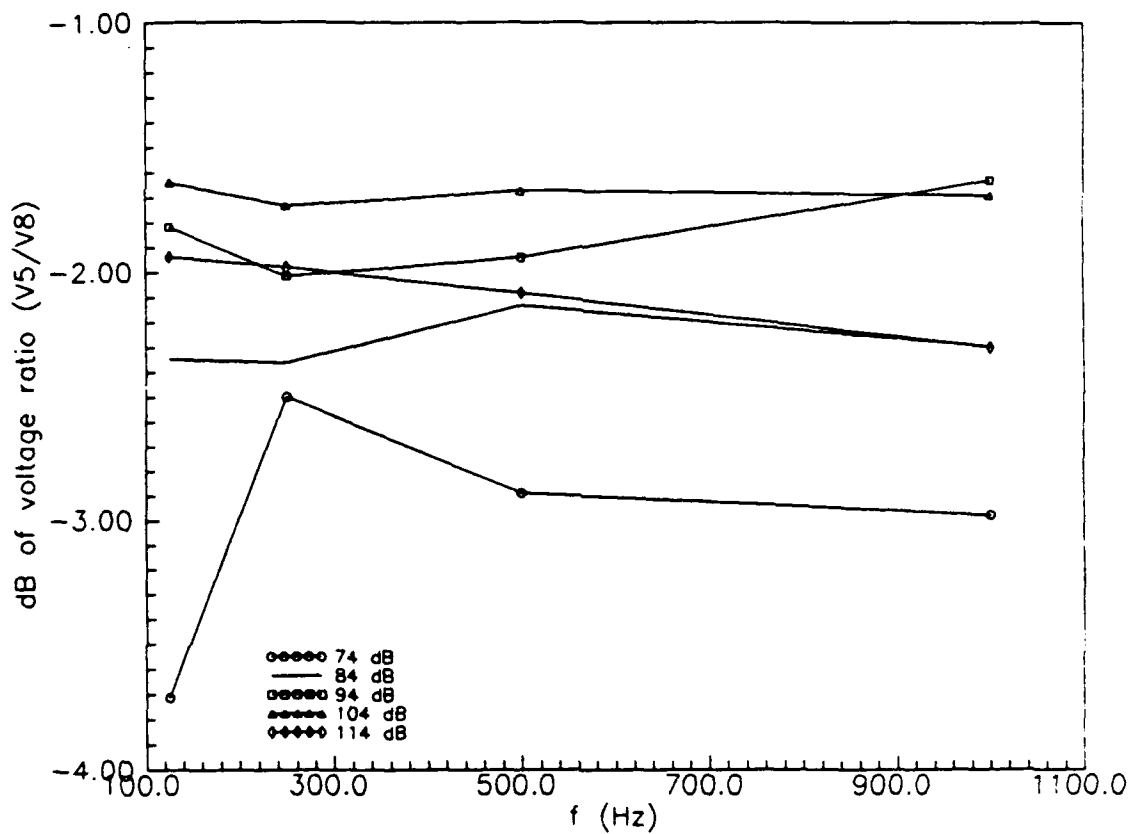
Figure 13:   Calibration of Sennheiser microphones. The Y axis is the output voltage ratio of 5 volts input over 8 volts input.
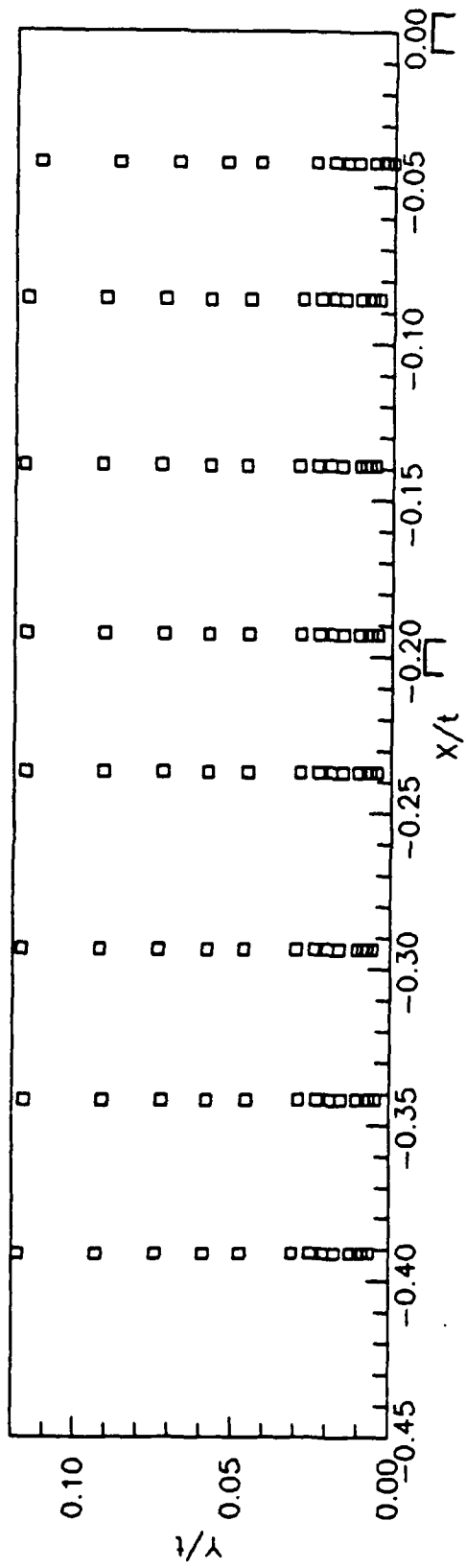
Figure 14: LDV measurement grid, □ indicates a laser measurement, and location ⊓ indicates a pressure measurement location.
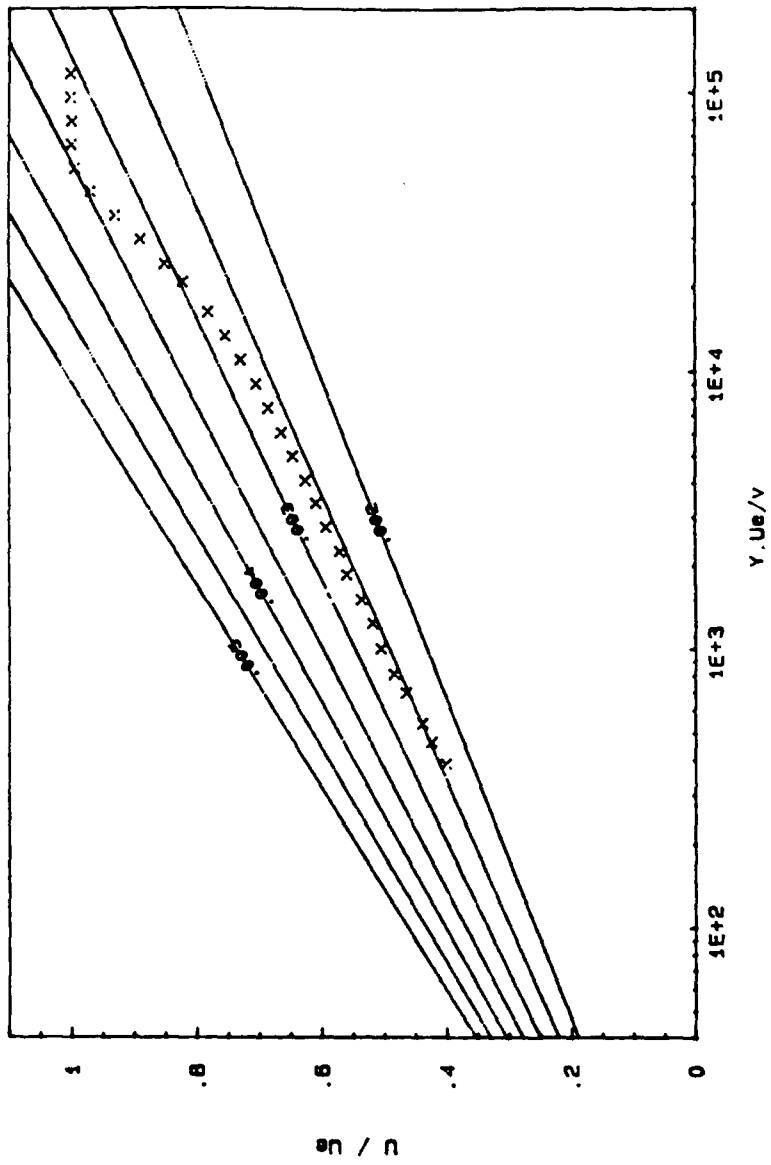
Figure 15: Clauser plot of the mean velocity profile of the onset boundary layer at $x/t = -2.15$, $z/t = 0$.
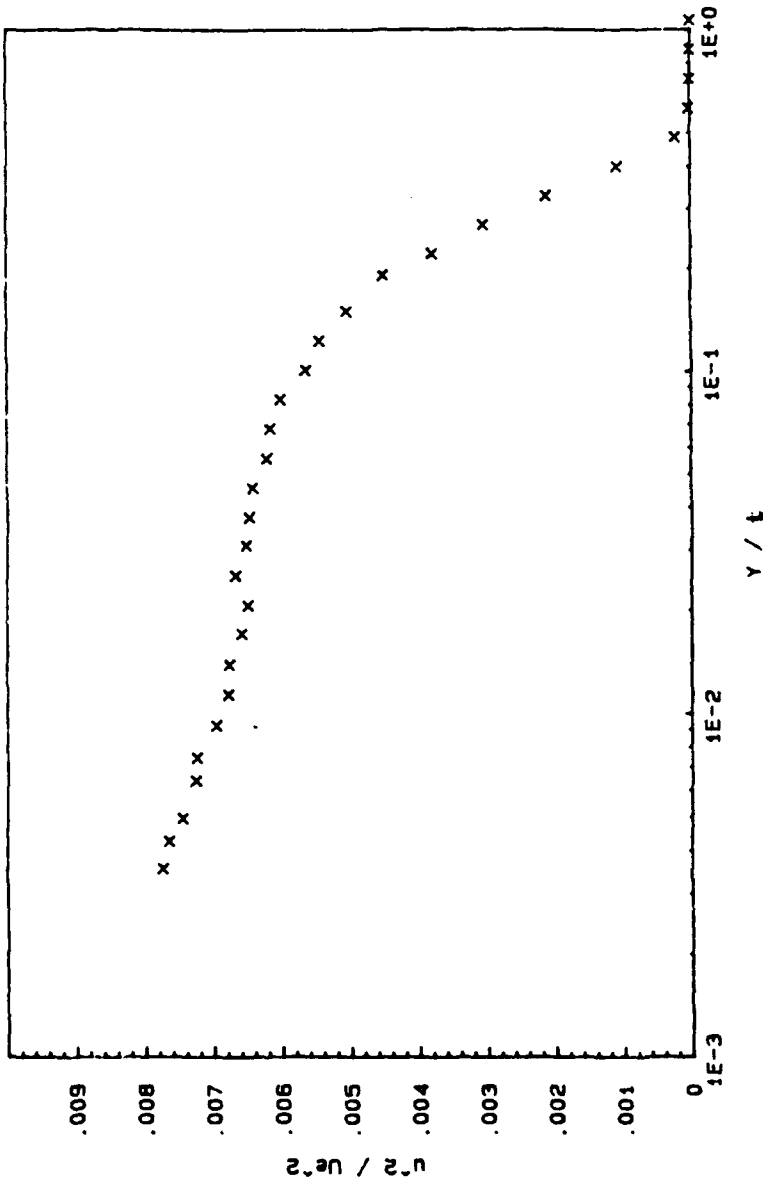
Figure 16: Profiles of normalized mean square velocity across the onset boundary layer.
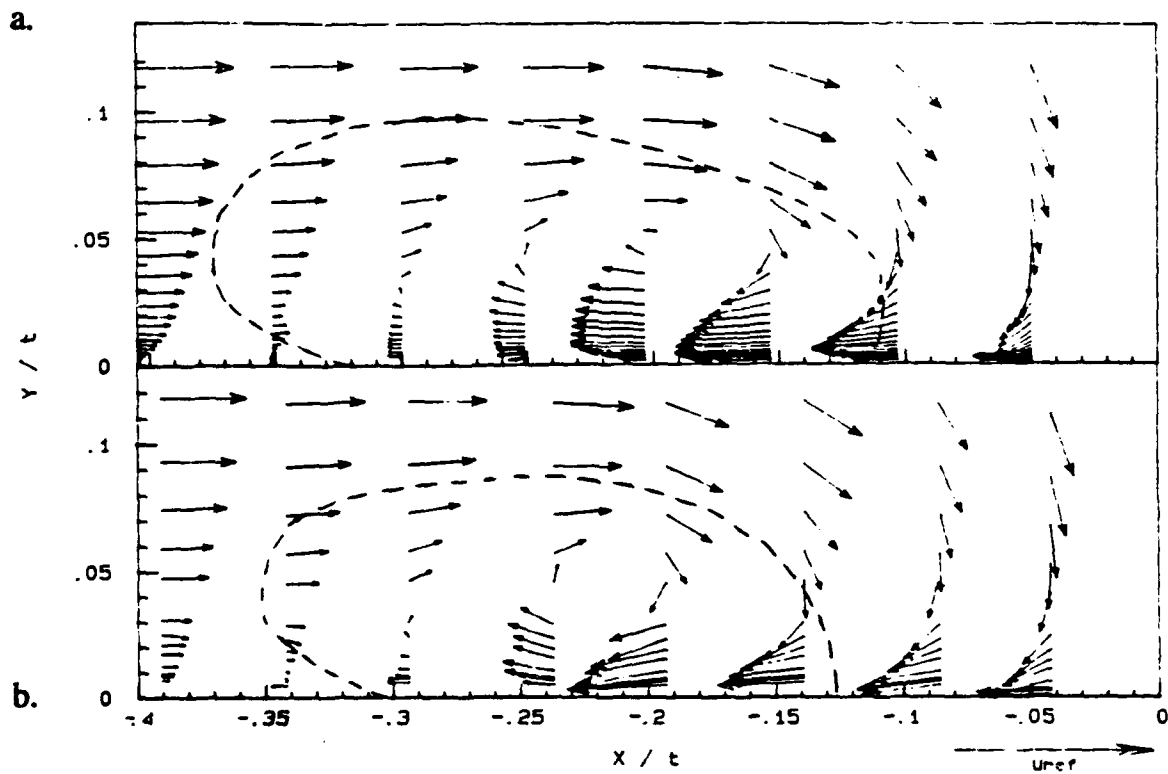
Figure 17:   Mean velocity vectors at the nose of the wing body junction of a.
              Devenport and Simpson (1989b) and b. Rife (1992). Dashed line
              indicates the composite (U and V) bimodal zone.
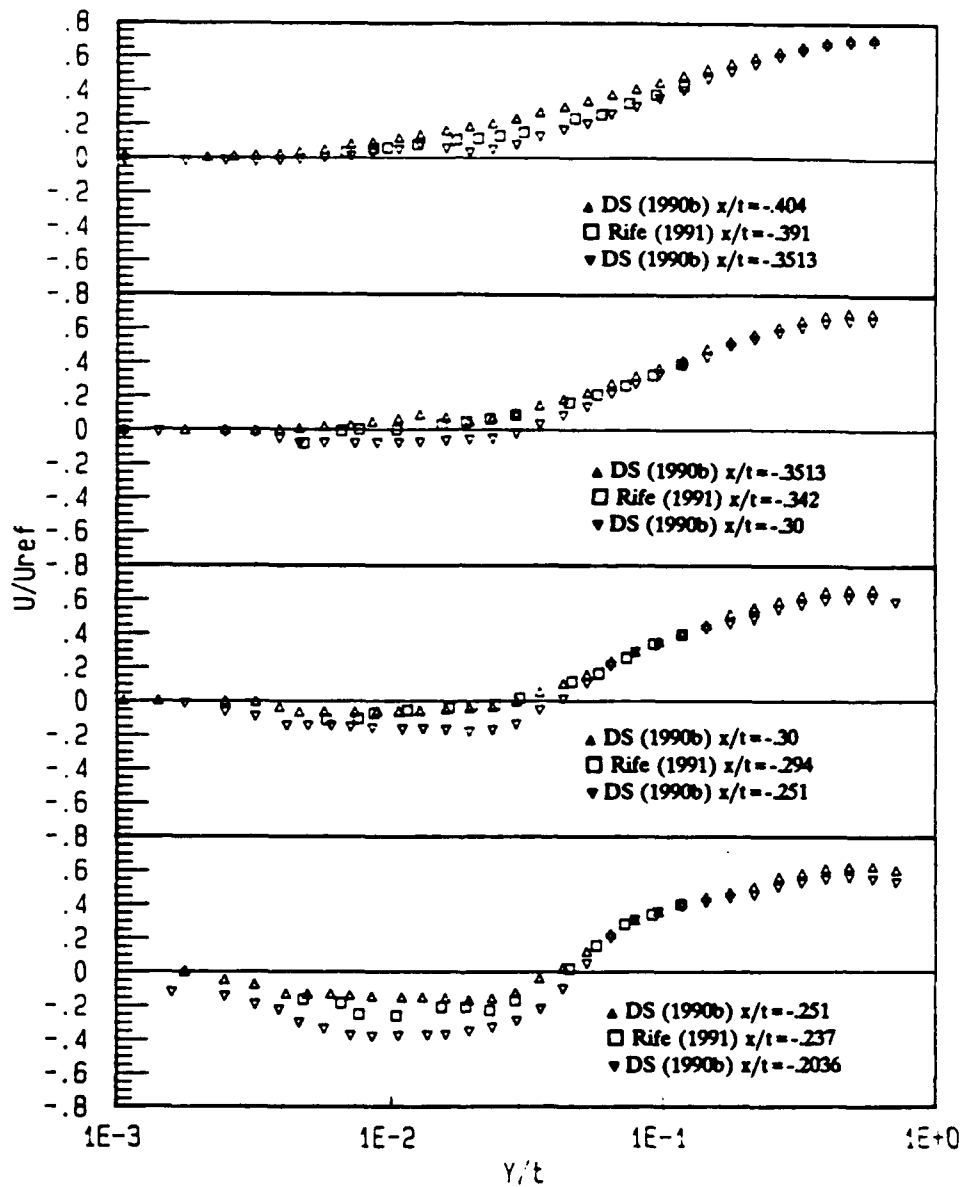
Figure 18a: U component mean velocity comparisons with Devenport and Simpson 1989.
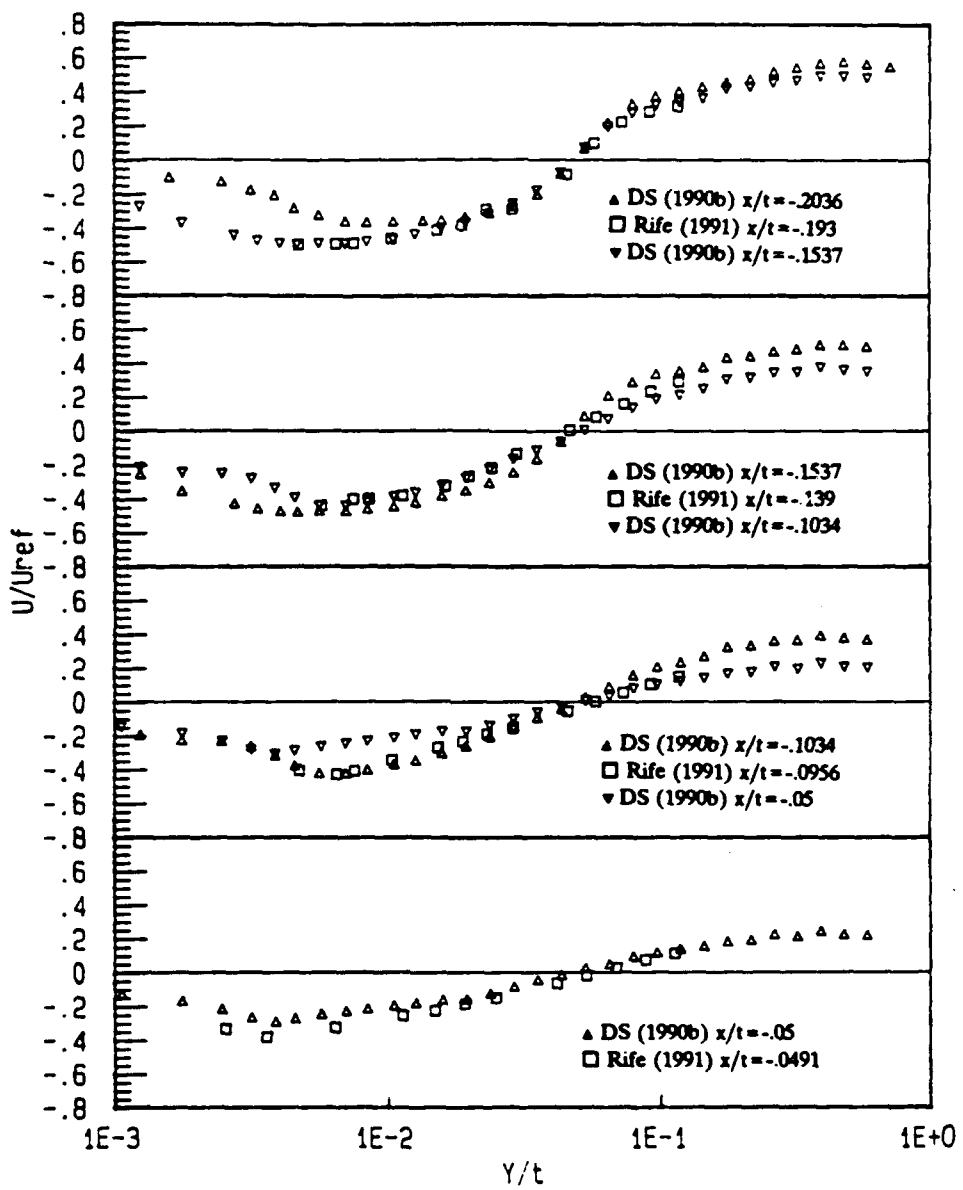
Figure 18b:
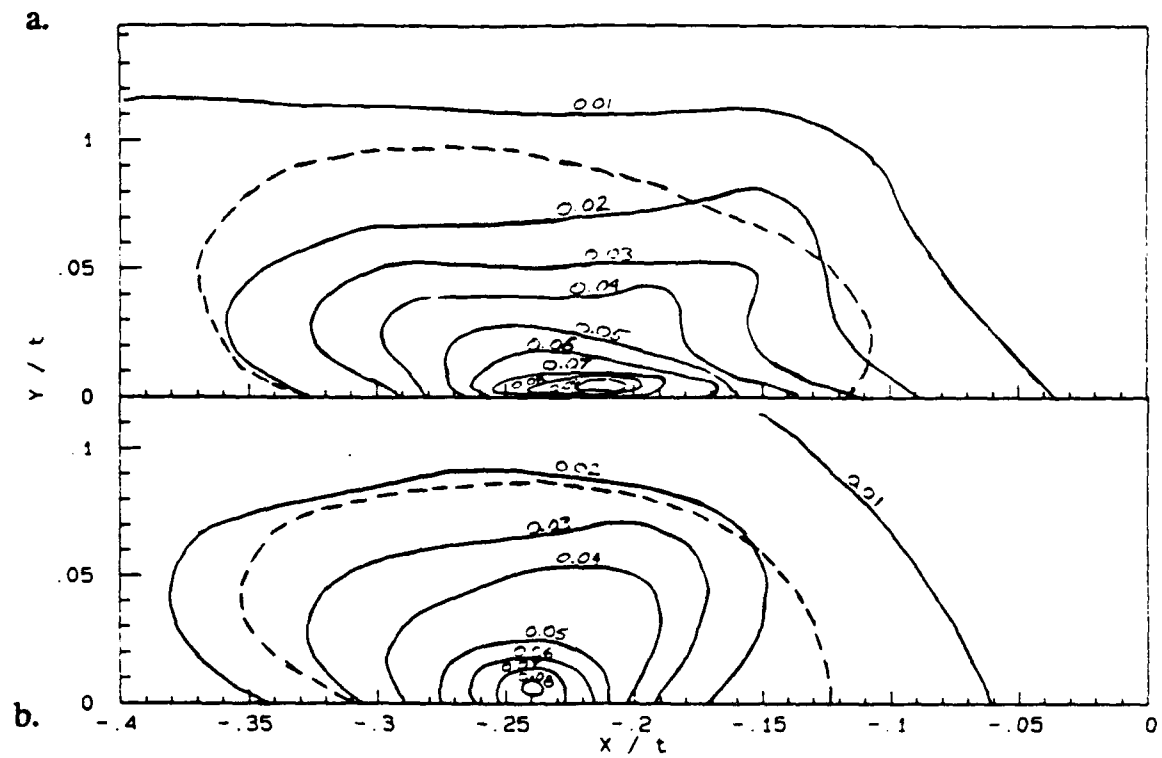
Figure 19: Contours of U component mean square velocity u^2/U_{ref}^2 of a. Devenport and Simpson (1989b) and b. Rife (1992). Dashed line is the composite (U and V) bimodal zone.
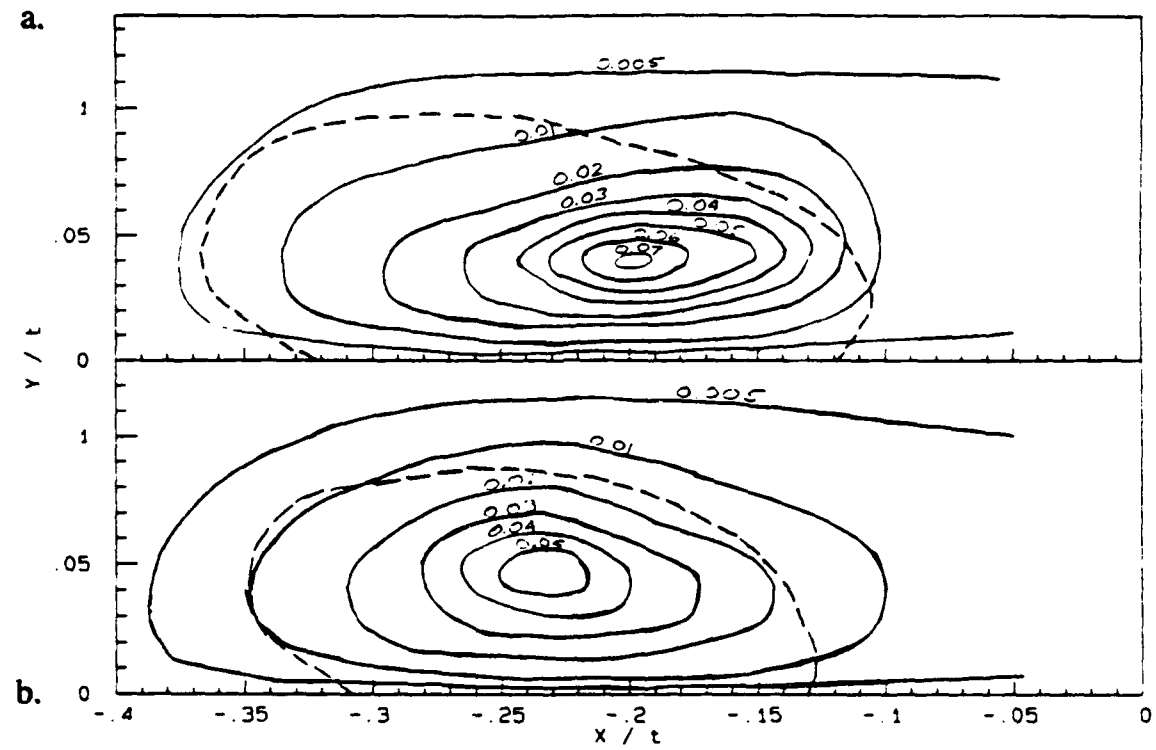
Figure 20:   Contours of V component mean square velocity v^2/U_{ref}^2 of a.
Devenport and Simpson (1989b) and b. Rife (1992). Dashed line
is the composite (U and V) bimodal zone.
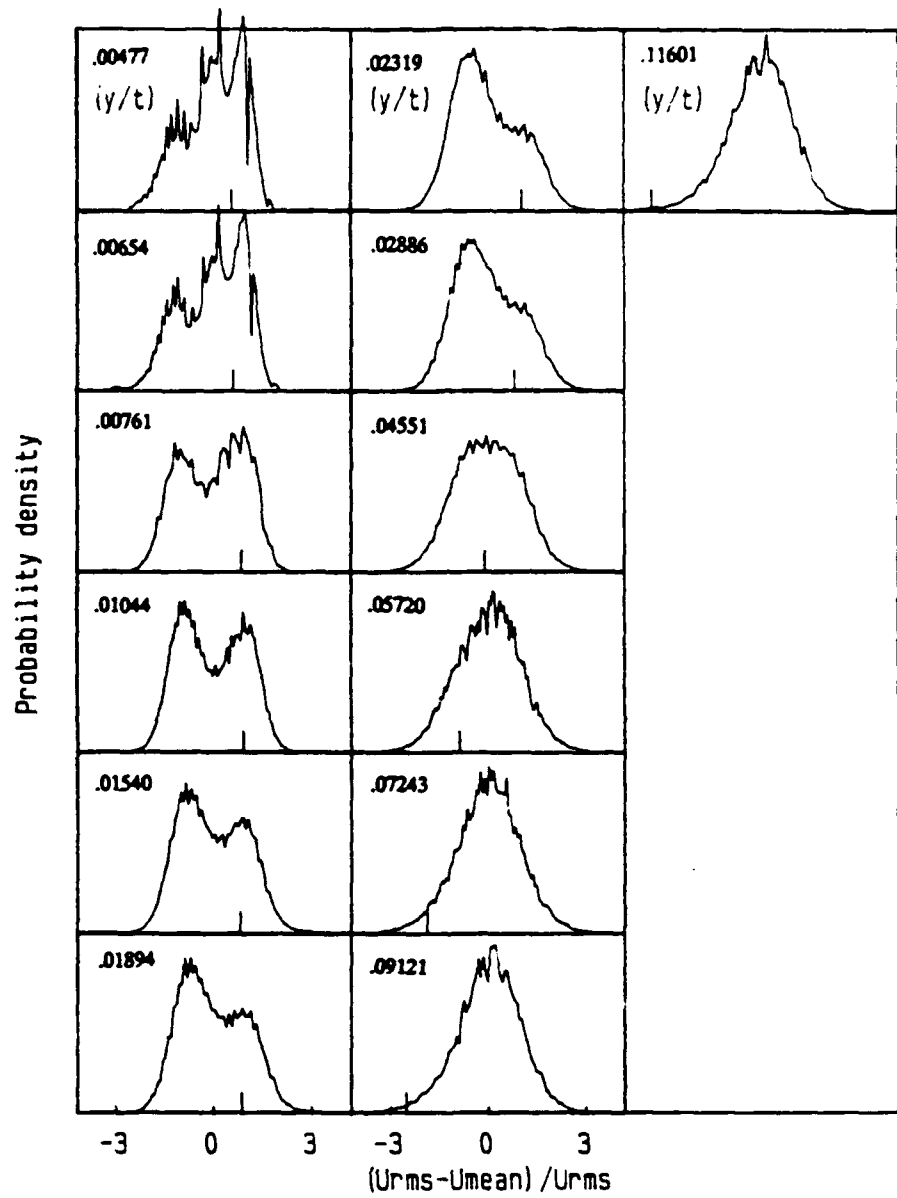
Figure 21: Histograms of U component velocity fluctuations at $x/t = -.237$
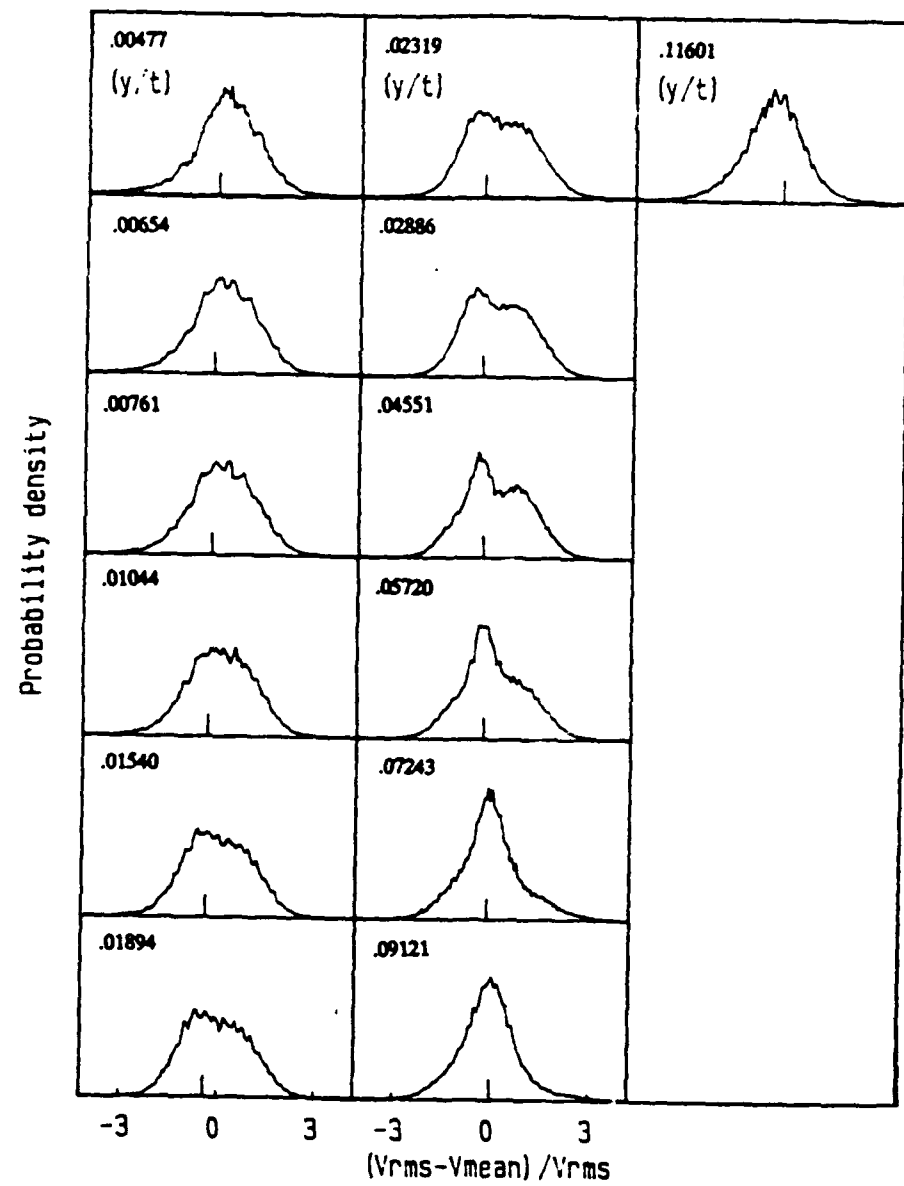
Figure 22:   Histograms of V component velocity fluctuations at x/t = -.237
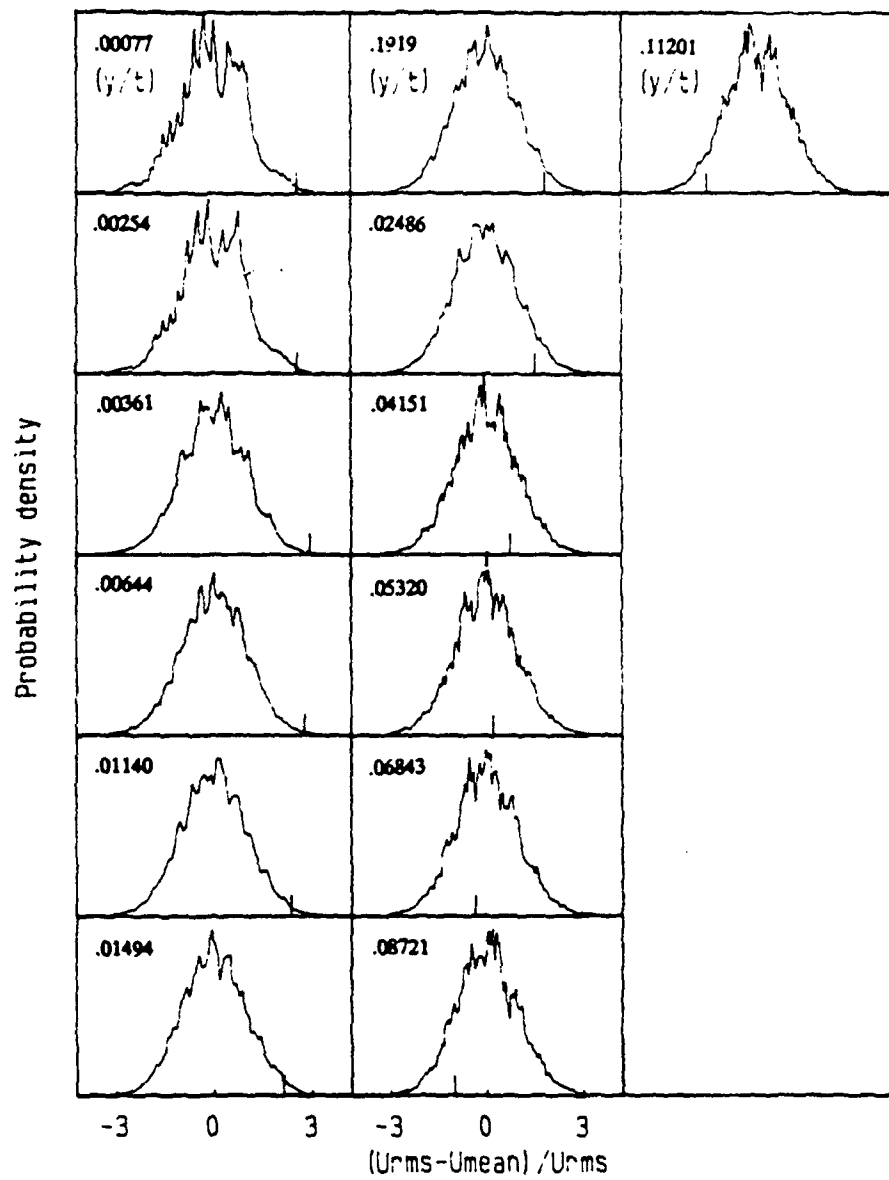
Figure 23:   Histograms of U component velocity fluctuations at $x/t \approx -.0421$
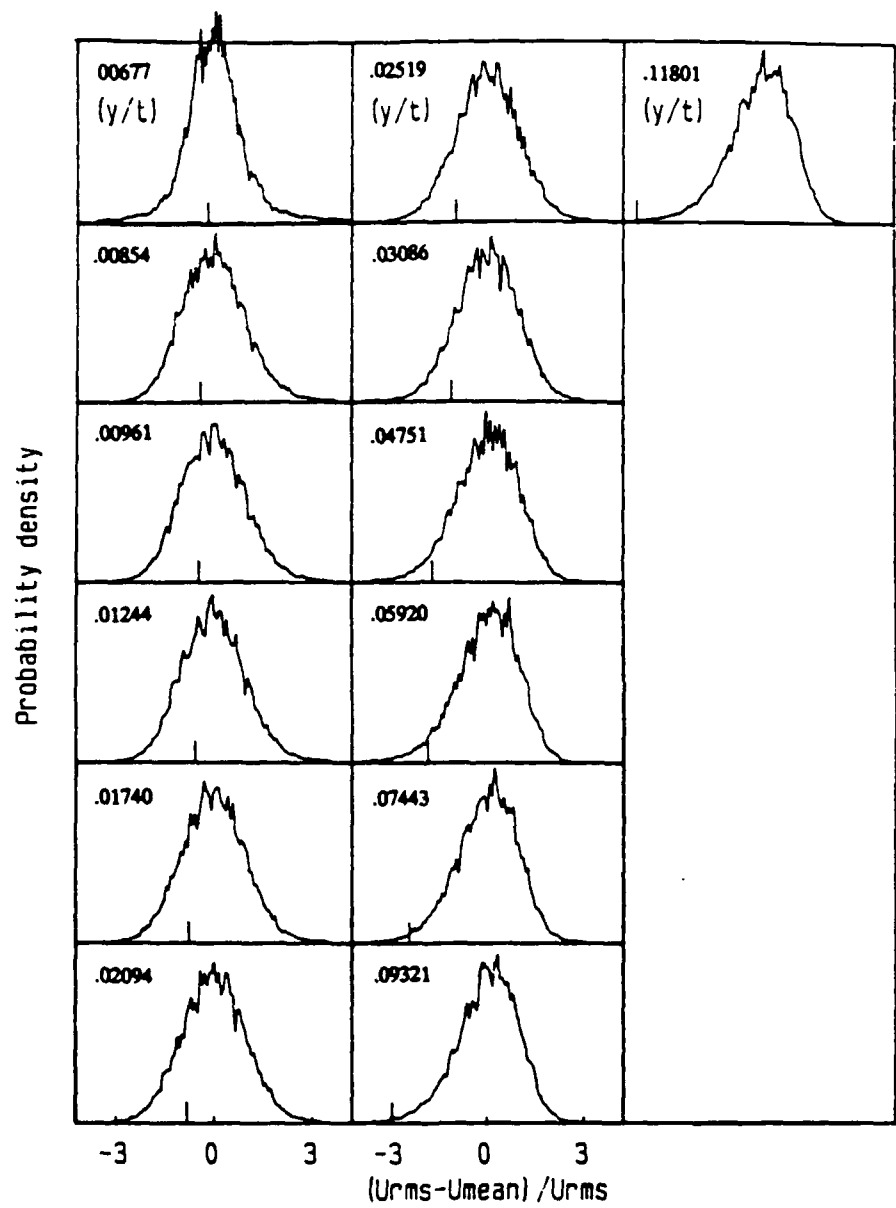
Figure 24: Histograms of U component velocity fluctuations at x/t = -.391
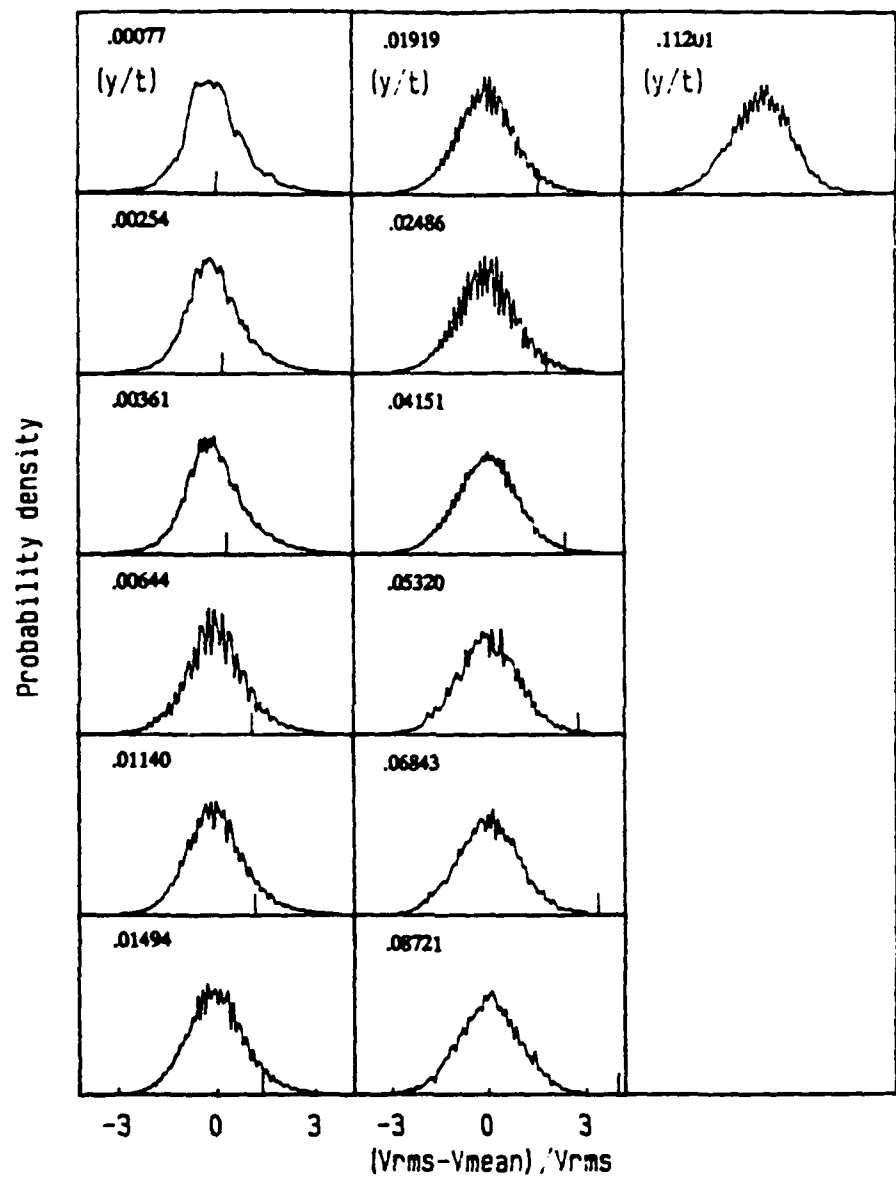
Figure 25:   Histograms of V component velocity fluctuations at x/t = -.0421
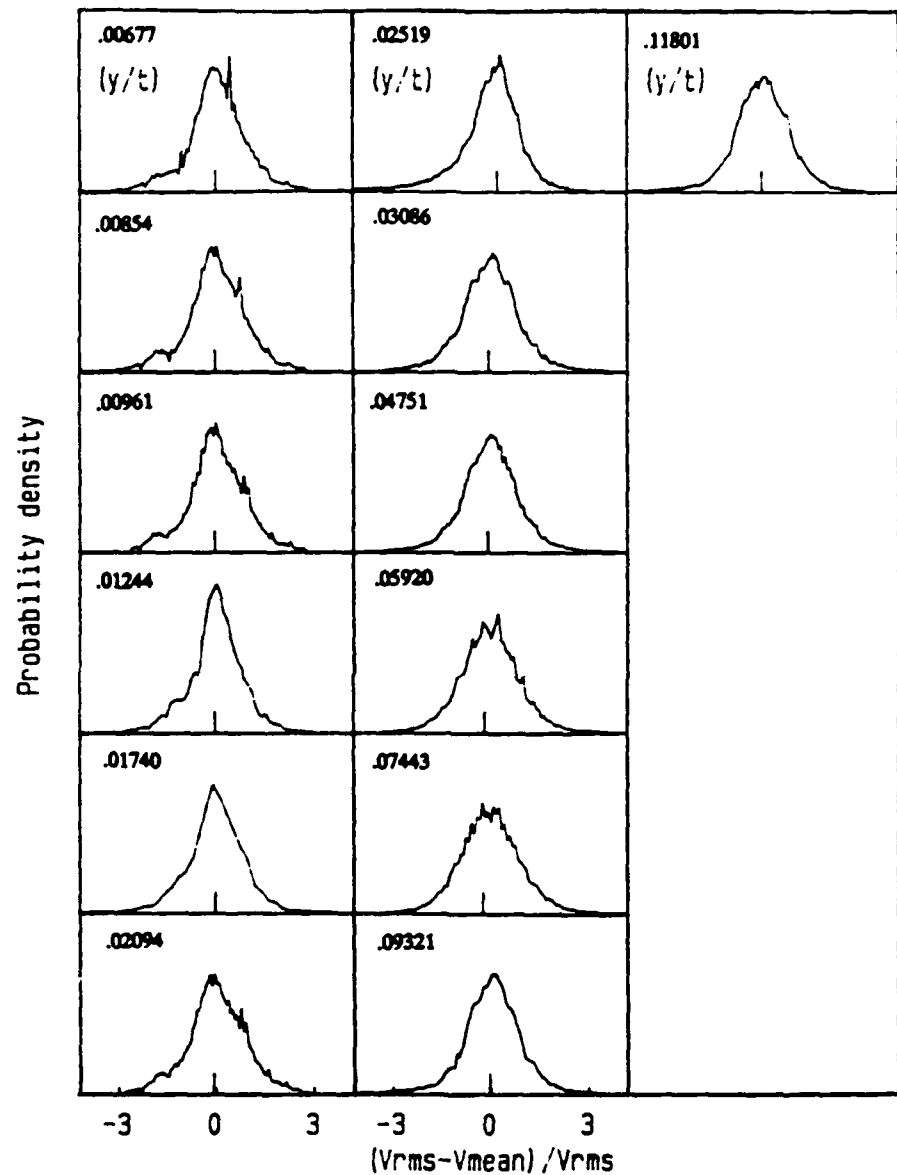
Figure 26:   Histograms of V component velocity fluctuations at $x/t = -.391$.
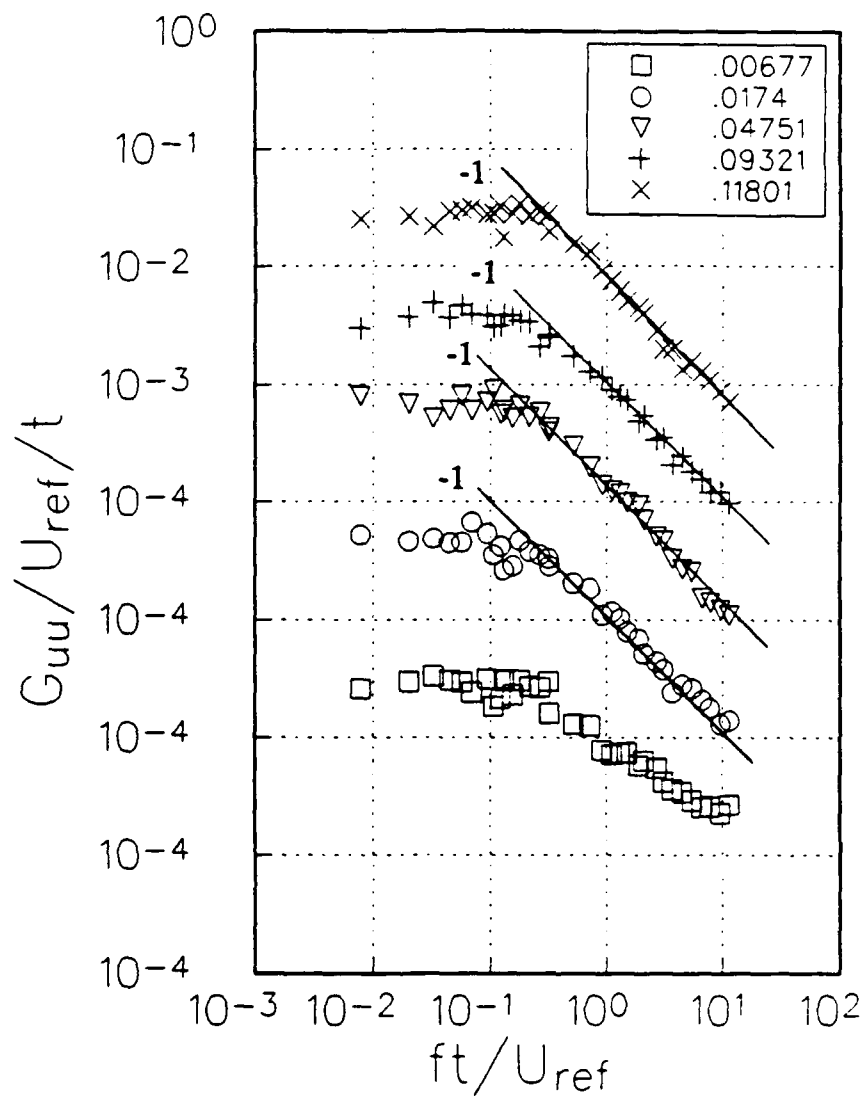
Figure 27: Normalized u power spectral distribution at x/t=-.391. Note offset ordinate and legend of y/t locations.
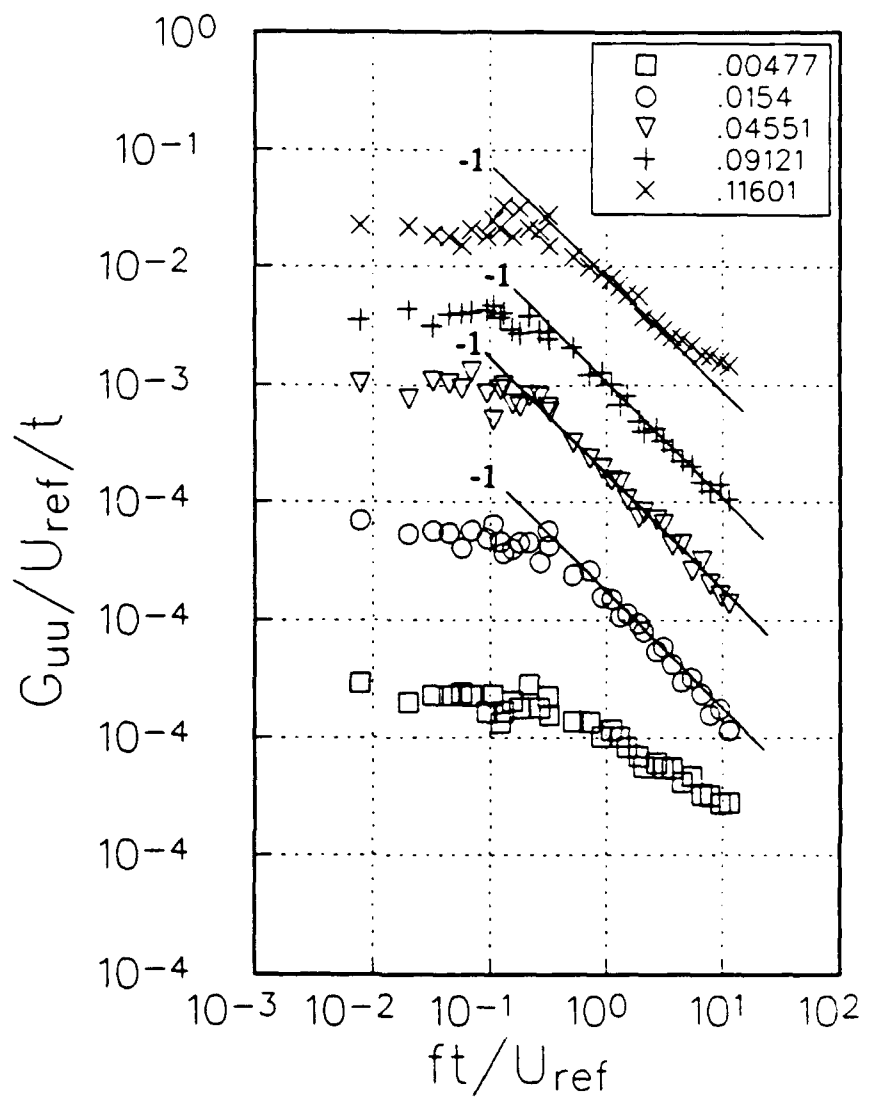
Figure 28: Normalized u power spectral distribution at $x/t = -.342$. Note offset ordinate and legend of y/t locations.
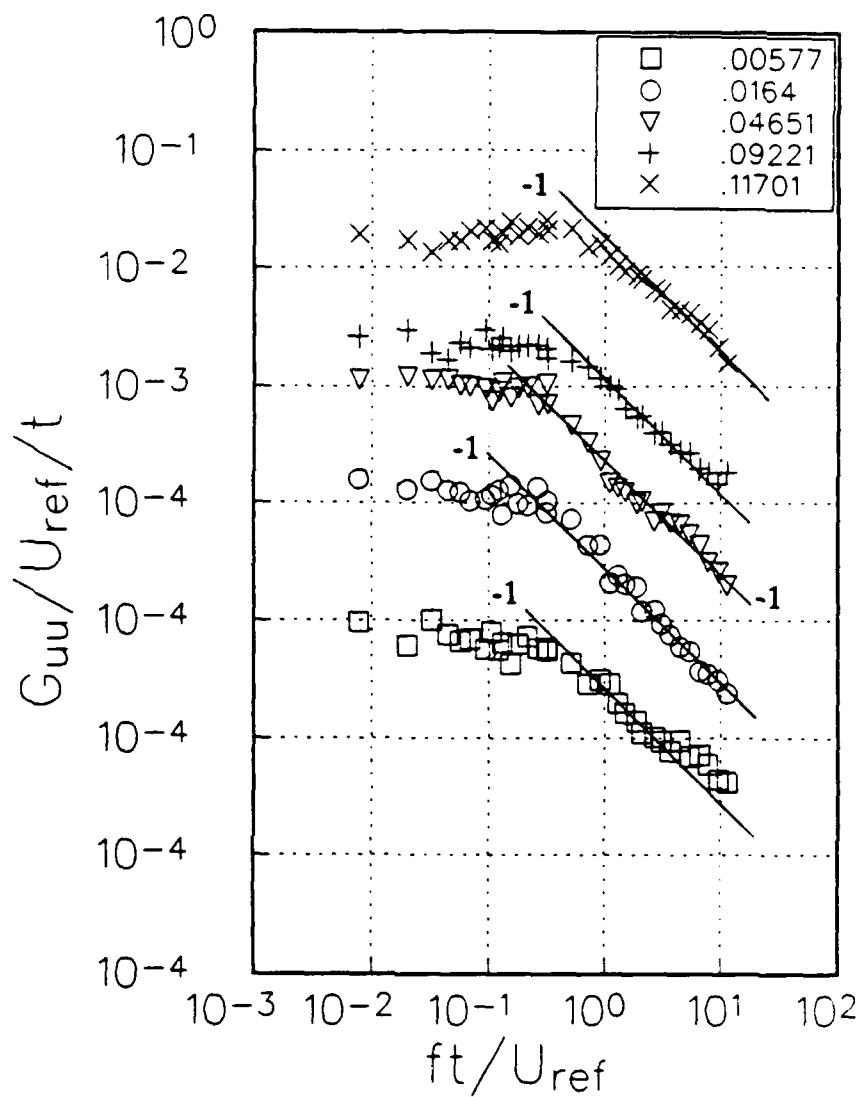
Figure 29: Normalized u power spectral distribution at x/t = -.294. Note offset ordinate and legend of y/t locations.
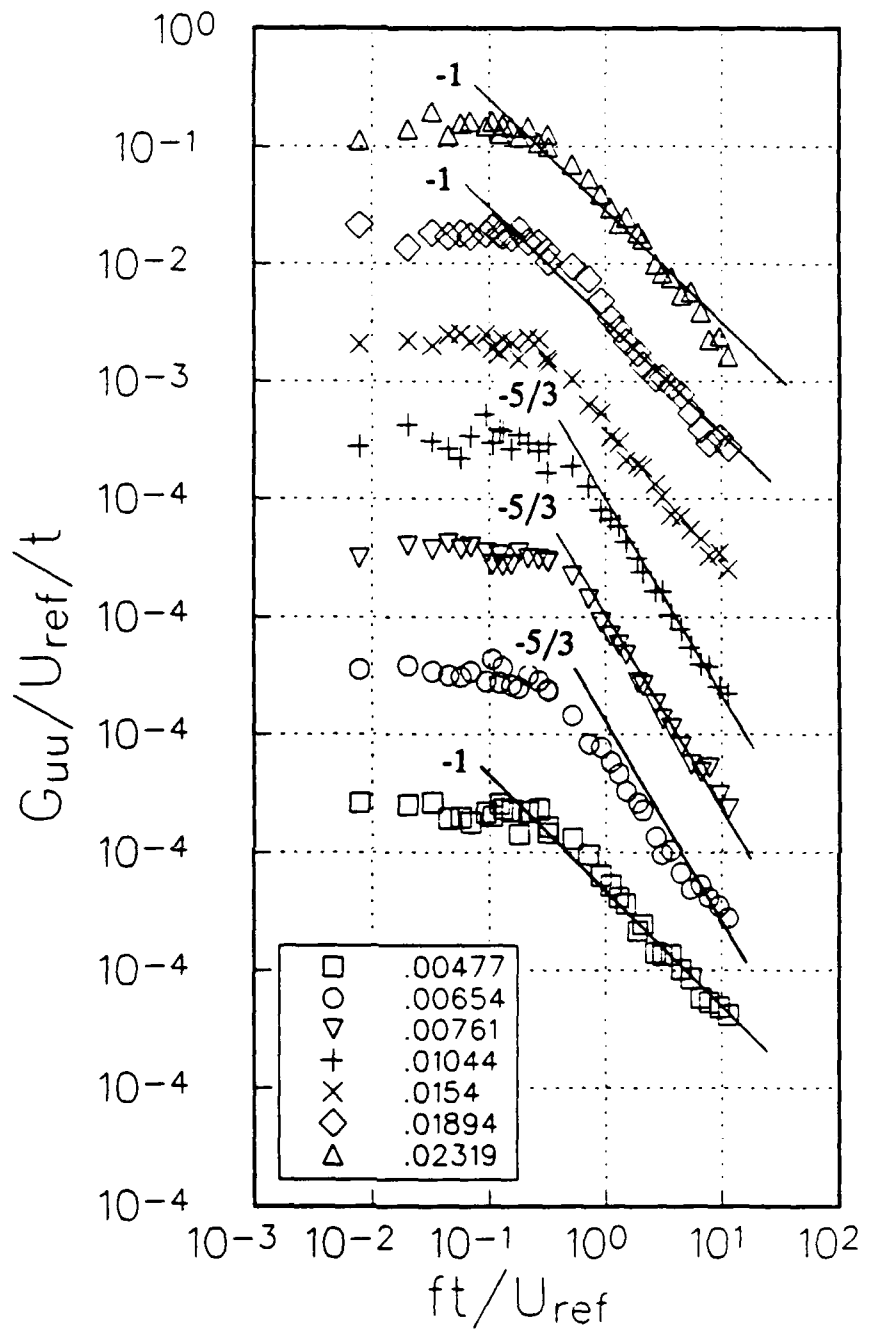
Figure 30a: Normalized u power spectral distribution at $x/t = -.237$. Note offset ordinate and legend of y/t locations.
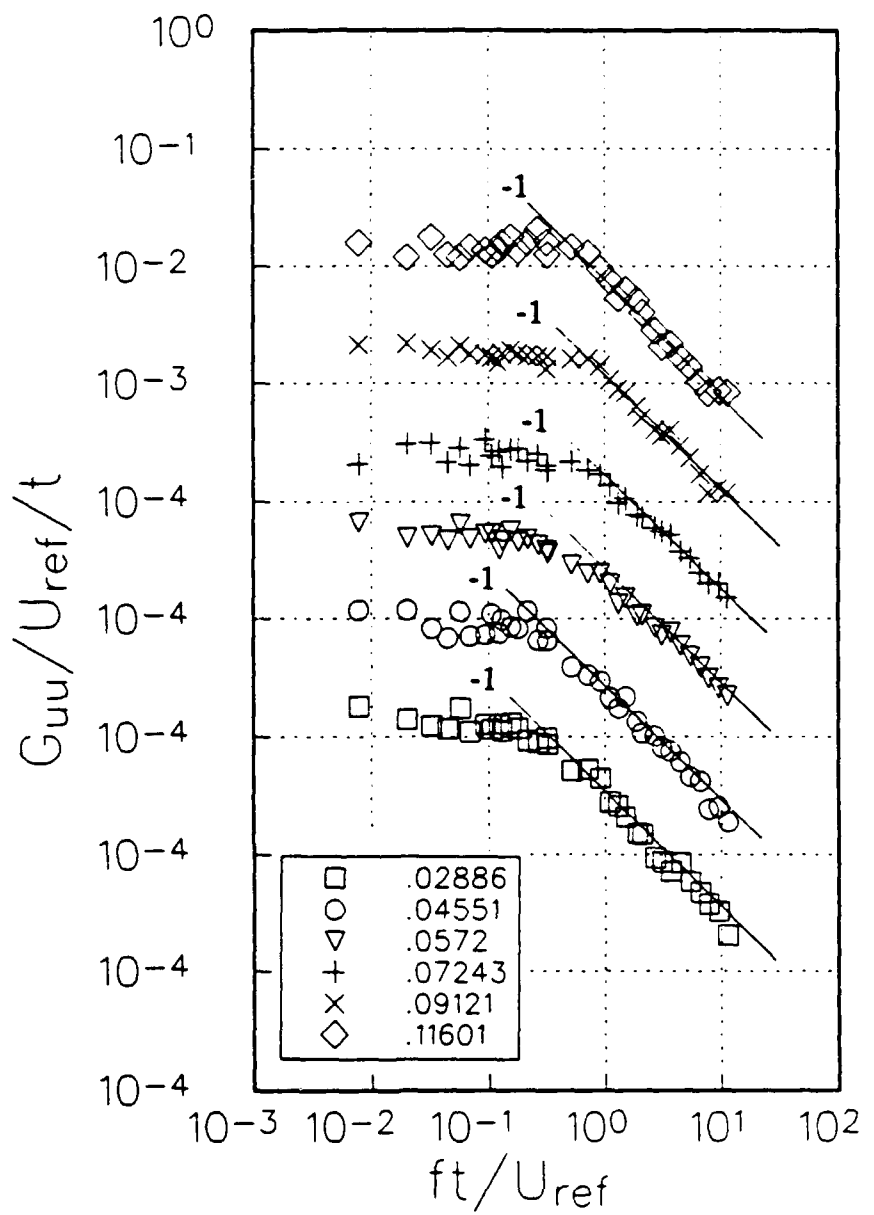
Figure 30b:
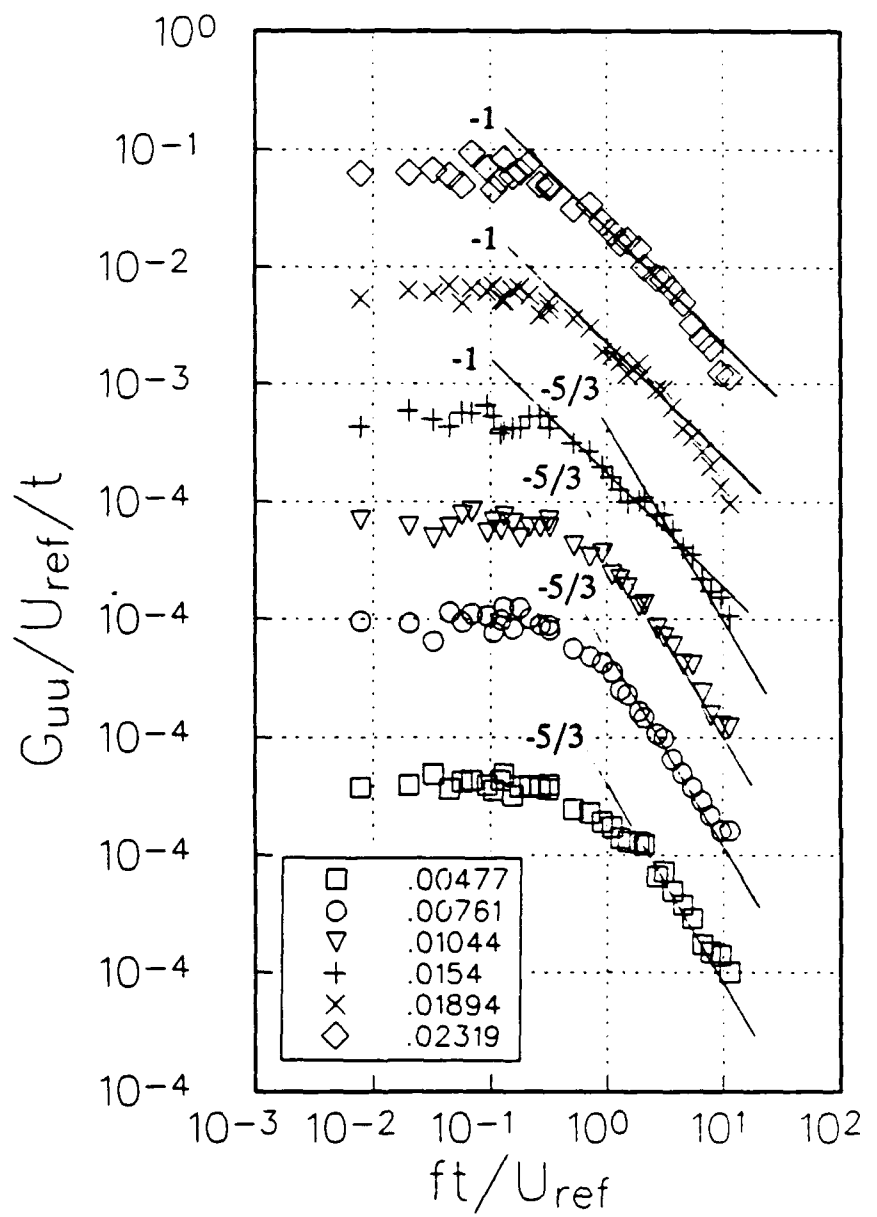
Figure 31a: Normalized u power spectral distribution at x/t = -.193. Note offset
ordinate and legend of y/t locations.
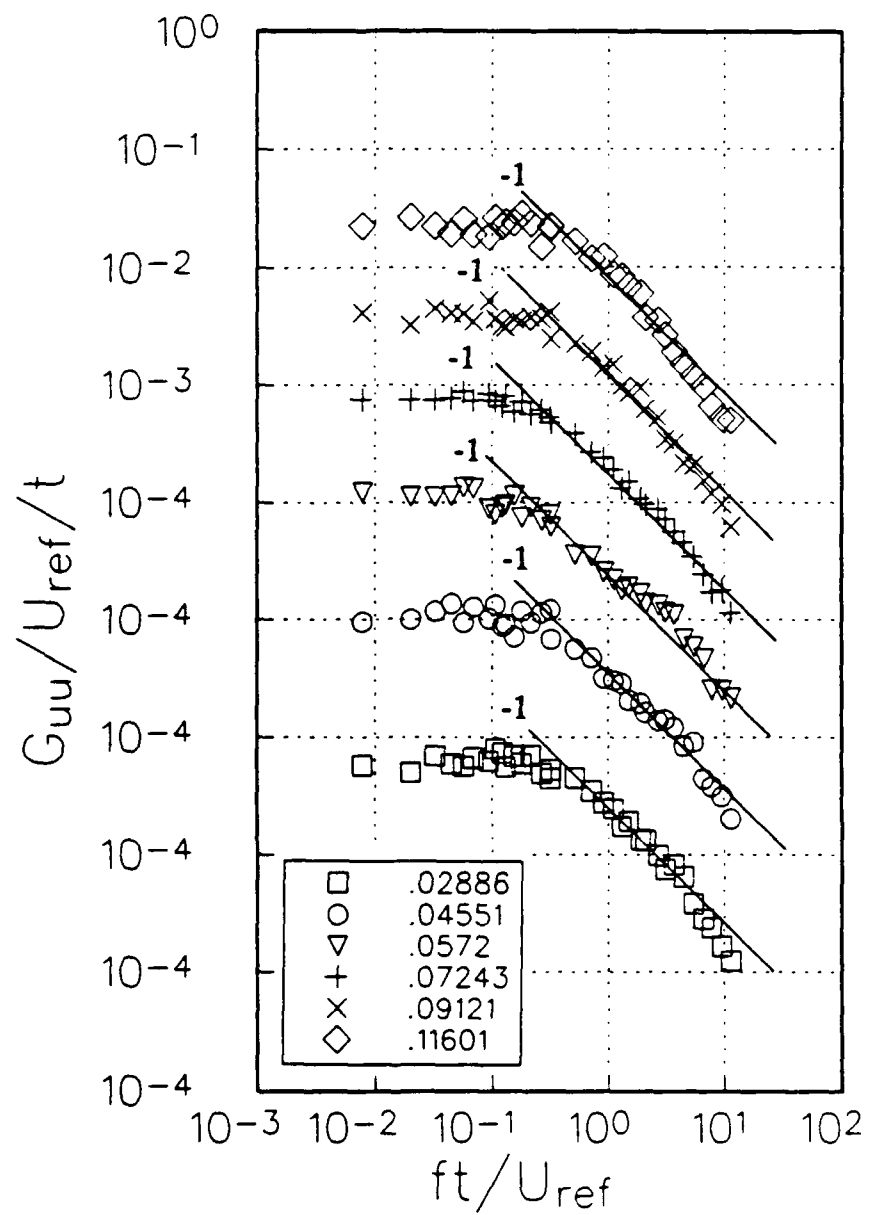
Figure 31b:
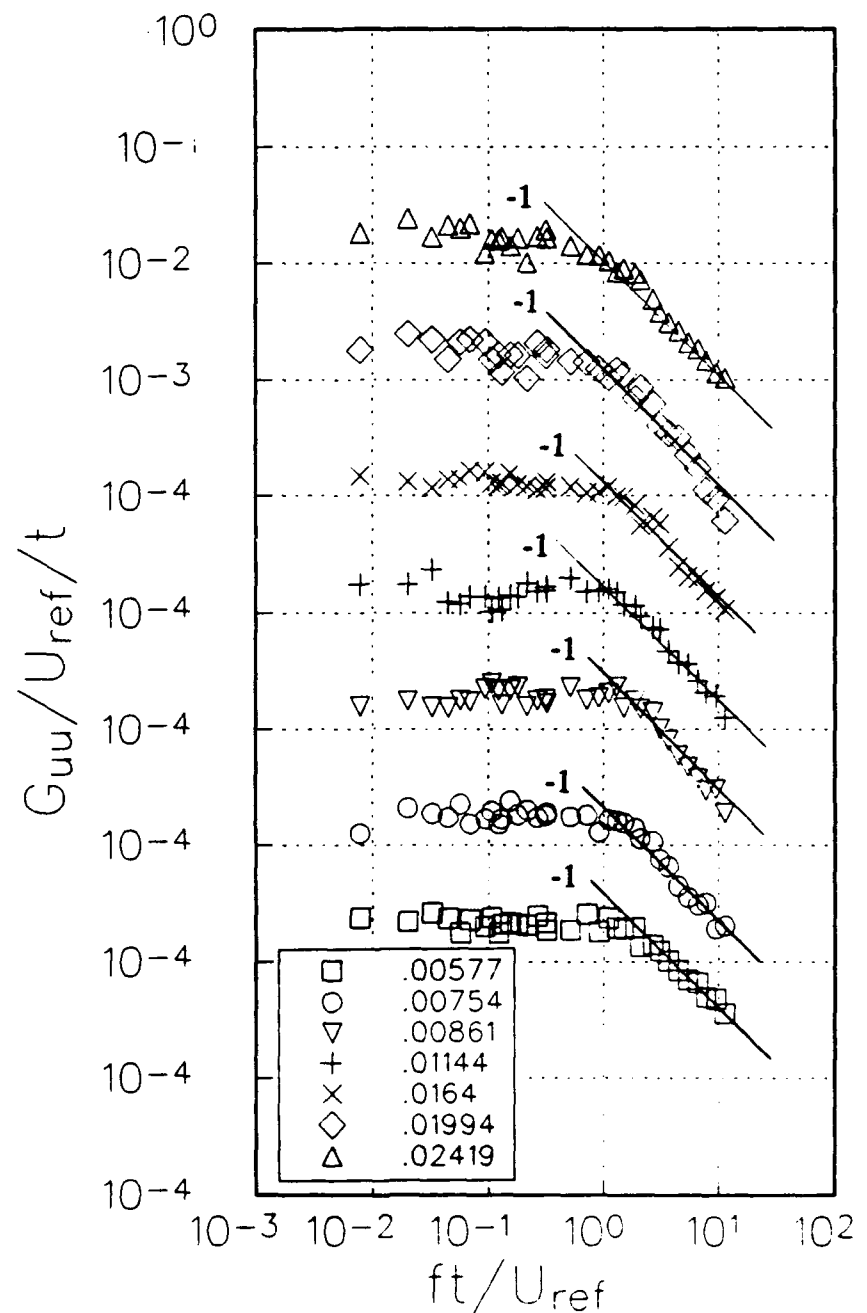
Figure 32a: Normalized u power spectral distribution at x/t = -.139. Note offset ordinate and legend of y/t locations.
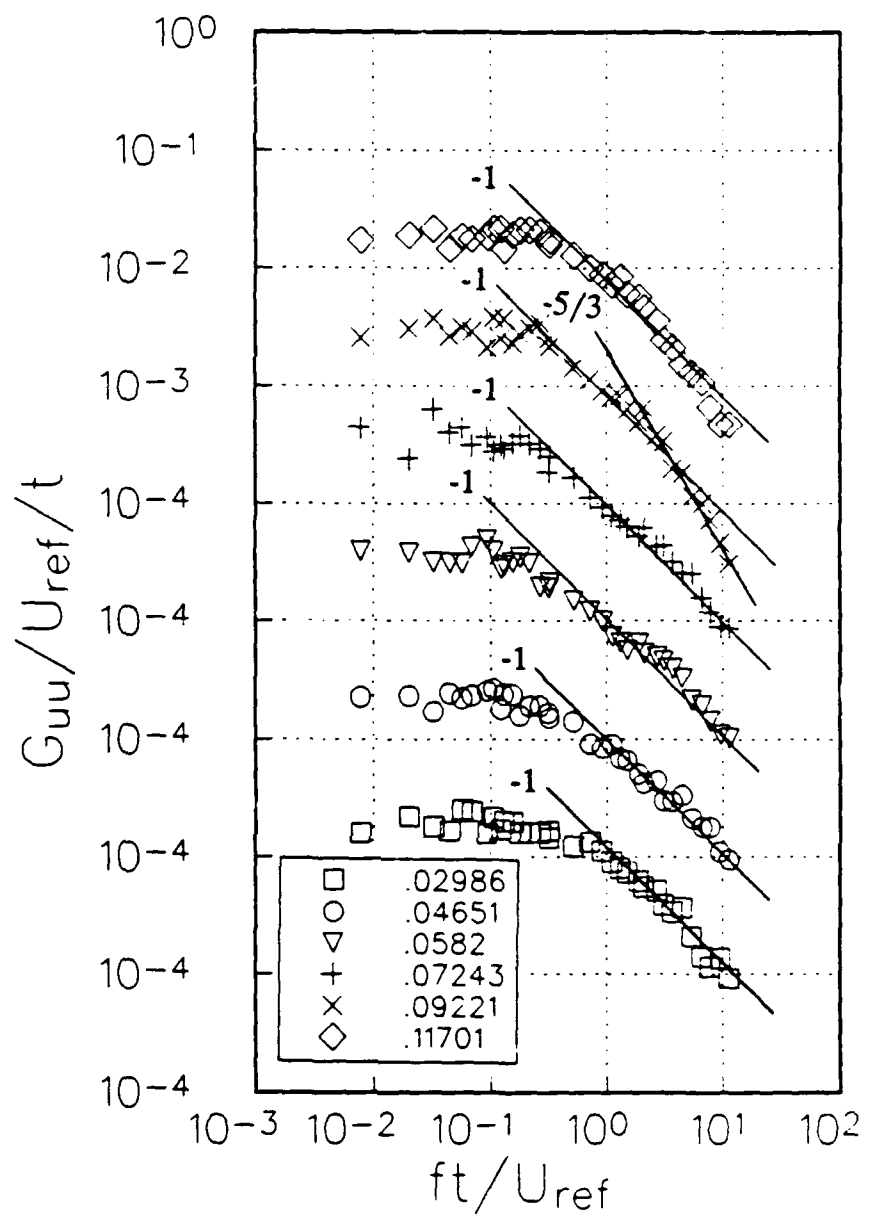
Figure 32b:
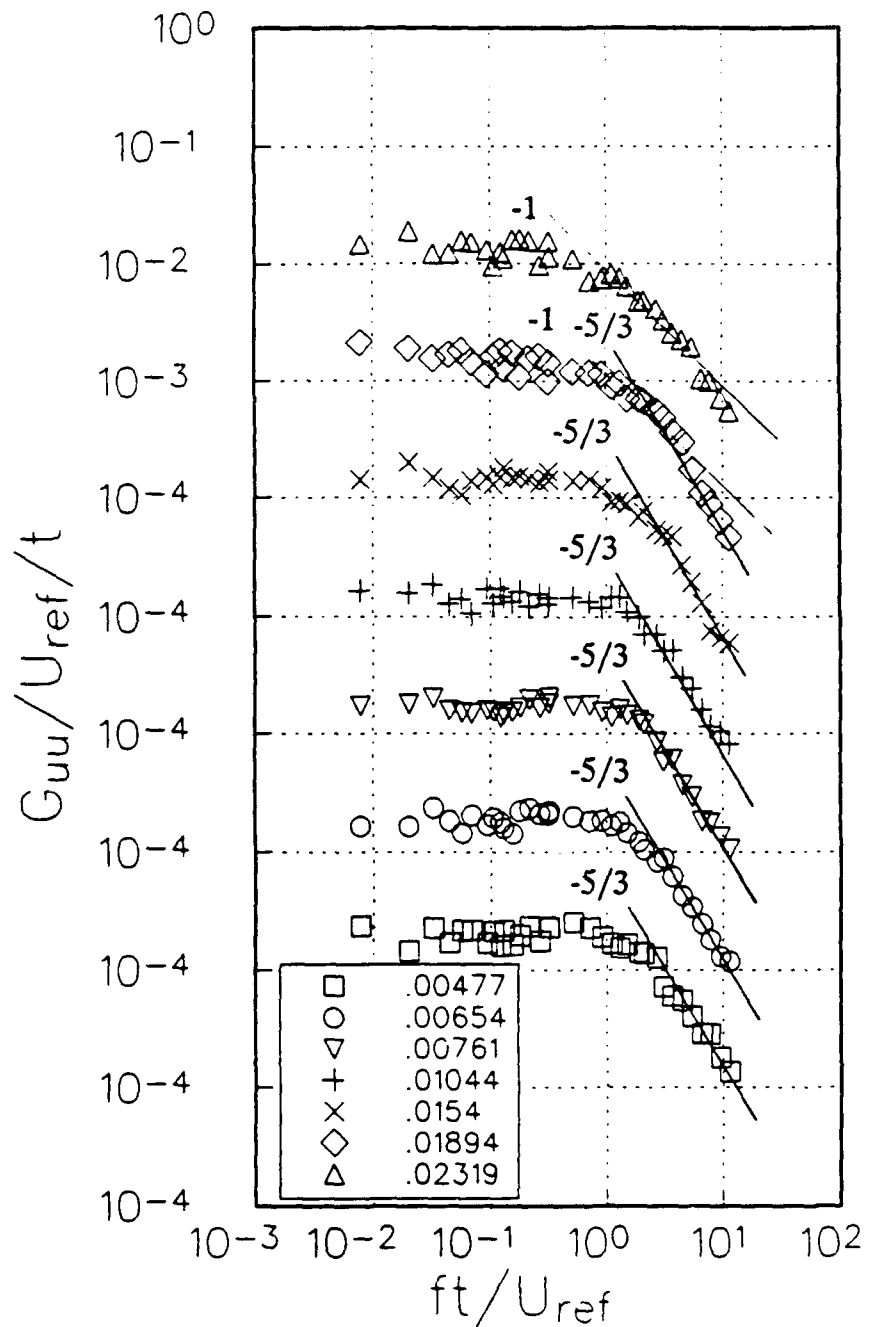
Figure 33a: Normalized u power spectral distribution at x/t = -.0856. Note offset ordinate and legend of y/t locations.
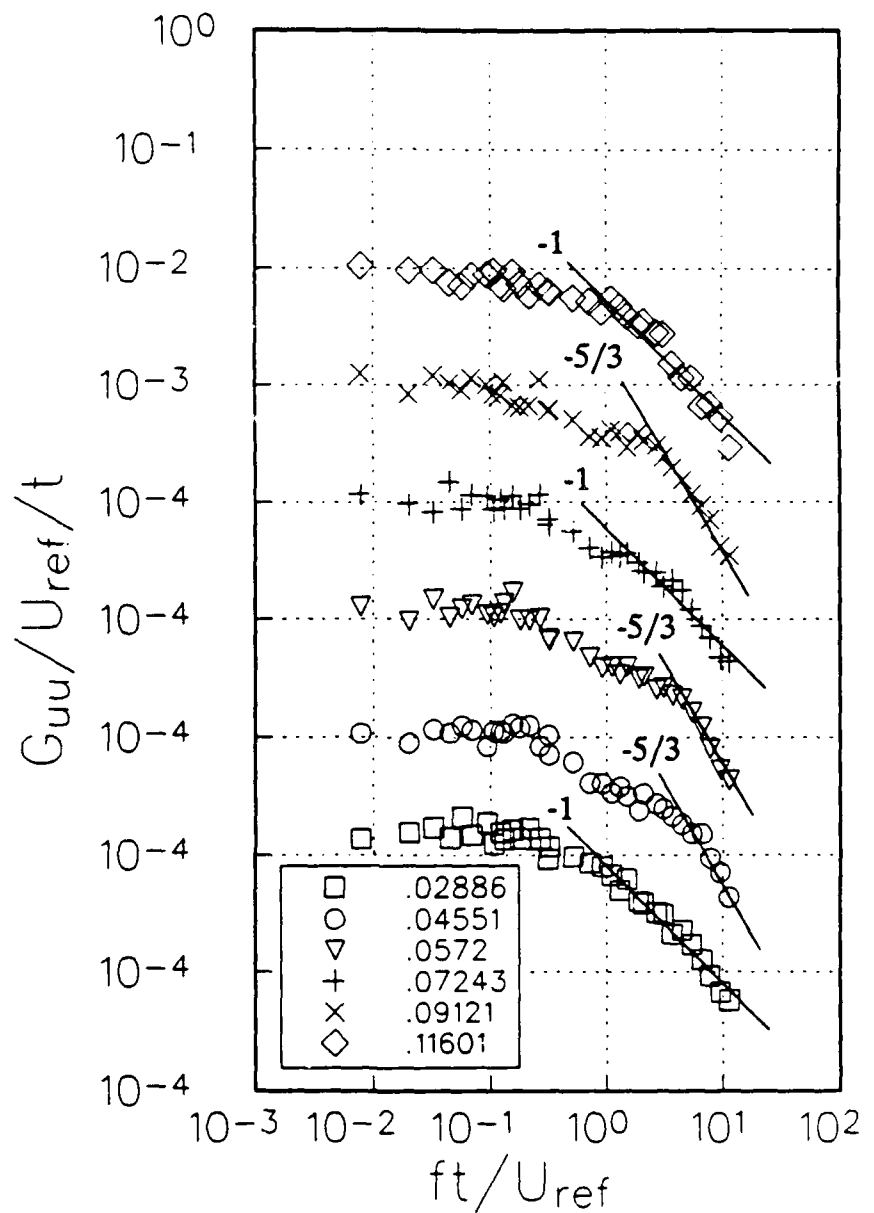
Figure 33b:
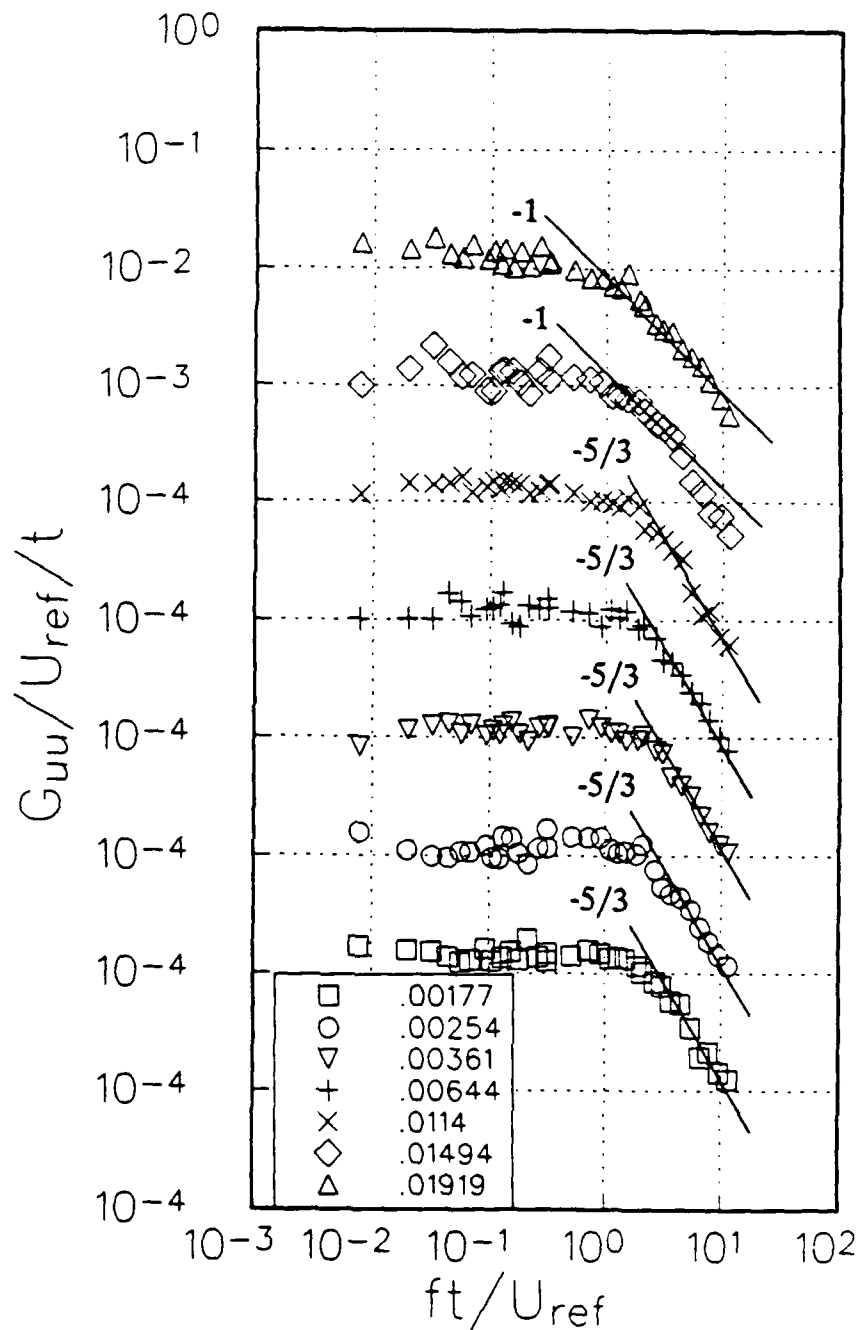
Figure 34a: Normalized u power spectral distribution at x/t = -.0421. Note offset ordinate and legend of y/t locations.
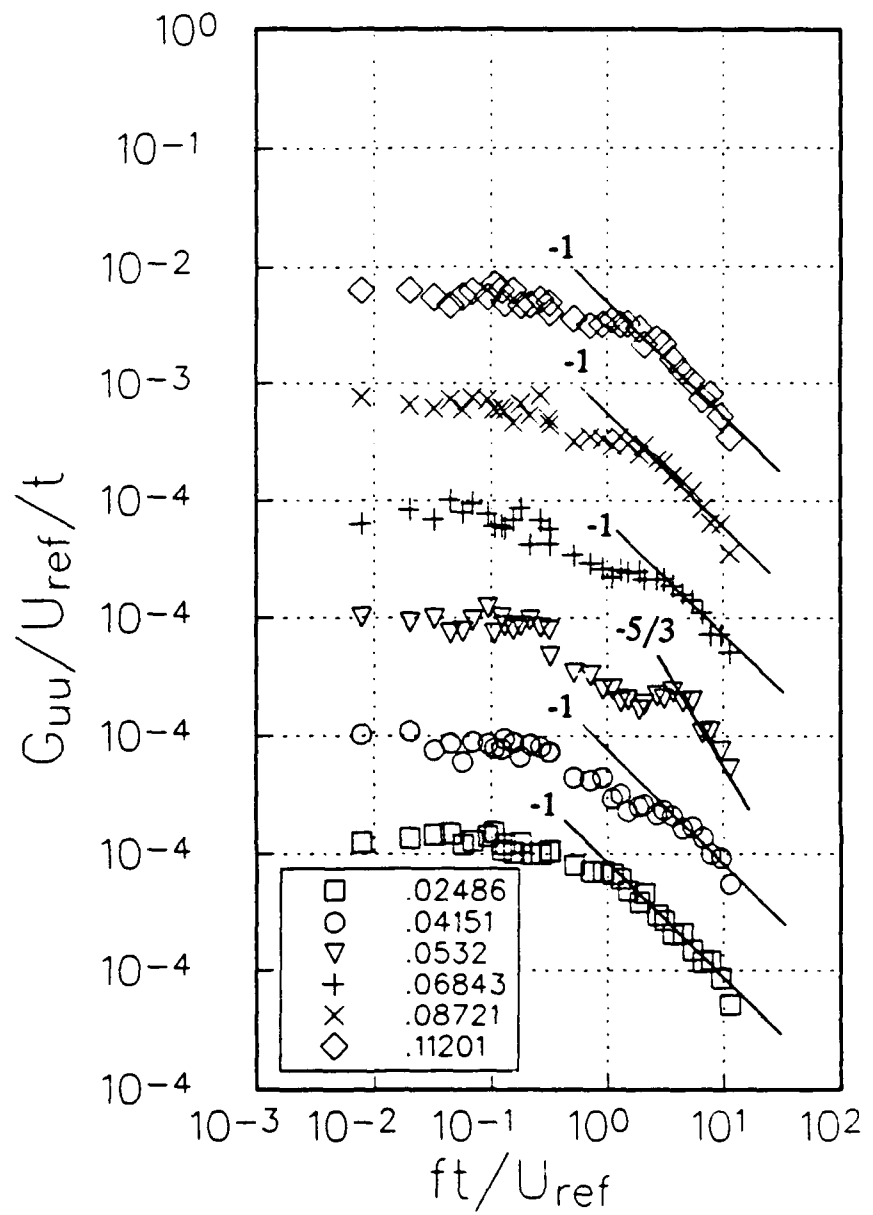
Figure 34b:
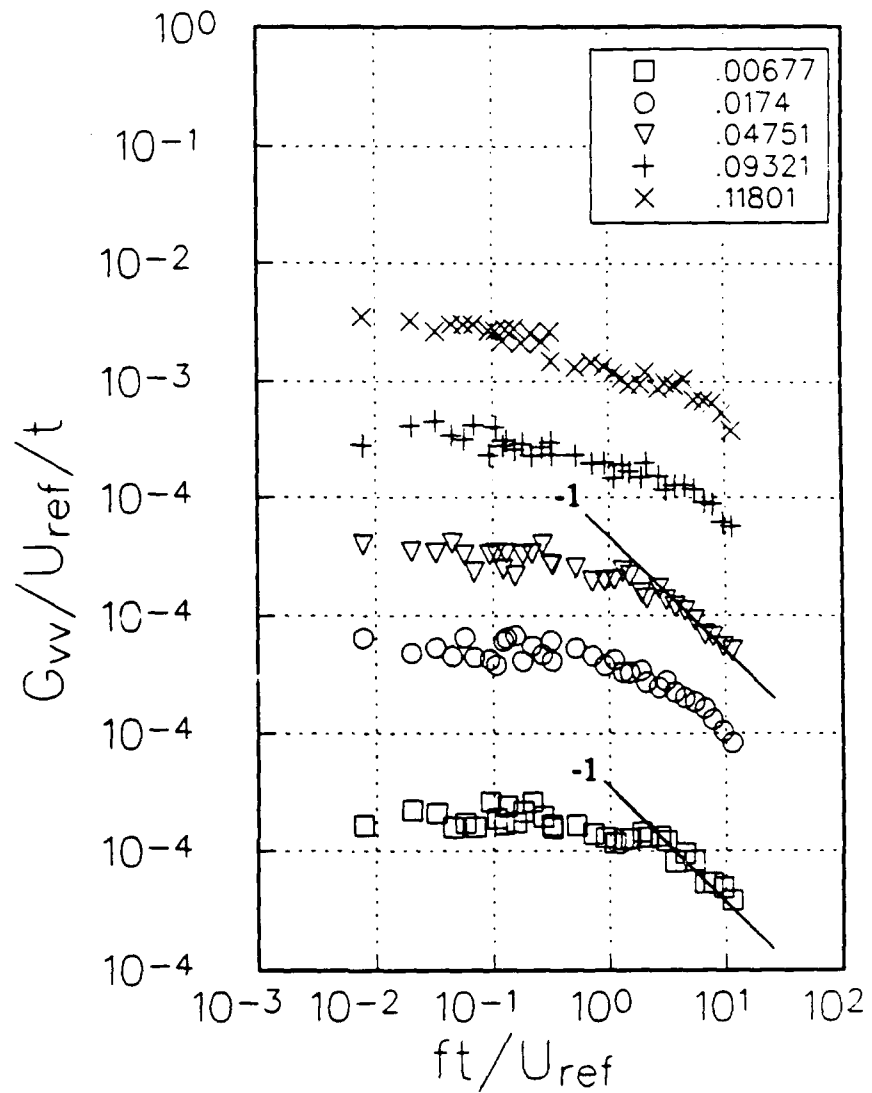
Figure 35: Normalized v power spectral distribution at x/t=-.391. Note offset ordinate and legend of y/t locations.
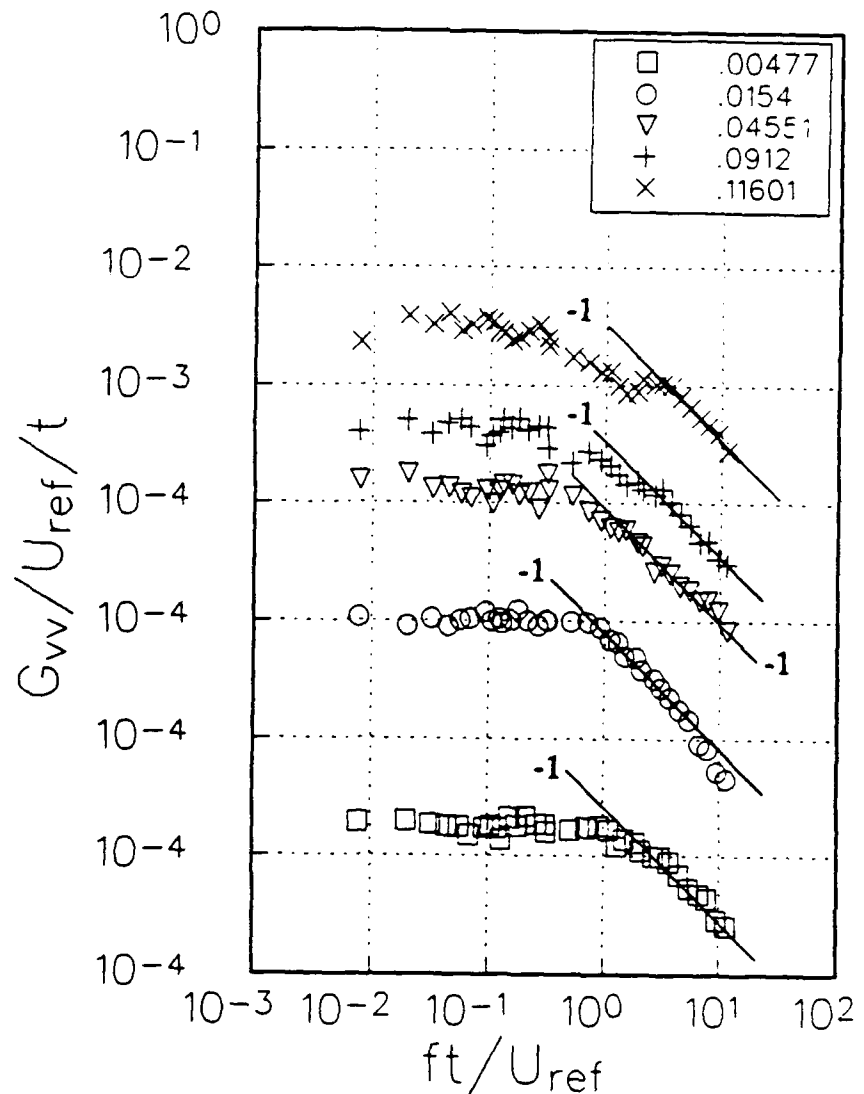
Figure 36: Normalized v power spectral distribution at x/t = -.342. Note offset ordinate and legend of y/t locations.
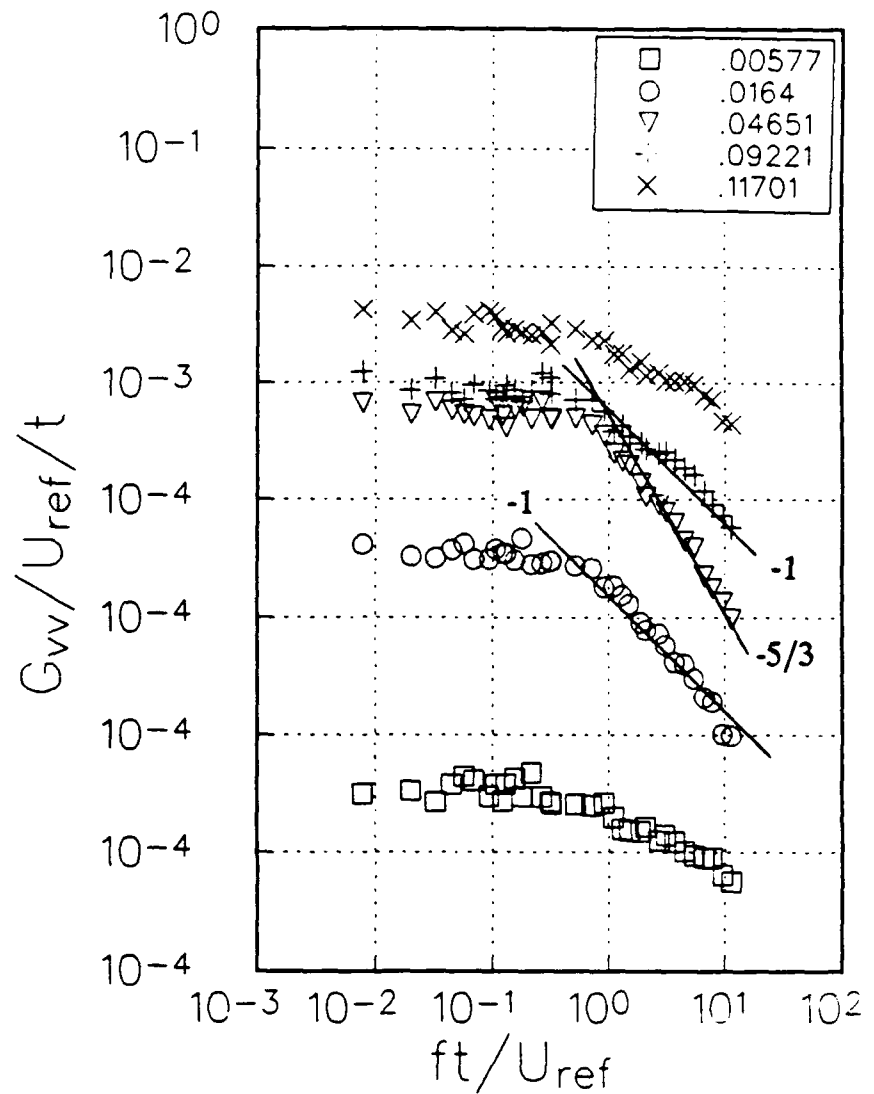
Figure 37: Normalized v power spectral distribution at $x/t = -.294$. Note offset y ordinate and legend of y/t locations.
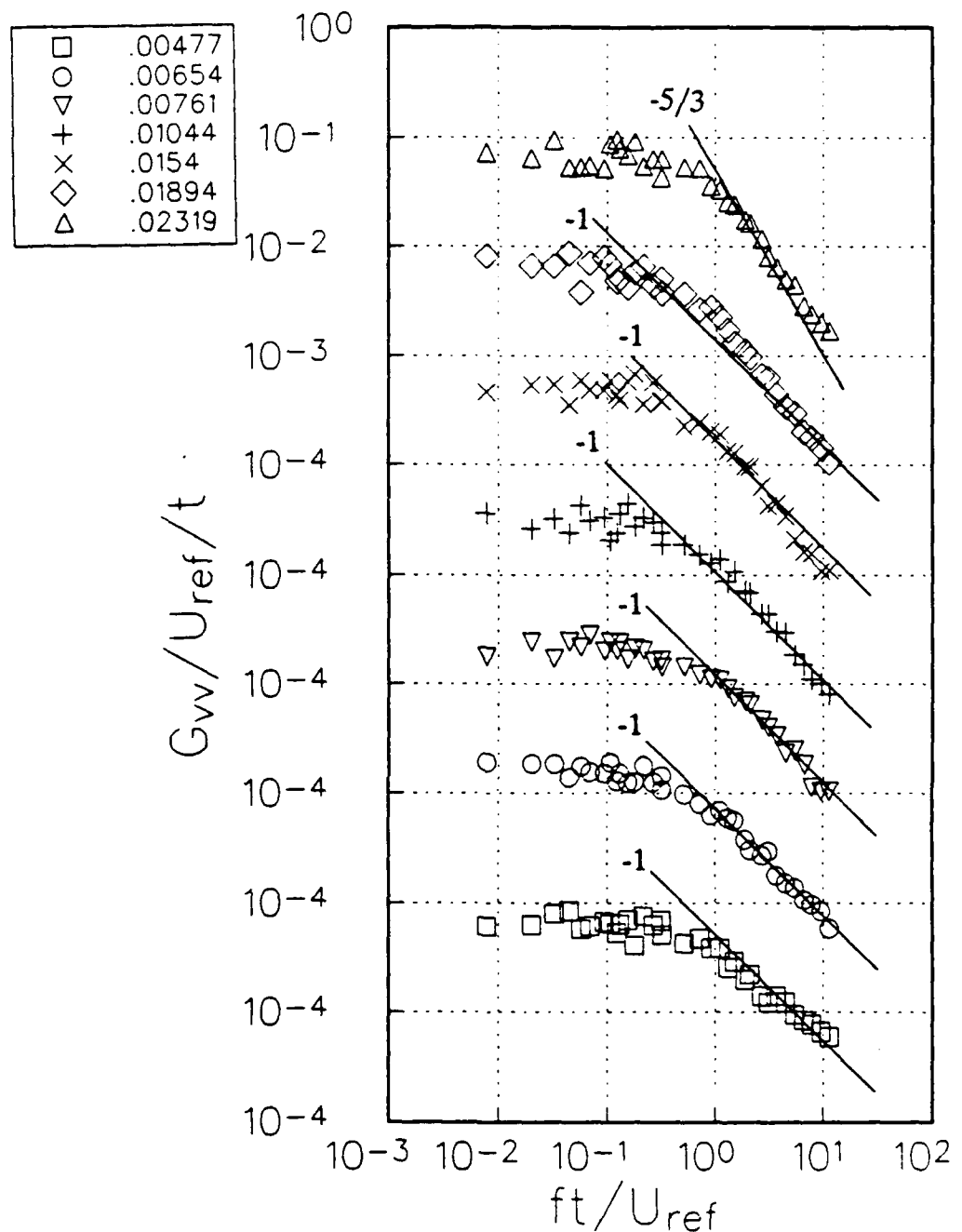
Figure 38a: Normalized v power spectral distribution at x/t = -.237. Note offset ordinate and legend of y/t locations.
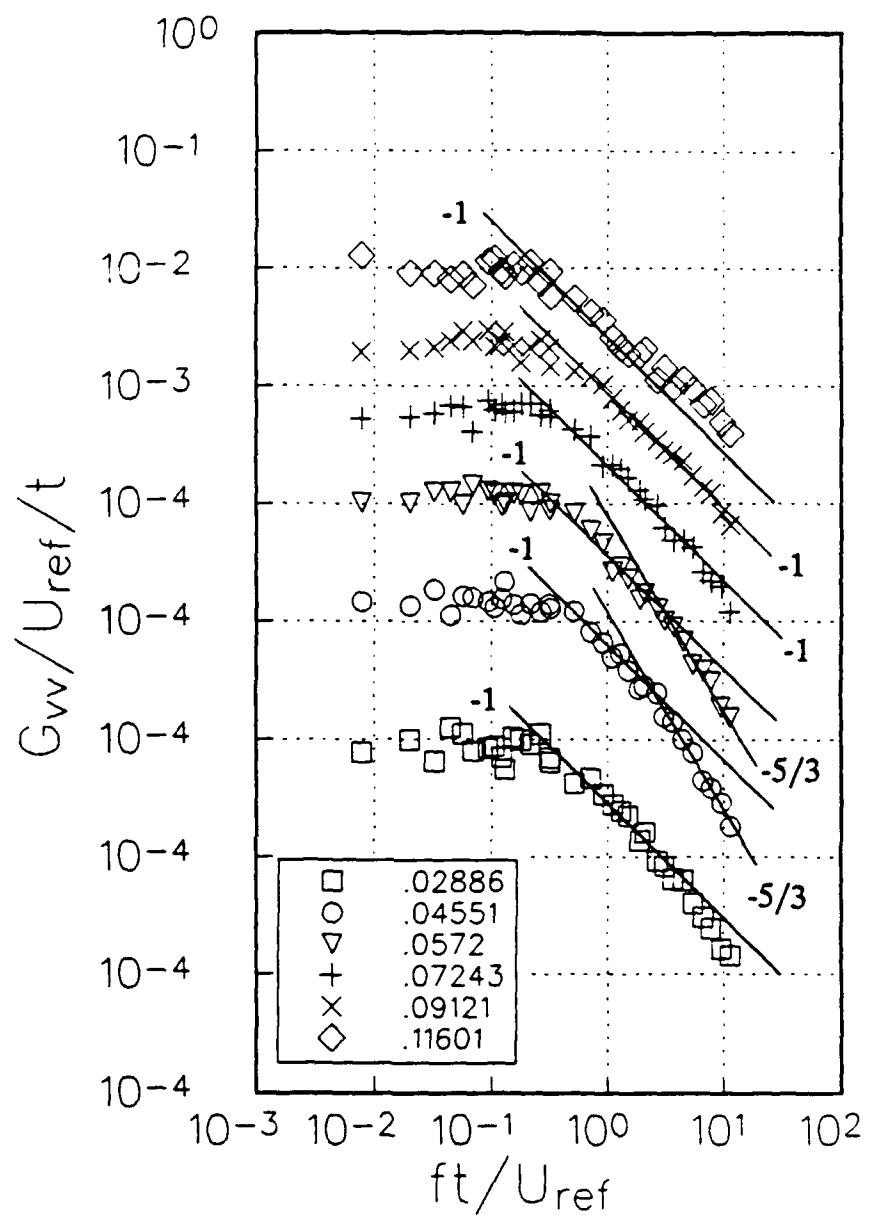
Figure 38b:
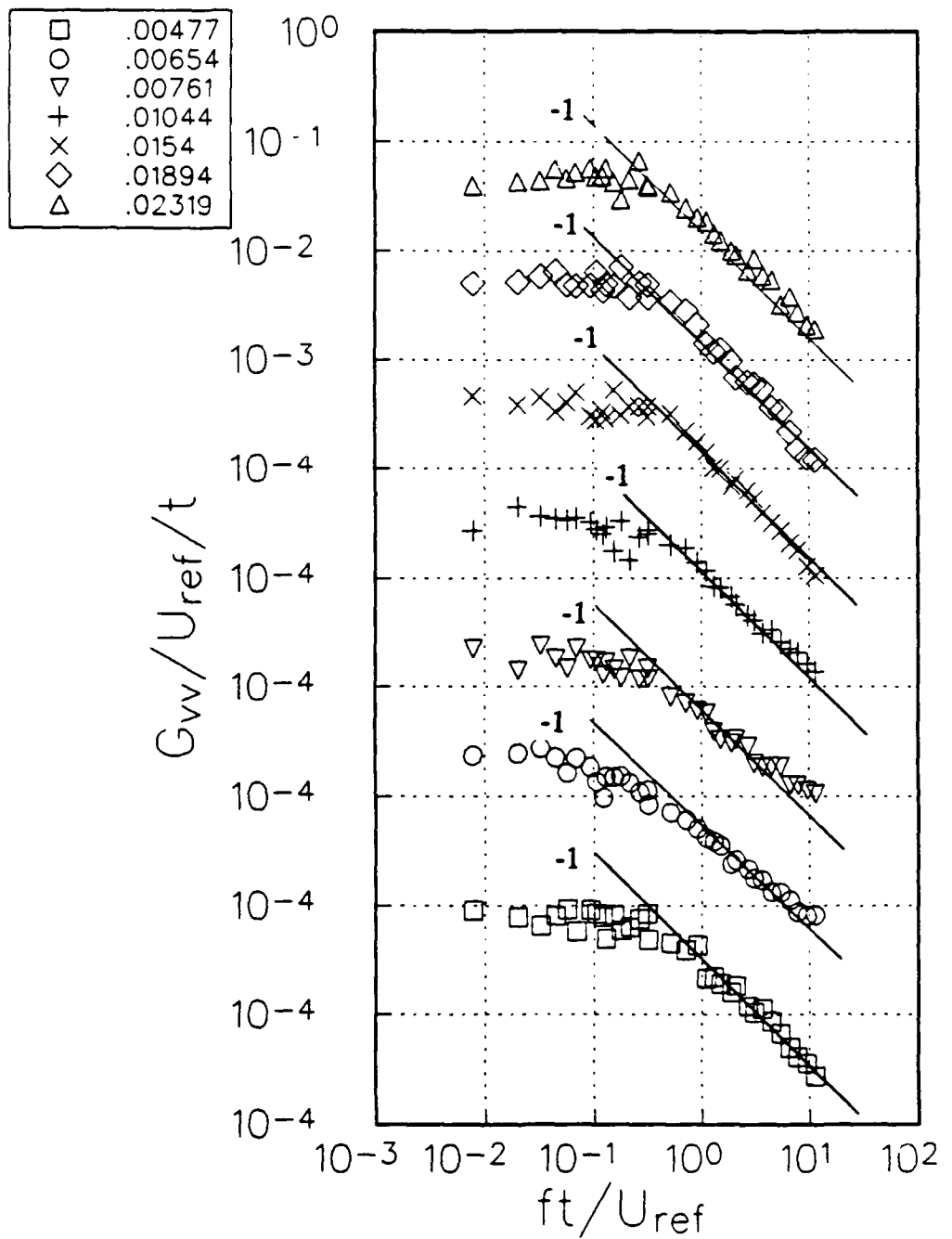
Figure 39a: Normalized v power spectral distribution at x/t = -.193. Note offset ordinate and legend of y/t locations.
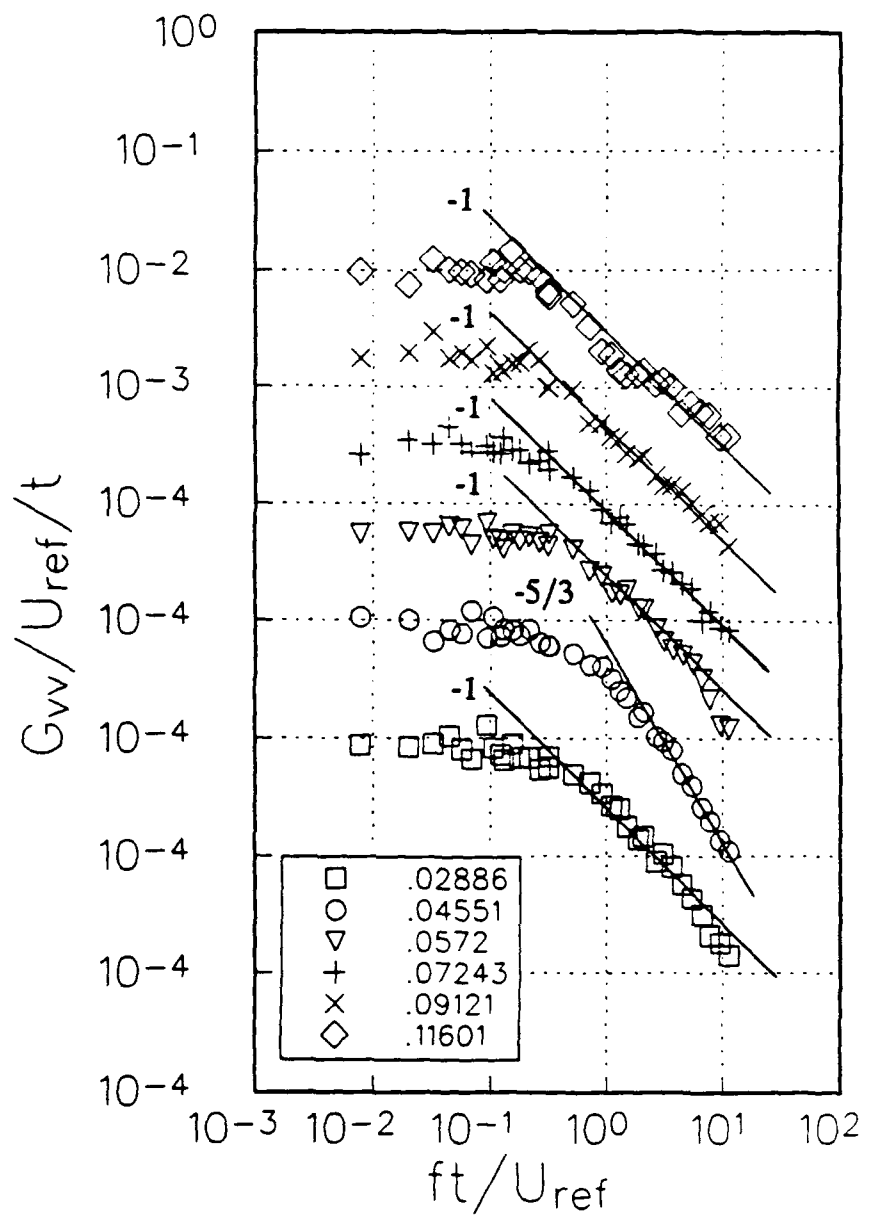
Figure 39b:
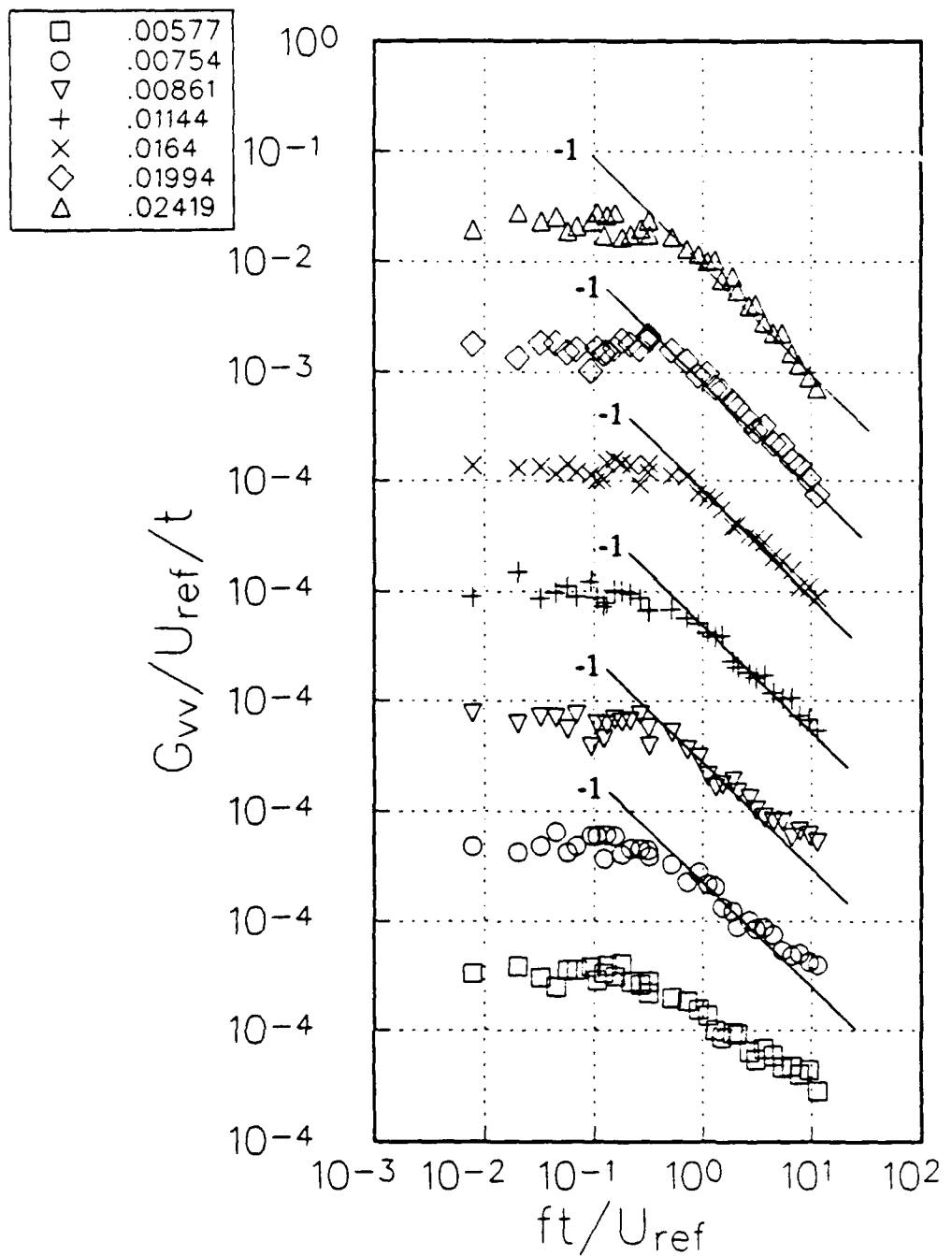
Figure 40a: Normalized v power spectral distribution at x/t = -.139. Note offset ordinate and legend of y/t locations.
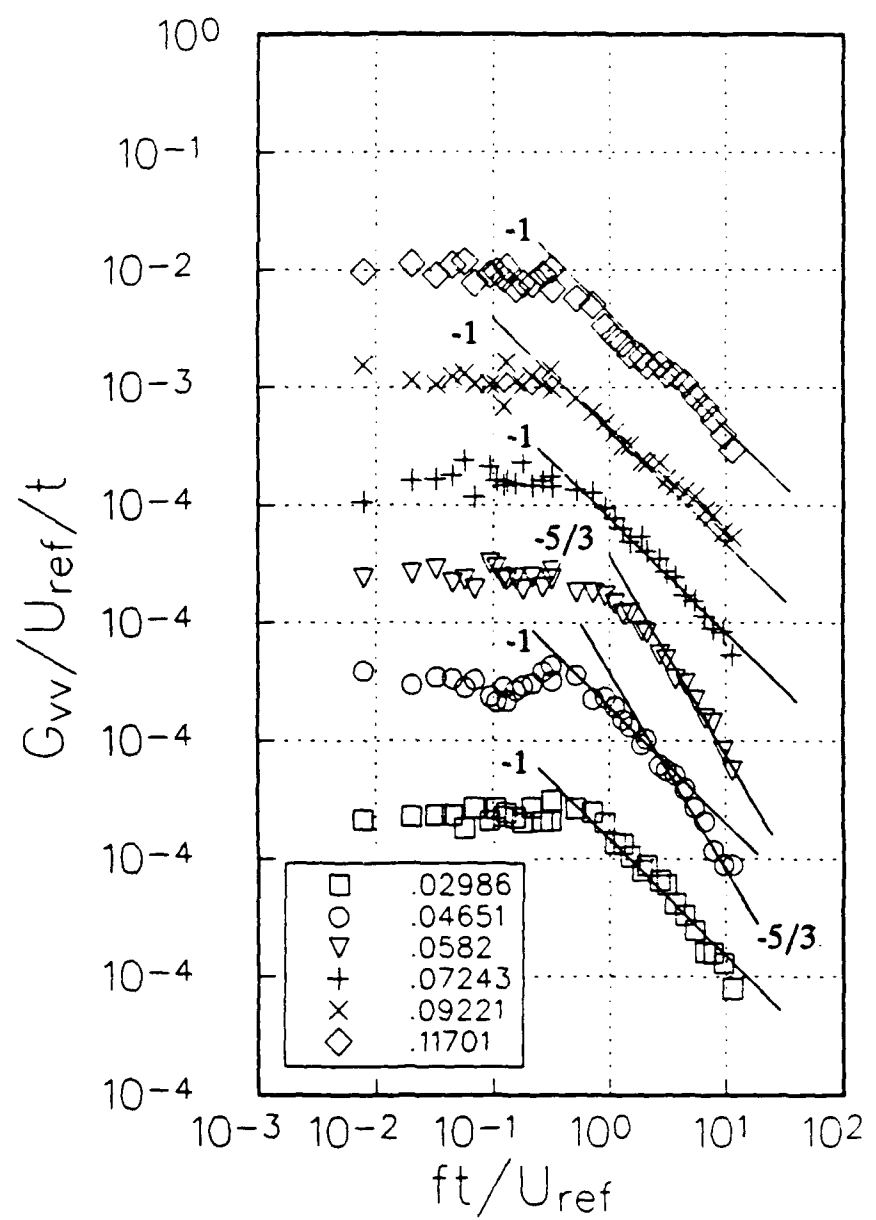
Figure 40b:
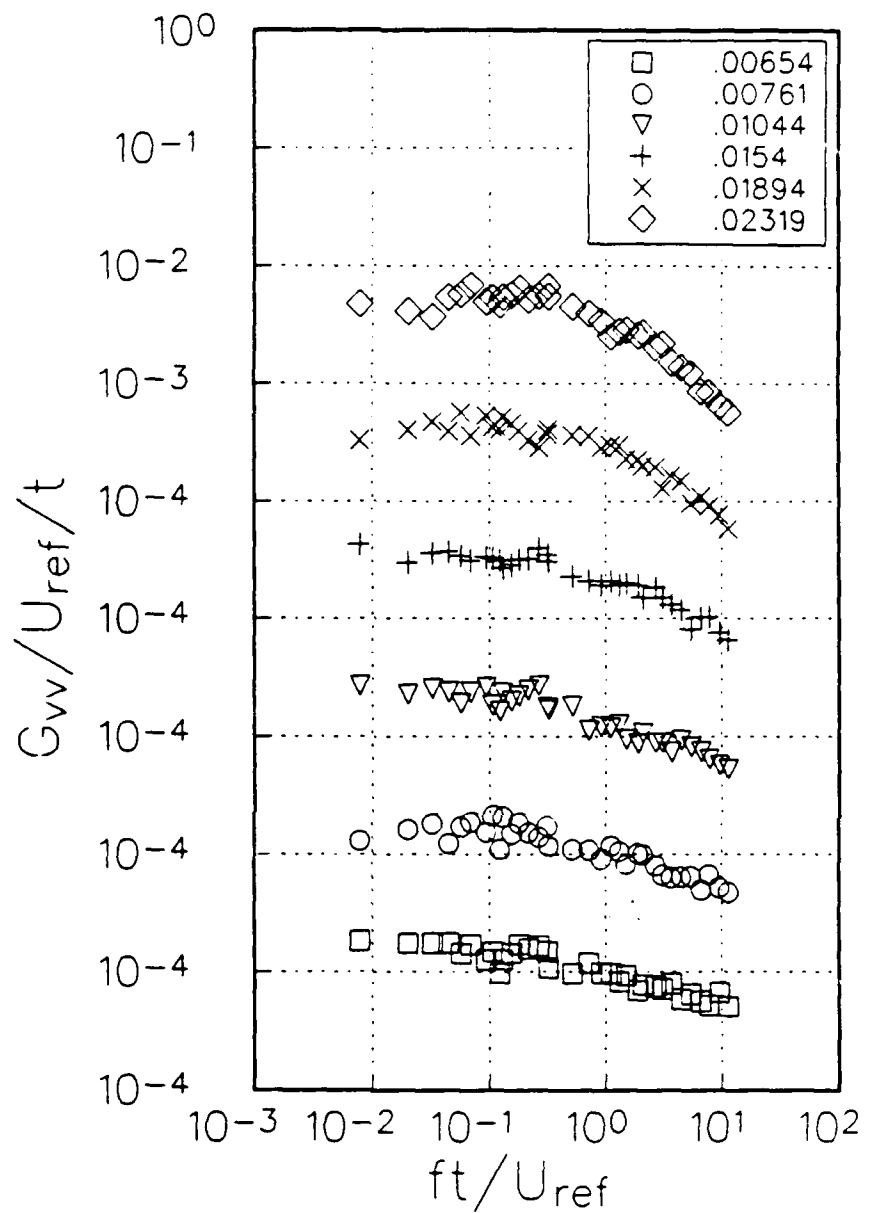
Figure 41a: Normalized v power spectral distribution at x/t = -.0856. Note offset ordinate and legend of y/t locations.
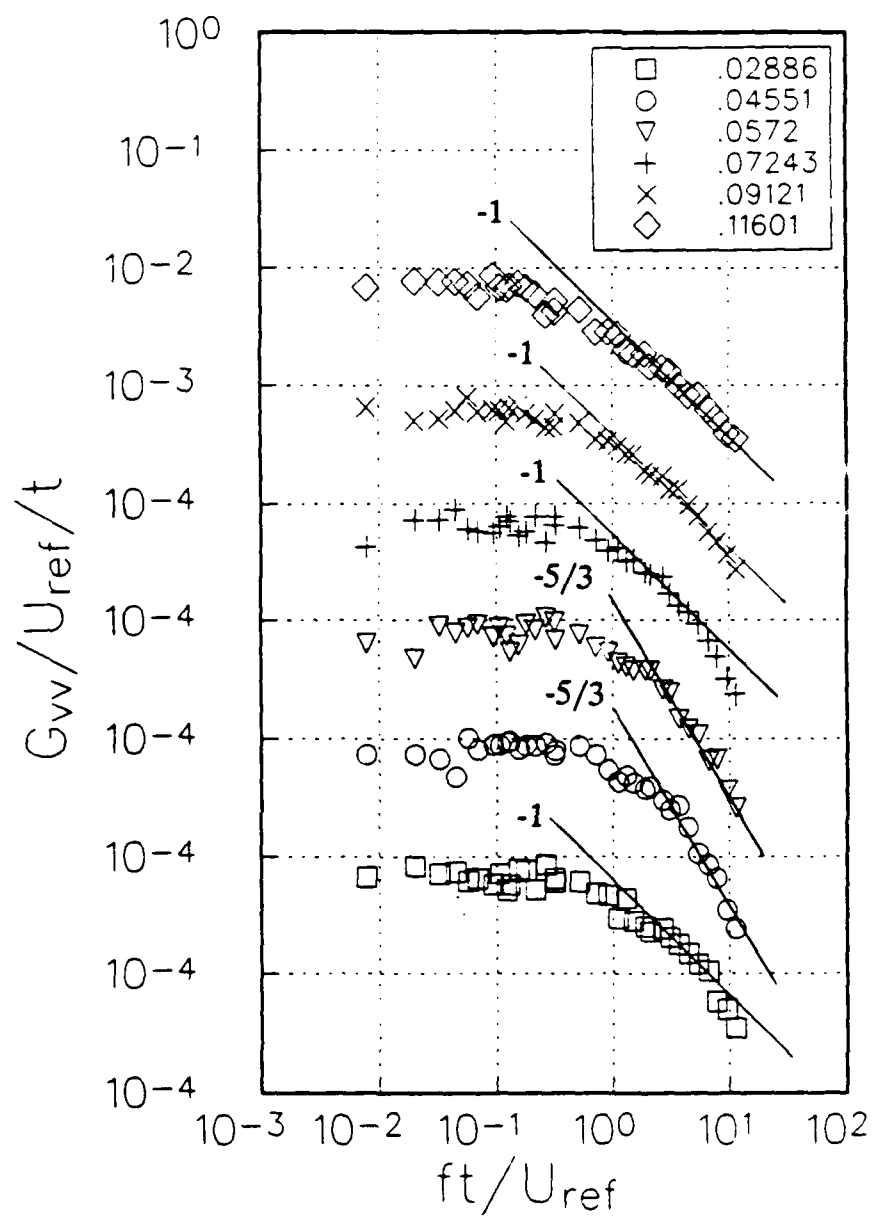
Figure 41b:
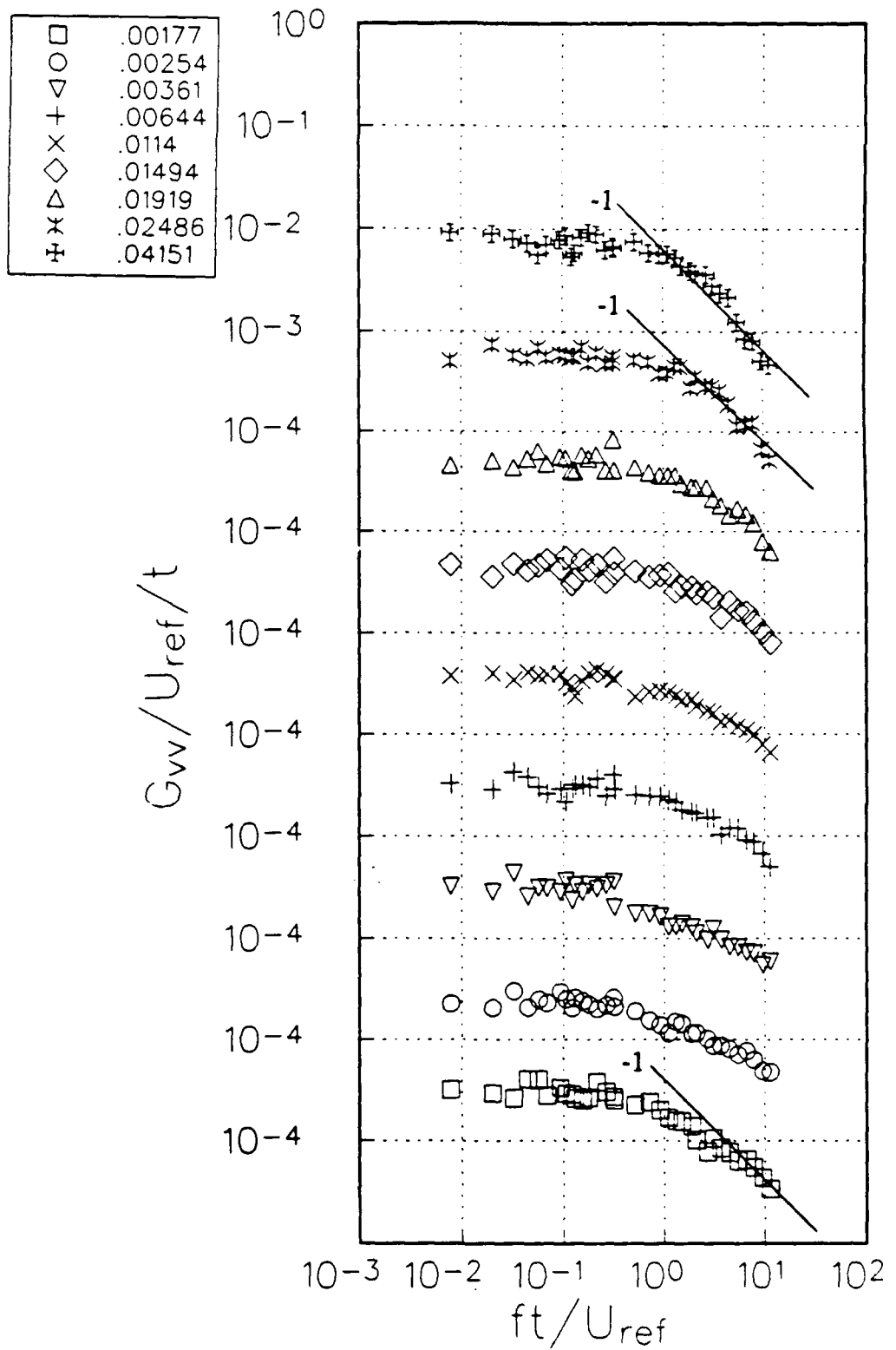
Figure 42: Normalized v power spectral distribution at $x/t = -.0421$. Note offset ordinate and legend of y/t locations.
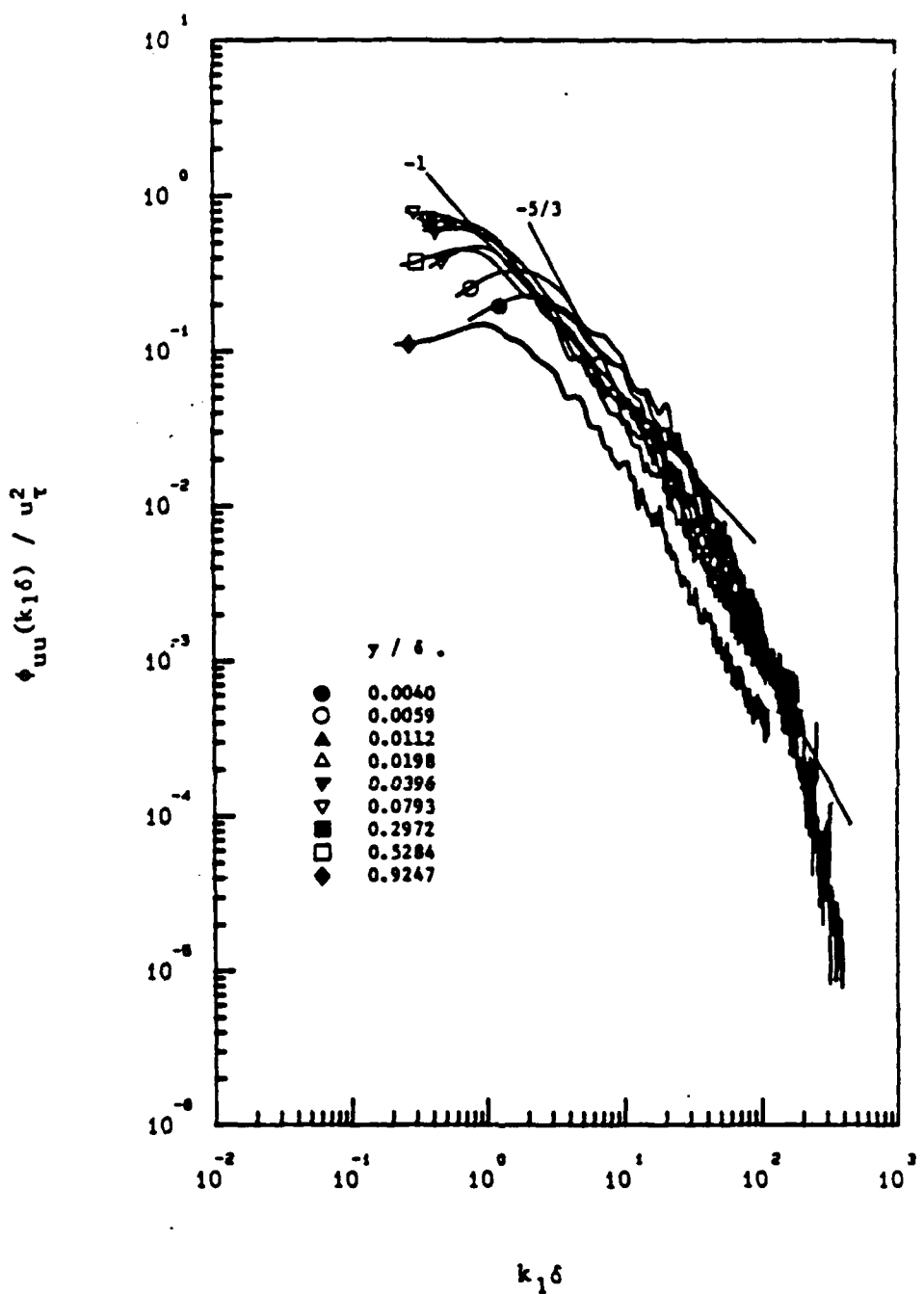
Figure 43: Normalized power spectral distribution of u^2 at $Re_\theta = 6428$, zero pressure gradient flow from Ahn (1986).
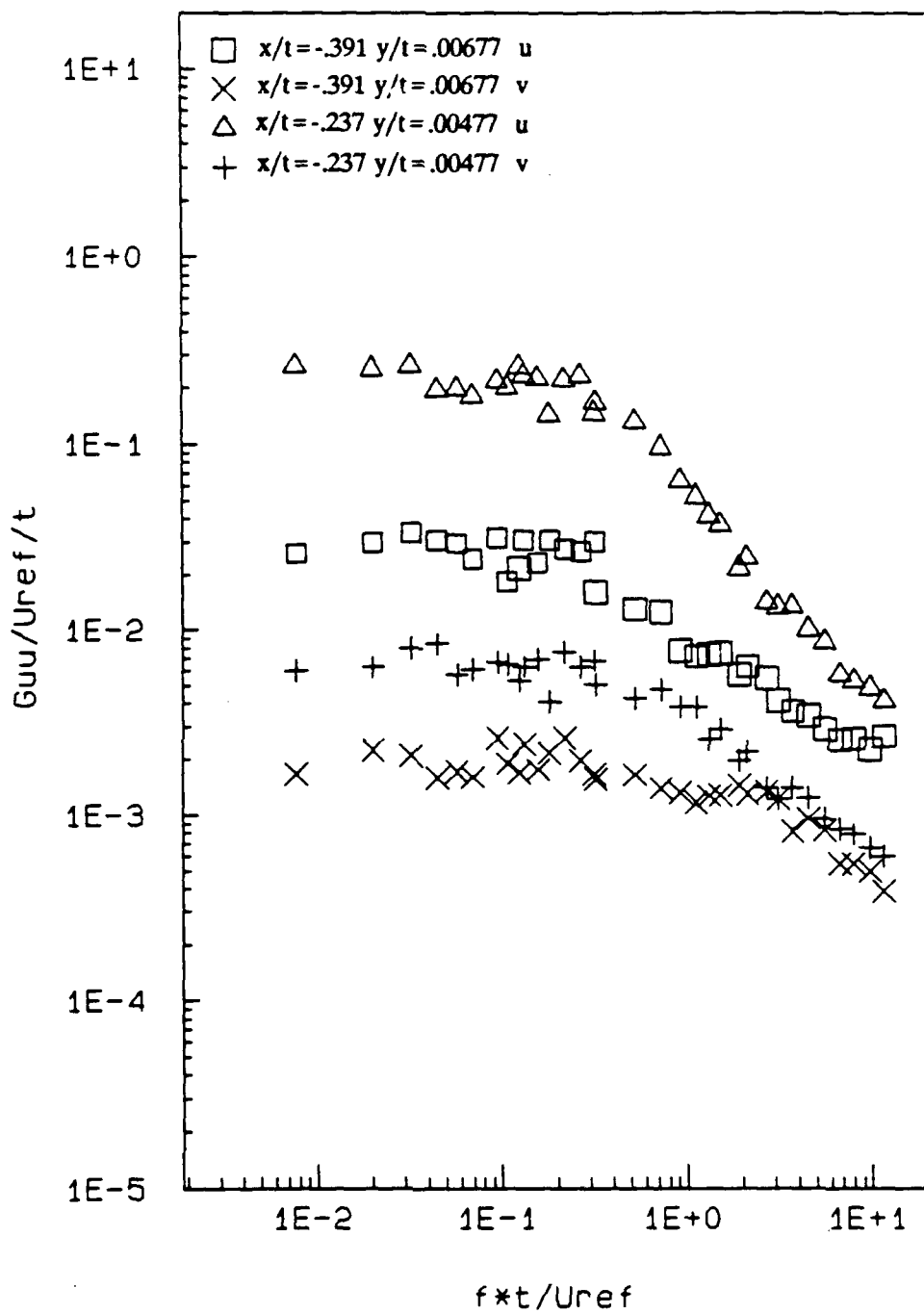
Figure 44:   Comparison of the normalized power spectral density of u and v
              components from the onset boundary layer, x/t=-.391 and
              y/t=.00677, and the bimodal zone, x/t=-.237 and y/t=.00477.
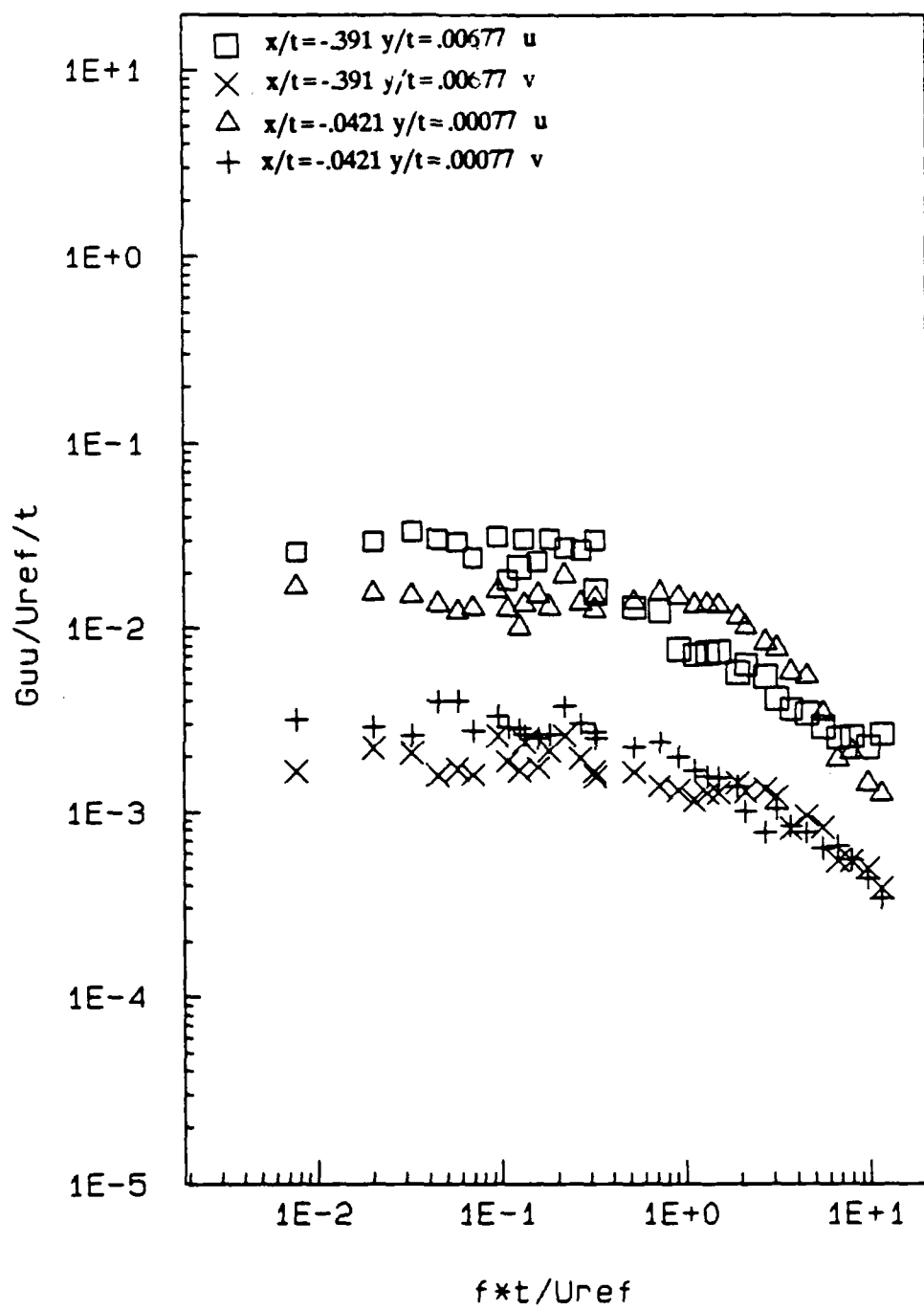
Figure 45: Comparisons of the normalized power spectral density of u and v components from the onset boundary layer, x/t=-.391 and y/t=.00677, and the juncture, x/t=-.0421 and y/t=.00077.
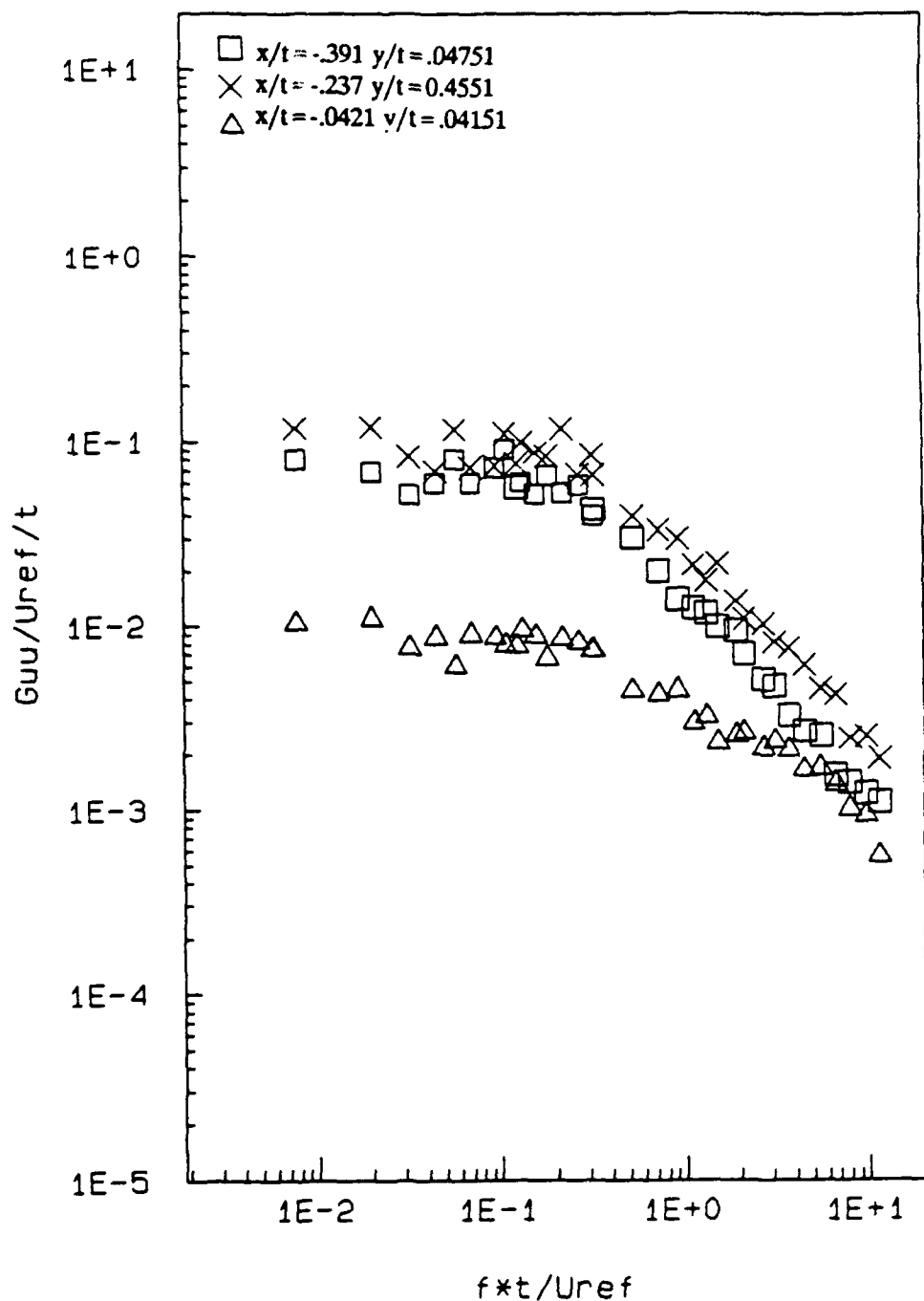
Figure 46:   Comparisons of the normalized power spectral density of the u
               component from the onset boundary layer, x/t=-.391 and
               y/t=.04751, the bimodal zone, x/t=-.237 and y/t=.04551, and the
               juncture, x/t=-.0421 and y/t=.04151.
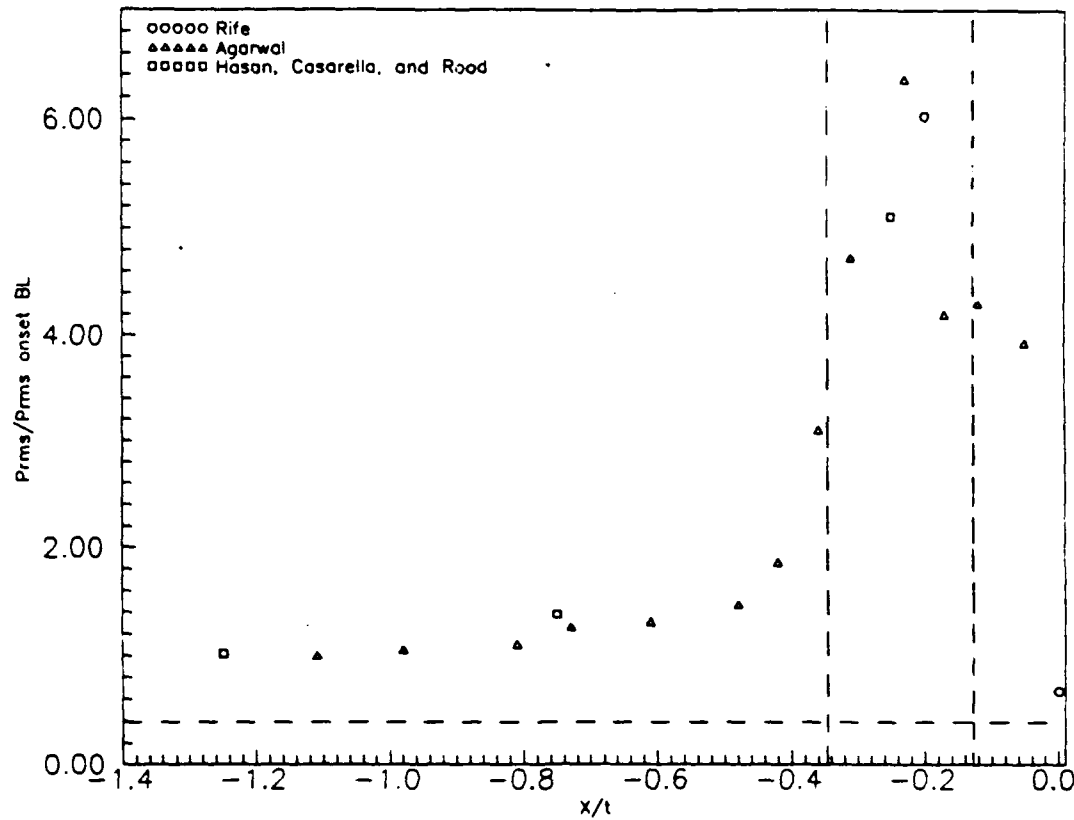
Figure 47:   Comparisons of $p_{rms}/(p_{rms})_{bl}$ versus streamwise position for ○ Rife (1992), △ Agarwal (1989), □ Hasan, Casarella, and Rood (1985). Horizontal dashed line indicates acoustic noise level of the Virginia Tech low speed boundary layer tunnel. Vertical dashed lines indicate region of bimodal flow.
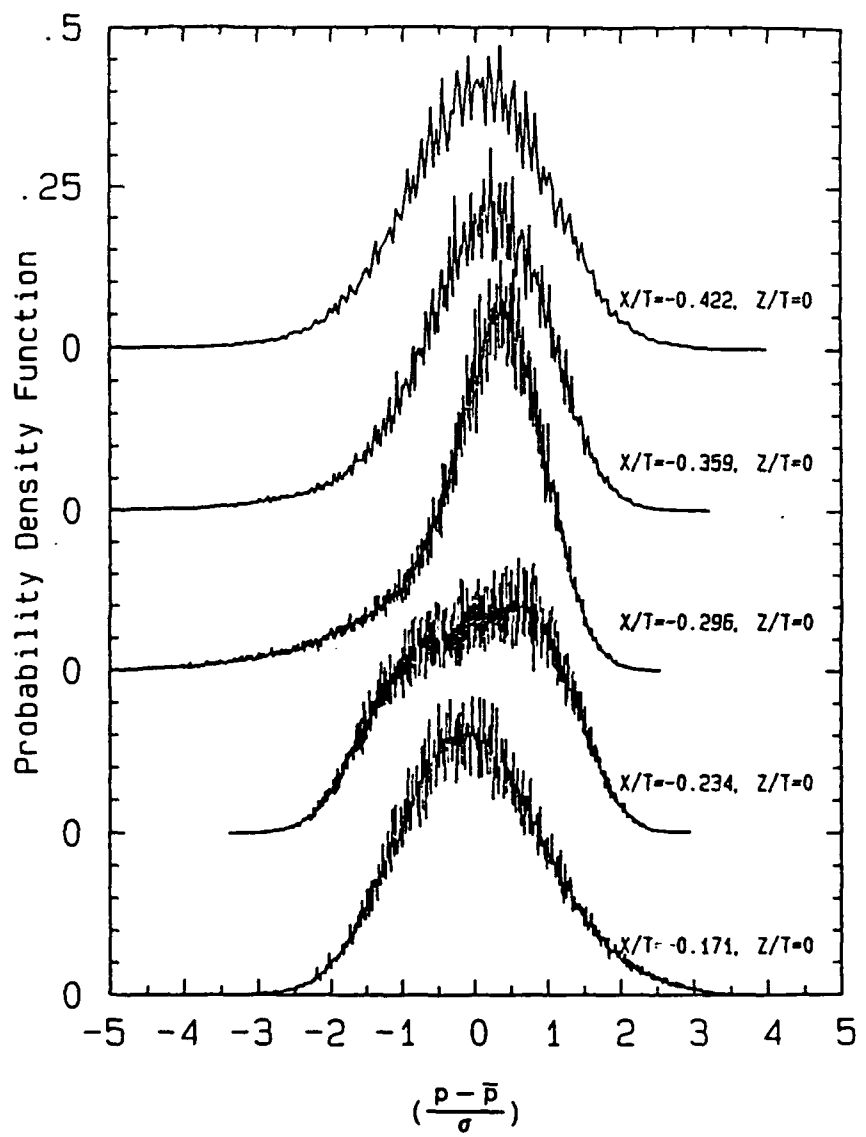
Figure 48: Probability density functions of pressure fluctuations from Agarwal (1989).
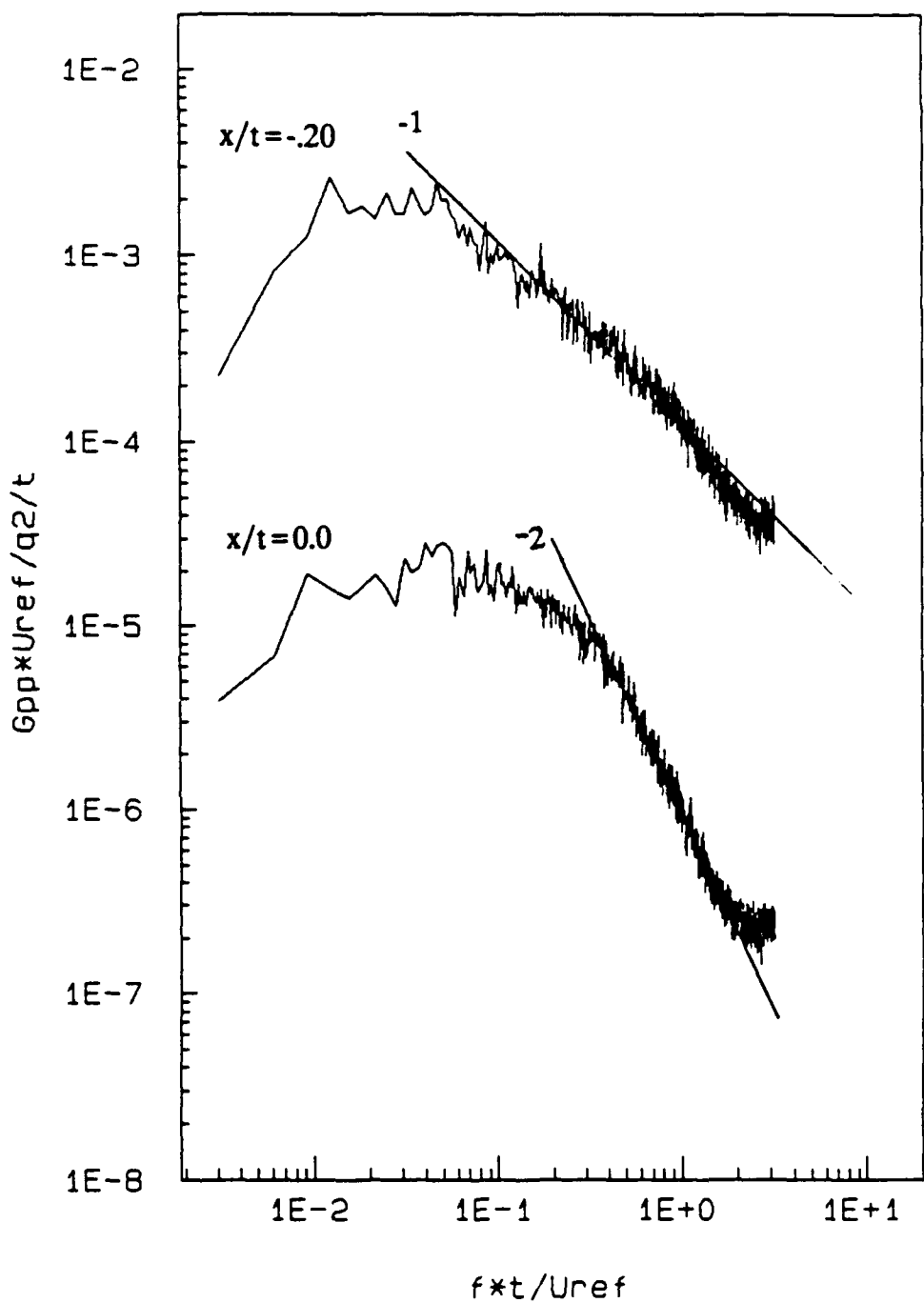
Figure 49: Normalized power spectral distribution of p^2 at $x/t=-.20$ $x/t=0.0$.
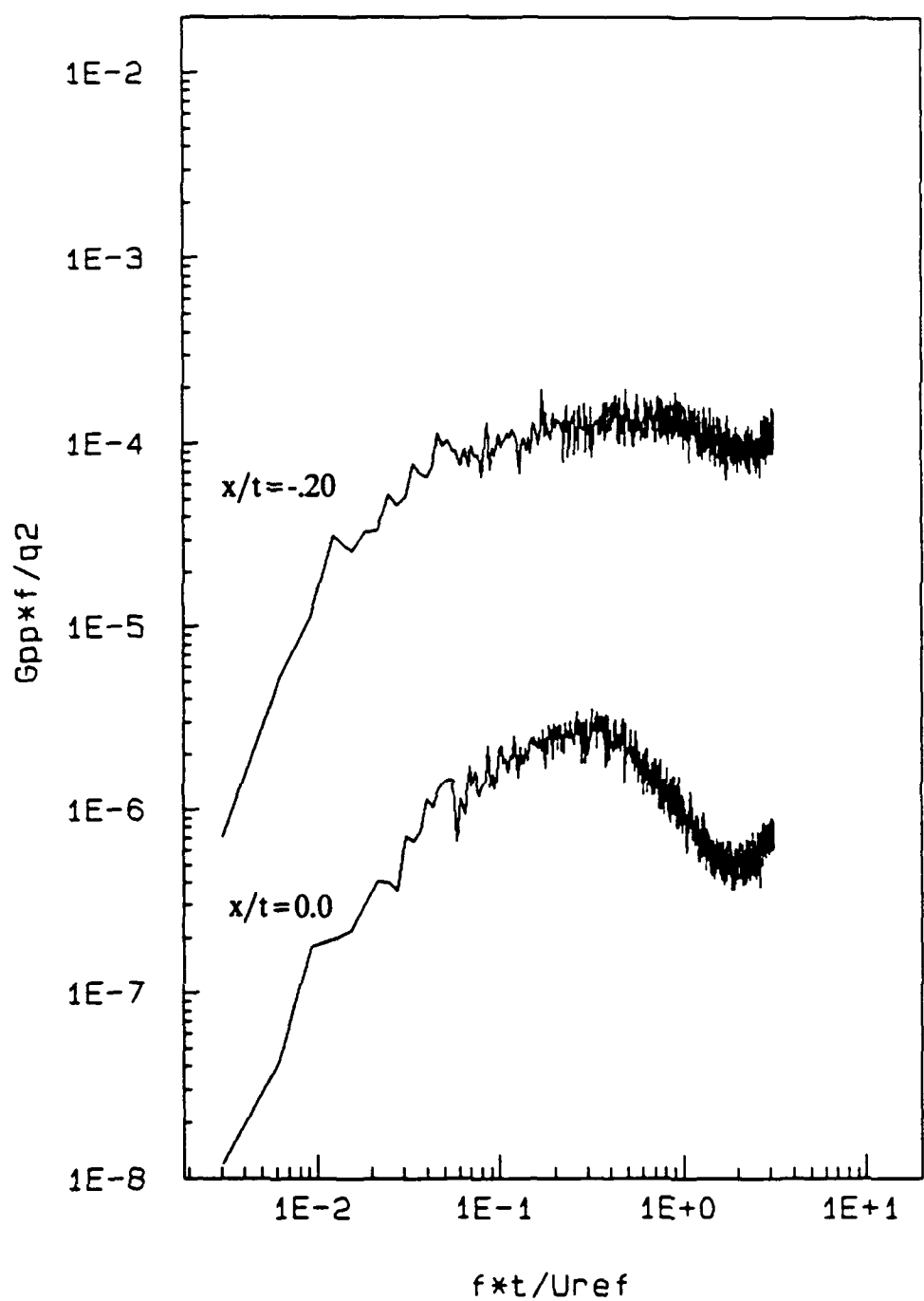
Figure 50:   Normalized first moment of the power spectral distribution of p^2 at $x/t=-.20$ $x/t=0.0$.
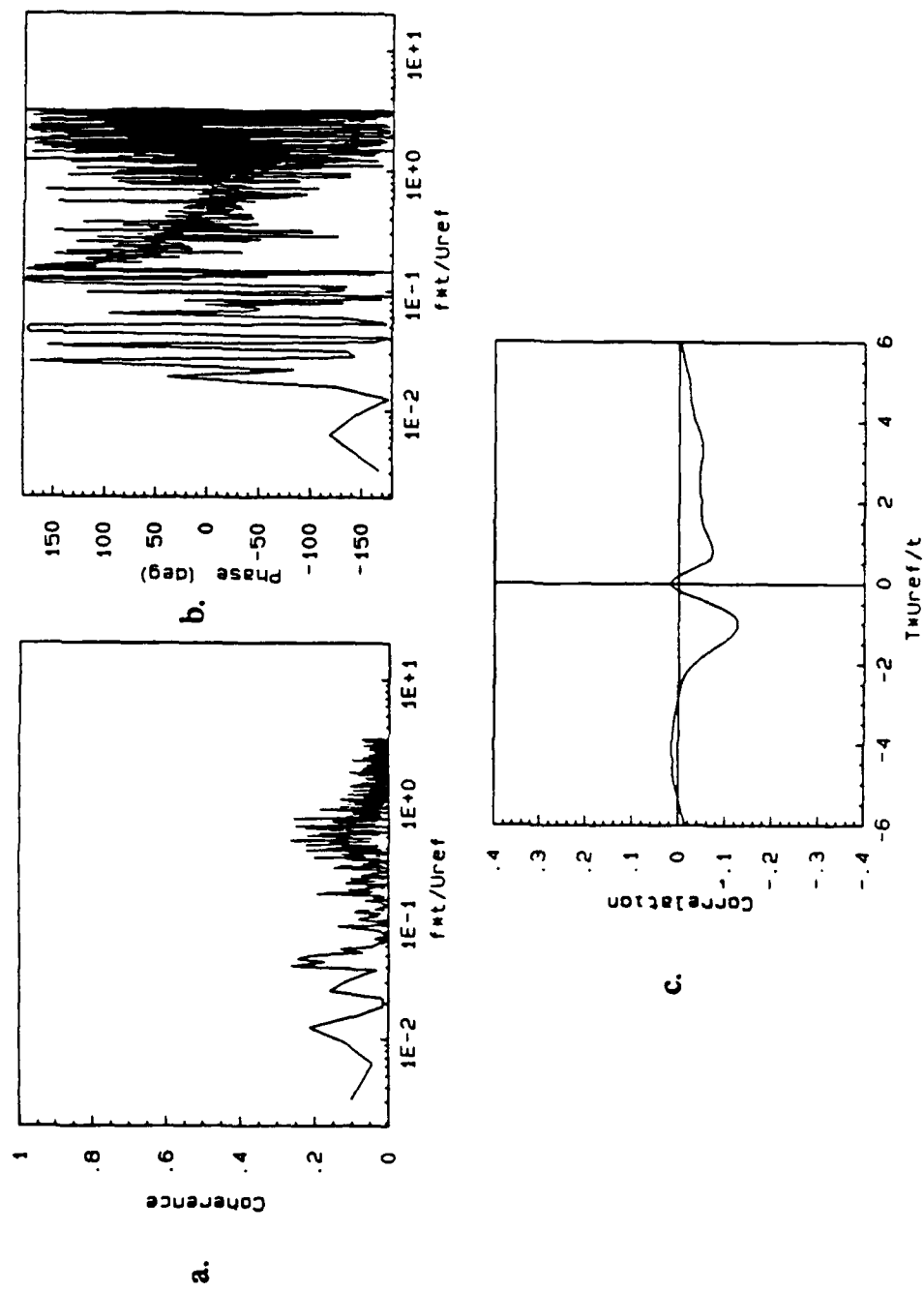
Figure 51: Functions of the relationship between the two pressure signals. a. ordinary coherence function b. phase angle c. cross-correlation coefficient function.
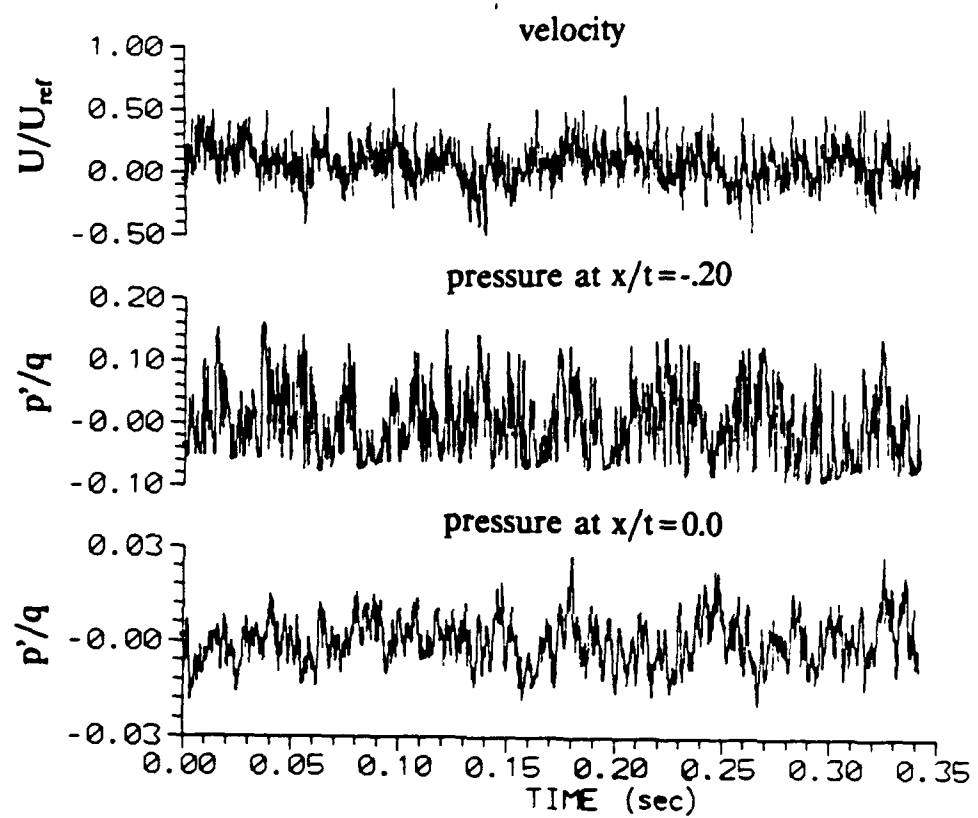
Figure 52:   U component time series data at velocity measurement location
x/t=-.391 and y/t=.01740.
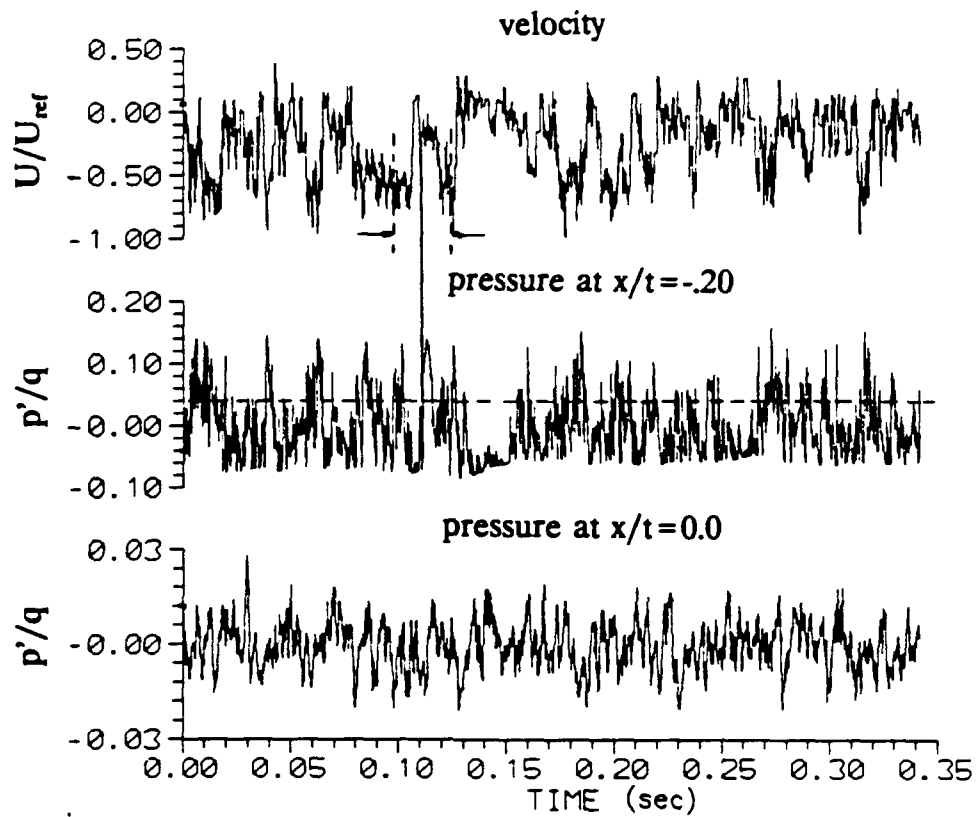
Figure 53:   U component time series data at velocity measurement location x/t=-.237 and y/t=.01044.   Horizontal dashed line is voltage threshold level, vertical dashed line is limits of conditional averaging on the velocity signal, solid vertical line shows the point in the velocity record corresponding to the switch in the pressure signal.
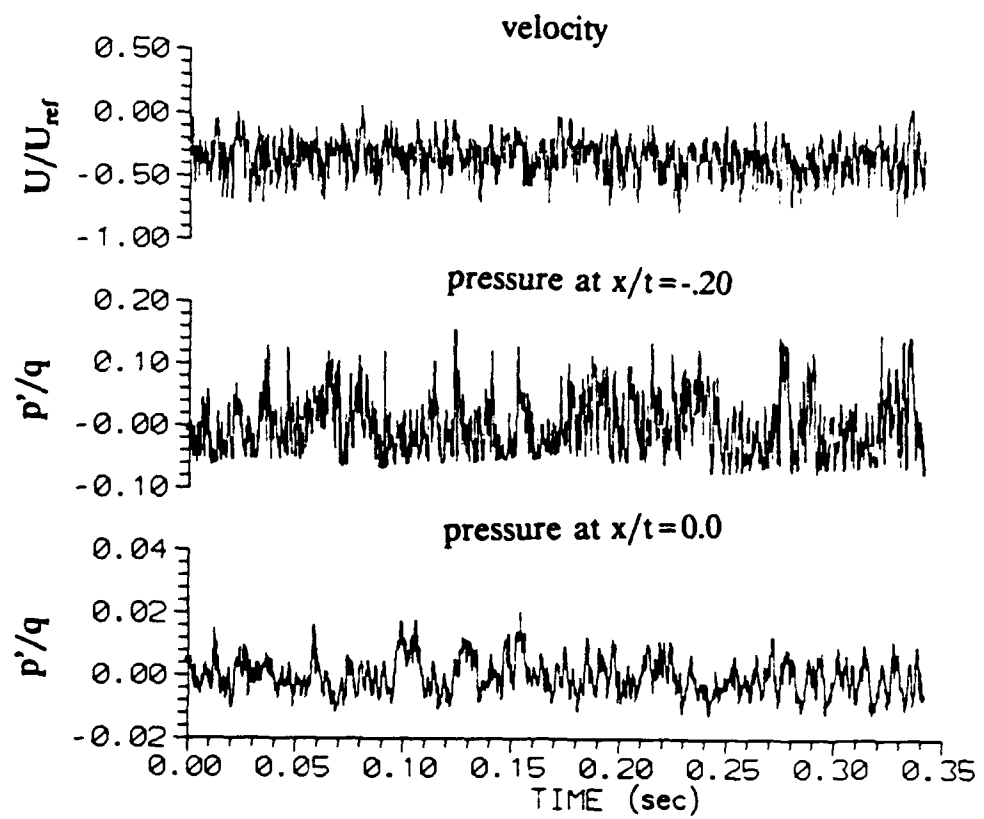
Figure 54: Time series data at velocity measurement location x/t = -.0421 and y/t = .00254.
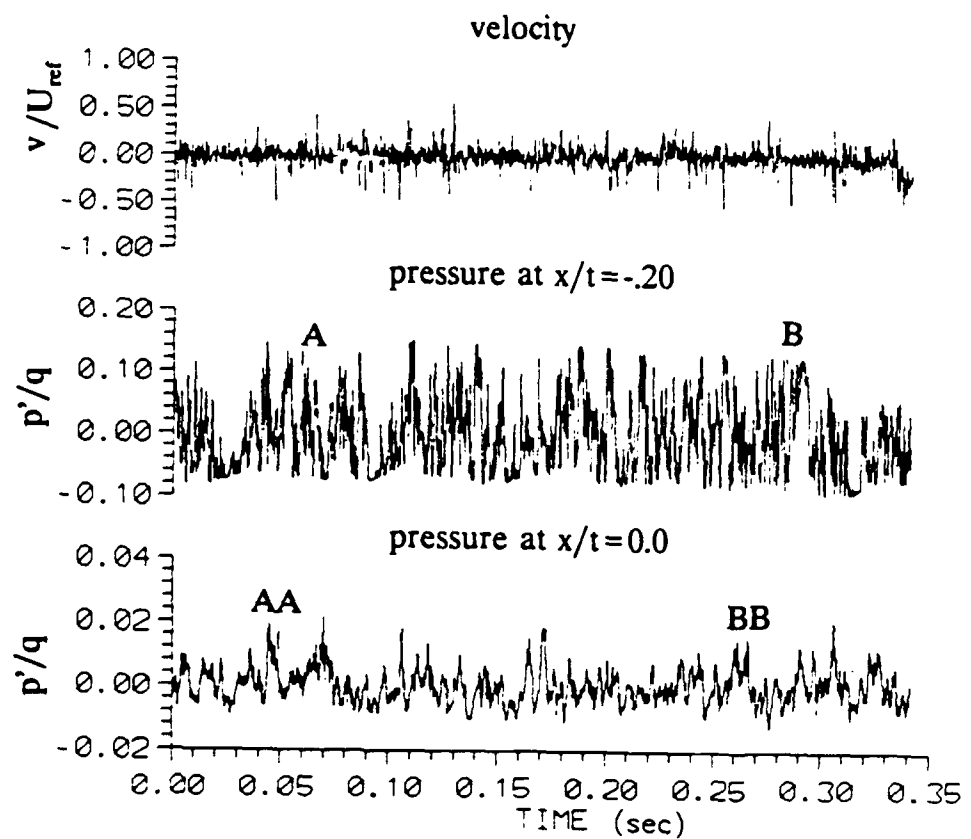
Figure 55:   V component time series data at veloci measurement location
               x/t=-.391 and y/t=.01740.

velocity

pressure at x/t = -.20
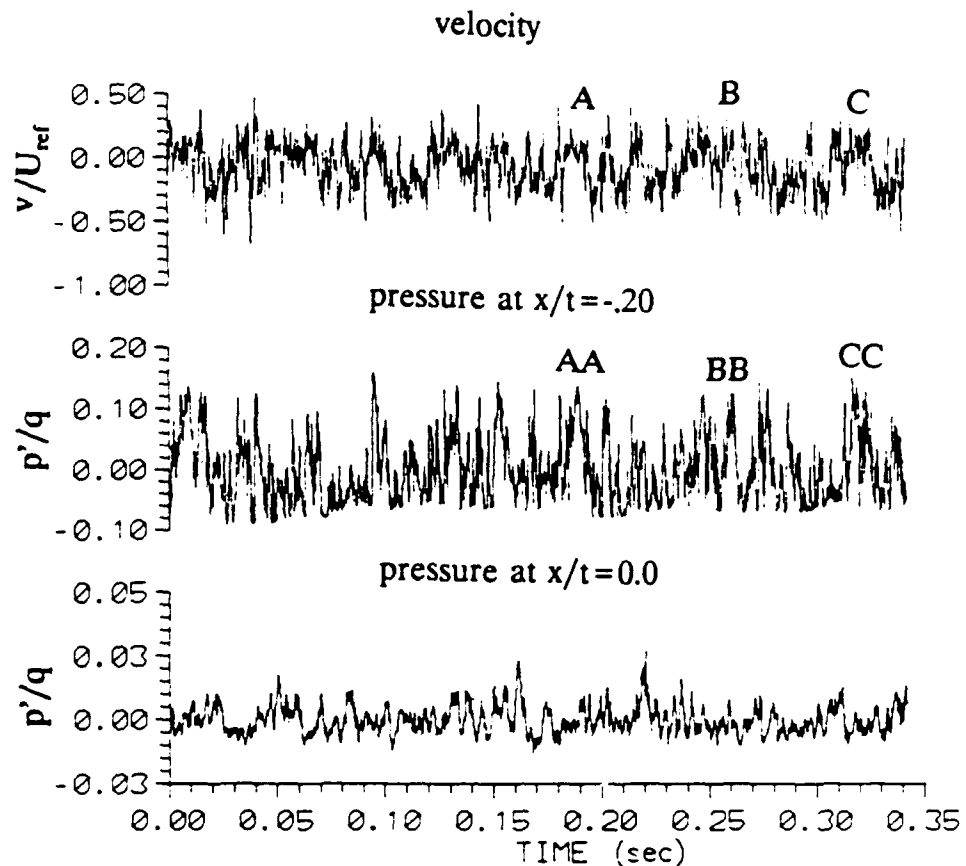
pressure at x/t = 0.0

Figure 56: V component time series data at velocity measurement location x/t = -.237 and y/t = .02319. Regions A, B, and C marked in the velocity signal appear to be correlated with features marked AA, BB, and CC in the pressure signal at x/t = -.20.

velocity

pressure at x/t = -.20
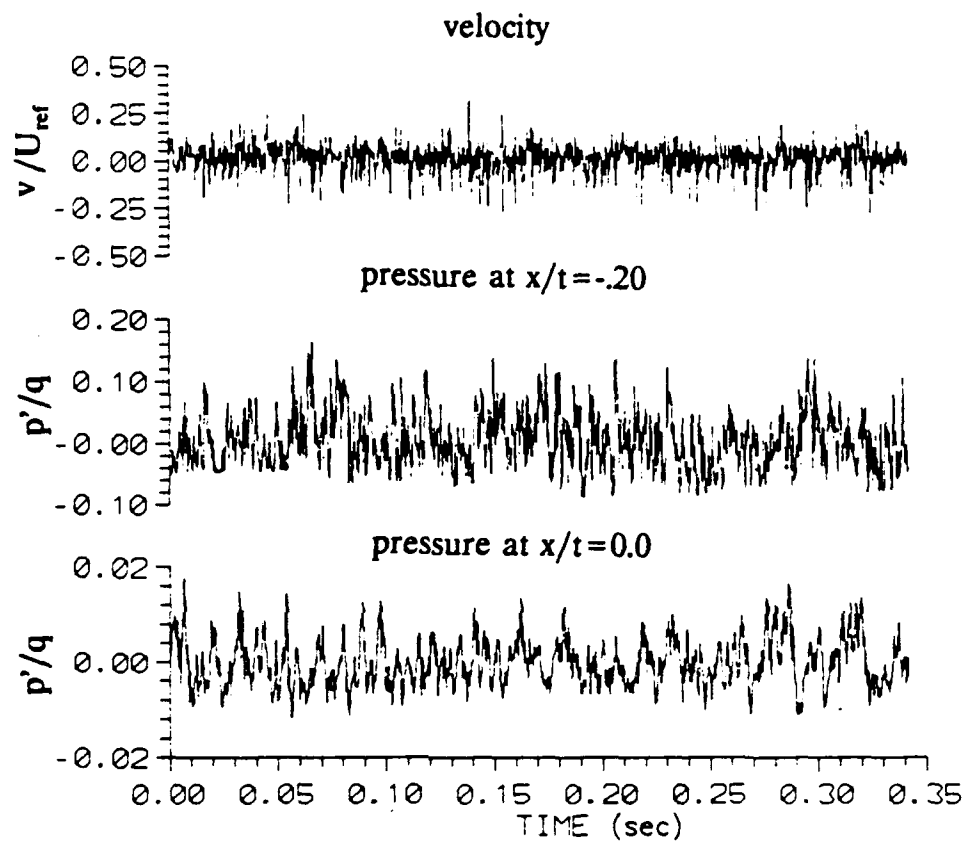
pressure at x/t = 0.0

Figure 57: Time series data at velocity measurement location $x/t = -.0421$ and $y/t = .00254$.
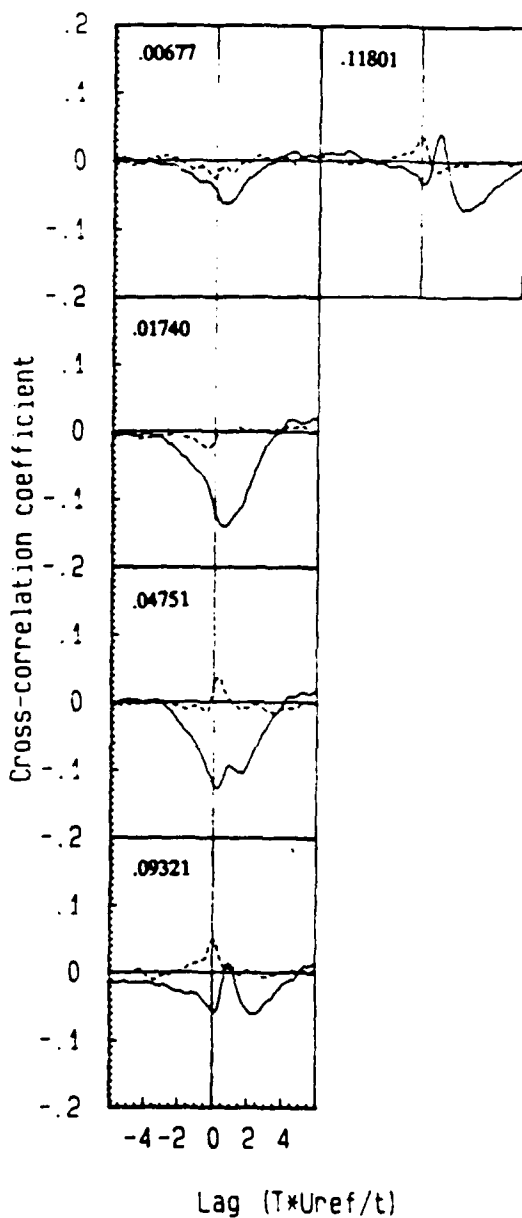
Figure 58:   Cross-correlation coefficient function between the two velocity components at x/t=-.391 and the pressure fluctuations at x/t=-.20. Solid line indicates u component velocity, dashed line is v component velocity.
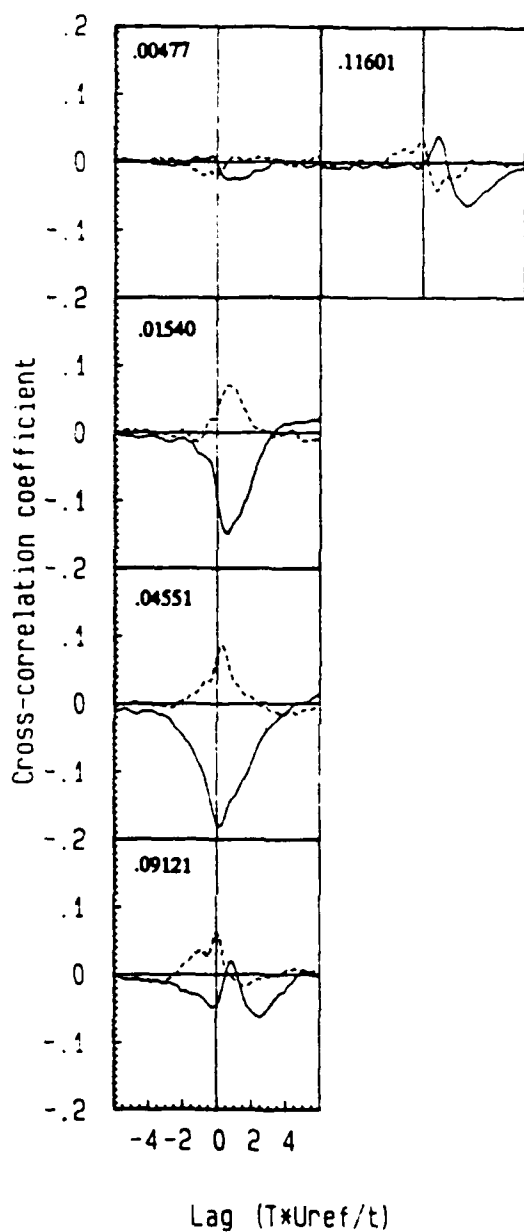
Figure 59: Cross-correlation coefficient function between the two velocity components $x/t=-.342$ and the pressure fluctuations at $x/t=-.20$. Solid line indicates u component velocity, dashed line is v component velocity.
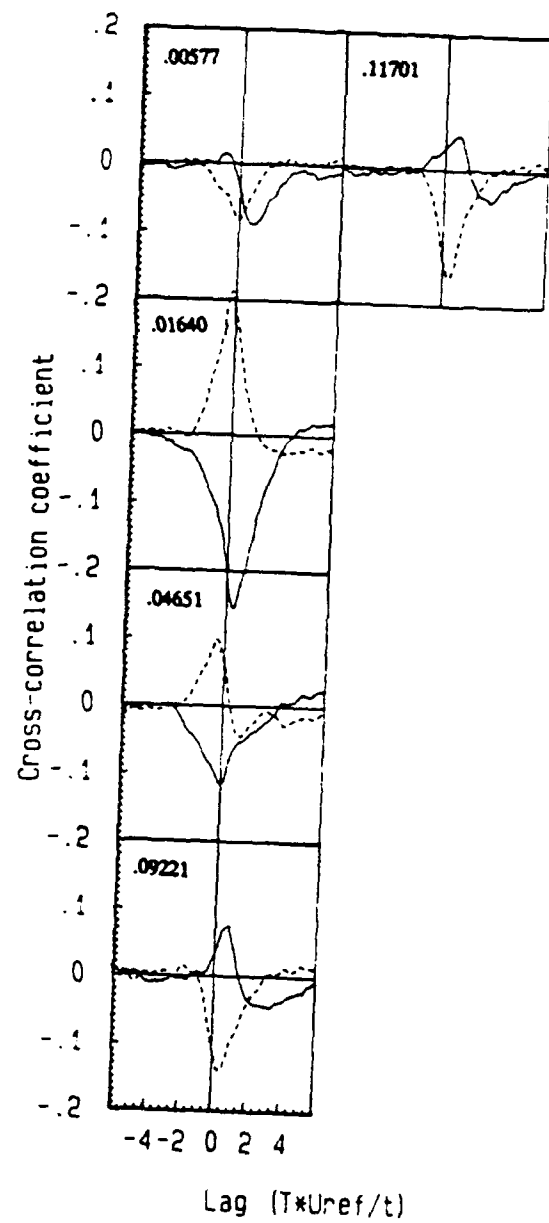
Figure 60:   Cross-correlation coefficient function between the two velocity components at x/t=-.294 and the pressure fluctuations at x/t=-.20. Solid line indicates u component velocity, dashed line is v component velocity.
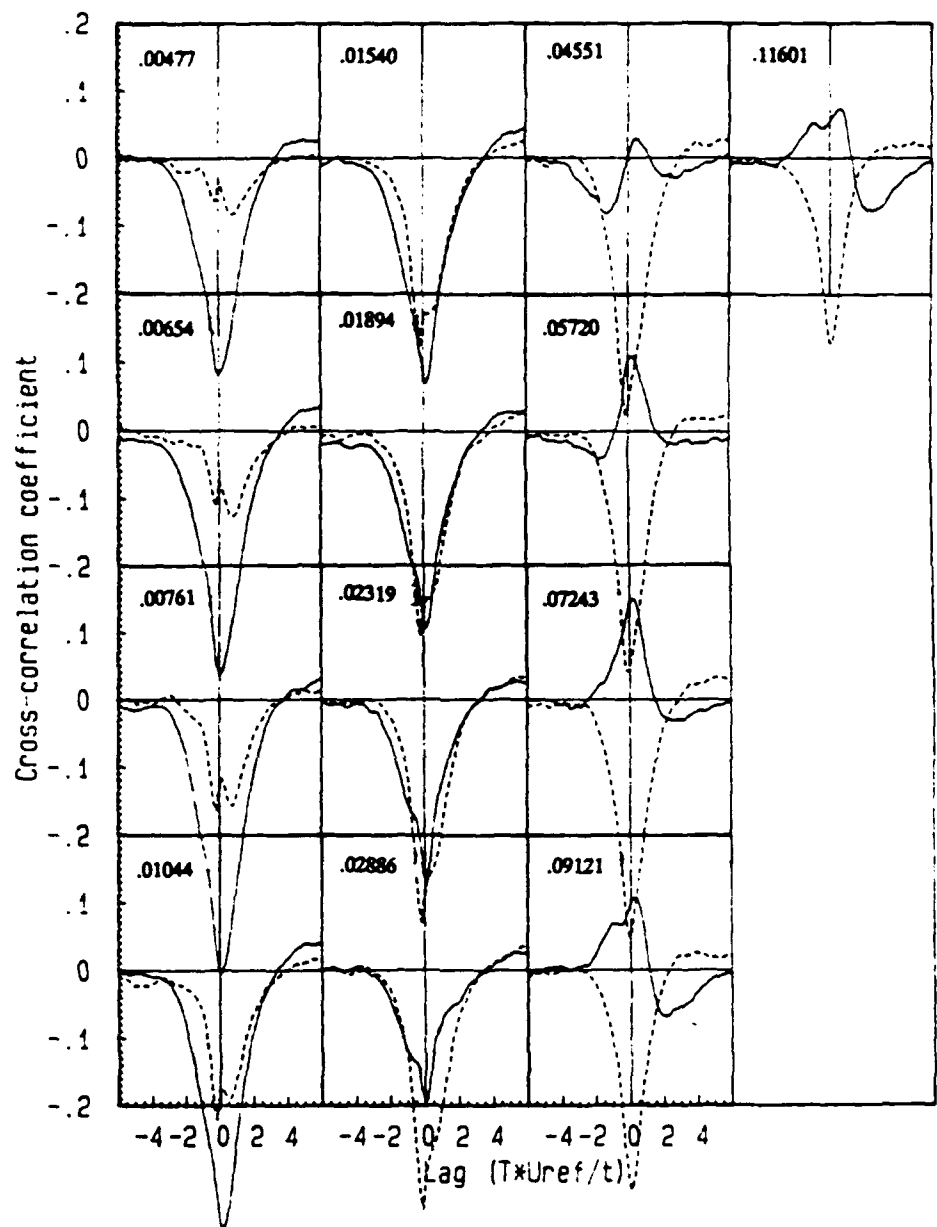
Figure 61: Cross-correlation coefficient function between the two velocity components at $x/t = -.237$ and the pressure fluctuations at $x/t = -.20$. Solid line indicates u component velocity, dashed line is v component velocity.
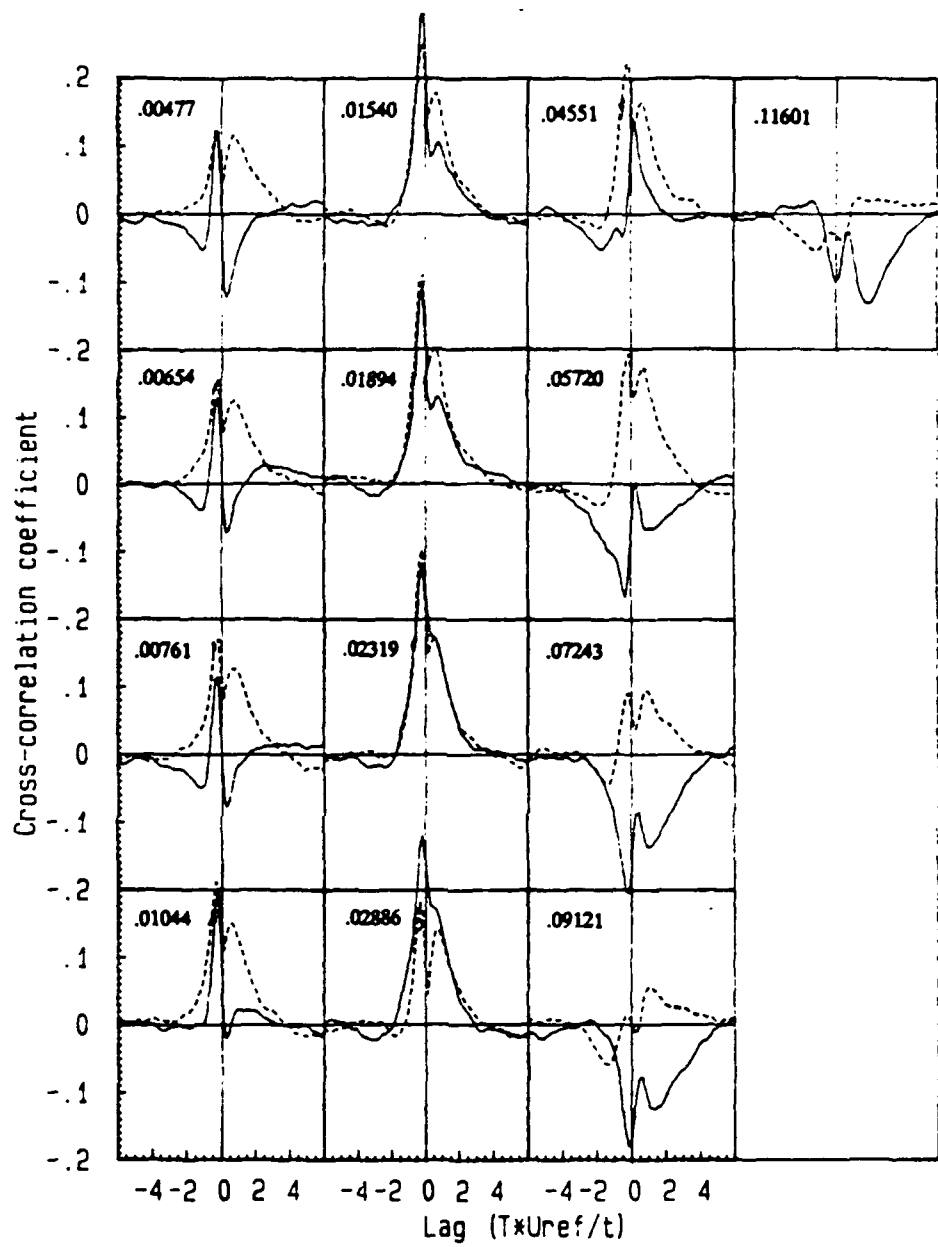
Figure 62: Cross-correlation coefficient function between the two velocity components at $x/t = -.193$ and the pressure fluctuations at $x/t = -.20$. Solid line indicates u component velocity, dashed line is v component velocity.
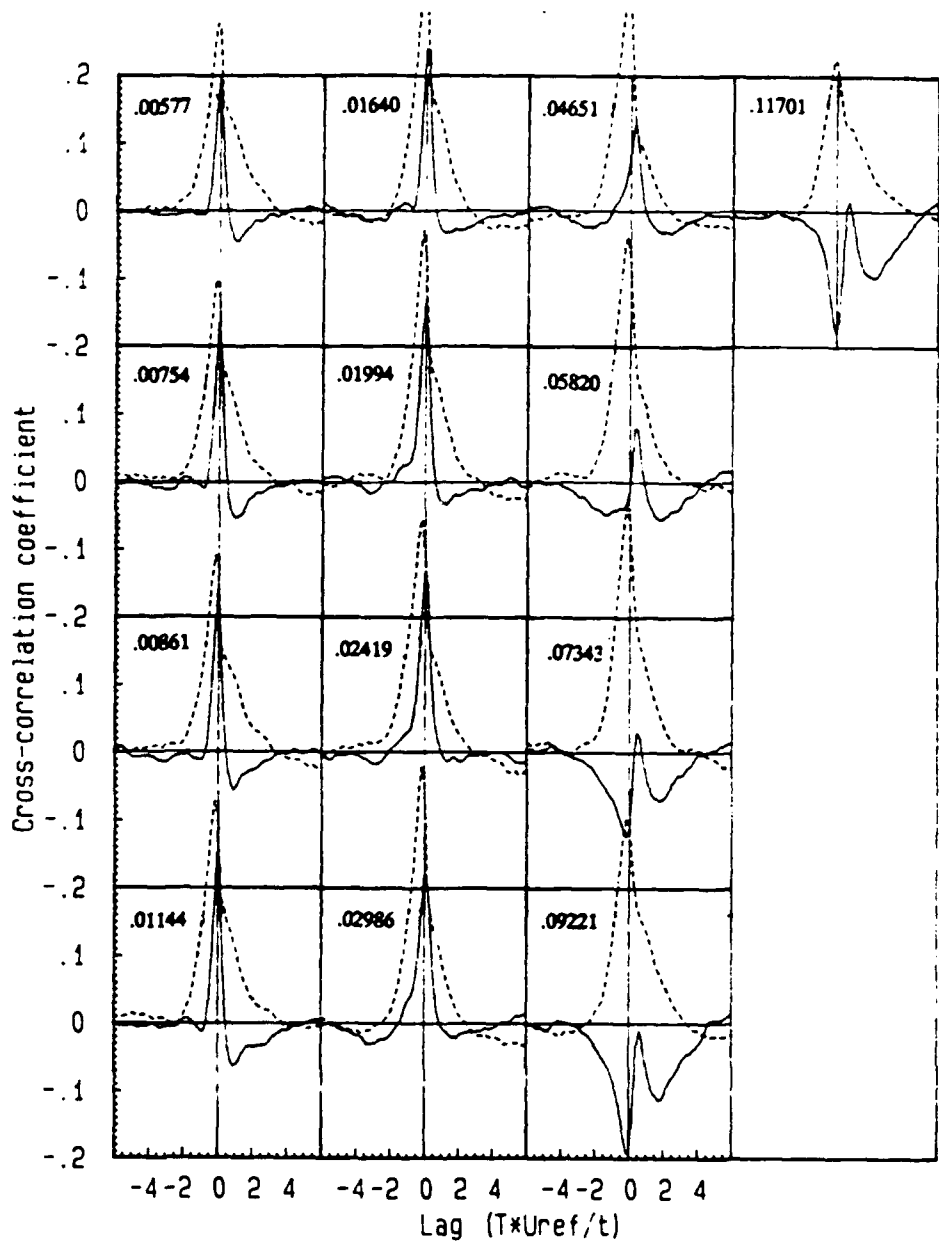
Figure 63: Cross-correlation coefficient function between the two velocity components at x/t = -.139 and the pressure fluctuations at x/t = -.20. Solid line indicates u component velocity, dashed line is v component velocity.
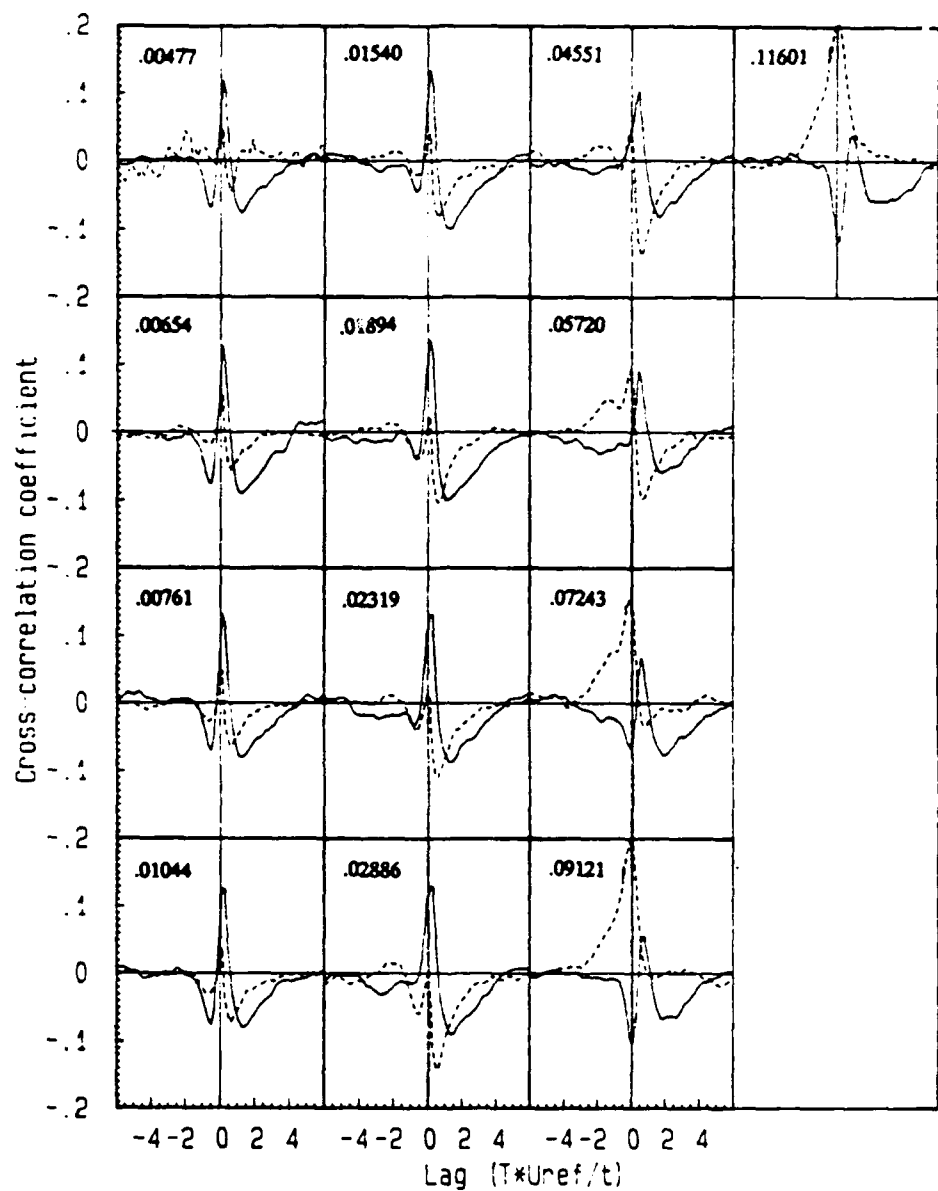
Figure 64: Cross-correlation coefficient function between the two velocity components at x/t =-.0856 and the pressure fluctuations at x/t=-.20. Solid line indicates u component velocity, dashed line is v component velocity.
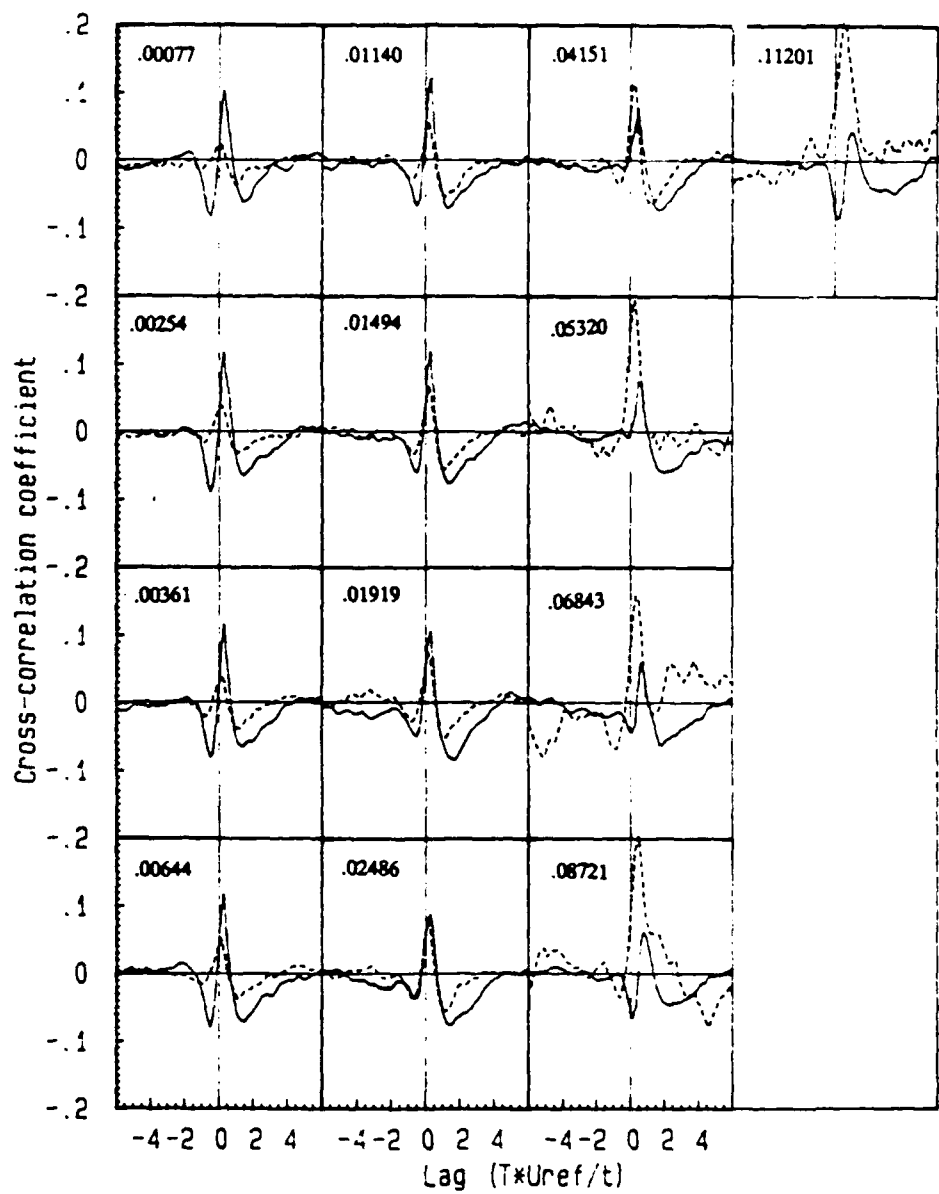
Figure 65:   Cross-correlation coefficient function between the two velocity components at x/t = -.0421 and the pressure fluctuations at x/t = -.20. Solid line indicates u component velocity, dashed line is v component velocity.

a.
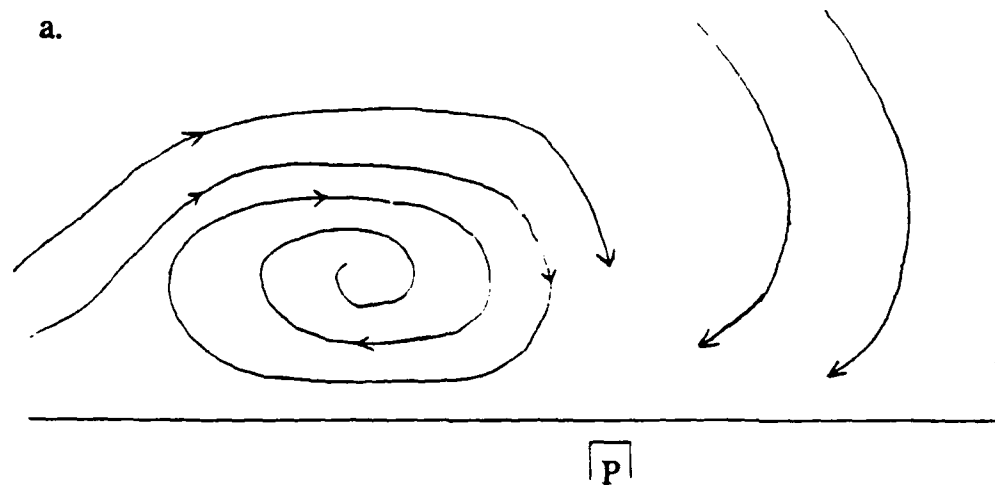
b.
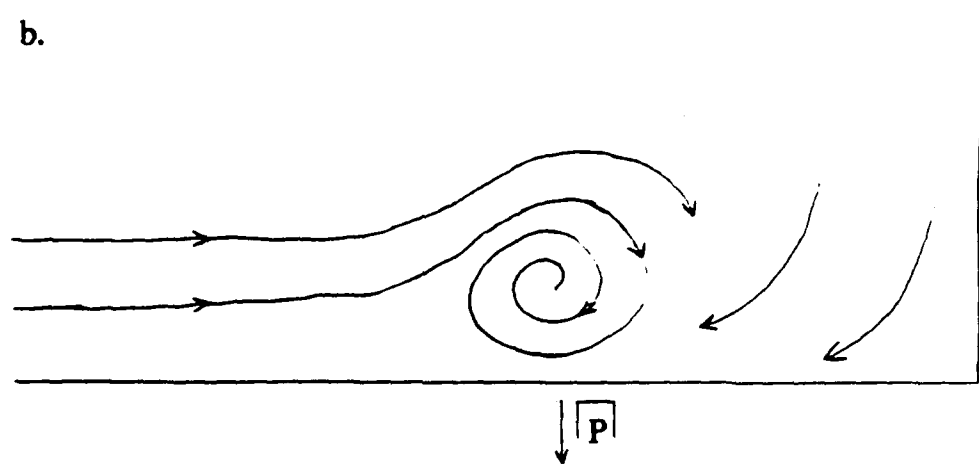
Figure 66:   Sketch of the model eddy as interpreted from the cross-correlation functions between the two velocity components and the pressure fluctuations at $x/t = -.20$. a. Fluid comes down the face of the wing energizing the eddy. b. The eddy rolls up and moves downstream as the pressure at $x/t = -.20$ drops.
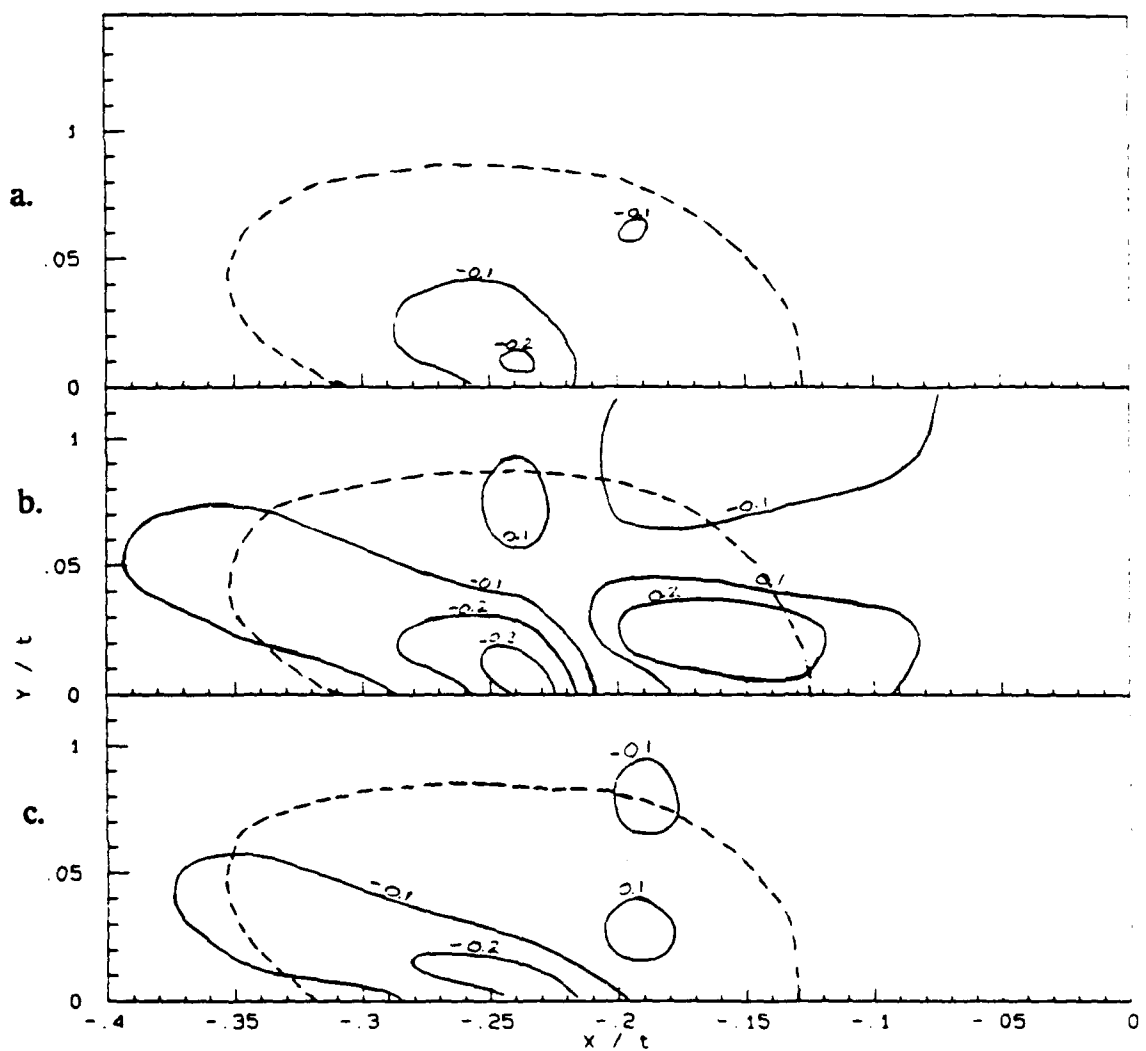
Figure 67:   Contours of maximum correlation between the u component and the pressure at $x/t = -.20$ at a specified non-dimensional time lag. a. $TU_{ref}/t = -.9403$ b. $TU_{ref}/t = 0$ c. $TU_{ref}/t = .9403$. Dashed line shows the composite (U and V) bimodal zone.
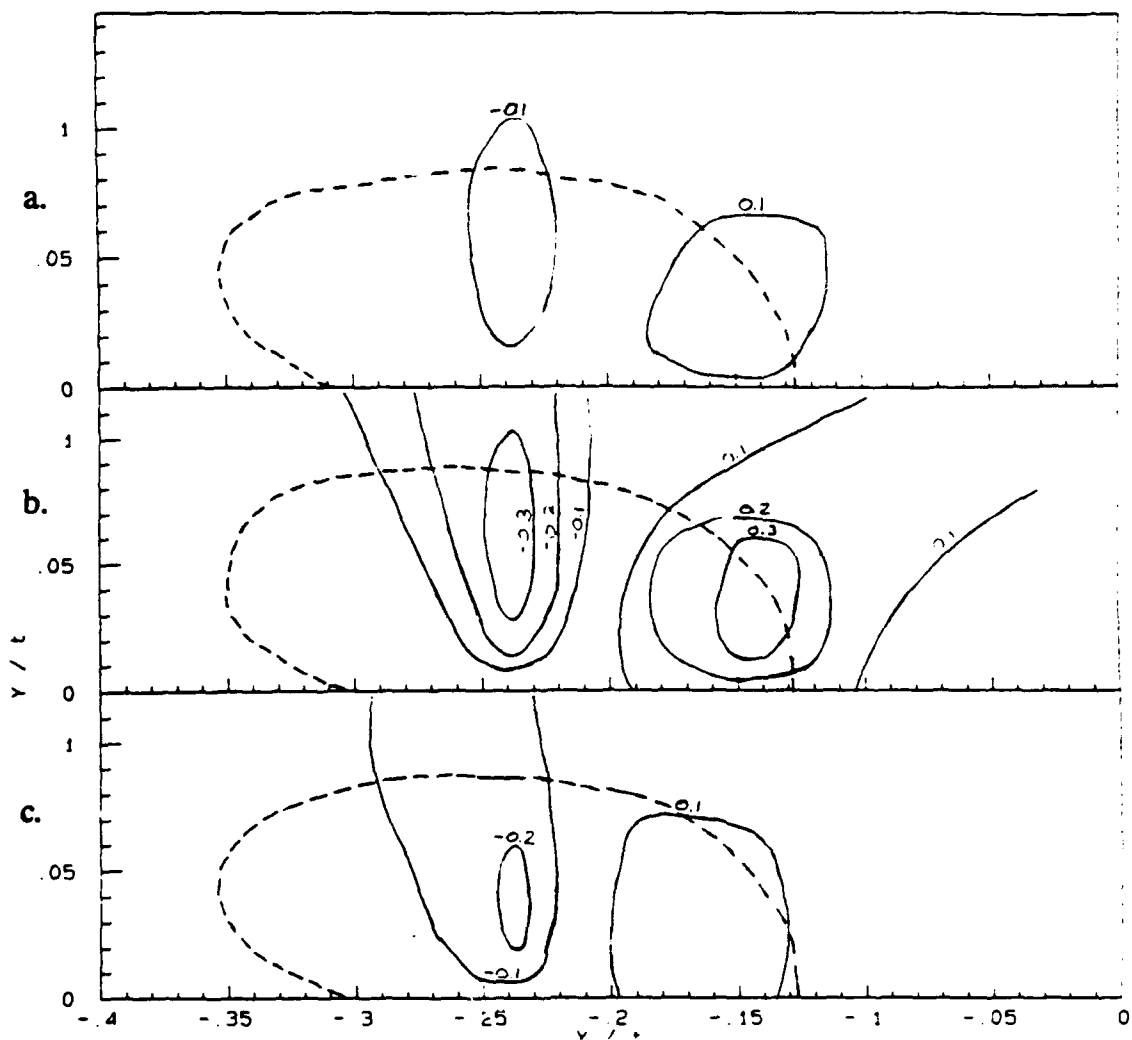
Figure 68: Contours of maximum correlation between the v component and the pressure at x/t=-.20 at a specified non-dimensional time lag. a. $TU_{ref}/t=-.9403$ b. $TU_{ref}/t=0$ c. $TU_{ref}/t=.9403$. Dashed line shows the composite (U and V) bimodal zone.
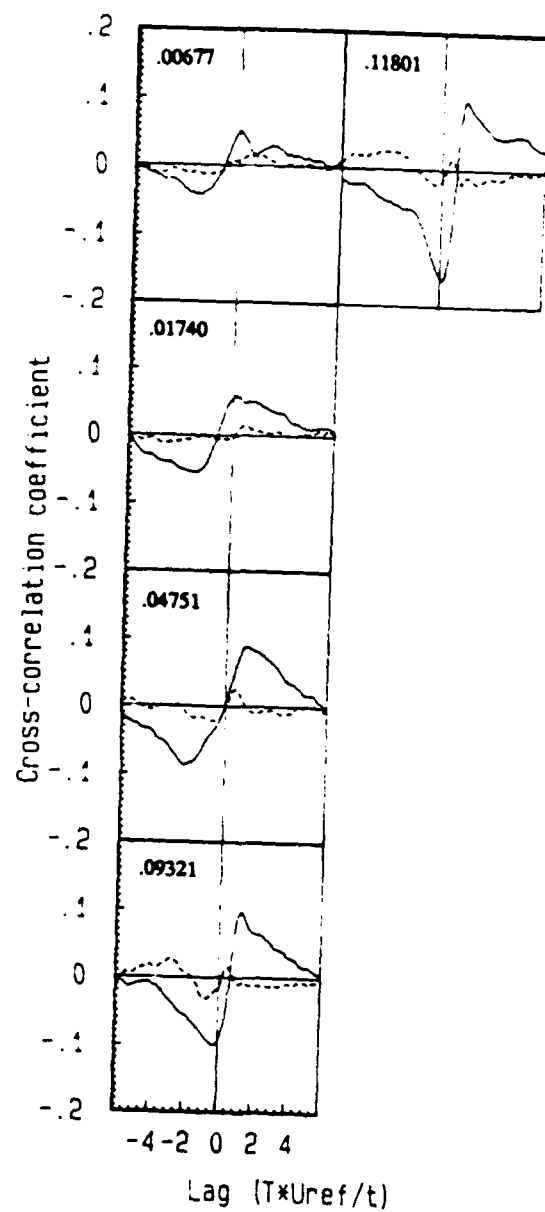
Figure 69: Cross-correlation coefficient function between the two velocity components at x/t=-.391 and the pressure fluctuations at x/t=0.0. Solid line indicates u component velocity, dashed line is v component velocity.
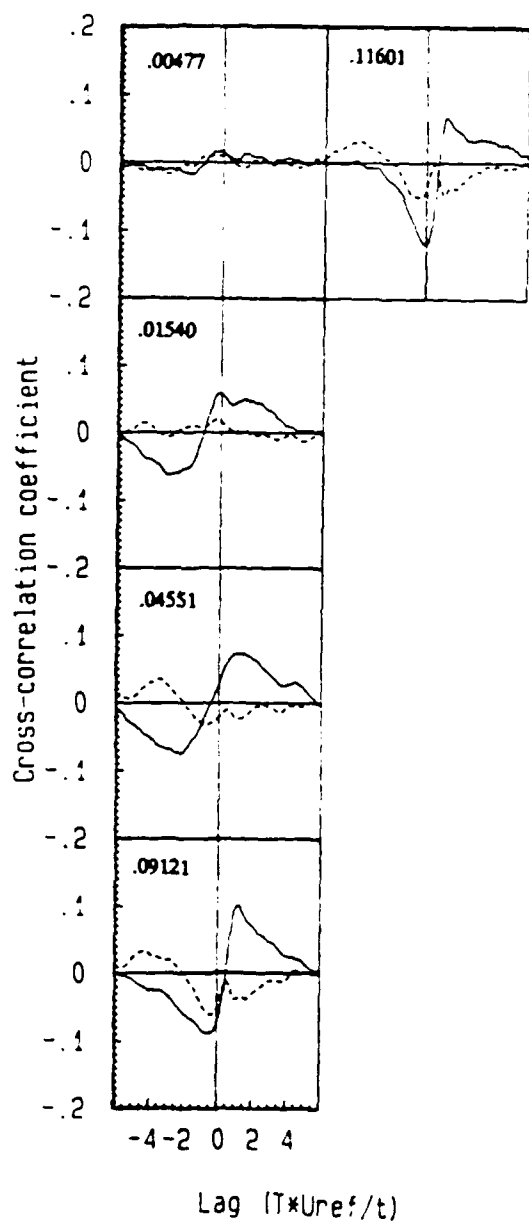
Figure 70: Cross-correlation coefficient function between the two velocity components x/t=-.342 and the pressure fluctuations at x/t=0.0. Solid line indicates u component velocity, dashed line is v component velocity.
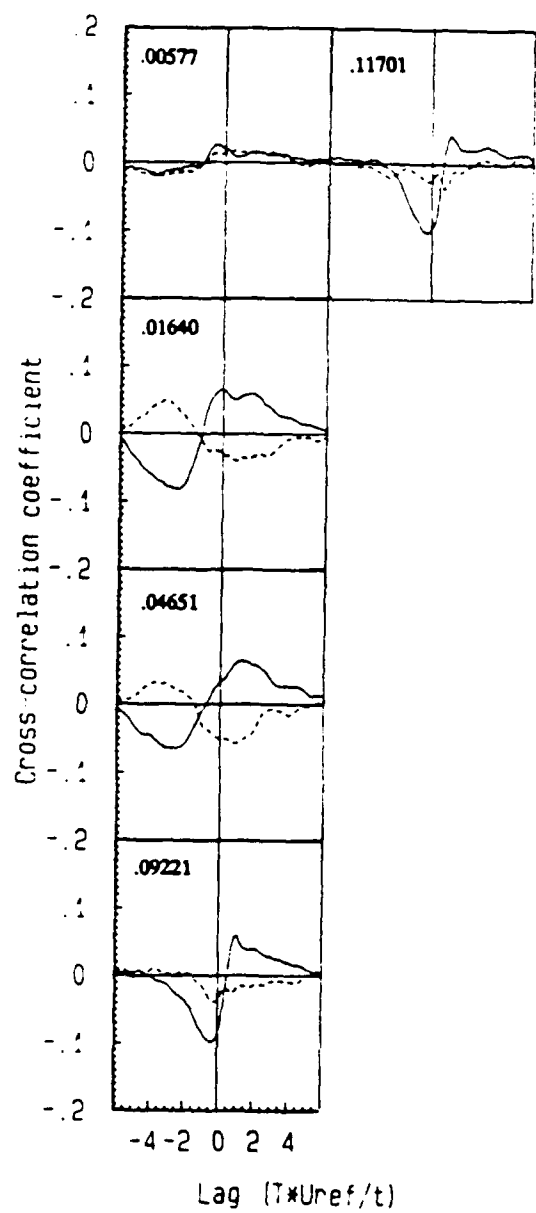
Figure 71:   Cross-correlation coefficient function between the two velocity components at $x/t = -.294$ and the pressure fluctuations at $x/t = 0.0$. Solid line indicates u component velocity, dashed line is v component velocity.
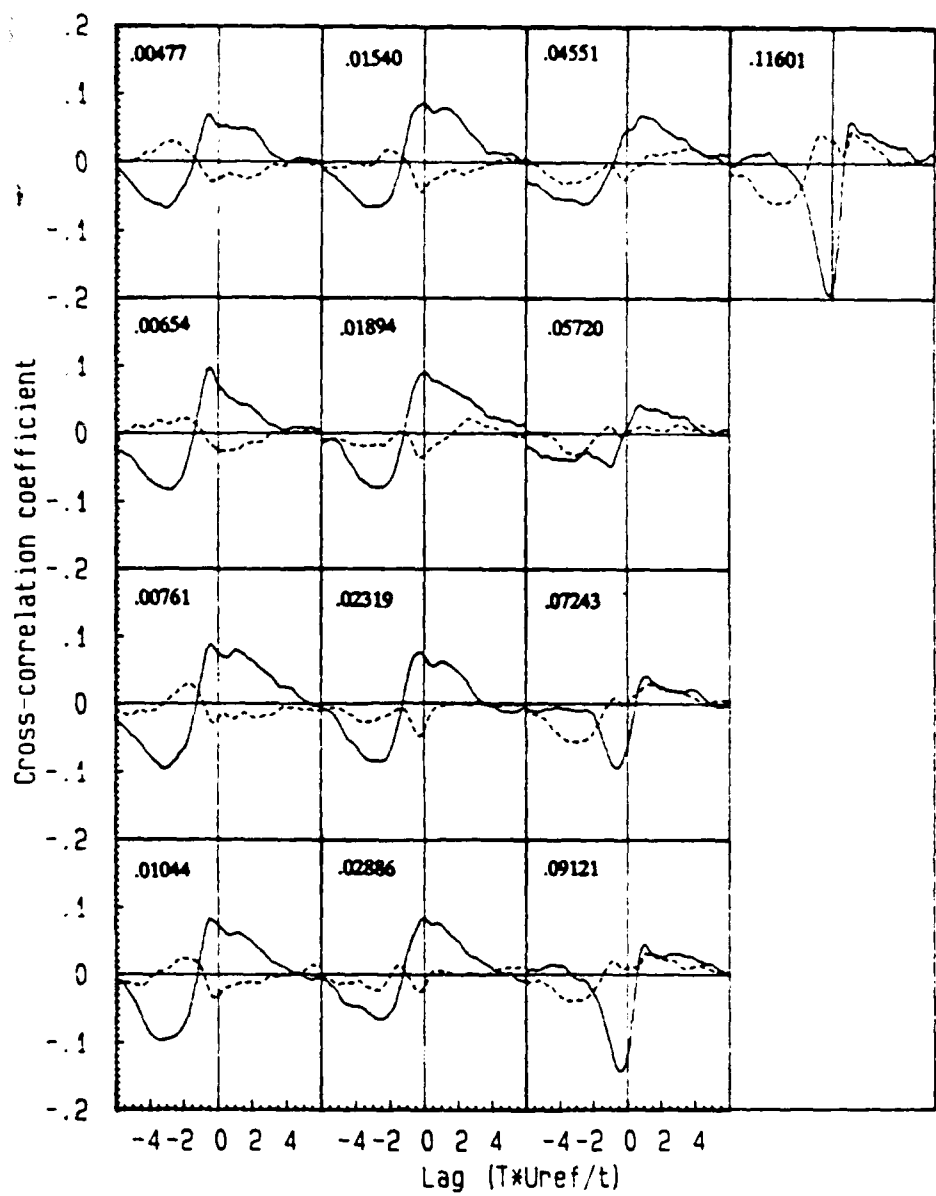
Figure 72: Cross-correlation coefficient function between the two velocity components at x/t=-.237 and the pressure fluctuations at x/t=0.0. Solid line indicates u component velocity, dashed line is v component velocity.
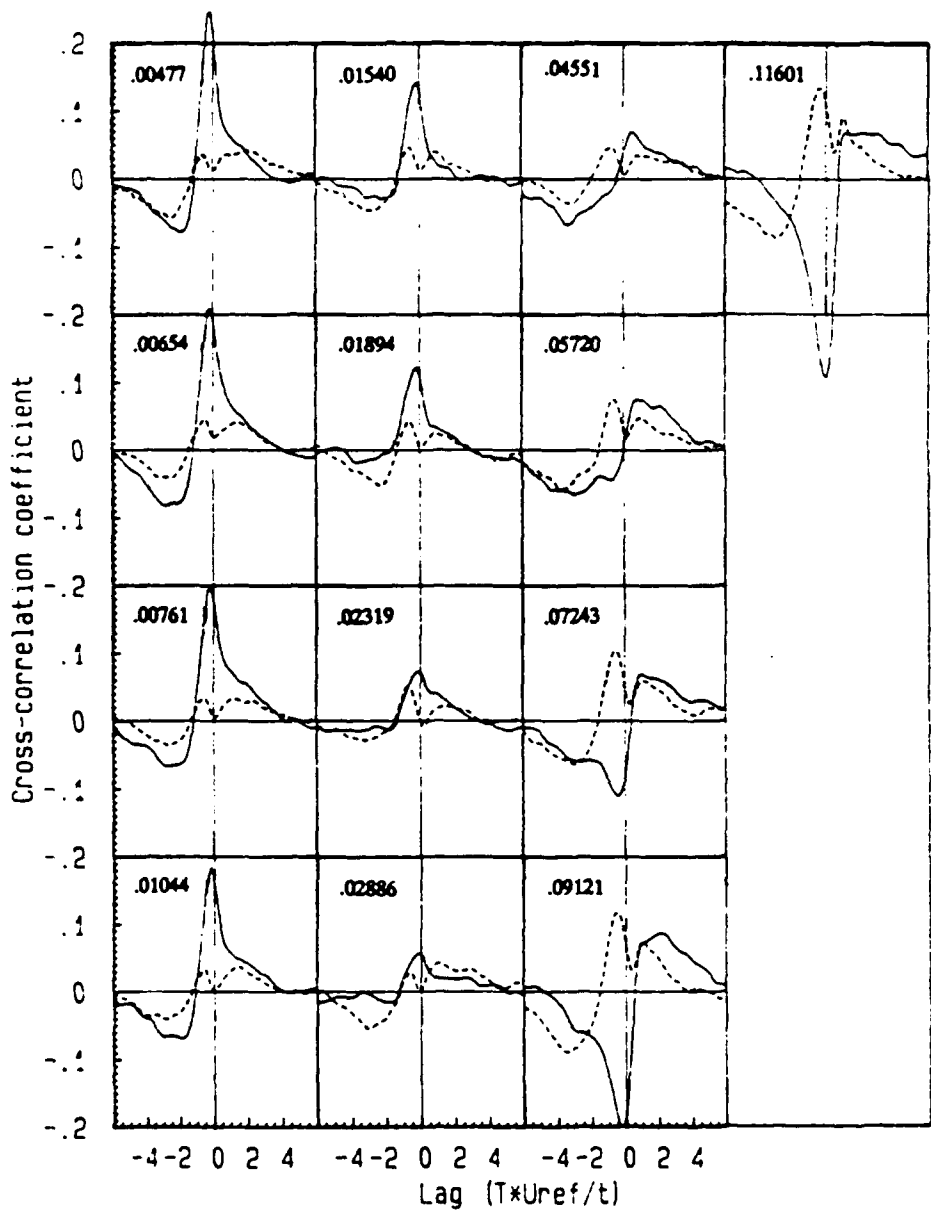
Figure 73: Cross-correlation coefficient function between the two velocity components at x/t=-.193 and the pressure fluctuations at x/t=0.0. Solid line indicates u component velocity, dashed line is v component velocity.
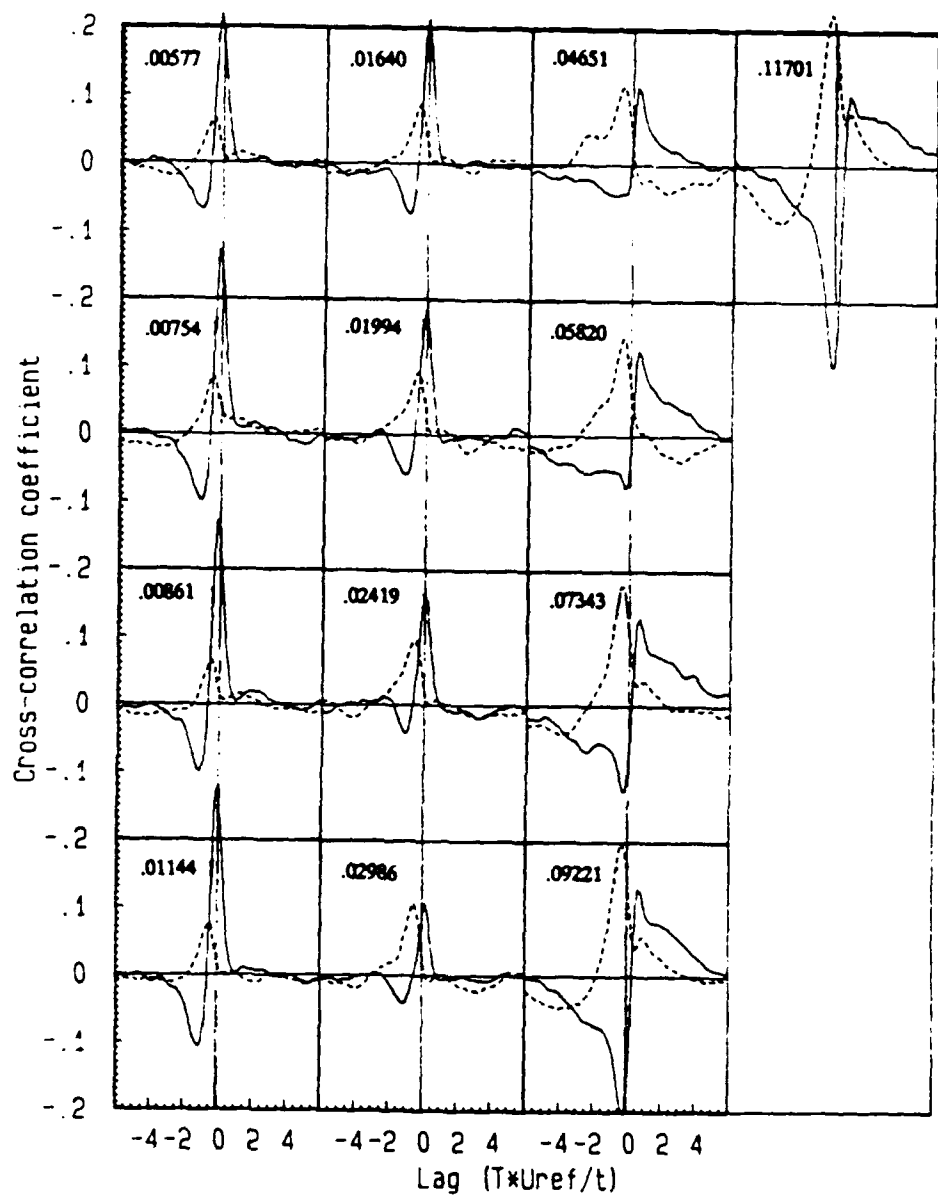
Figure 74: Cross-correlation coefficient function between the two velocity components at x/t=-.139 and the pressure fluctuations at x/t=0.0. Solid line indicates u component velocity, dashed line is v component velocity.
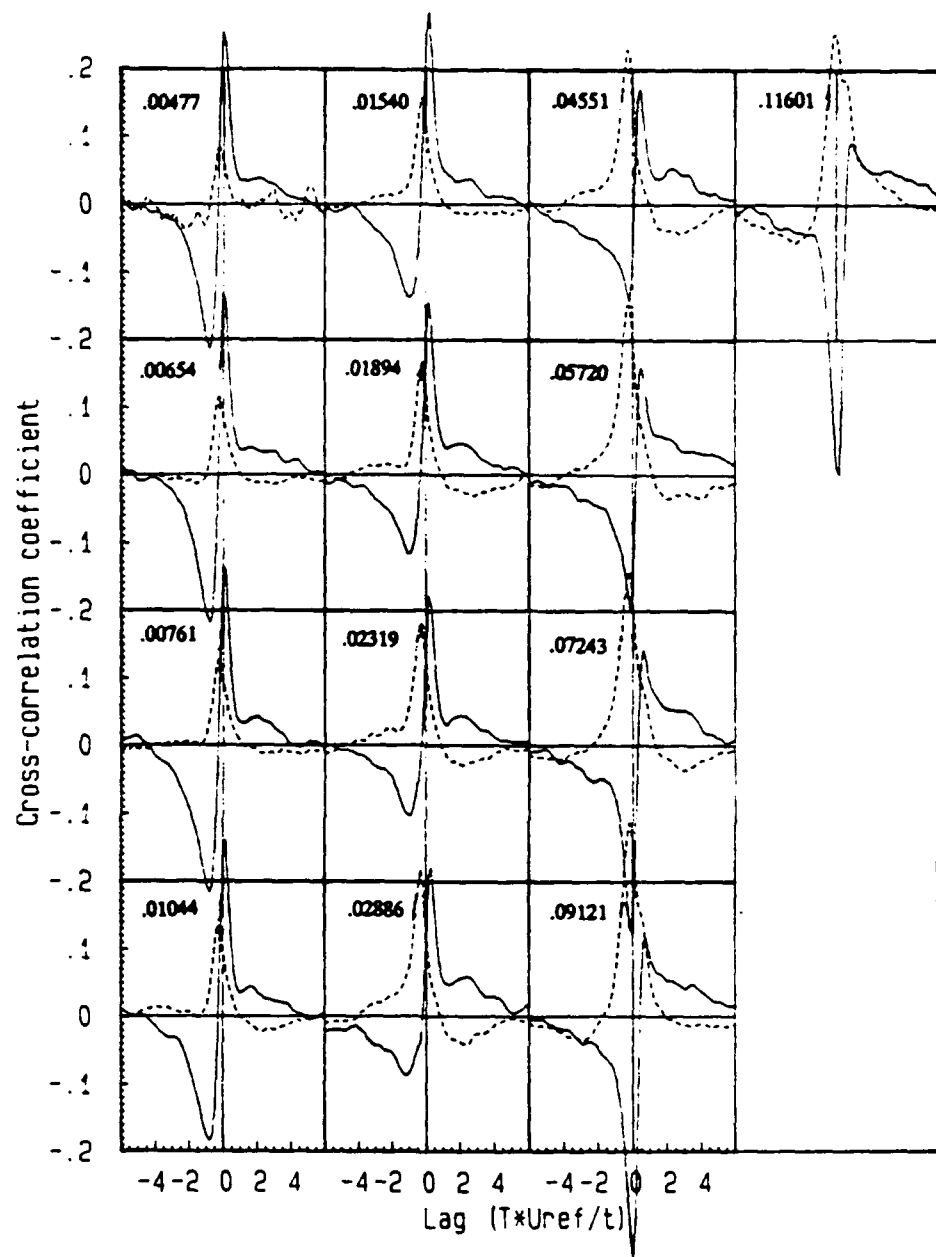
Figure 75:   Cross-correlation coefficient function between the two velocity
               components at x/t = -.0856 and the pressure fluctuations at x/t = 0.0.
               Solid line indicates u component velocity, dashed line is v
               component velocity.
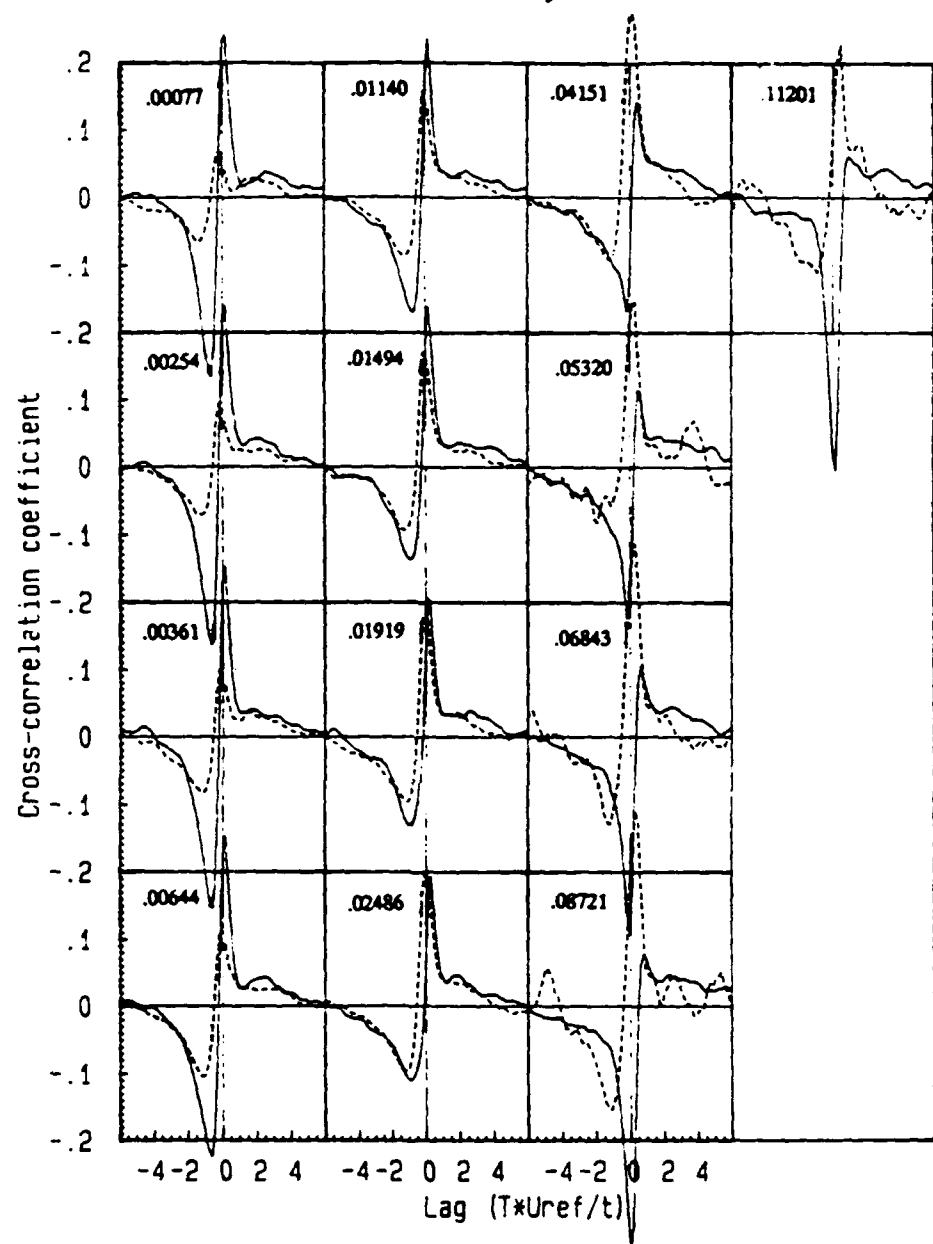
Figure 76: Cross-correlation coefficient function between the two velocity components at $x/t = -.0421$ and the pressure fluctuations at $x/t = 0.0$. Solid line indicates u component velocity, dashed line is v component velocity.
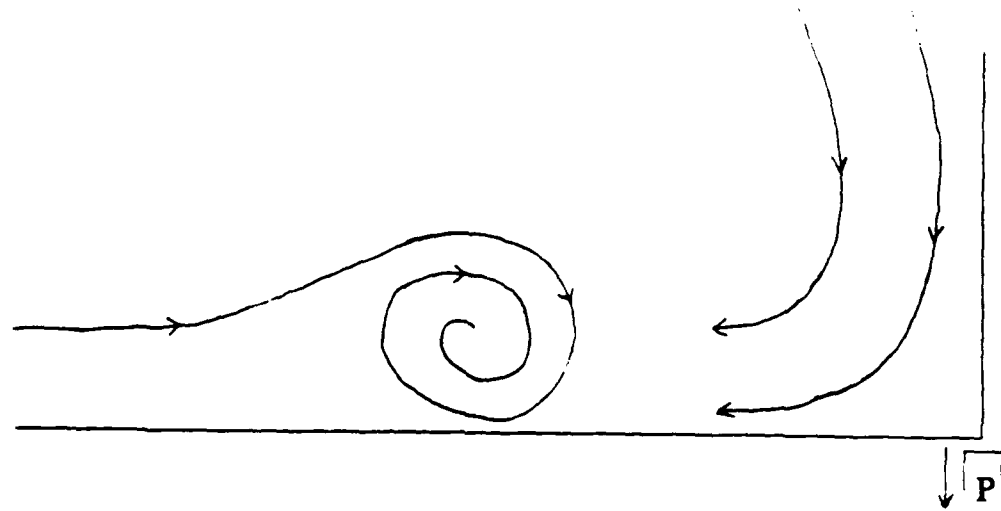
Figure 77:   Sketch of the model eddy as interpreted from the cross-correlation
              functions between the two velocity components and the pressure
              fluctuations at $x/t = 0.0$.
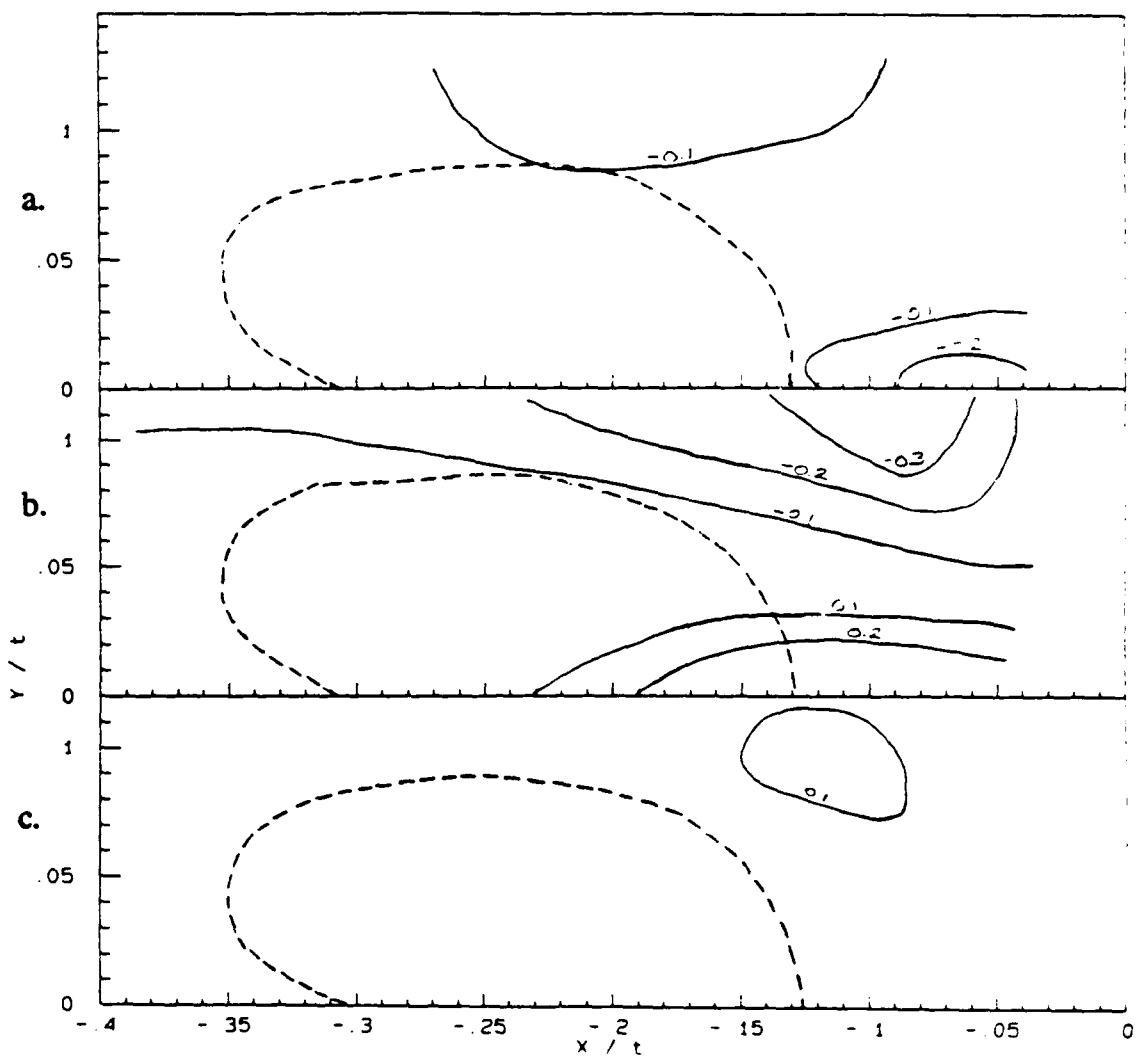
Figure 78: Contours of maximum correlation between the u component and the pressure at $x/t = 0.0$ at a specified non-dimensional time lag. a. $TU_{ref}/t = -.9403$ b. $TU_{ref}/t = 0$ c. $TU_{ref}/t = .9403$. Dashed line shows the composite (U and V) bimodal zone.
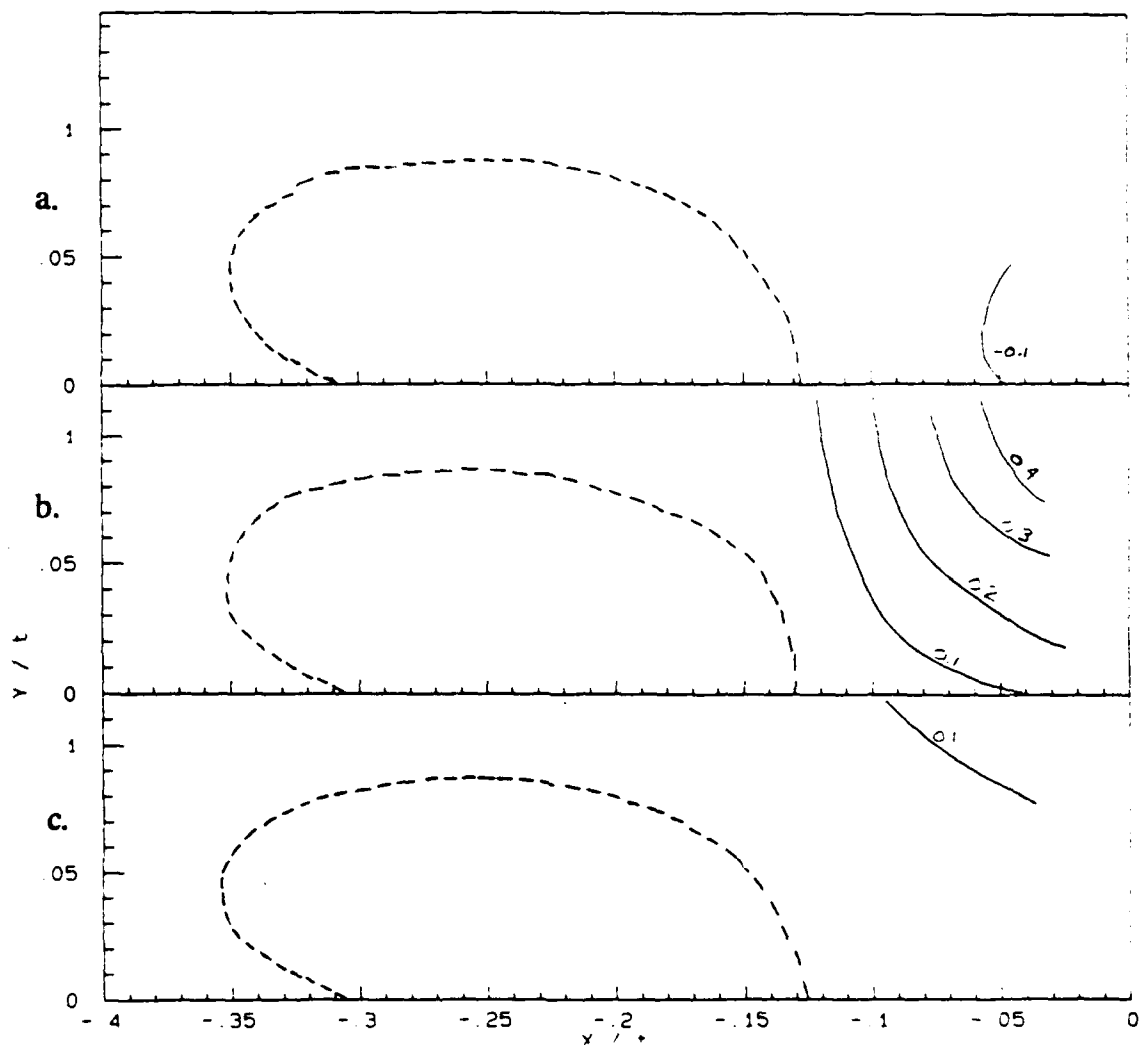
Figure 79: Contours of maximum correlation between the v component and the pressure at $x/t=0.0$ at a specified non-dimensional time lag. a. $TU_{ref}/t=-.9403$ b. $TU_{ref}/t=0$ c. $TU_{ref}/t=.9403$. Dashed line shows the composite (U and V) bimodal zone.
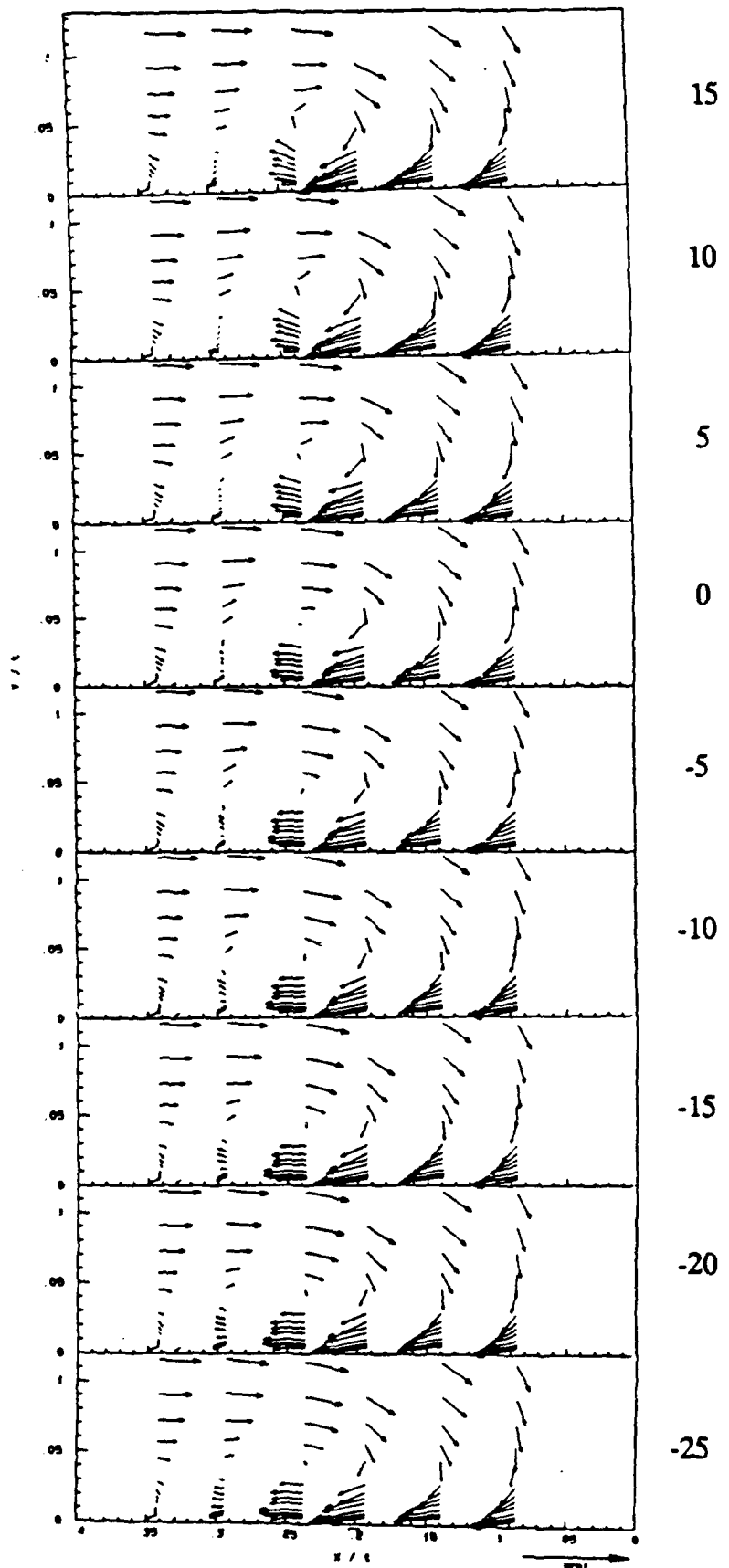
Figure 80: Vectors of velocity conditionally averaged on a pressure fall at $x/t=-.20$. Numbers indicate time before pressure switch in 10,000 ths of a second.
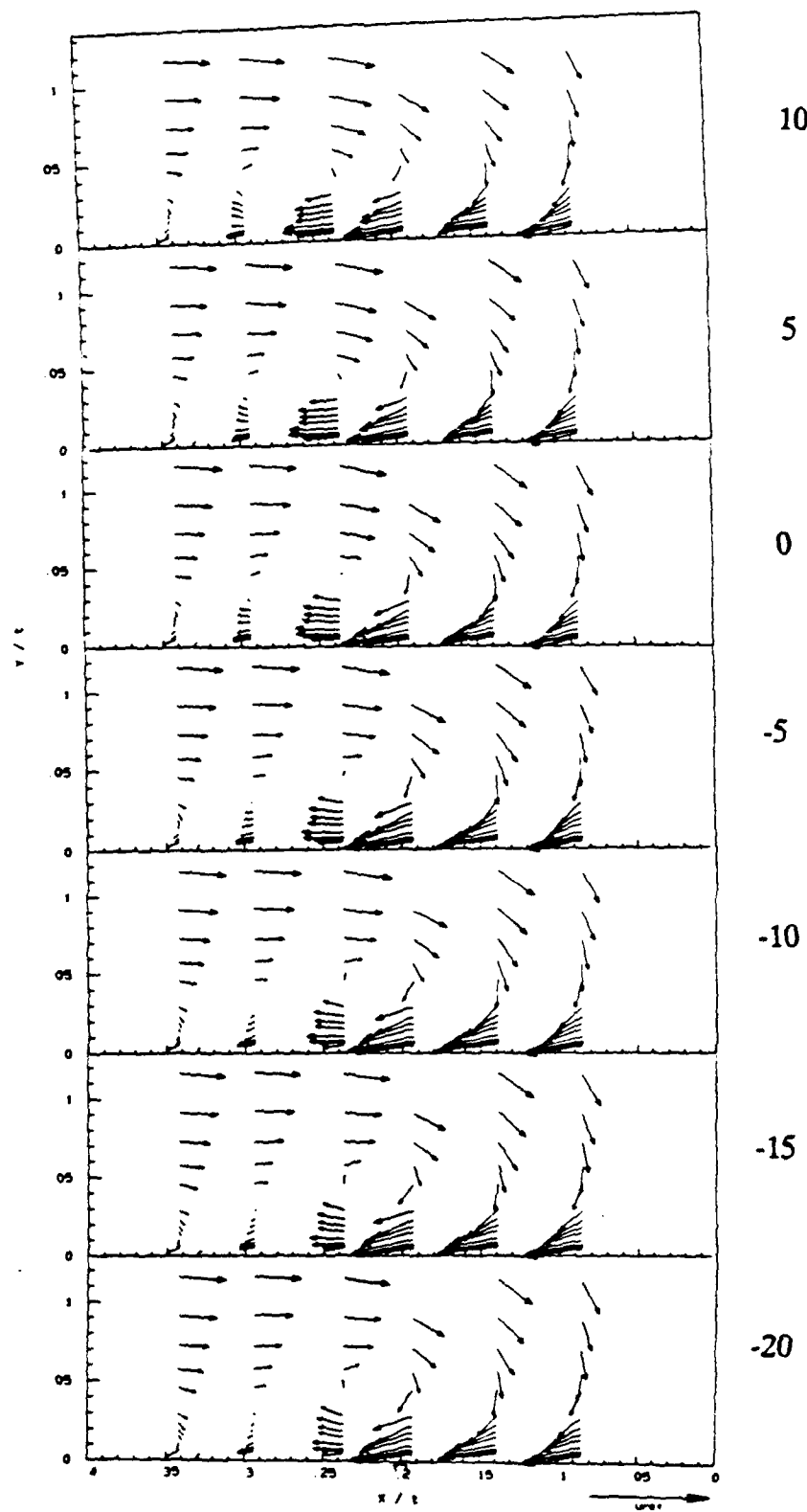
Figure 81: Vectors of velocity conditionally averaged on a pressure rise at $x/t = -.20$. Numbers indicate time before pressure switch in 10,000 ths of a second.
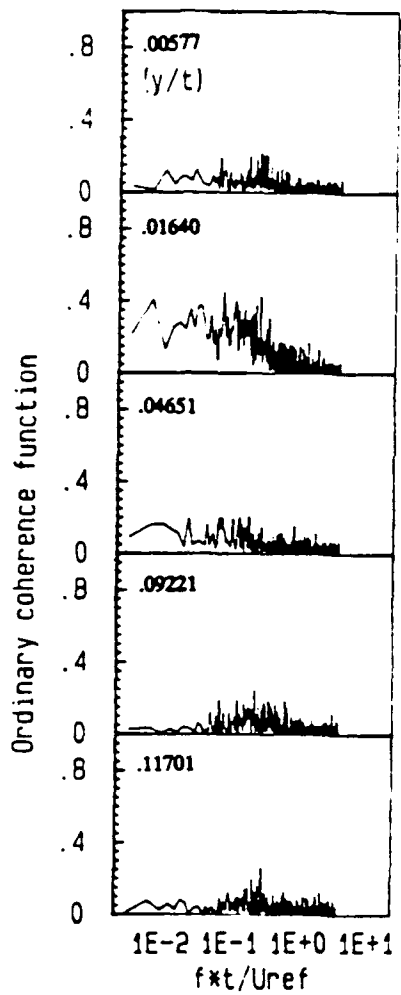
Figure 82:   Ordinary coherence function of u component of velocity at x/t=-.294 and pressure at x/t=-.20.
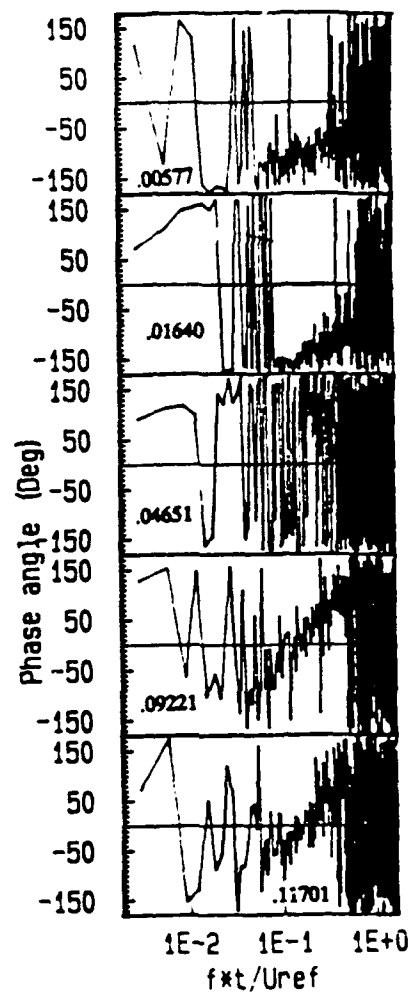
Figure 83:   Phase u component of velocity at x/t=-.284 and pressure at x/t=-.20.
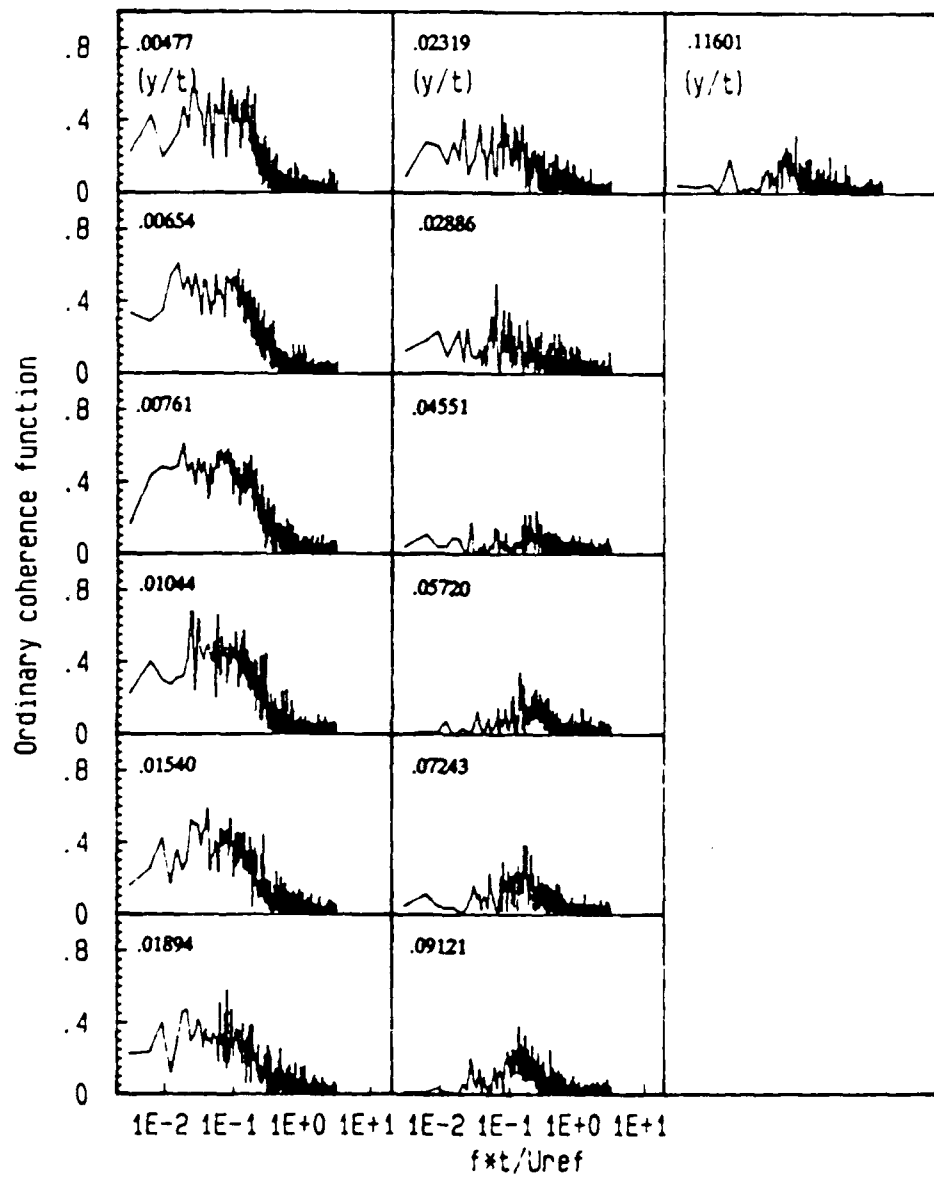
Figure 84: Ordinary coherence function of u component of velocity at x/t=-.237 and pressure at x/t=-.20.
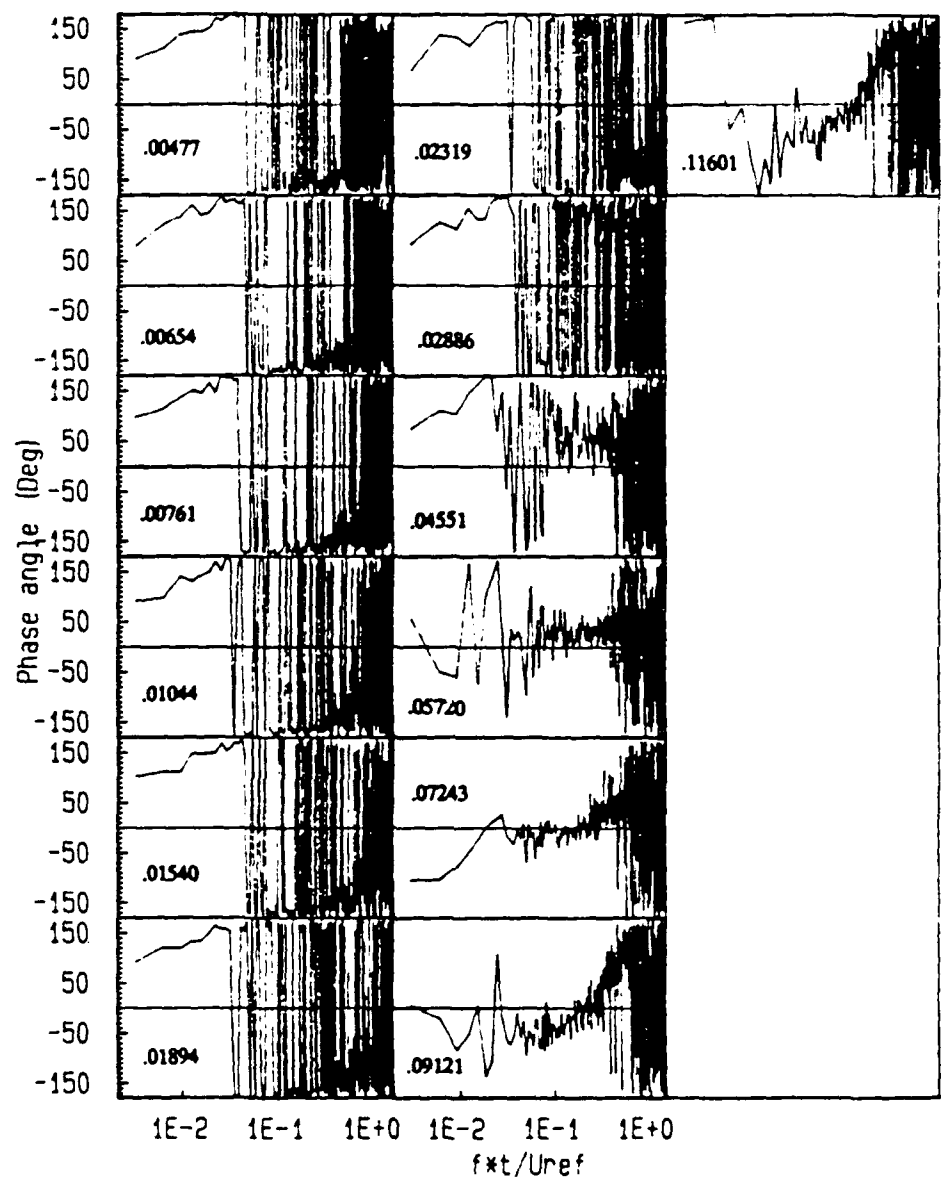
Figure 85:   Phase u component of velocity at x/t = -.237 and pressure at x/t = -.20.
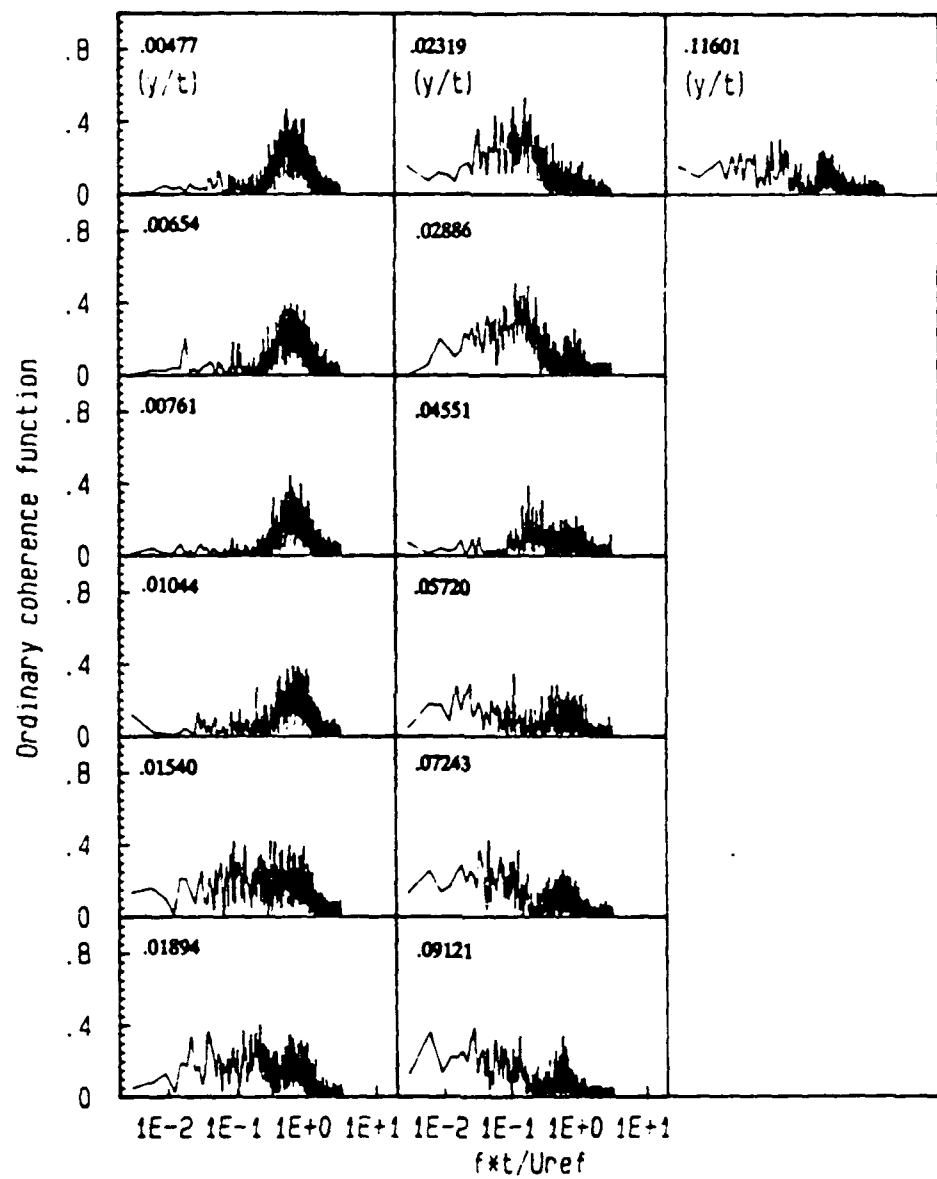
Figure 86: Ordinary coherence function of u component of velocity at x/t=-.193 and pressure at x/t=-.20.
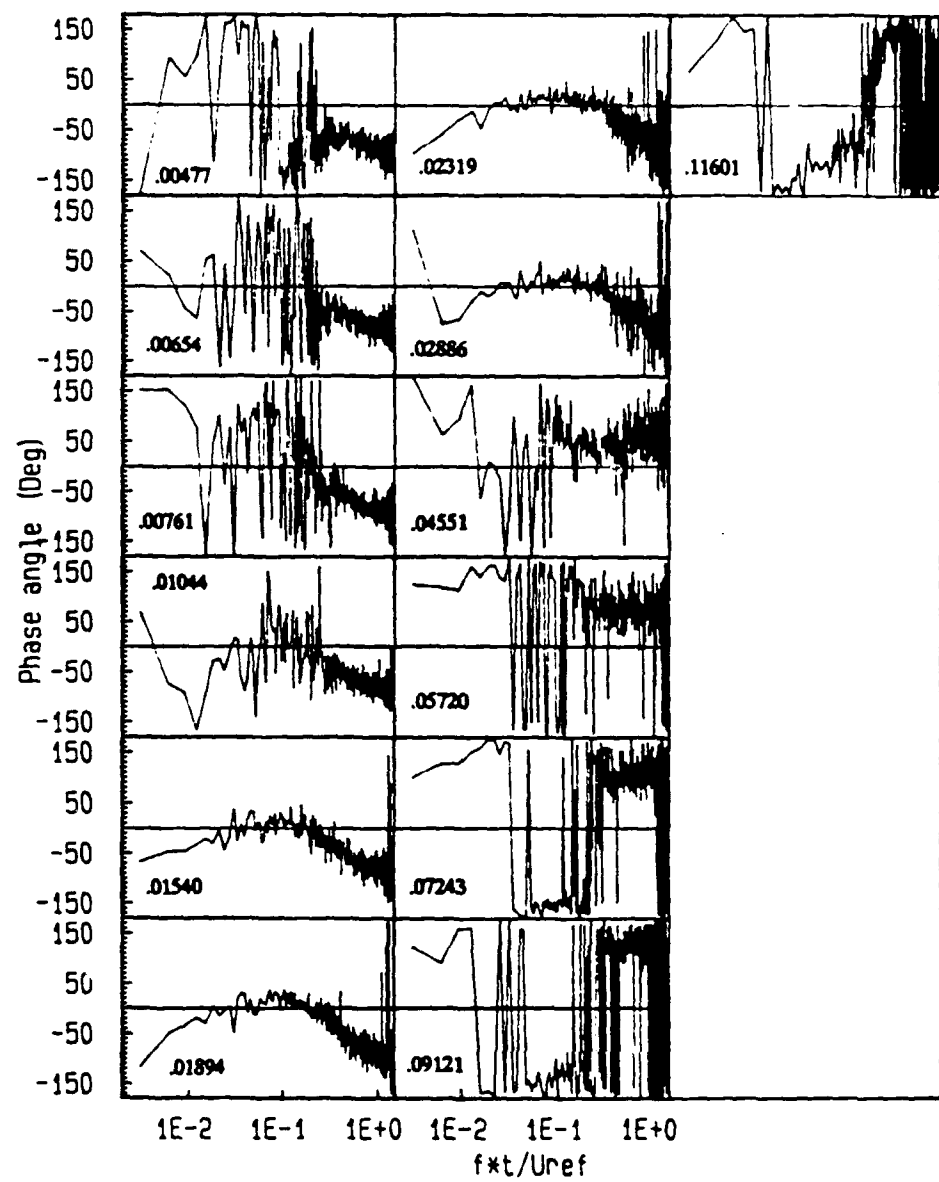
Figure 87: Phase u component of velocity at x/t=-.193 and pressure at x/t=-.20.
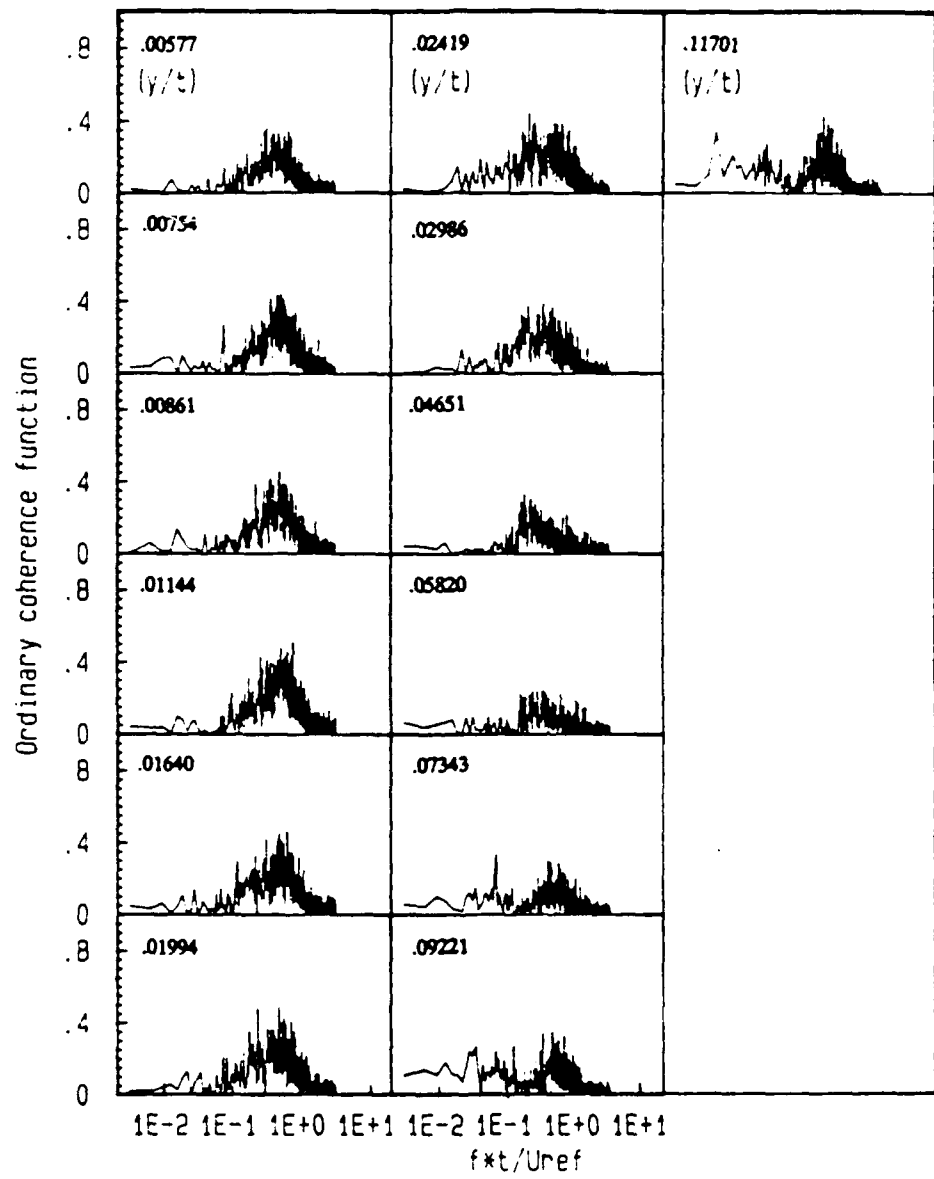
Figure 88:   Ordinary coherence function of u component of velocity at x/t=-.139 and pressure at x/t=-.20.
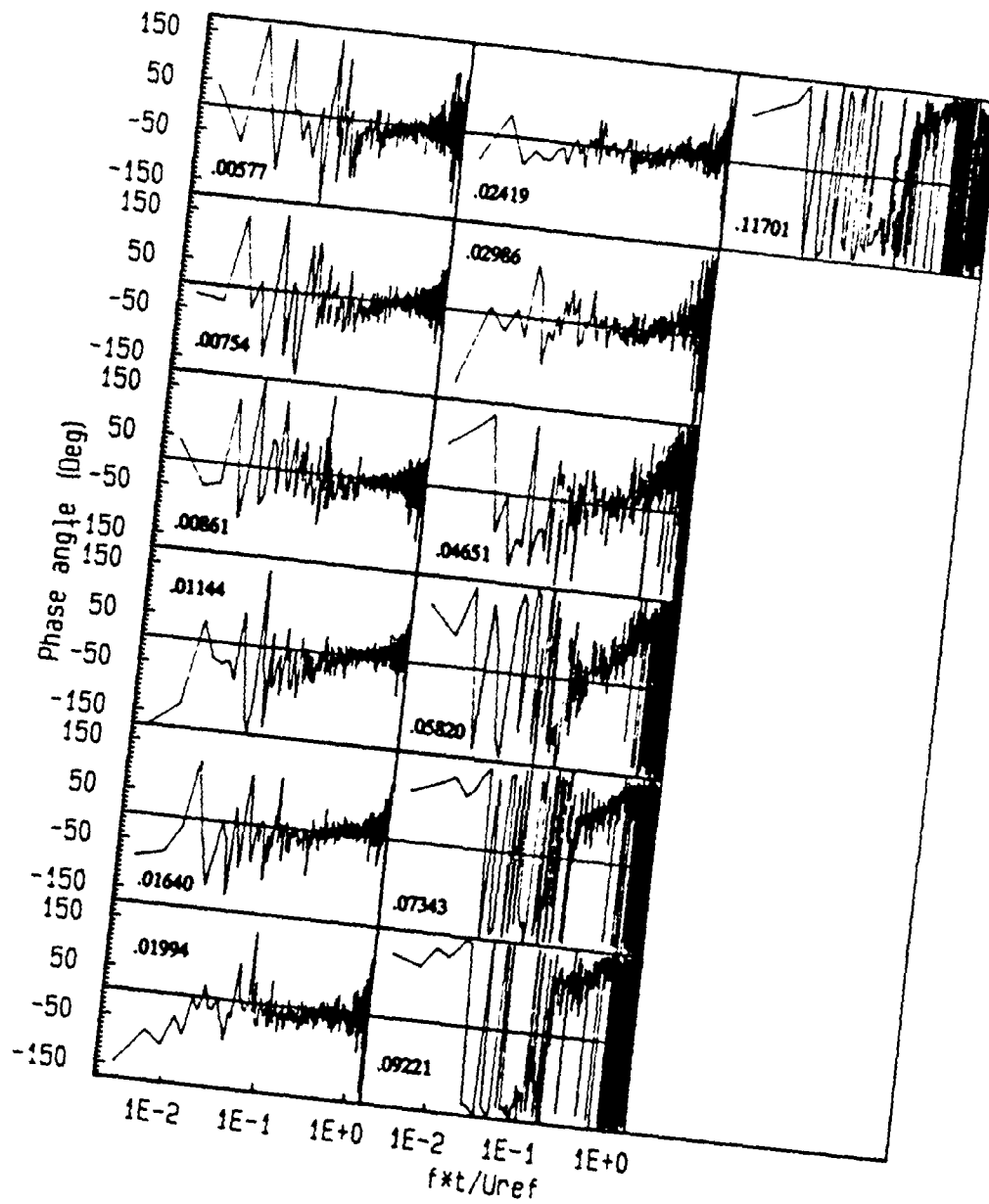
Figure 89: Phase u component of velocity at $x/t = -.139$ and pressure at $x/t = -.20$.
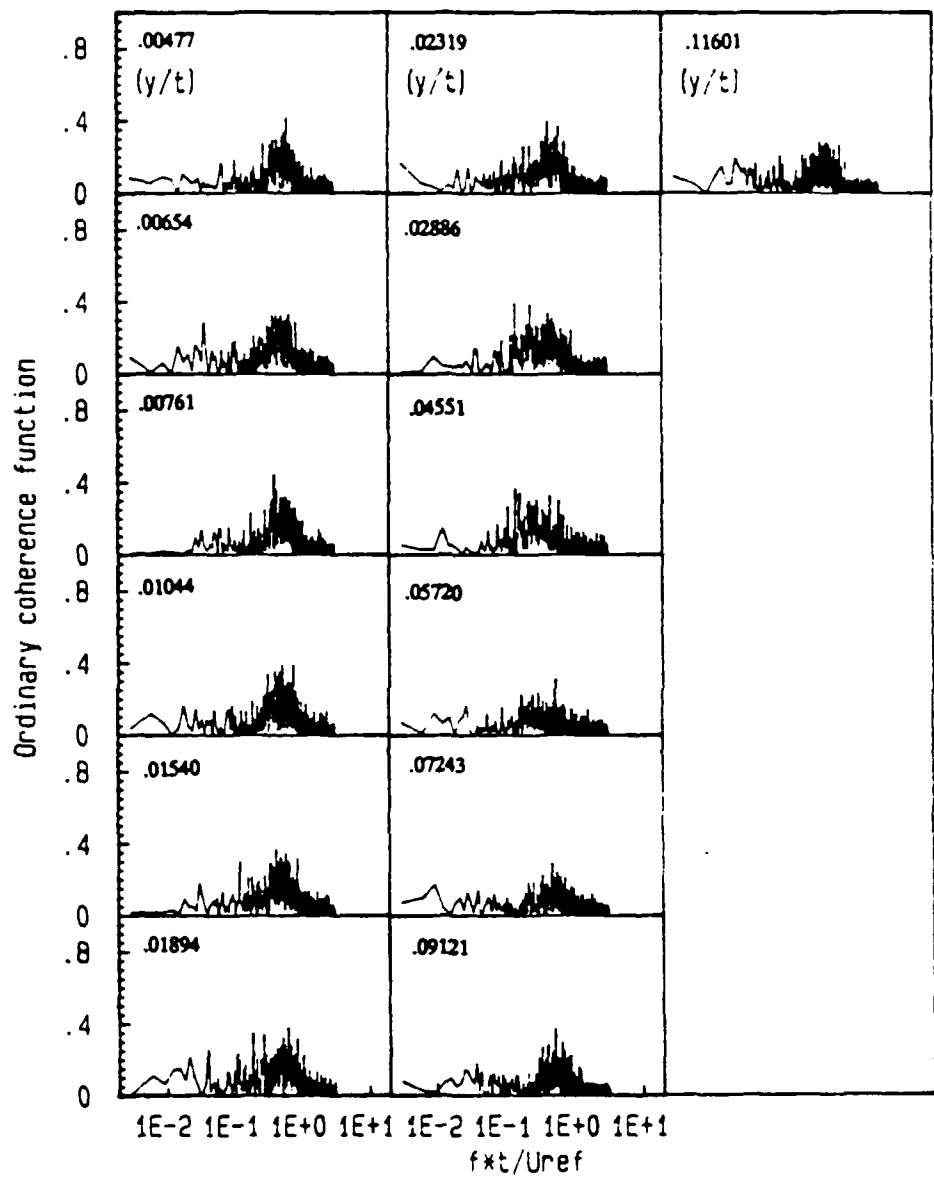
Figures

Figure 90: Ordinary coherence function of u component of velocity at x/t=-.0856 and pressure at x/t=-.20.
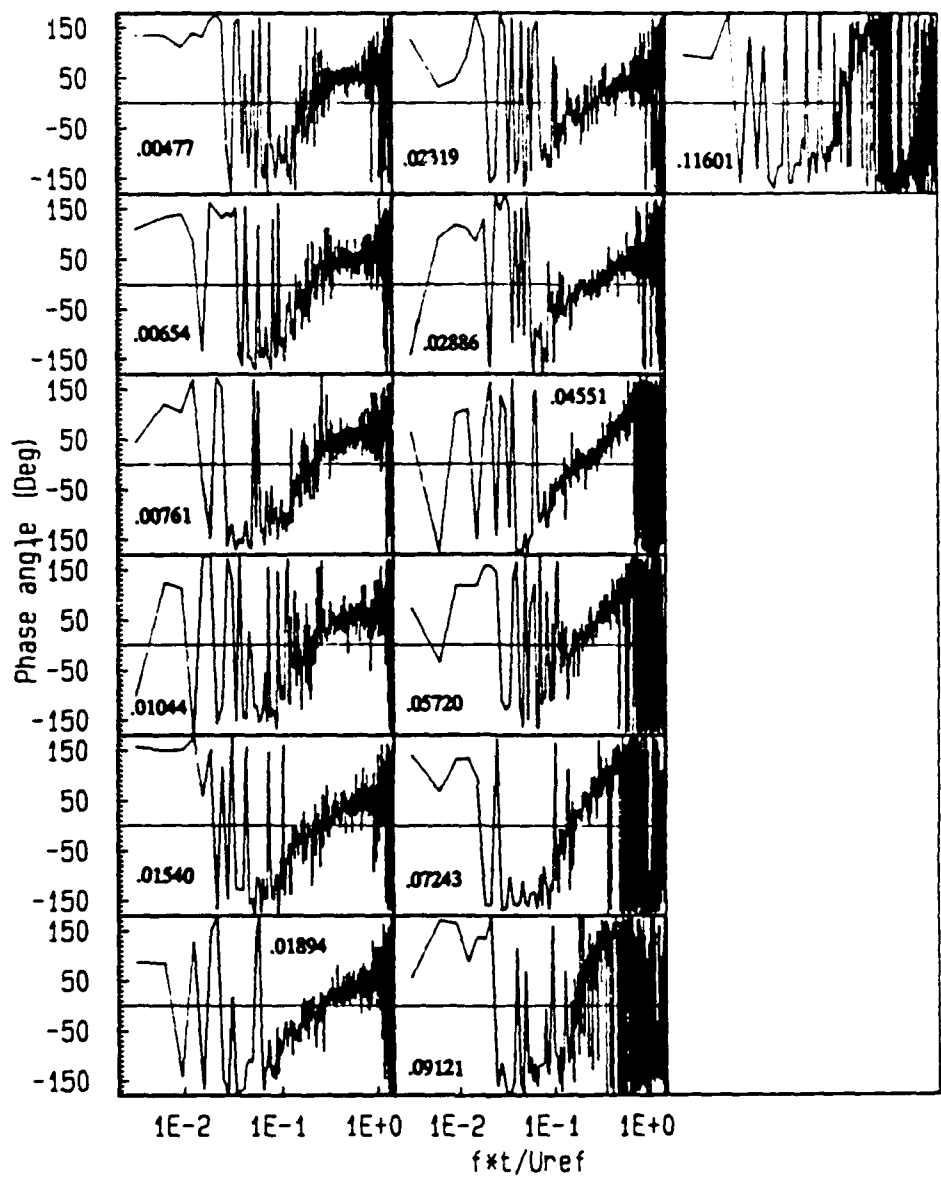
Figure 91:   Phase u component of velocity at x/t = -.0856 and pressure at x/t = -.20.
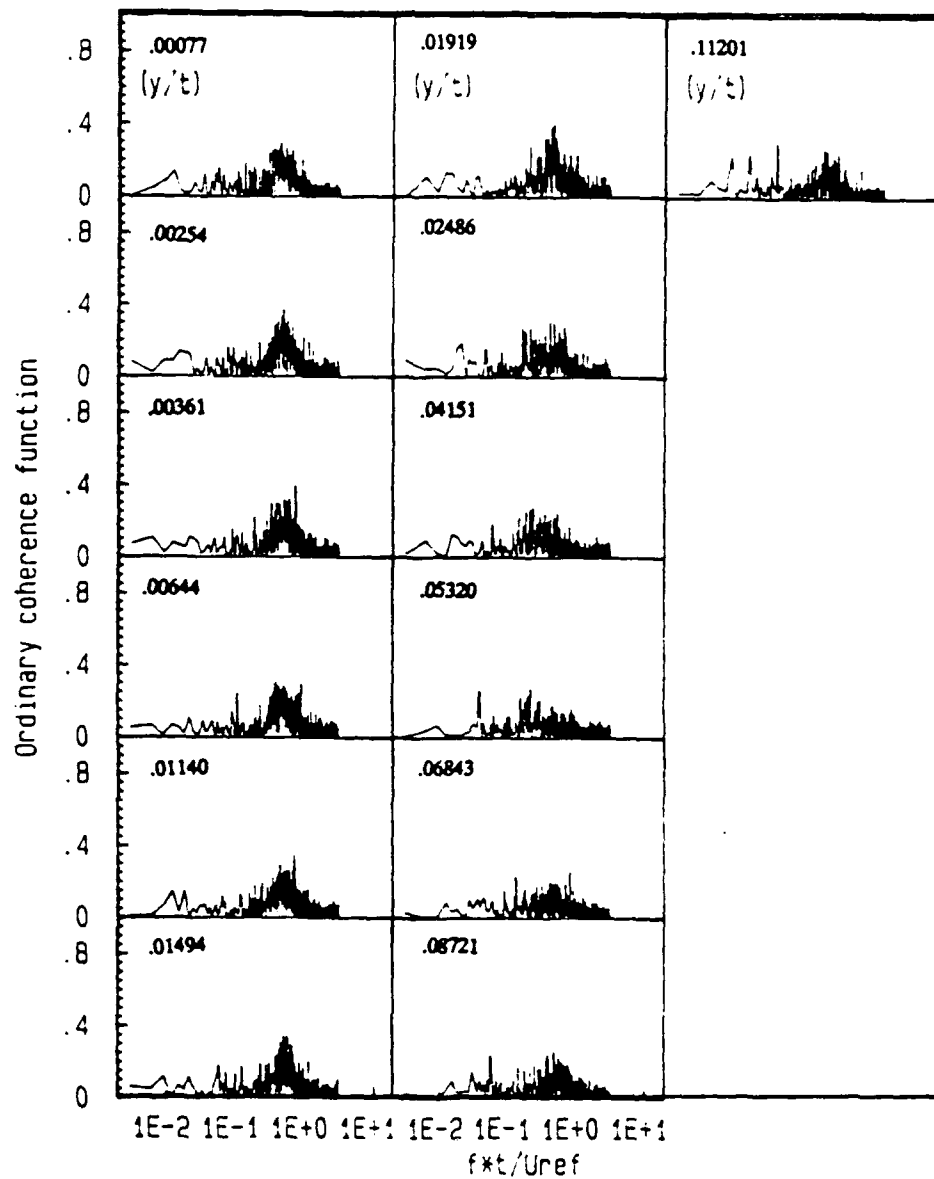
Figure 92:   Ordinary coherence function of u component of velocity at x/t=-.0421 and pressure at x/t=-.20.
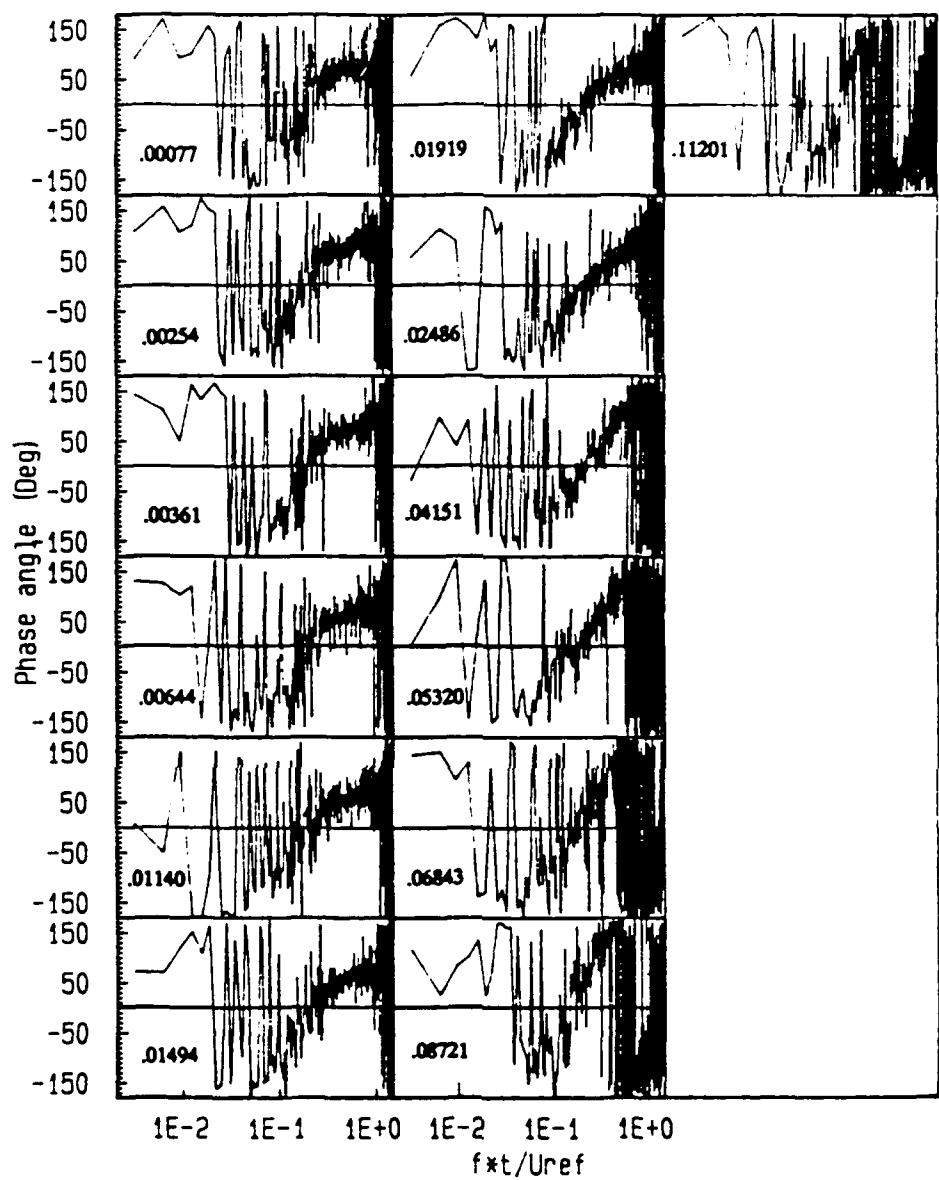
Figure 93:   Phase u component of velocity at x/t=-.0421 and pressure at x/t=-.20.
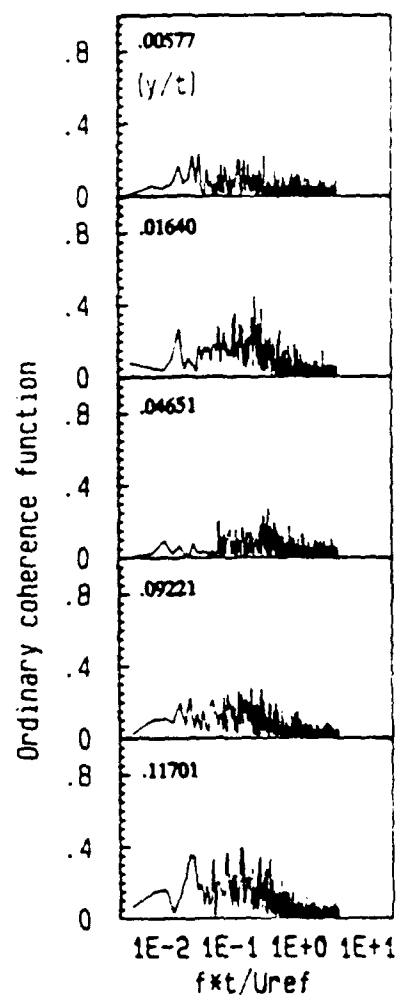
Figure 94: Ordinary coherence function of v component of velocity at x/t=-.294 and pressure at x/t=-.20.
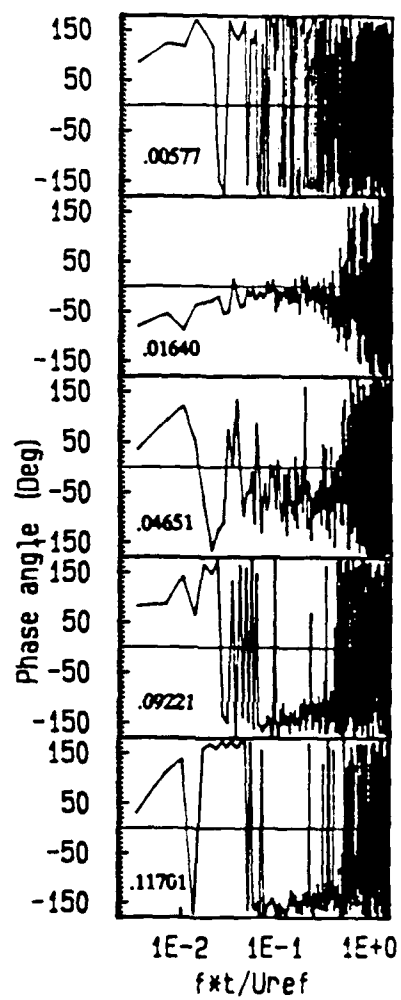
Figure 95:   Phase v component of velocity at x/t = -.294 and pressure at x/t = - .20.
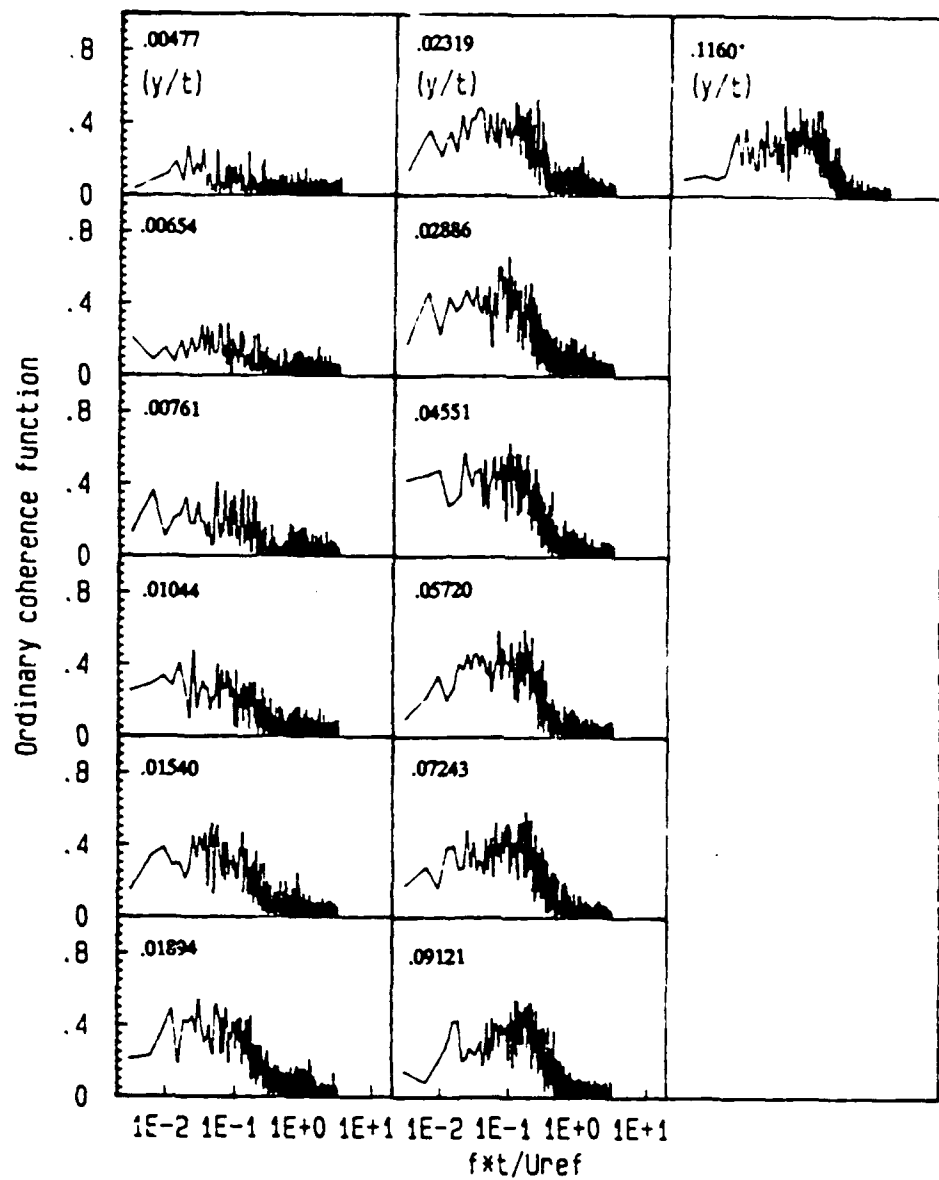
Figure 96:   Ordinary coherence function of v component of velocity at x/t=-.237 and pressure at x/t=-.20.
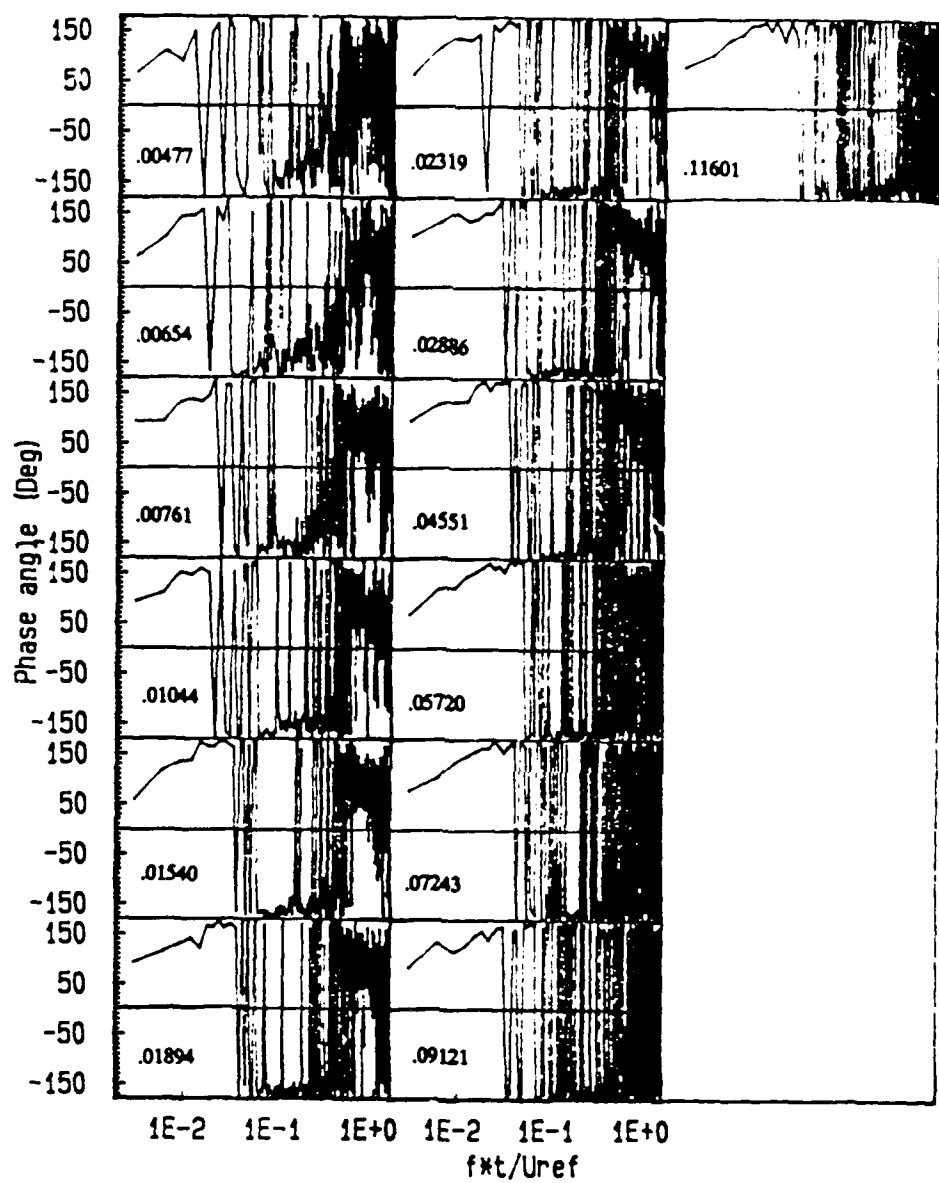
Figure 97: Phase v component of velocity at x/t = -.237 and pressure at x/t = -.20.
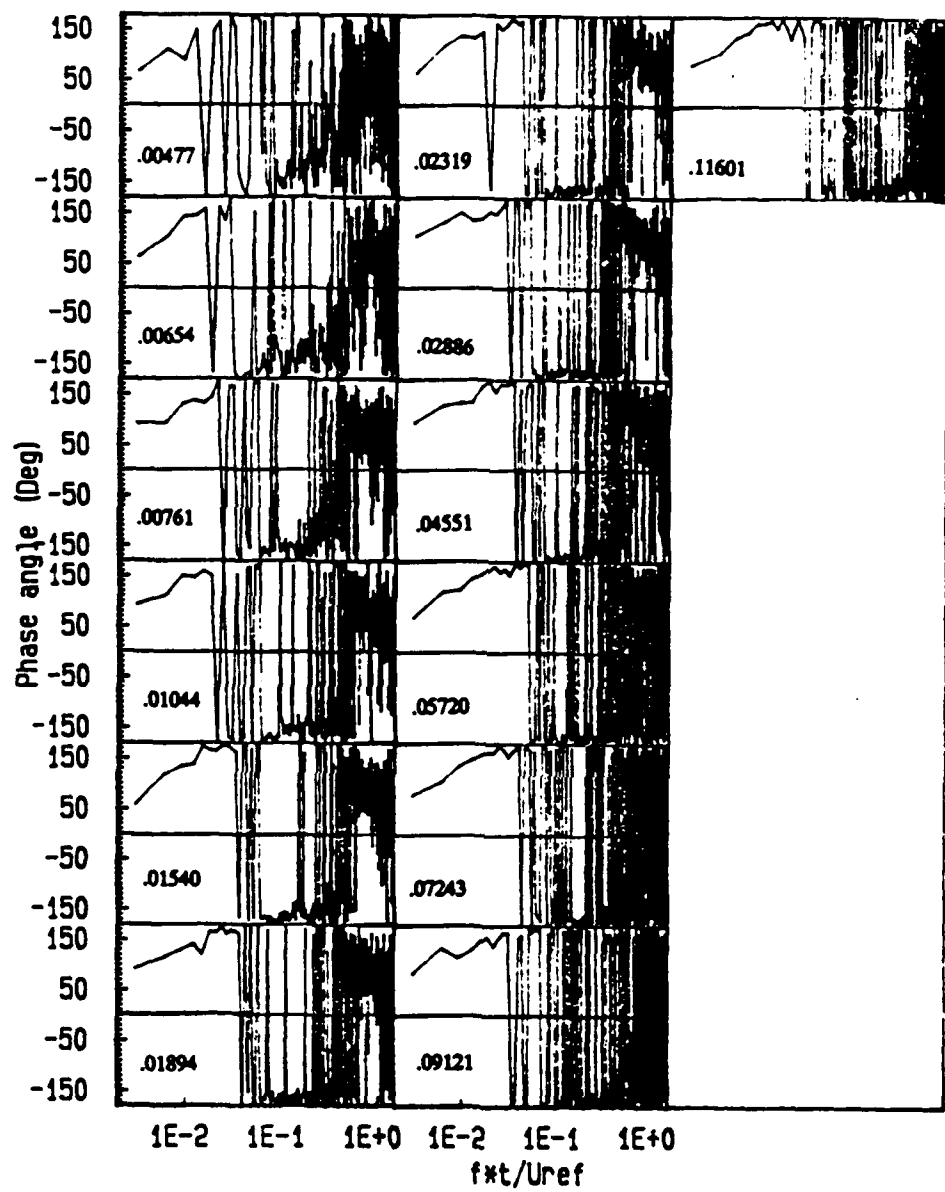
Figure 97: Phase v component of velocity at x/t=-.237 and pressure at x/t=-.20.
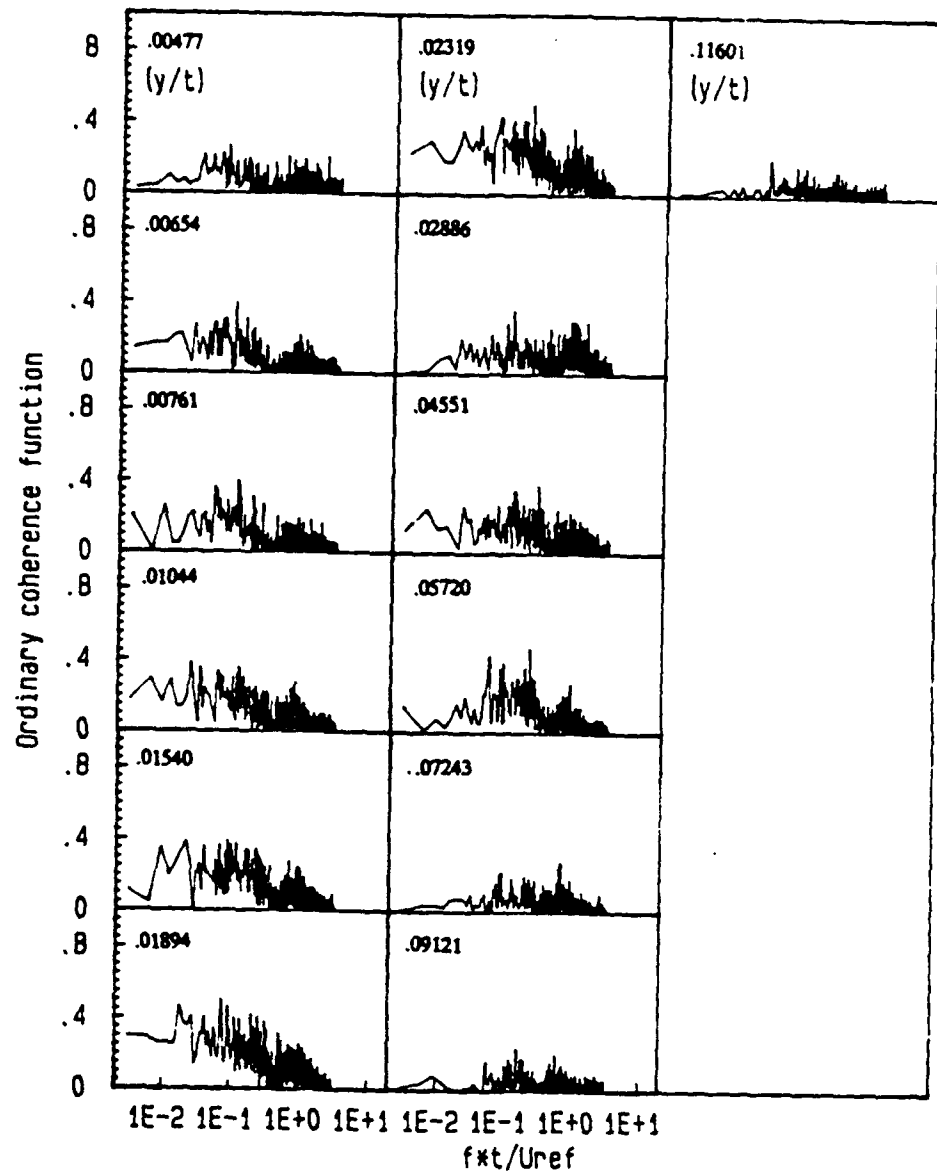
Figure 98:   Ordinary coherence function of v component of velocity at x/t=-.193 and pressure at x/t=-.20.
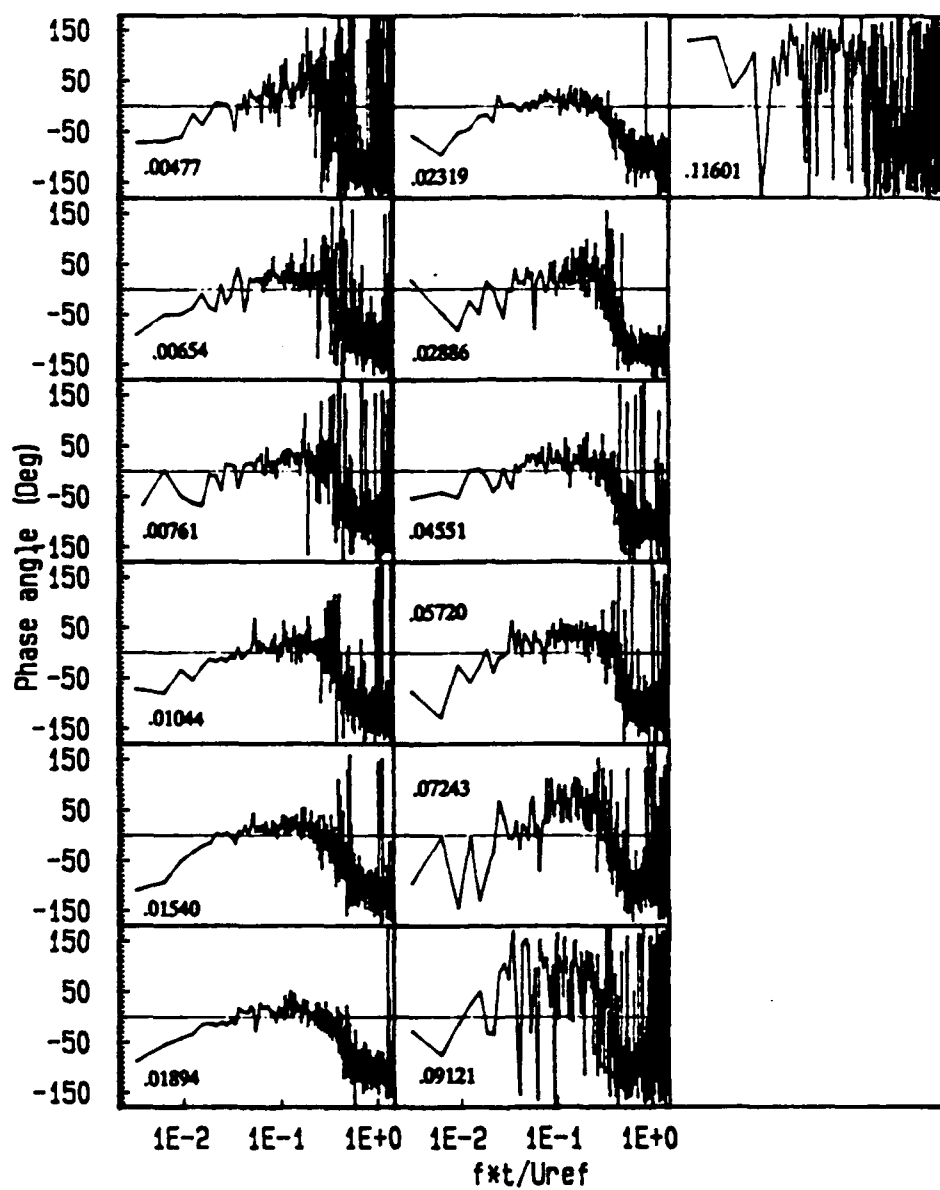
Figure 99: Phase v component of velocity at x/t=-.193 and pressure at x/t=-.20.
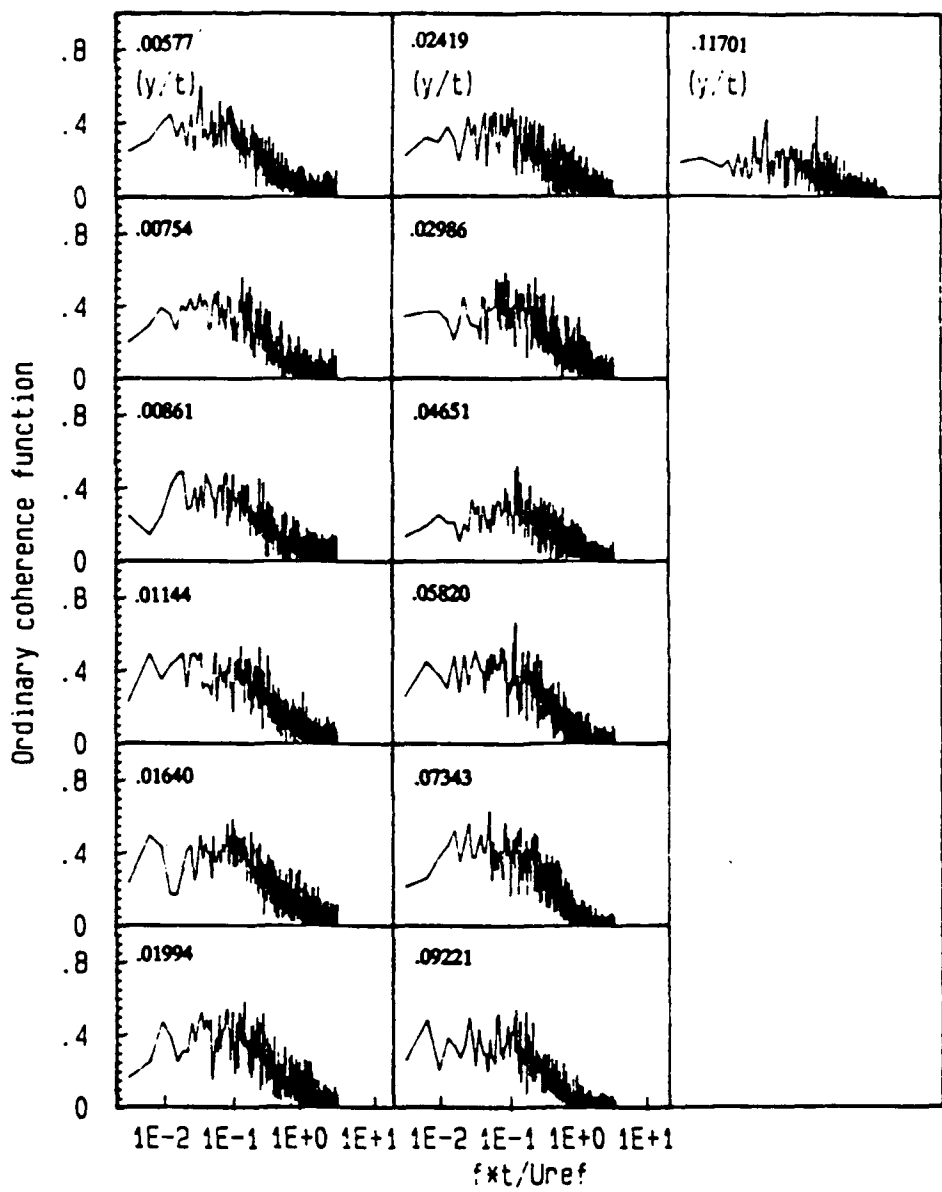
Figure 100:   Ordinary coherence function of v component of velocity at x/t=-.139 and pressure at x/t=-.20.
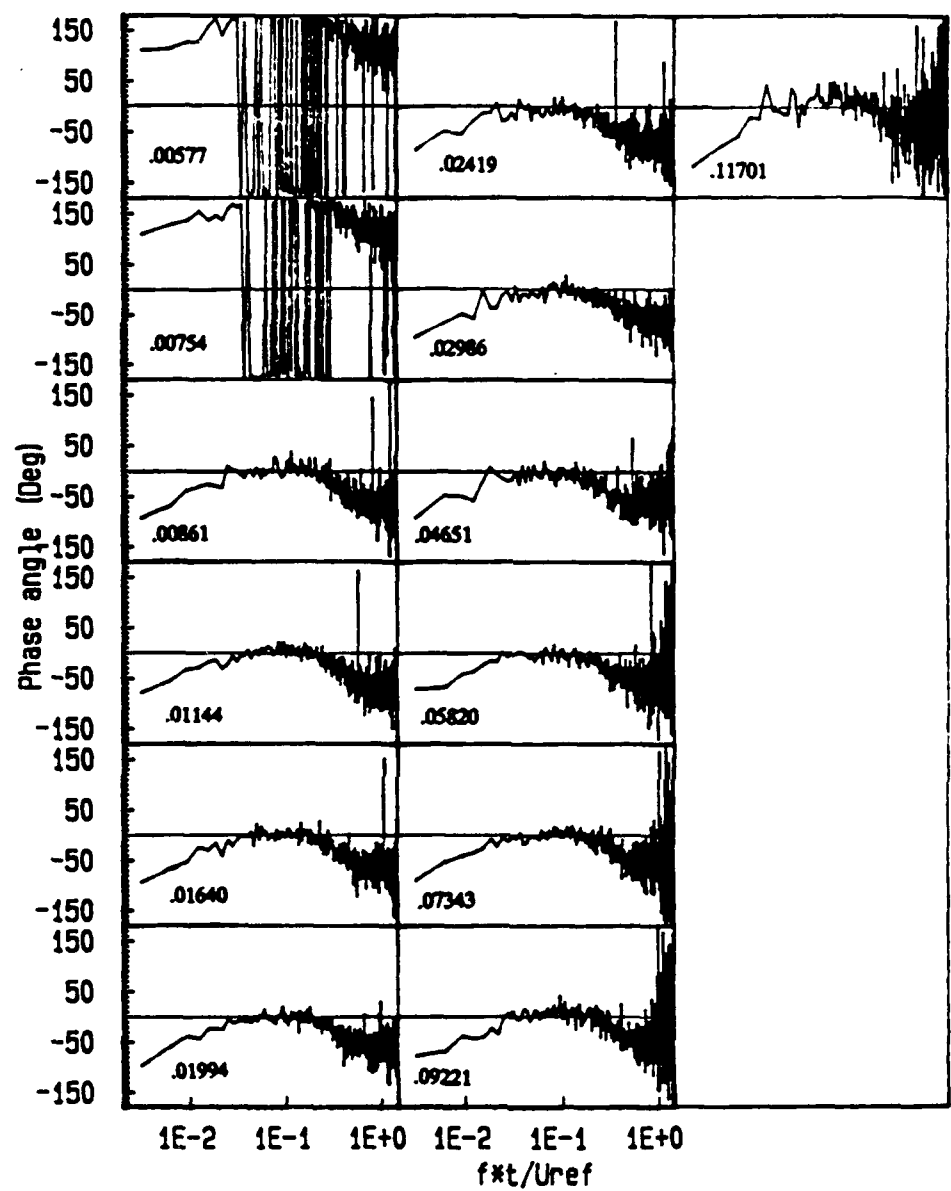
Figures

Figure 101:   Phase v component of velocity at x/t=-.139 and pressure at x/t=-.20.
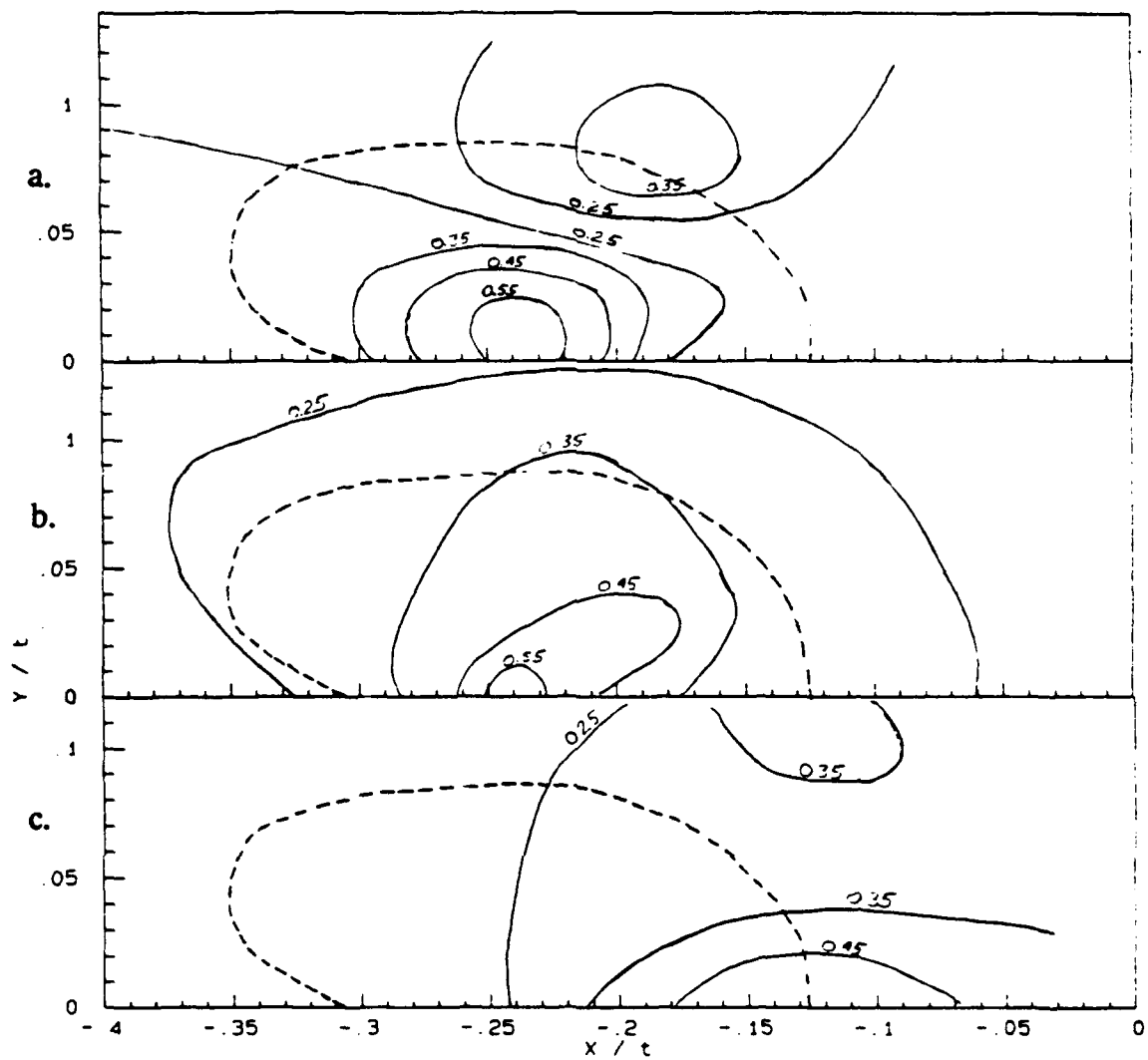
Figure 102:   Contours of the maximum u ordinary coherence function with the pressure fluctuations at $x/t = -.20$ in the frequency range a. $ft/U_{ref} = 6 \times 10^{-3}$ to $ft/U_{ref} = 0.5$, b. $ft/U_{ref} = 7 \times 10^{-2}$ to $ft/U_{ref} = 0.3$, and c. $ft/U_{ref} = 0.4$ to $ft/U_{ref} = 0.9$. Dashed line indicates the composite (U and V) bimodal zone.
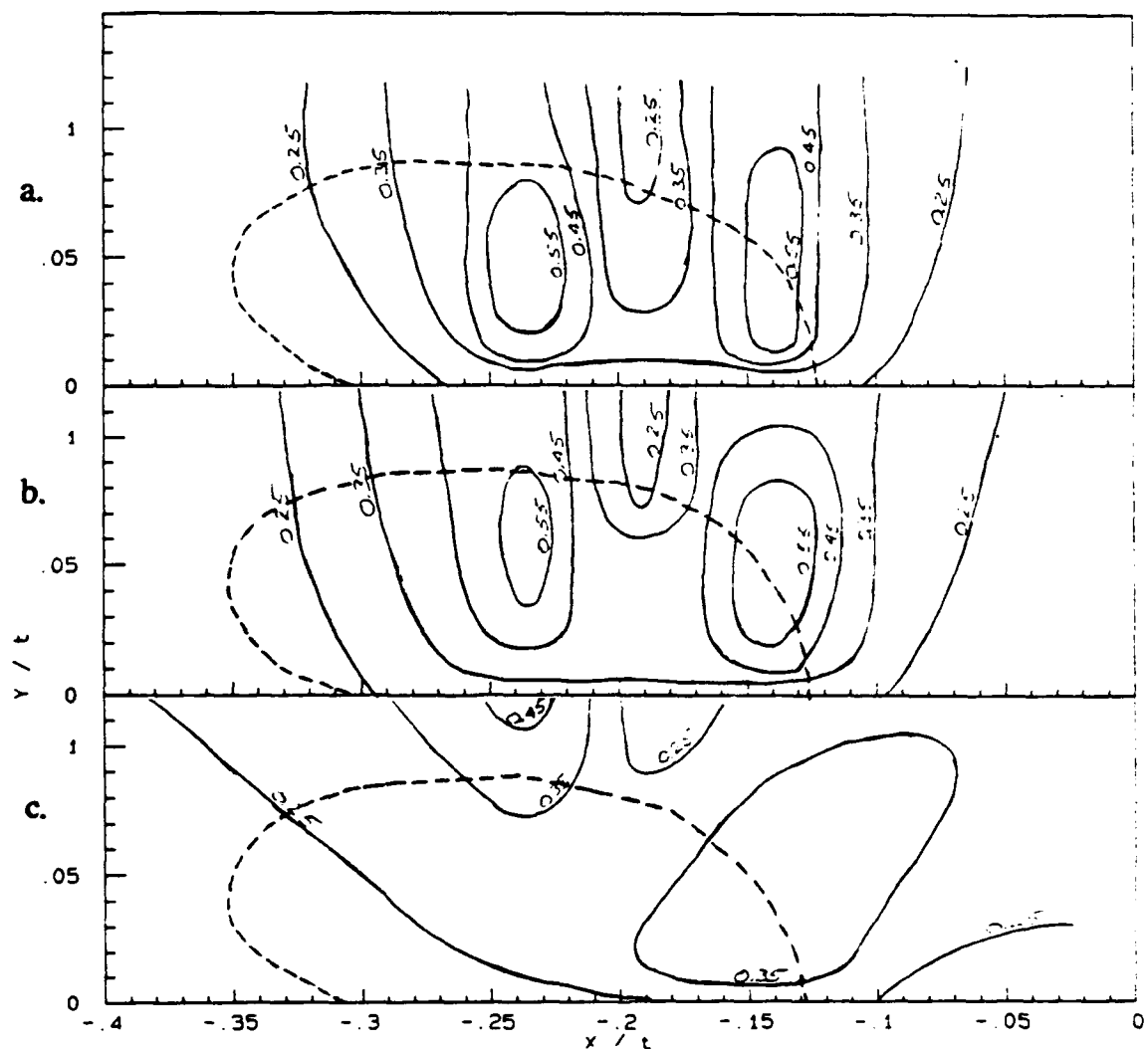
Figure 103:   Contours of the maximum v ordinary coherence function with the pressure fluctuations at $x/t = -.20$ in the frequency range a. $ft/U_{ref} = 6 \times 10^{-3}$ to $ft/U_{ref} = 0.5$, b. $ft/U_{ref} = 7 \times 10^{-2}$ to $ft/U_{ref} = 0.3$, and c. $ft/U_{ref} = 0.4$ to $ft/U_{ref} = 0.9$. Dashed line indicates the composite (U and V) bimodal zone.
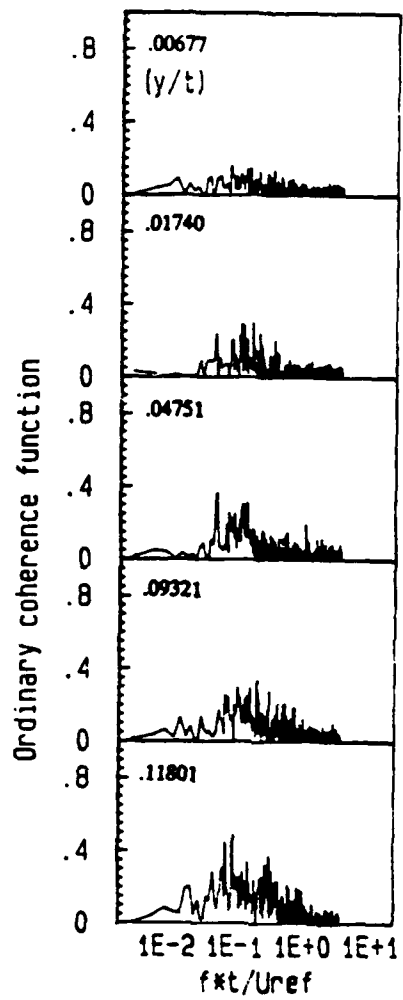
Figure 104: Ordinary coherence function of u component of velocity at x/t=-.391 and pressure at x/t=0.0.
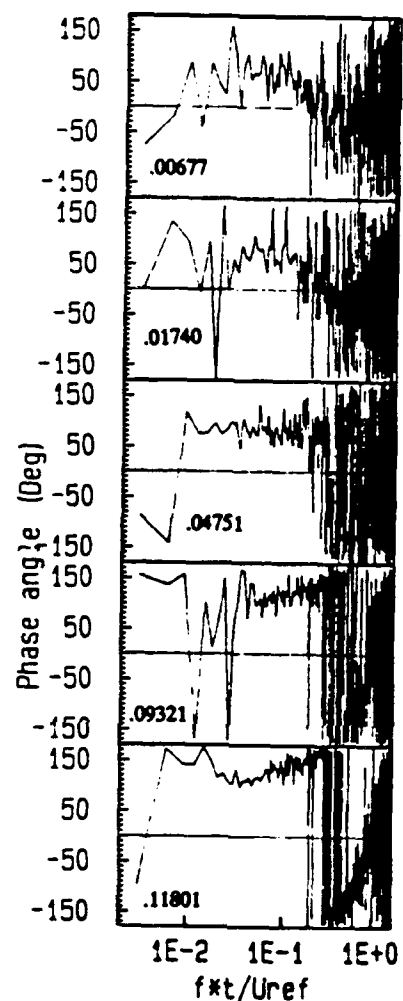
Figure 105:   Phase u component of velocity at x/t = -.391 and pressure at x/t = 0.0.
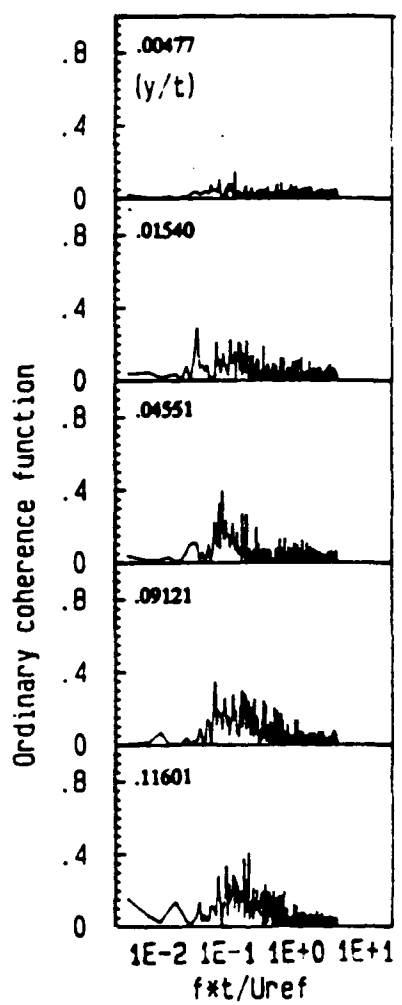
Figure 106: Ordinary coherence function of u component of velocity at x/t=-.342 and pressure at x/t=0.0.
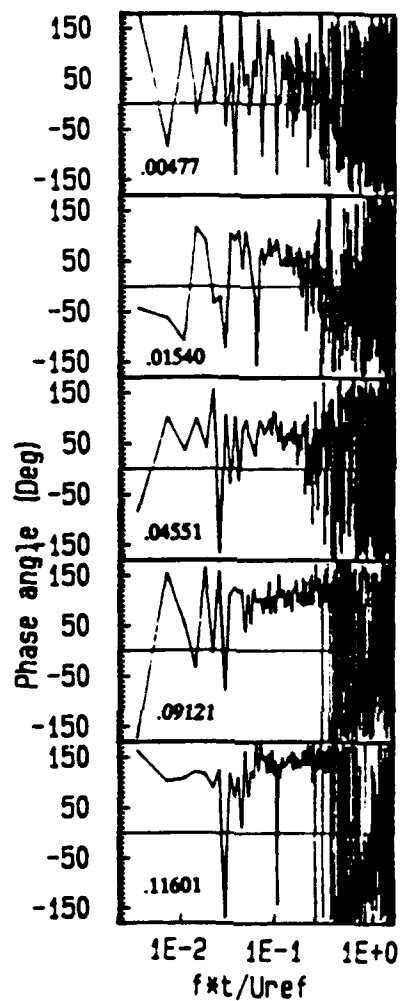
Figure 107:   Phase u component of velocity at x/t = -.342 and pressure at x/t = 0.0.
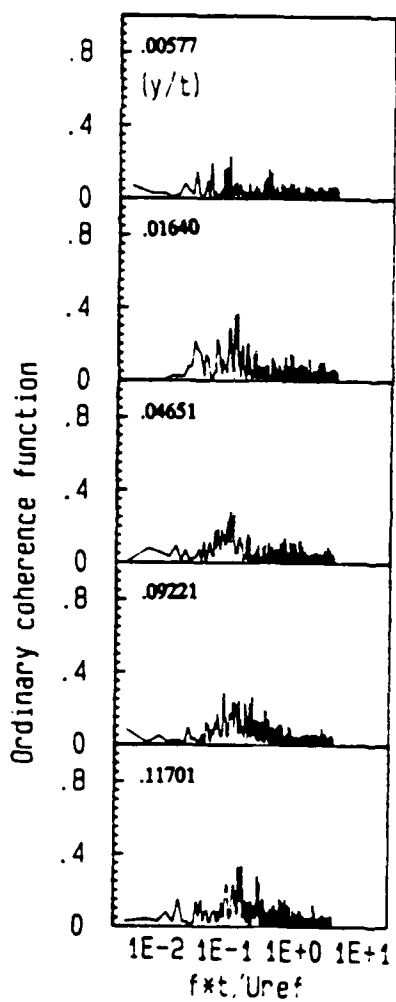
Figure 108:   Ordinary coherence function of u component of velocity at x/t=-.294 and pressure at x/t=0.0.
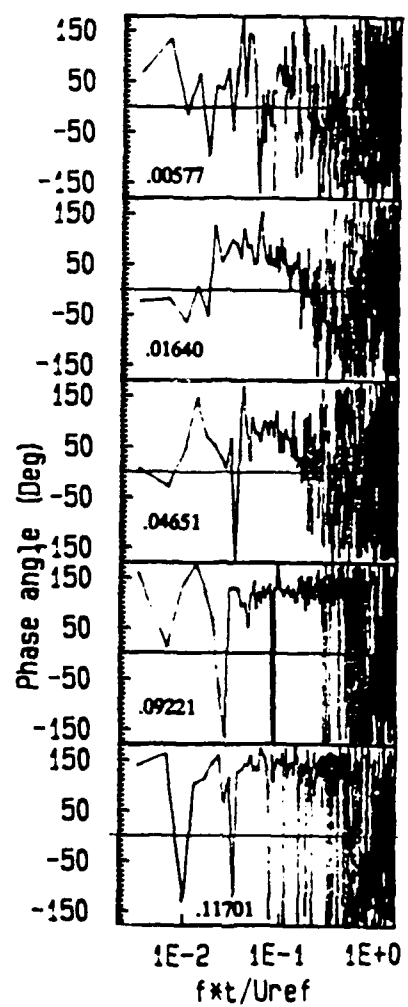
Figure 109:   Phase u component of velocity at x/t = -.284 and pressure at x/t = 0.0.
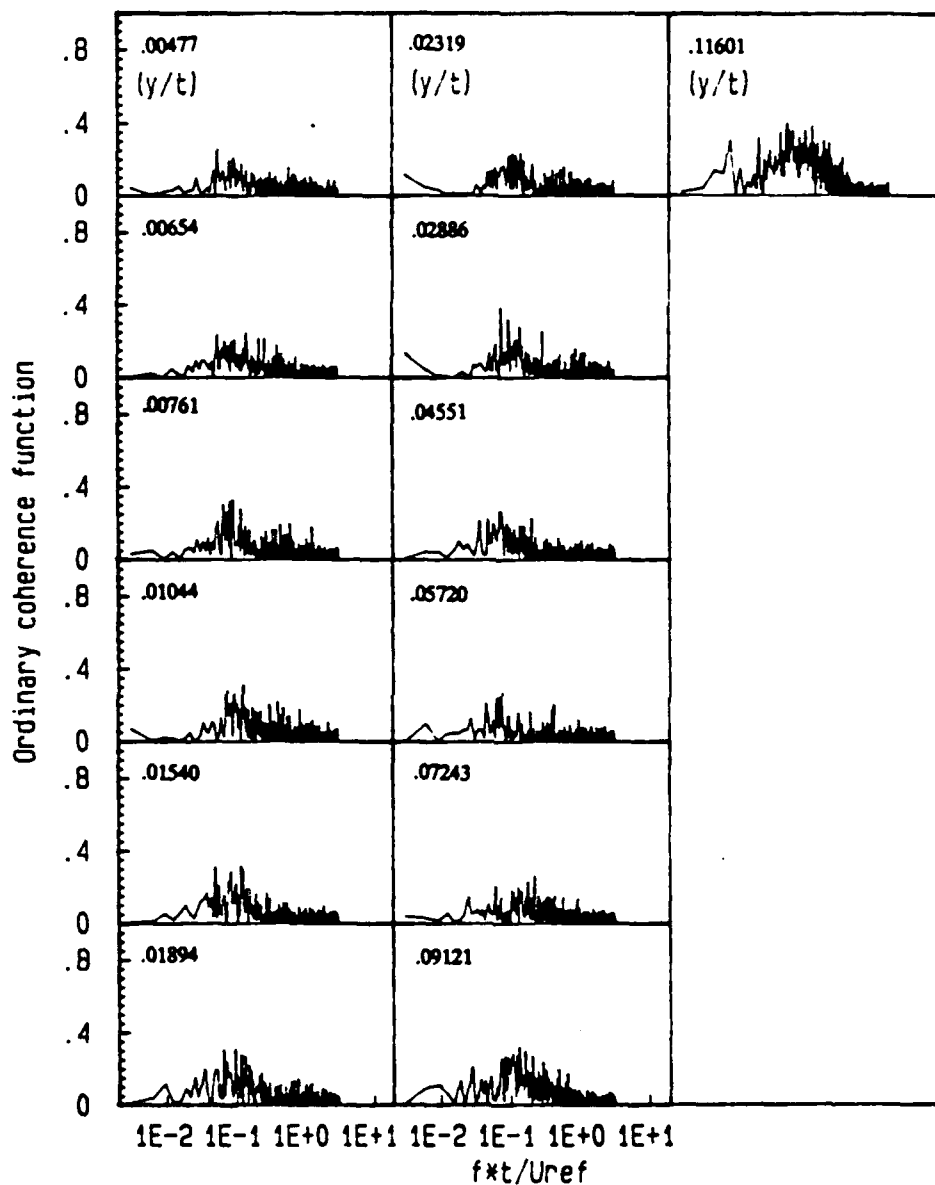
Figure 110:   Ordinary coherence function of u component of velocity at $x/t = -.237$ and pressure at $x/t = 0.0$.
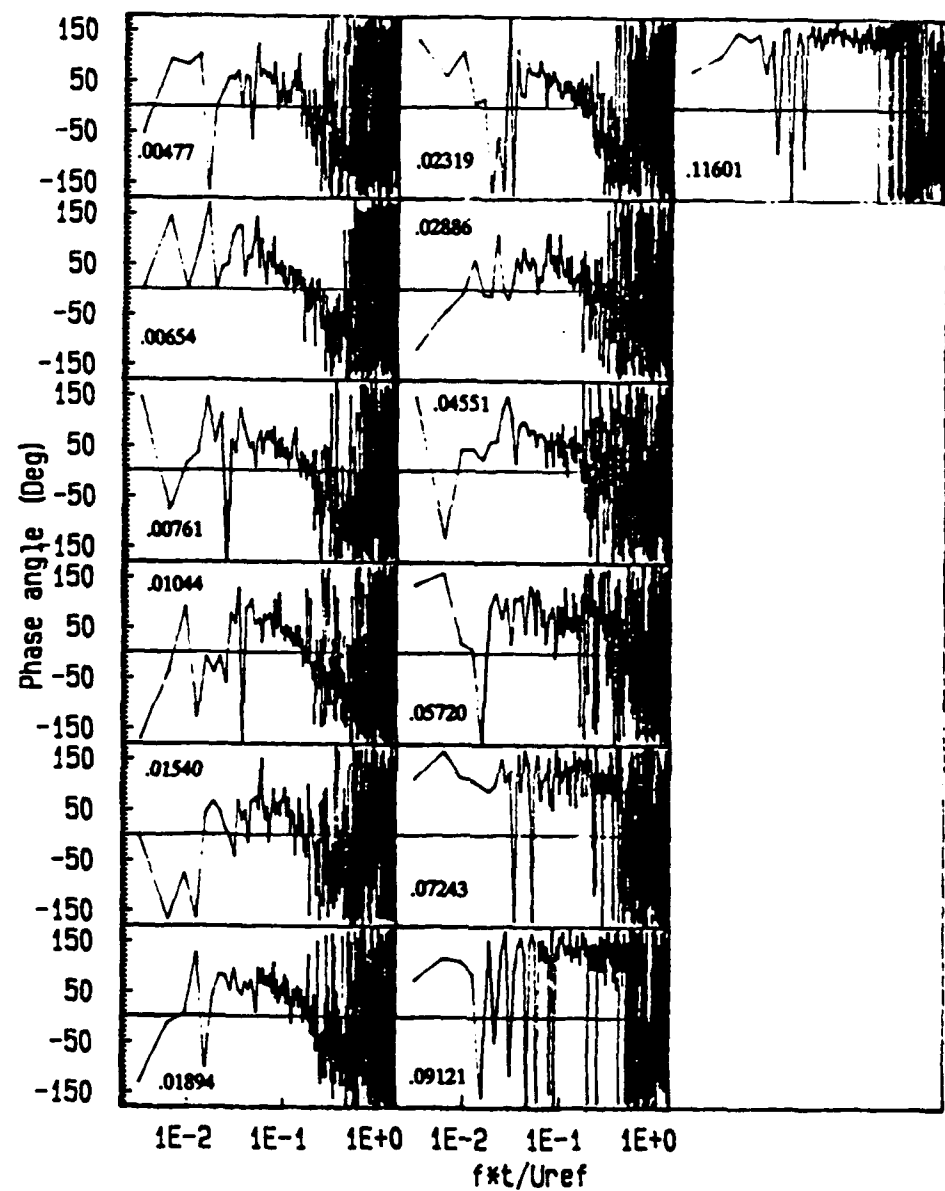
Figure 111: Phase u component of velocity at x/t = -.237 and pressure at x/t = 0.0.
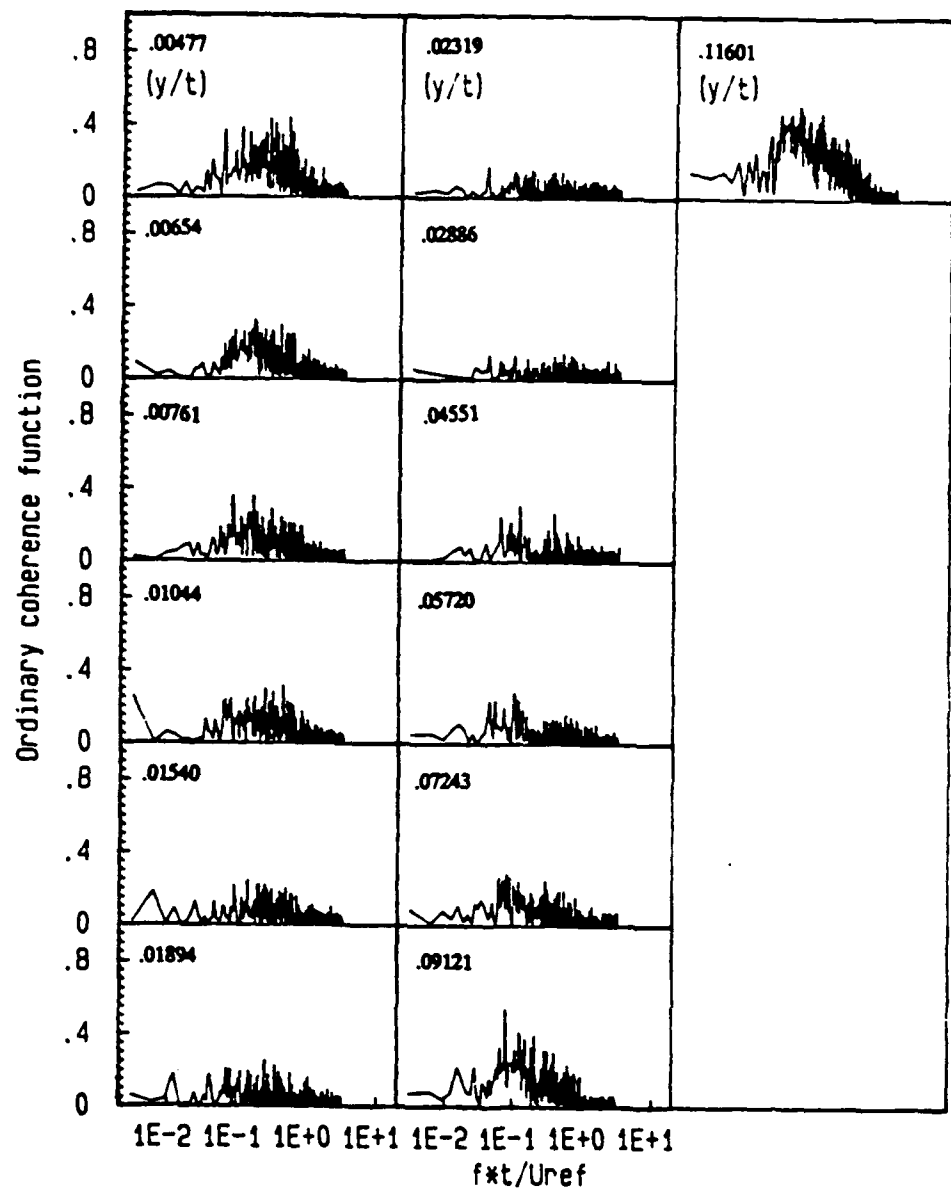
Figure 112: Ordinary coherence function of u component of velocity at x/t=-.193 and pressure at x/t=0.0.
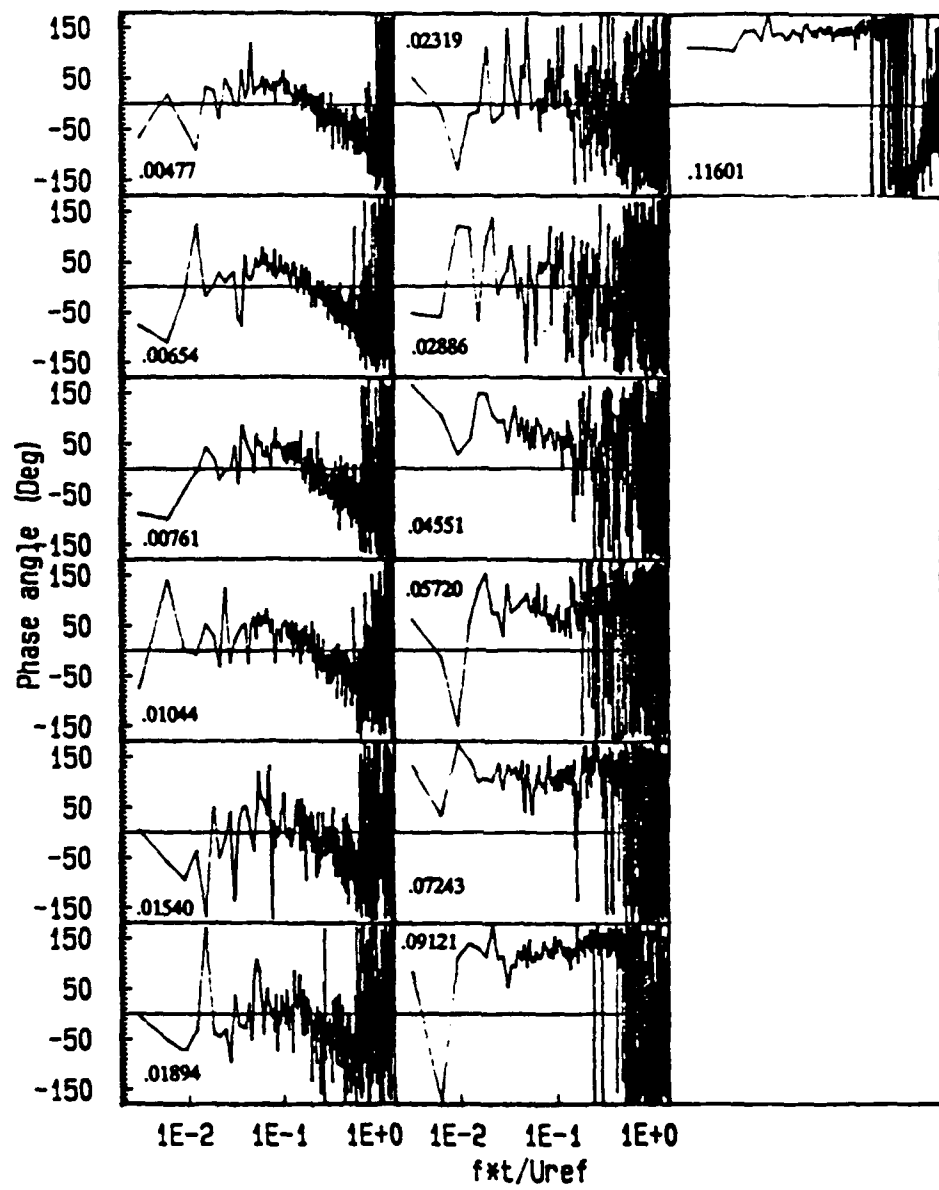
Figure 113:   Phase u component of velocity at x/t = -.193 and pressure at x/t = 0.0.
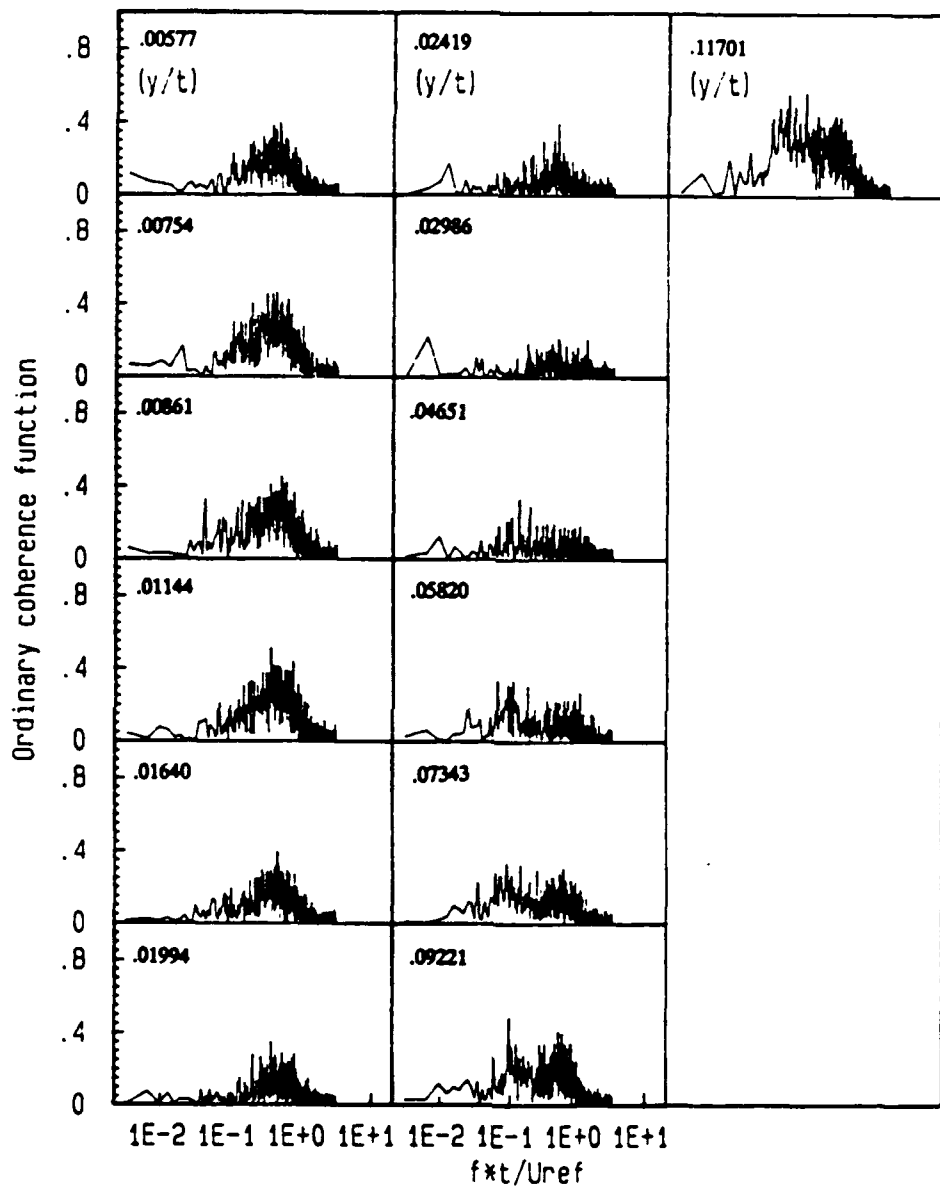
Figure 114:   Ordinary coherence function of u component of velocity at x/t=-
.139 and pressure at x/t=0.0.
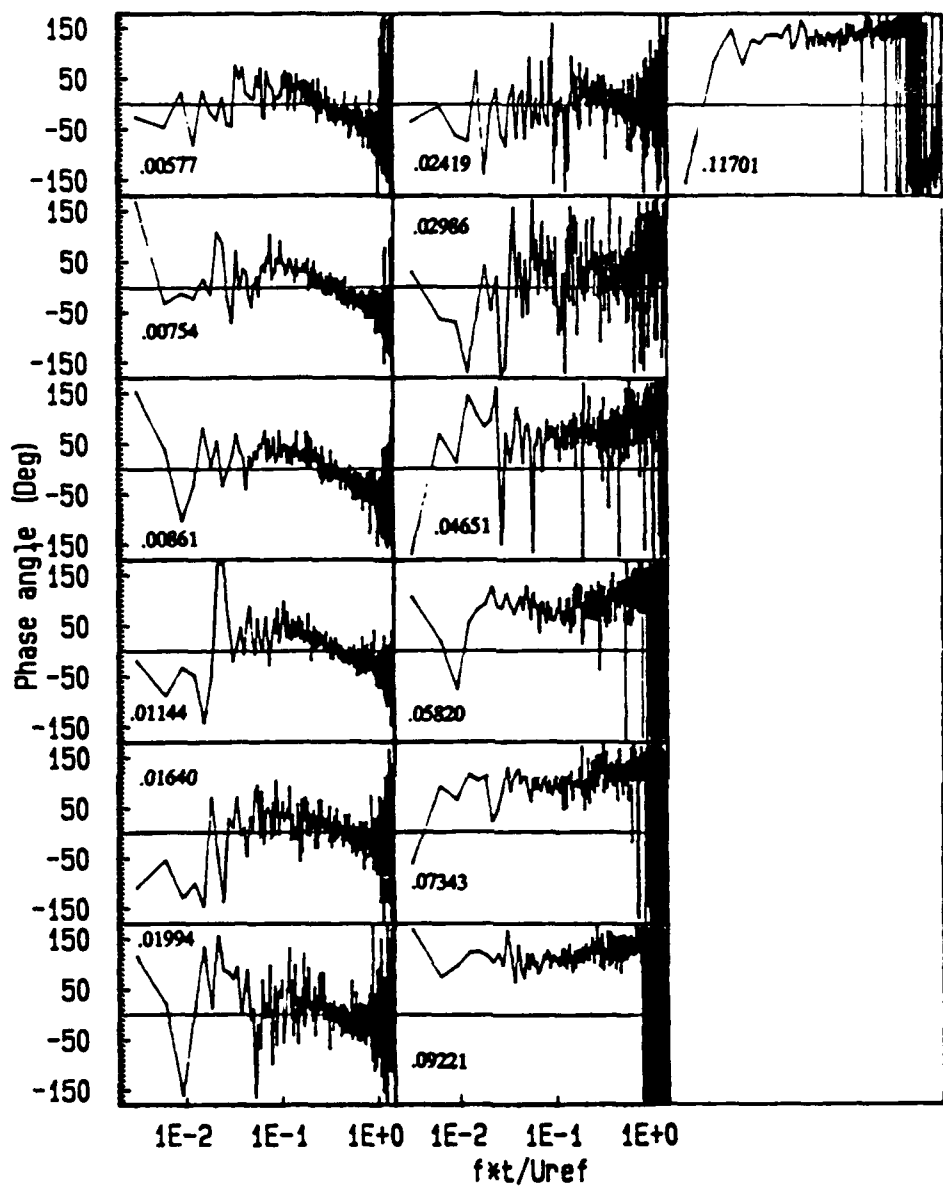
Figure 115:   Phase u component of velocity at x/t = -.139 and pressure at x/t = 0.0.
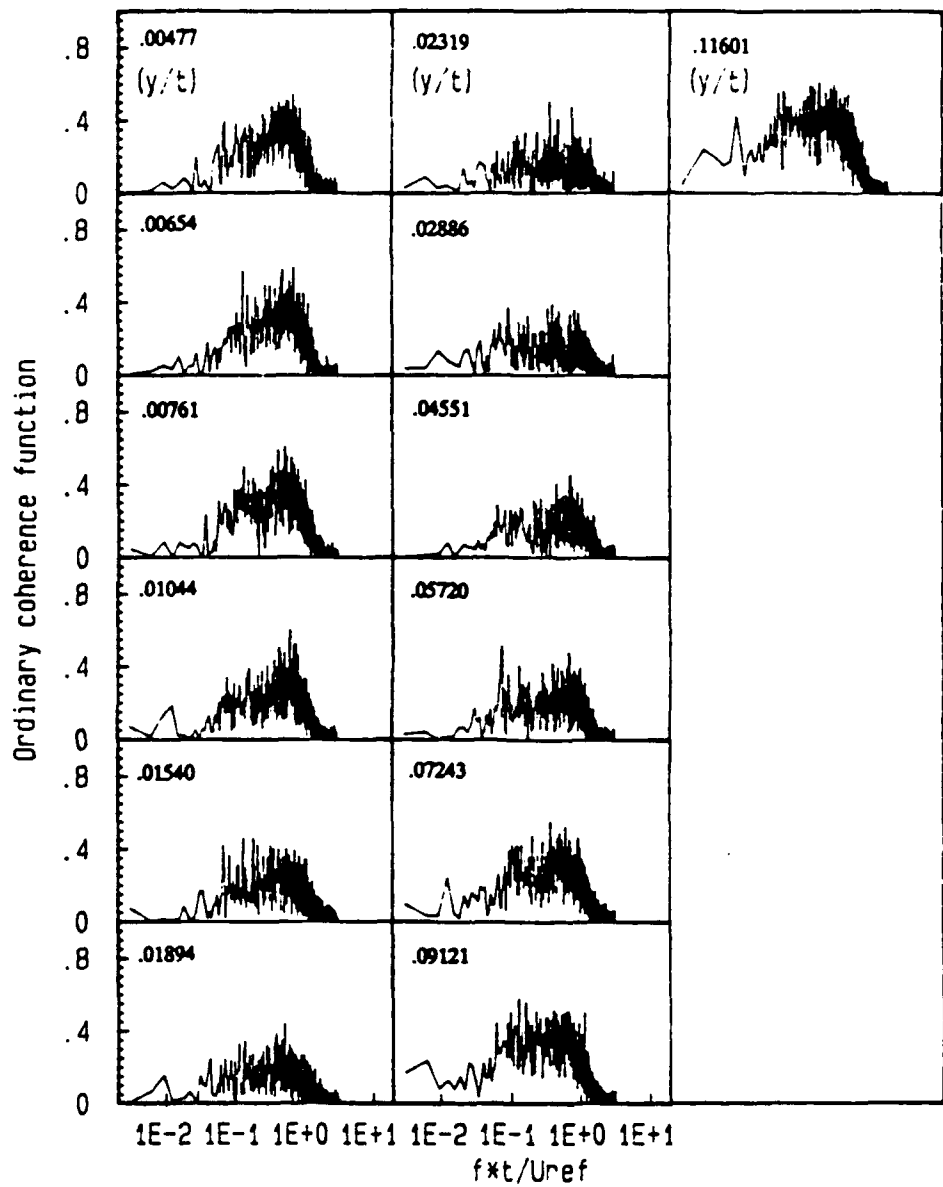
Figure 116: Ordinary coherence function of u component of velocity at x/t=-.0856 and pressure at x/t=0.0.
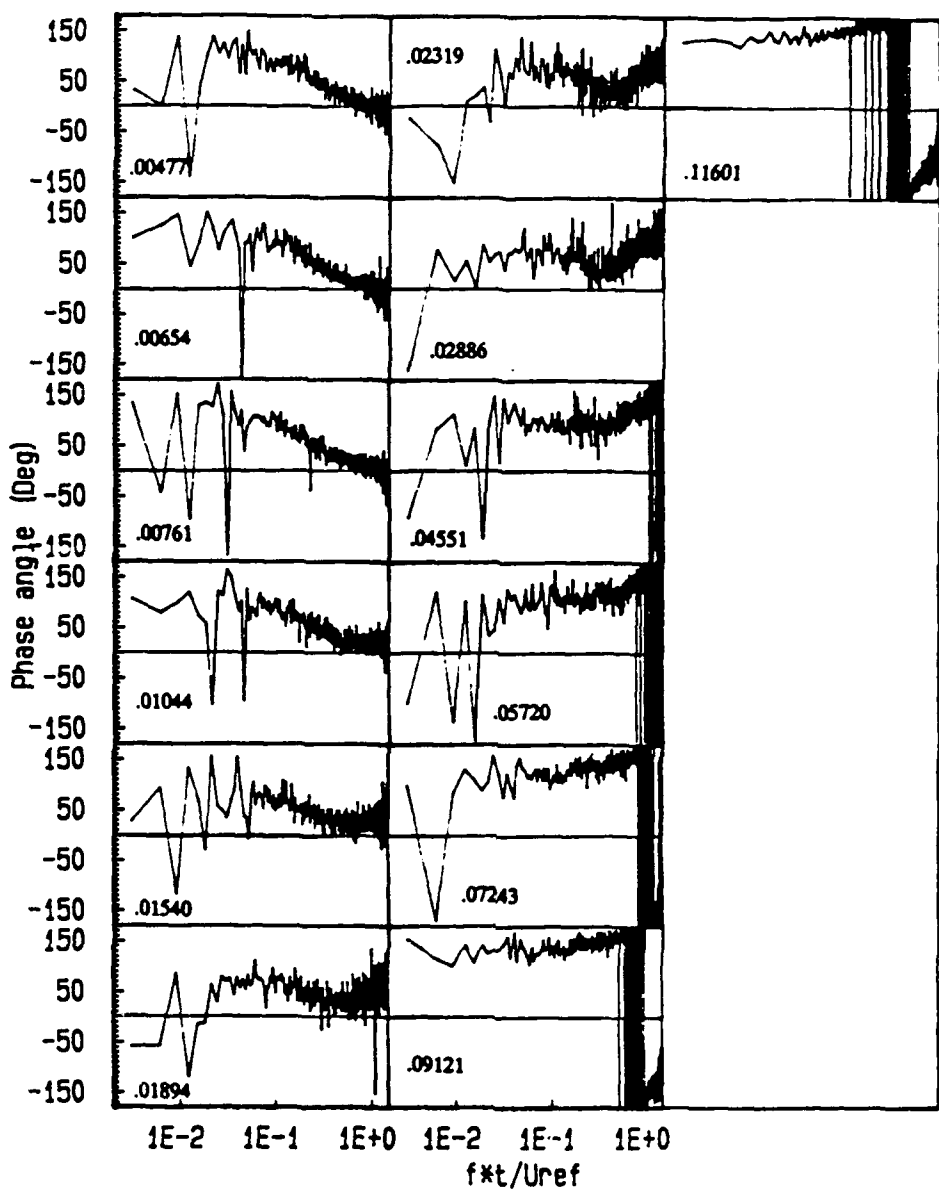
Figure 117:   Phase u component of velocity at x/t = -.0856 and pressure at x/t = 0.0.
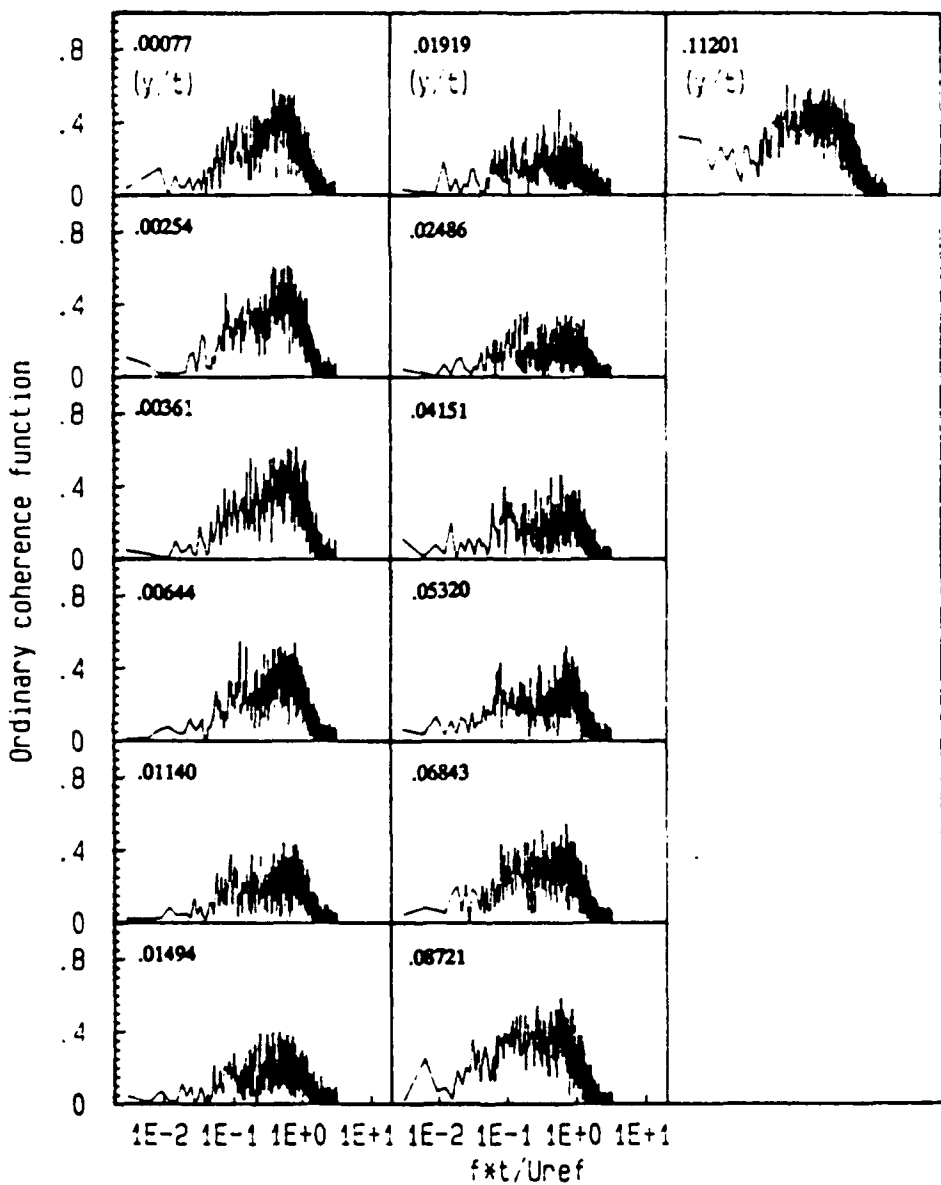
Figure 118: Ordinary coherence function of u component of velocity at x/t=-.0421 and pressure at x/t=0.0.
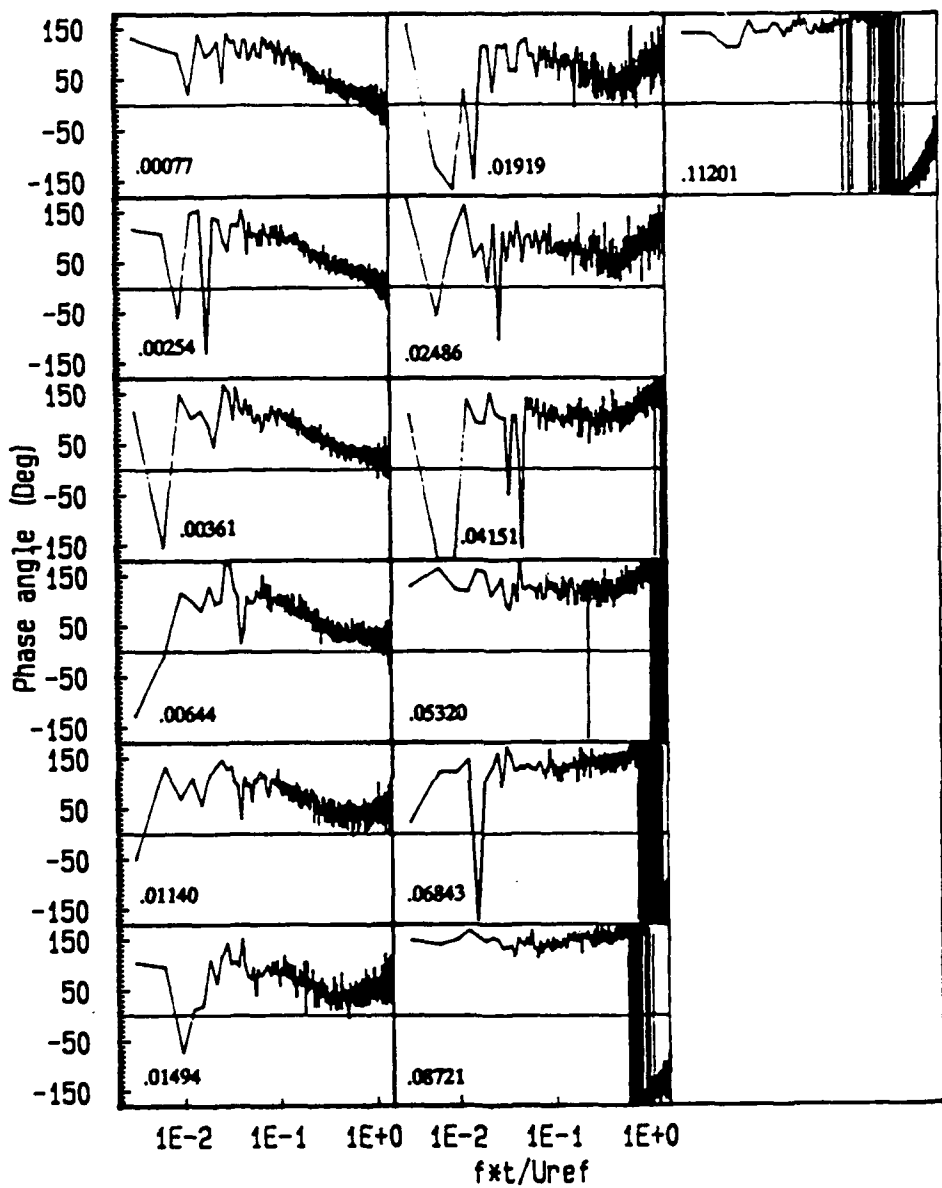
Figure 119: Phase u component of velocity at x/t=-.0421 and pressure at x/t=0.0.
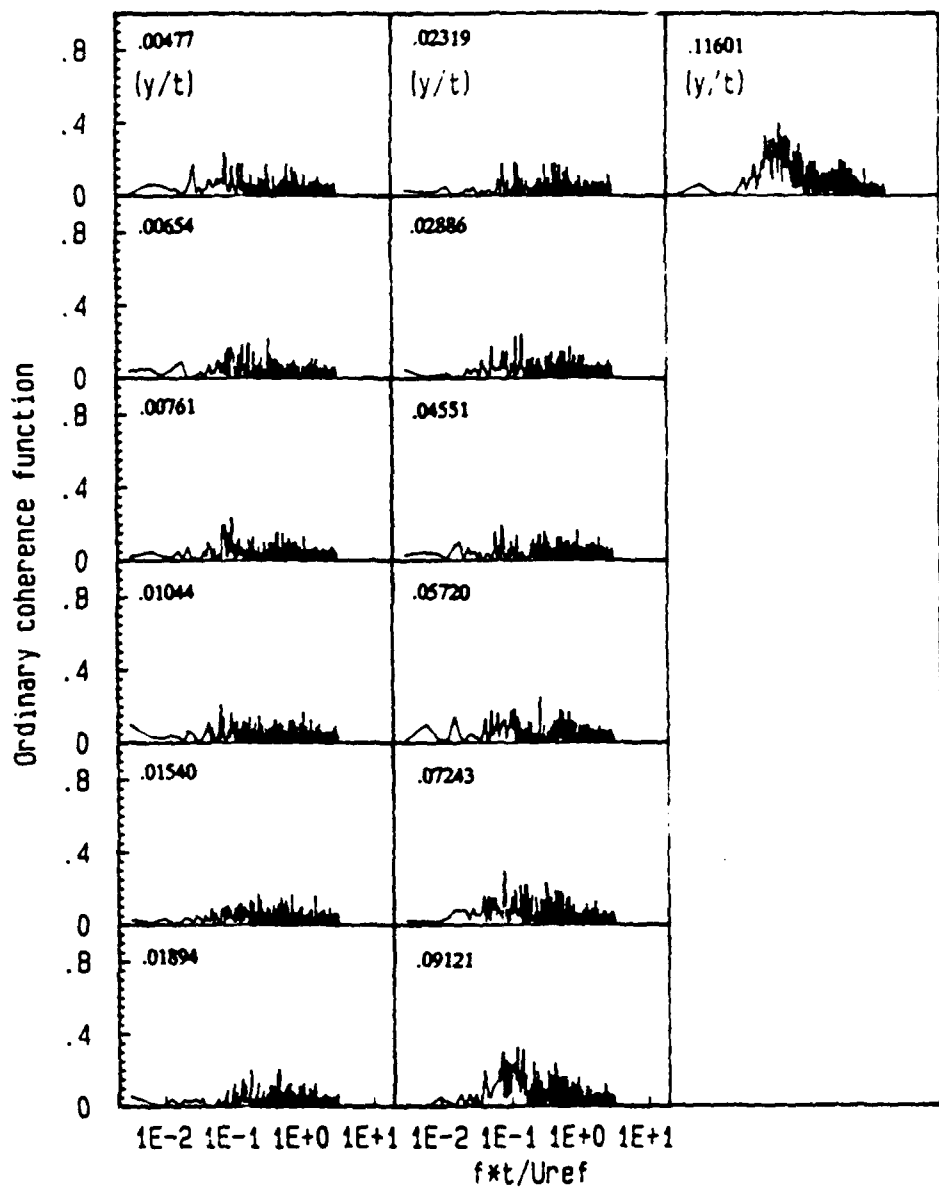
Figure 120:   Ordinary coherence function of v component of velocity at x/t=-.193 and pressure at x/t=0.0.
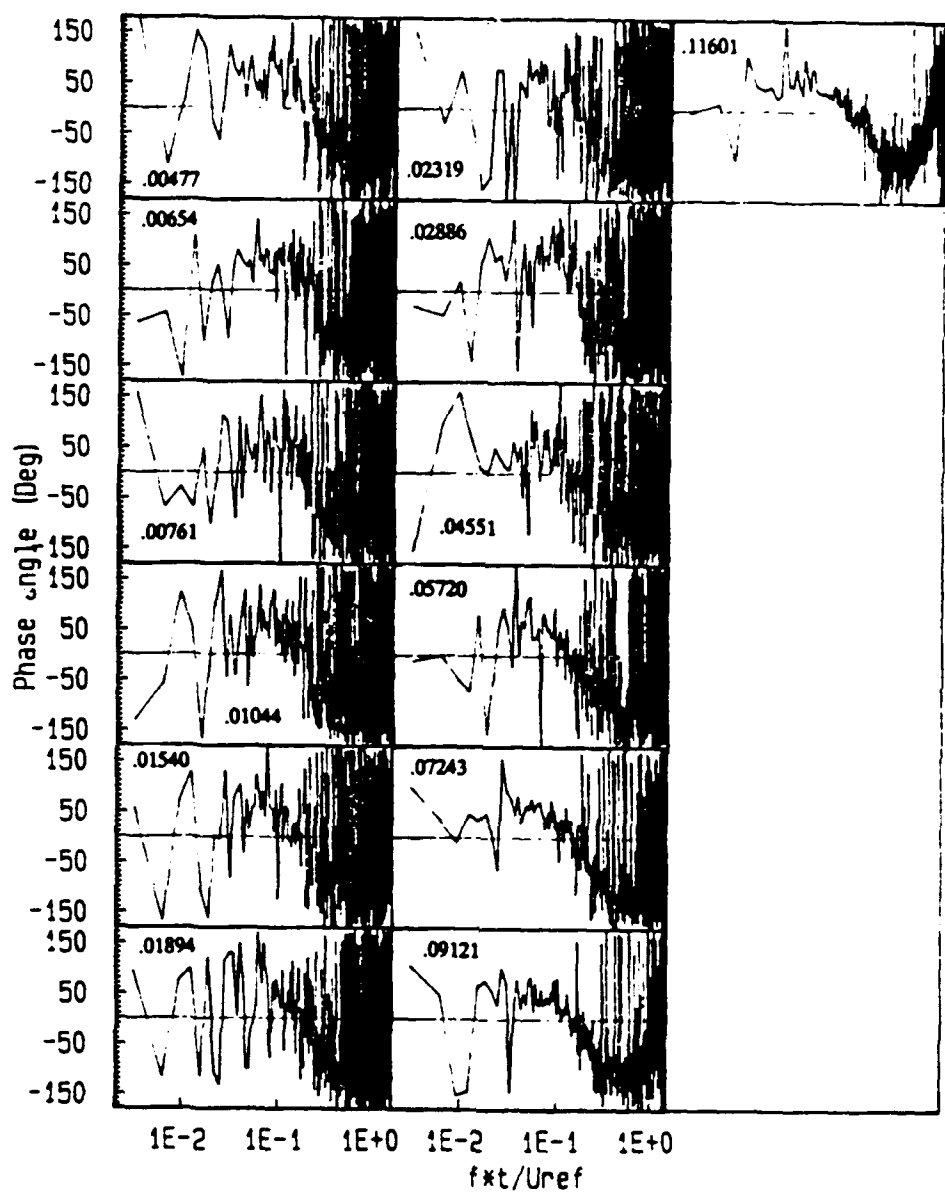
Figure 121: Phase v component of velocity at x/t = -.193 and pressure at x/t = 0.0.
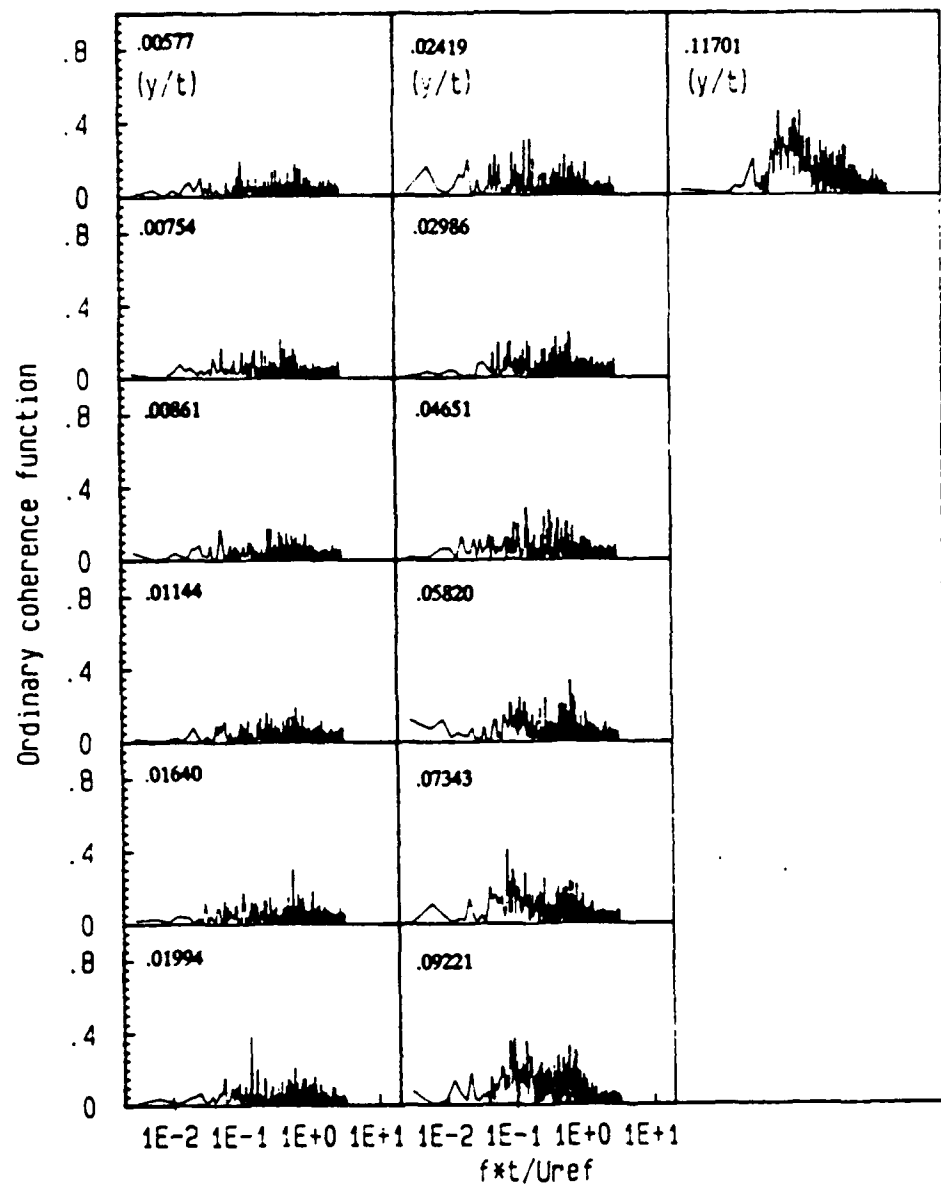
Figure 122: Ordinary coherence function of v component of velocity at x/t=-.139 and pressure at x/t=0.0.
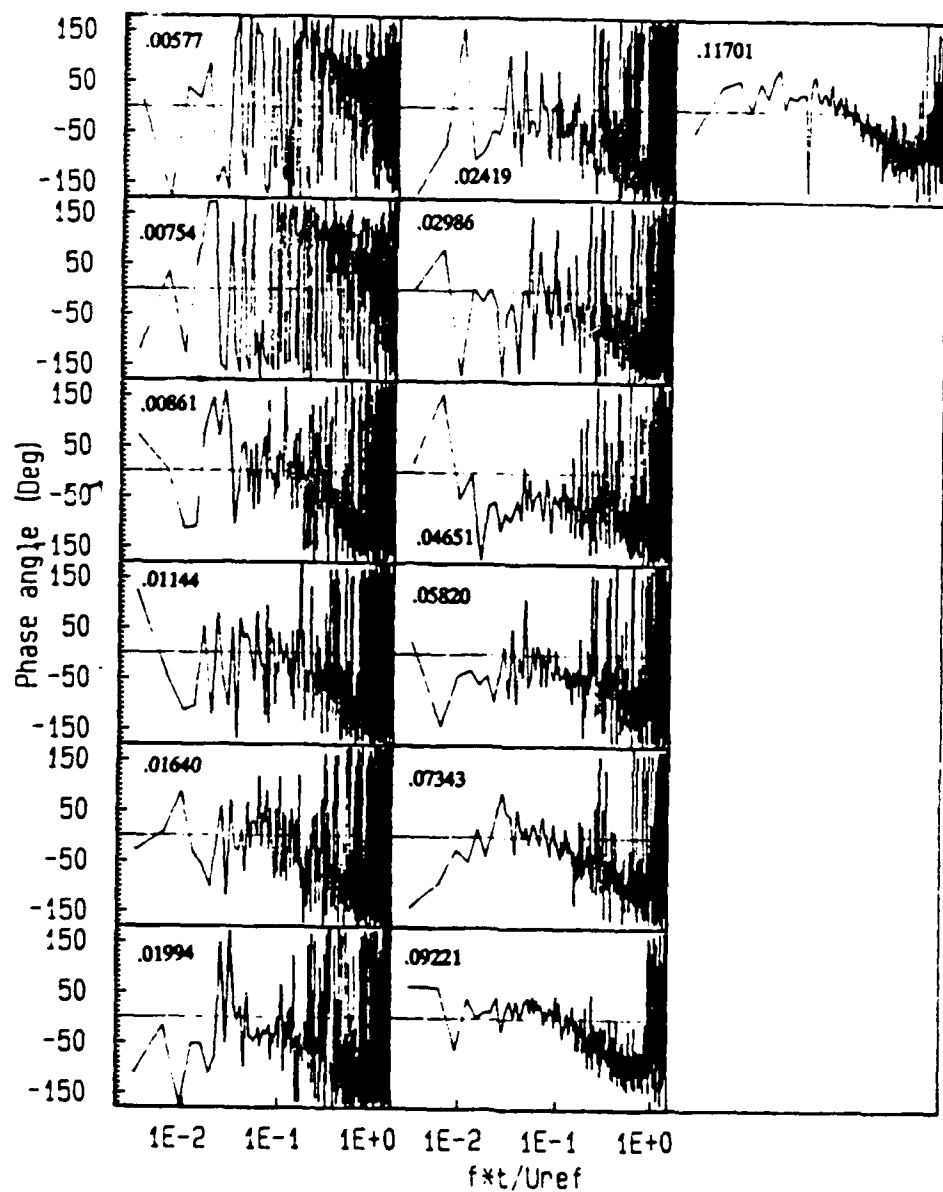
Figure 123:   Phase v component of velocity at x/t = -.139 and pressure at x/t = 0.0.
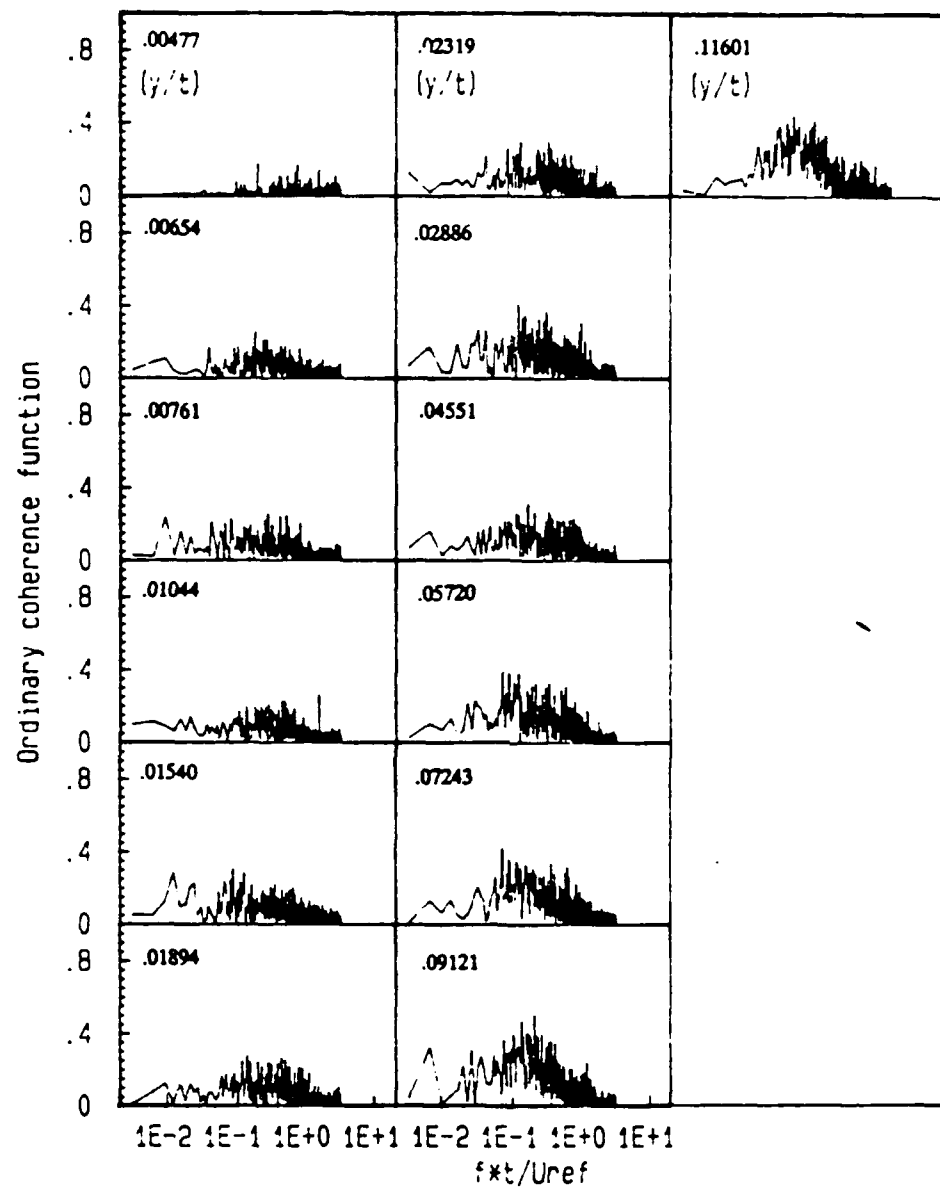
Figure 124: Ordinary coherence function of v component of velocity at x/t=-.0856 and pressure at x/t=0.0.
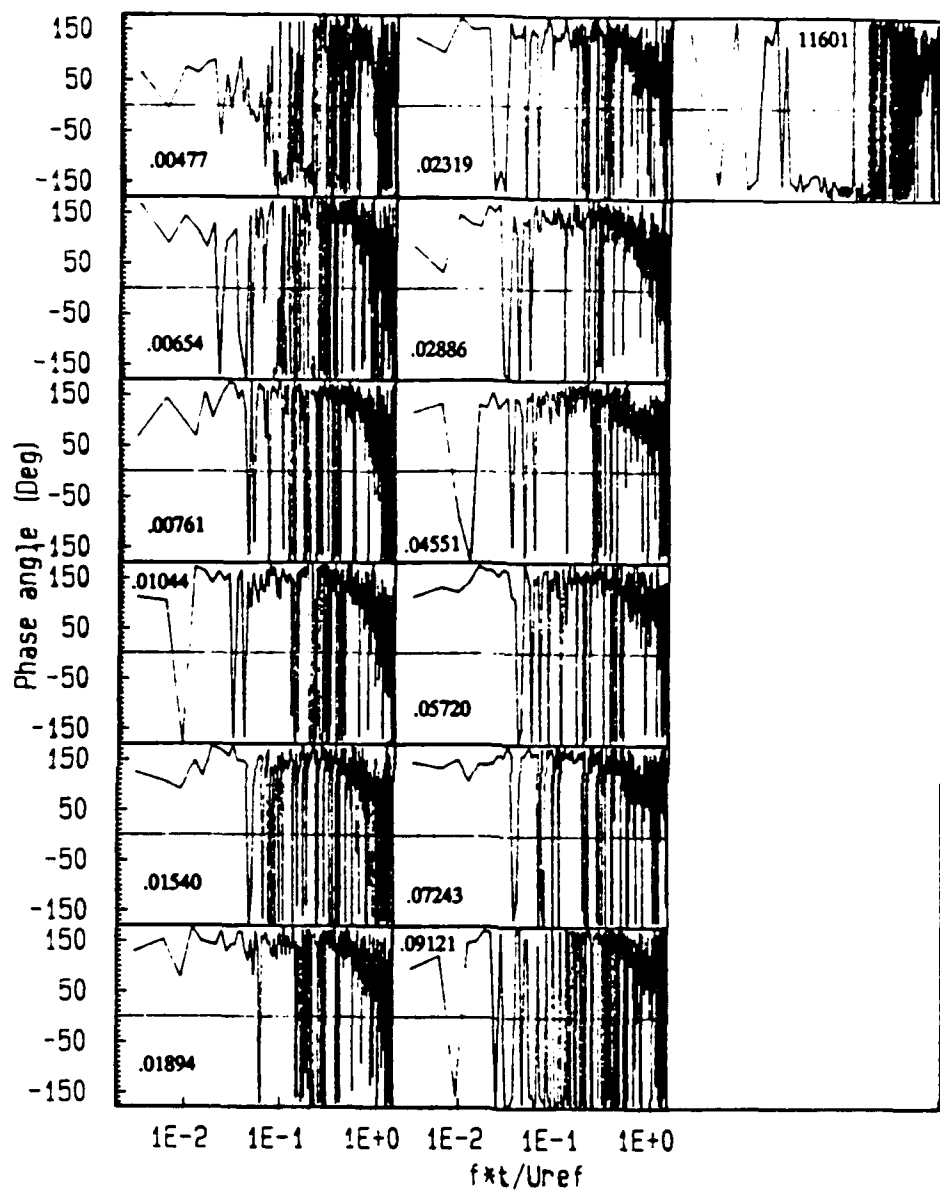
Figure 125:   Phase v component of velocity at x/t=-.0856 and pressure at x/t=0.0.
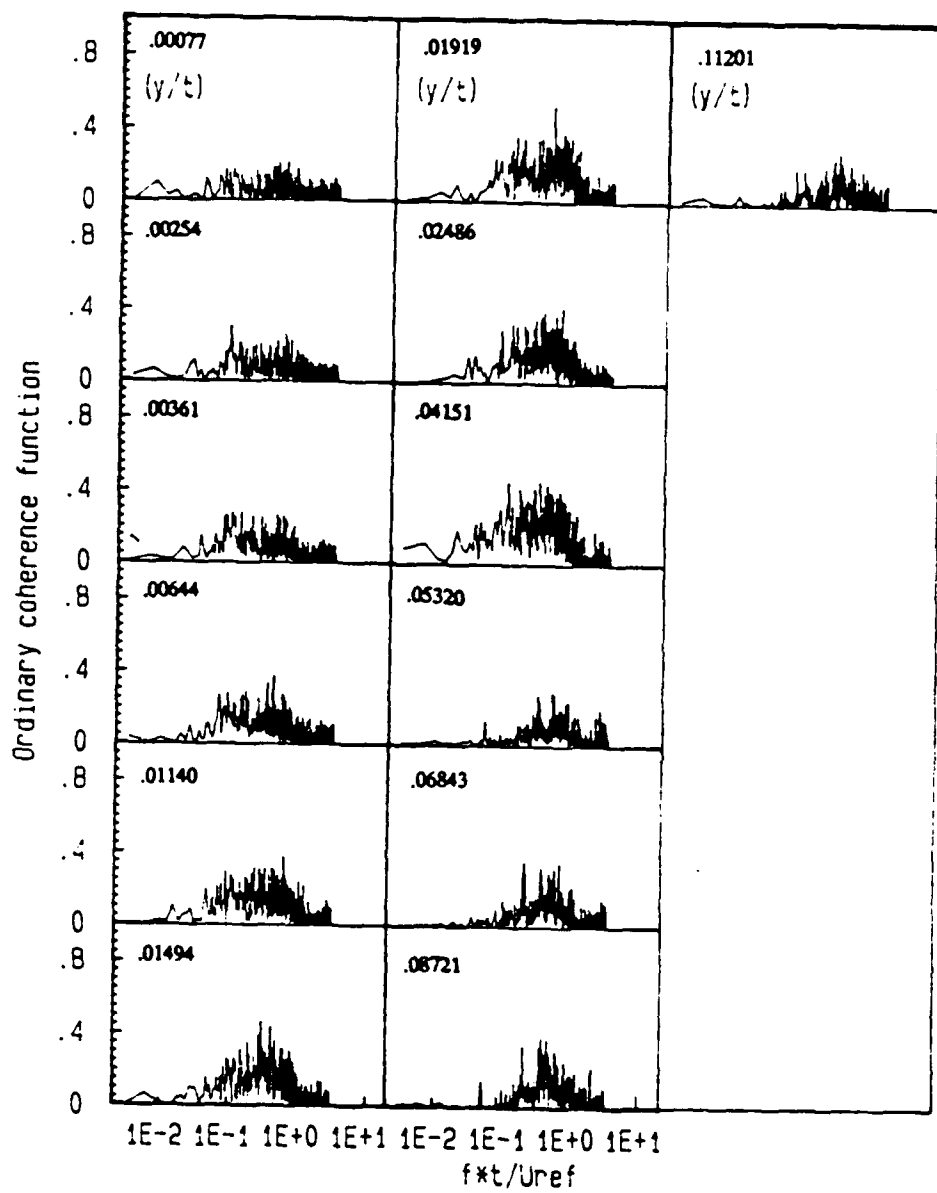
Figure 126: Ordinary coherence function of v component of velocity at x/t=-.0421 and pressure at x/t=0.0.
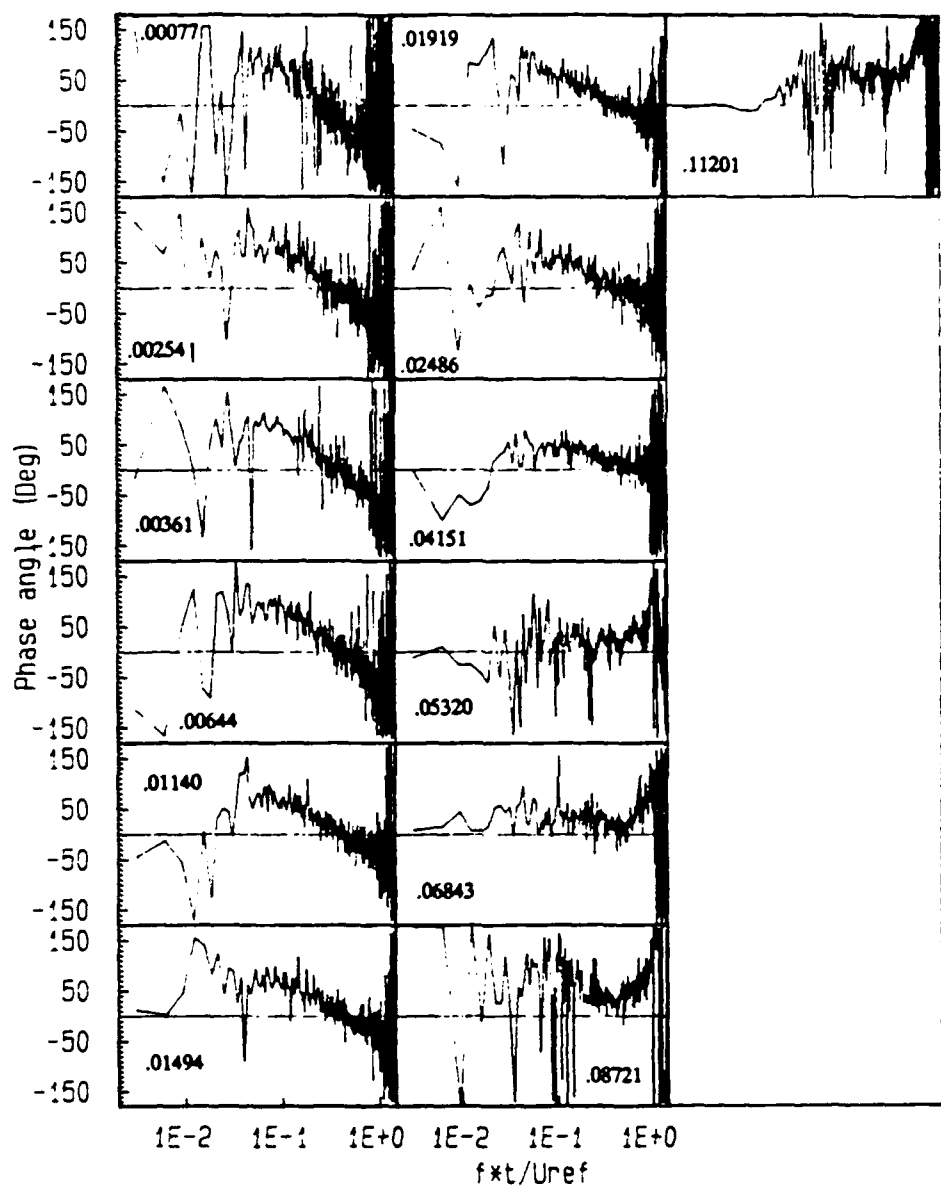
Figure 127: Phase v component of velocity at x/t = -.0421 and pressure at x/t = 0.0.
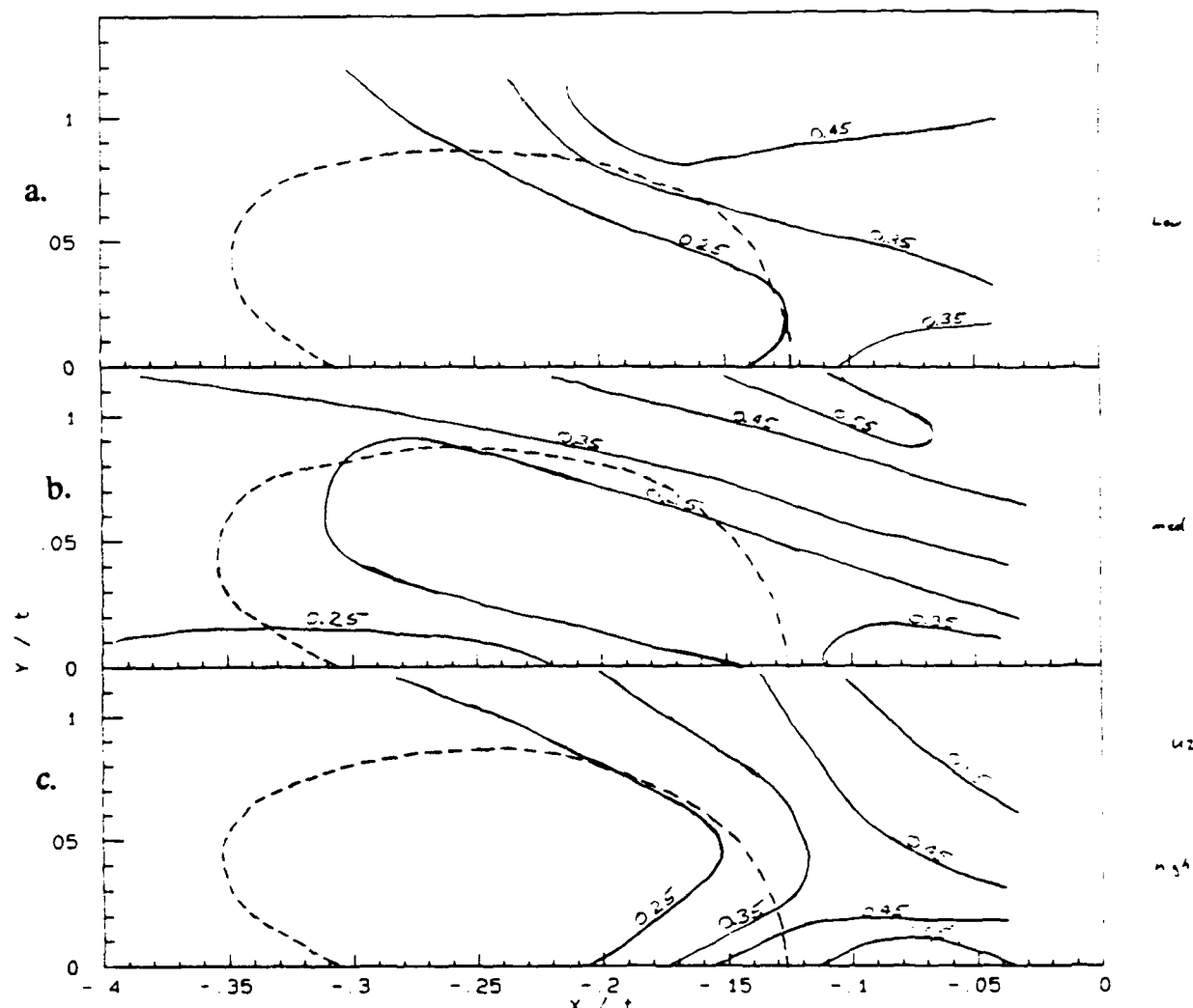
Figure 128: Contours of the maximum u ordinary coherence function with the pressure fluctuations at x/t=0.0 in the frequency range a. ft/U$_{ref}$=6×10^{-3} to ft/U$_{ref}$=0.5, b. ft/U$_{ref}$=7×10^{-2} to ft/U$_{ref}$=0.3, and c. ft/U$_{ref}$=0.4 to ft/U$_{ref}$=0.9. Dashed line indicates the composite (U and V) bimodal zone.
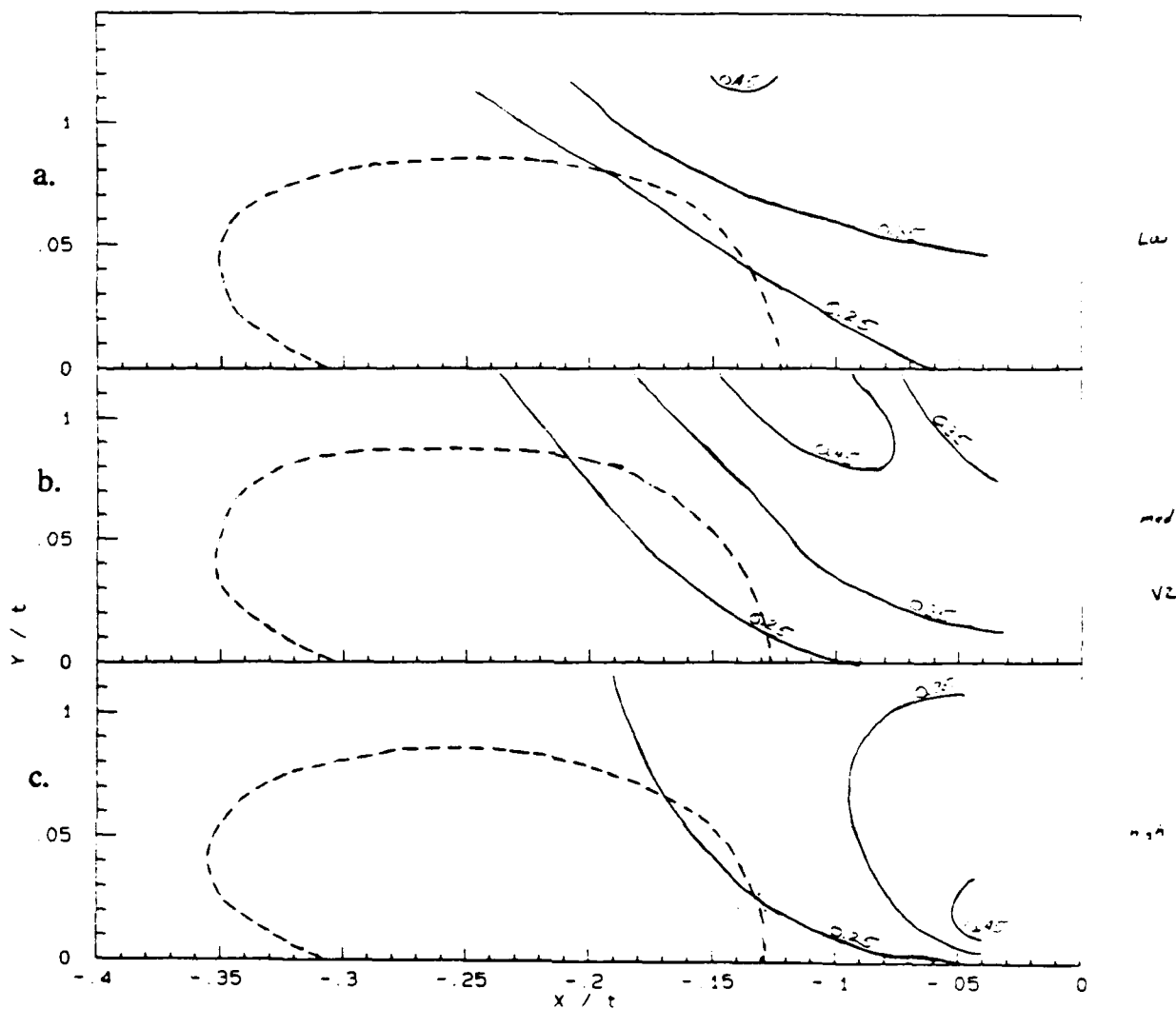
Figure 129:   Contours of the maximum v ordinary coherence function with the pressure fluctuations at $x/t=0.0$ in the frequency range a. $ft/U_{ref}=6\times10^{-3}$ to $ft/U_{ref}=0.5$, b. $ft/U_{ref}=7\times10^{-2}$ to $ft/U_{ref}=0.3$, and c. $ft/U_{ref}=0.4$ to $ft/U_{ref}=0.9$. Dashed line indicates the composite (U and V) bimodal zone.

Tables

Table 1:   Velocity measurement uncertainties. Note that $\delta(\ )/U_{ref}$ refers to a mean velocity and $\delta(^-)^{-2}/U_{ref}^2$ is a mean square velocity.

x/t	y/t	Velocity component	$\delta(\ )/U_{ref}$	$\delta(^-)^{-2}/U_{ref}^2$
-.0421	.00744	U	.01502	.008148
-.237	.00654	U	.01532	.009241
-.391	.11801	U	.01955	.001511
-.0421	.00644	V	.004554	.0006386
-.237	.00654	V	.004429	.0001310
-.391	.11801	V	.002905	.0005774

Table 2: Uncertainty estimates on the ordinary coherence function and standard deviations for the phase angle for various values of the coherence function.

γ_{xy}^2	$\epsilon[\gamma_{xy}^2]$	$\dfrac{e[\gamma_{xy}^2]}{\gamma_{xy}^2}$	$s.d.[\Phi_{xy}]$
.235	.2352	1.001	.1345
.3	.1905	.635	.1139
.4	.1414	.354	.0913
.5	.1054	.211	.0745
.6	.0770	.128	.0609
.7	.0535	.0764	.0488
.8	.0333	.0416	.0373
.9	.0157	.0174	.0248

Table 3: Uncertainties on the cross-correlation coefficient function at several velocity measurement locations for the u component.

	Velocity Measurement Position					
	x/t = -.0421 y/t = .00644		x/t = -.237 y/t = .00654		x/t = -.391 y/t = .11801	
	Pressure Measurement Position					
$/\rho_{xy}/$	x/t = 0.0	x/t = -.20	x/t = 0.0	x/t = -.20	x/t = 0.0	x/t = -.20
0.0	.00128	.00118	6.02×10^{-5}	7.12×10^{-5}	.00156	.00115
0.2	.00160	.00158	1.83×10^{-4}	2.08×10^{-4}	.00179	.00155
0.4	.00136	.00129	1.09×10^{-4}	1.20×10^{-4}	.00162	.00126
0.6	.00132	.00123	8.95×10^{-5}	9.69×10^{-5}	.00159	.00120
0.8	.00130	.00121	8.13×10^{-5}	8.63×10^{-5}	.00157	.00118
1.0	.001296	.001205	7.71×10^{-5}	8.12×10^{-5}	.00156	.00117

Table 4: Uncertainties on the cross-correlation coefficient function at several velocity measurement locations for the v component.

	Velocity Measurement Position					
	x/t=-.0421 y/t=.00644		x/t=-.237 y/t=.00654		x/t=-.391 y/t=.11801	
	Pressure Measurement Position					
$/\rho_{xy}/$	x/t=0.0	x/t=-.20	x/t=0.0	x/t=-.20	x/t=0.0	x/t=-.20
0.0	.00134	.00385	9.44×10^{-5}	1.29×10^{-4}	2.17×10^{-4}	2.61×10^{-4}
0.2	.00167	.0181	2.90×10^{-4}	3.09×10^{-4}	4.72×10^{-4}	4.74×10^{-4}
0.4	.00143	.00967	1.66×10^{-4}	1.91×10^{-4}	3.02×10^{-4}	3.28×10^{-4}
0.6	.00138	.00706	1.31×10^{-4}	1.59×10^{-4}	2.58×10^{-4}	2.93×10^{-4}
0.8	.00136	.00587	1.16×10^{-4}	1.47×10^{-4}	2.41×10^{-4}	2.79×10^{-4}
1.0	.00135	.00524	1.09×10^{-4}	1.41×10^{-4}	2.33×10^{-4}	2.73×10^{-4}

Table 5:   Boundary layer properties measured by Devenport and Simpson (1990a) in the boundary layer wind tunnel.

x/t	U_{ref} (m/s)	θ/t	δ^*/t	$\delta_{99.5}/t$	C_f	Re_θ
-2.15	27	.057	.077	.501	.0026	6561